CD-ROM

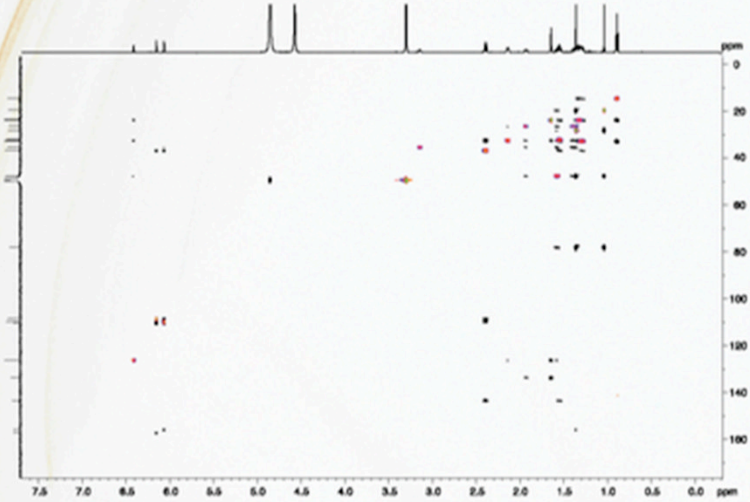

A Primer of NMR Theory with Calculations in *Mathematica*®

ALAN J. BENESI

WILEY

A PRIMER OF NMR THEORY WITH CALCULATIONS IN MATHEMATICA®

A PRIMER OF NMR THEORY WITH CALCULATIONS IN MATHEMATICA®

ALAN J. BENESI
Former Director
NMR Facility
The Pennsylvania State University
University Park, PA, USA

WILEY

Copyright © 2015 by John Wiley & Sons, Inc. All rights reserved

Published by John Wiley & Sons, Inc., Hoboken, New Jersey
Published simultaneously in Canada

No part of this publication may be reproduced, stored in a retrieval system, or transmitted in any form or by any means, electronic, mechanical, photocopying, recording, scanning, or otherwise, except as permitted under Section 107 or 108 of the 1976 United States Copyright Act, without either the prior written permission of the Publisher, or authorization through payment of the appropriate per-copy fee to the Copyright Clearance Center, Inc., 222 Rosewood Drive, Danvers, MA 01923, (978) 750-8400, fax (978) 750-4470, or on the web at www.copyright.com. Requests to the Publisher for permission should be addressed to the Permissions Department, John Wiley & Sons, Inc., 111 River Street, Hoboken, NJ 07030, (201) 748-6011, fax (201) 748-6008, or online at http://www.wiley.com/go/permissions.

Limit of Liability/Disclaimer of Warranty: While the publisher and author have used their best efforts in preparing this book, they make no representations or warranties with respect to the accuracy or completeness of the contents of this book and specifically disclaim any implied warranties of merchantability or fitness for a particular purpose. No warranty may be created or extended by sales representatives or written sales materials. The advice and strategies contained herein may not be suitable for your situation. You should consult with a professional where appropriate. Neither the publisher nor author shall be liable for any loss of profit or any other commercial damages, including but not limited to special, incidental, consequential, or other damages.

For general information on our other products and services or for technical support, please contact our Customer Care Department within the United States at (800) 762-2974, outside the United States at (317) 572-3993 or fax (317) 572-4002.

Wiley also publishes its books in a variety of electronic formats. Some content that appears in print may not be available in electronic formats. For more information about Wiley products, visit our web site at www.wiley.com.

Library of Congress Cataloging-in-Publication Data:

Benesi, Alan J., 1950–
A primer of NMR theory with calculations in Mathematica® / Alan J. Benesi.
pages cm
Includes bibliographical references and index.
ISBN 978-1-118-58899-4 (cloth)
1. Nuclear magnetic resonance spectroscopy–Data processing. I. Title. II. Title: Primer of nuclear magnetic resonance theory with calculations in Mathematica.
QD96.N8B46 2015
538′.362028553–dc23
2014048320

Set in 10/12pt Times by SPi Global, Pondicherry, India

Printed in the United States of America

10 9 8 7 6 5 4 3 2 1

Mathematica® is a registered trademark of Wolfram Research, Inc.

1 2015

CONTENTS

PREFACE

> There are two ways to live: you can live as if nothing is a miracle; you can live as if everything is a miracle.
>
> —*Albert Einstein*

The faint radiofrequency signals detected in nuclear magnetic resonance (NMR) spectroscopy provide a window into the structure and dynamics of atoms in solids, liquids, and gases. No other experimental technique comes close to the range of atomic-level information that NMR can provide. To me, NMR is a miracle. In order to understand NMR, one must master both its experimental and its theoretical aspects. It also helps to be knowledgeable in chemistry. Although experimental NMR is becoming easier as commercial spectrometers evolve, the theory of NMR is still "hard" and is the area in which many NMR spectroscopists are weak. Therefore, in this primer, the theory of NMR is presented concisely and is used in calculations to understand, predict, and simulate the results of NMR experiments. The focus is on the beautiful physics of NMR. The basics of experimental NMR are included to provide perspective and a clear connection with theory. This primer is not comprehensive and is limited to material covered in a graduate-level theoretical NMR class I taught at Penn State for 25 years. There is only cursory discussion of some important NMR topics such as cross polarization or unpaired electron spin–nuclear spin interactions. Nevertheless, a person who has "made it" through this book will be well equipped to understand most topics in the NMR literature.

Throughout my quest to master NMR spectroscopy, I have used the programming language Mathematica, or its predecessor SMP. Here, Mathematica notebooks are used to carry out most of the calculations. These notebooks are also intended to provide useful calculation templates for NMR researchers. Although it is not necessary to have Mathematica to gain understanding from this book, I highly recommend it.

I am grateful to the many pioneers, colleagues, professors, friends, and mentors in the NMR community who have personally or in their publications answered my questions along the way, including but not limited to A. Abragam, H.W. Spiess, M. Levitt, M. Mehring, Burkhard Geil, Paul Ellis, Lloyd Jackman, Juliette Lecomte, Chris Falzone, Ad Bax, Karl Mueller, Richard Ernst, Attila Szabo, Dennis Torchia, Bernie Gerstein, Kurt Wuthrich, Mike Geckle, Clemens Anklin, Matt Augustine, David Boehr, Scott Showalter, John Lintner, Kevin Geohring, Ted Claiborne, Tom Gerig, Tom Raidy, and Alex Pines. The NMR community is lucky to include such kind and inspiring human beings.

Alan J. Benesi

CHAPTER 1

INTRODUCTION

Nuclear magnetic resonance (NMR) spectroscopy can provide detailed information about nuclei of almost any element. NMR allows one to determine the chemical environment and dynamics of molecules and ions that contain the observed nuclei. With modern NMR spectrometers, one can observe nuclei of several elements at once. Biological NMR, for example, often employs radio frequency pulses on ^{1}H, ^{13}C, and ^{15}N nuclei within a single experiment. Some of the most useful NMR experiments obtain information by using 20 or more radio frequency pulses applied to the different NMR nuclei at specific times. What makes these sophisticated experiments possible is the mathematical perfection of the quantum mechanics that underlies NMR.

Whether one looks at liquids, solids, or gases, the nuclei being observed are selected by their unique resonance (Larmor) frequencies in the radio frequency range of the electromagnetic spectrum. Choosing a nucleus for observation is analogous to choosing a radio station.

NMR requires a magnet, usually with a very homogeneous magnetic field except when pulsed magnetic field gradients are applied. The magnetic field splits the quantized nuclear spin angular momentum states, thereby allowing transitions between them that can be stimulated by radio frequency excitation. Only transitions between adjacent levels are allowed, and since the levels for a given nucleus are equally separated in energy, the transitions all occur at the same resonance (Larmor) frequency.[1] The resonance frequency of a given nucleus is proportional to the strength of the magnetic field and is generally in the radio frequency range of 10^{6} to 10^{9} sec^{-1} on superconducting magnets of 1–25 Tesla magnetic field strength. Several specific advantages of high magnetic fields are that they give stronger NMR signals, better resolution of chemical shifts, and better resolution for solid samples of odd-half-integer quadrupolar nuclei.

Magnetic resonance imaging is a special type of NMR that takes advantage of the linear relationship between the resonance frequency of a nucleus and the magnetic field. In the presence of a magnetic field gradient, the observed resonance frequency varies with position within the sample, allowing for direct correlation between frequency and position that can be used to create an image. Pulsed magnetic field gradients are also used to select desired NMR signals in nonimaging experiments.

---

[1] But higher order transitions can be observed in some cases.

A Primer of NMR Theory with Calculations in Mathematica®, First Edition. Alan J. Benesi.

The quantum mechanics that is the basis of NMR spectroscopy has been covered beautifully in books by Abragam (1983), Spiess (1978), Mehring (1983), Ernst et al. (1987), Gerstein and Dybowski (1985), Levitt (2008), and Jacobsen (2007). In this book, the goal is to review the theoretical basis of NMR in a concise, cohesive manner and demonstrate the mathematics and physics *explicitly* with Mathematica notebooks. Readers are urged to go through all the Mathematica notebooks as they are presented and to use the notebooks as templates for homework problems and for real research problems. The notebooks are a "toolbox" for NMR calculations.

The primer is intended for graduate students and researchers who use NMR spectroscopy. The chapters are short but become longer and more involved as the primer progresses. The primer starts with chapters describing the NMR spectrometer and the NMR experiment and proceeds with the classical view of magnetism, the Bloch equation, and the vector model of NMR. Then it goes directly to quantum mechanics by introducing the density operator, whose evolution can be predicted by using either matrix representation of the spin angular momentum operators or commutation relations between them (product operator theory). It then transitions to coherence order pathways, phase cycles, pulsed magnetic field gradients, and the *design* of NMR pulse sequences. With the help of Mathematica notebooks, it presents the elegant mathematics of solid state NMR, including spherical tensors and Wigner rotations. Then the focus changes to the effects of atomic and molecular motions in solids and liquids on NMR spectra, including mathematical methods needed to understand slow, intermediate, and fast exchange. Finally, it finishes with the amazing and perfect connection between molecular-level reorientational dynamics and NMR relaxation.

CHAPTER 2

USING MATHEMATICA; HOMEWORK PHILOSOPHY

In this primer, the version 8.0.4.0 Mathematica programming language was used to carry out calculations presented in Mathematica notebooks (e.g., *xyz.nb*). All of the notebooks are provided in a DVD included with the book. It is assumed that the reader has Mathematica and can therefore carry out the calculations step by step or carry them out by evaluating the entire notebook. Step-by-step calculations are advantageous because they enable the user to see the mathematics and learn about the Mathematica language, syntax, and programming at the same time.

The user is urged to make extensive use of the Help→Documentation Center→Search routine to learn about Mathematica. Some useful searches are "Mathematica syntax," "Mathematica syntax characters," "Immediate and Delayed Definitions," and "Defining Variables and Functions." Once one learns the basics of Mathematica, the notebooks used in this book become almost transparent.

Explanation of the Mathematica programming is presented explicitly in the text when the notebooks are first discussed. These are simply called "Explanation of *xyz.nb*" at the end of the chapter. The first notebooks and their text explanations are encountered in Chapters 5, 6, 7, and 9. The explanations in the early chapters provide more detailed descriptions of the programming than those in the later chapters.

The user is encouraged to make changes in the provided notebooks and see how they affect the results. It is advisable to go through every calculation in the notebooks step by step, not only to see how physics works in detail but also to learn the Mathematica language and syntax. Be forewarned that crashes can occur, so keep in mind that the correct starting notebook(s) can always be reloaded from the DVD or other storage media.

For those who cannot purchase Mathematica, a free download of the Mathematica CDF Player is available online. This form of Mathematica does not allow the user to change input lines and thereby learn step by step, but it does enable the entire notebook to be evaluated. The Mathematica notebooks (*xyz.nb*) are also provided as (*xyz.cdf*) on the DVD provided with the primer.

The homework problems are placed at the end of each chapter. Answers are *not* provided. The Mathematica notebooks, references, and text explanations provide the necessary help.

A Primer of NMR Theory with Calculations in Mathematica®, First Edition. Alan J. Benesi.

CHAPTER 3

THE NMR SPECTROMETER

A modern NMR spectrometer consists of a superconducting magnet, a probe that holds the NMR sample in the strongest and most homogeneous part of the magnetic field of the magnet, a console containing radio frequency (rf)–generating electronics, amplifiers, and a receiver; a preamplifier that amplifies the very small NMR signals emitted by the sample after rf excitation; and a computer to control the hardware and process the NMR signals to yield spectra. The rf signals to and from the sample are carried in coaxial cables and propagate at about two-thirds the speed of light. A schematic of a modern NMR spectrometer is shown in Figure 3.1.

A superconducting magnet consists of a coil of superconducting wire, typically Niobium–Tin or Niobium–Titanium alloy, immersed in liquid Helium. The boiling temperature of liquid Helium at 1 atm pressure is 4.2 K, well below the superconducting critical temperature of the wire, allowing a current to flow without resistance in the coil. The current flow through the coil generates the magnetic field used in NMR. To accomodate NMR samples at room temperature or other temperatures, the liquid helium–immersed superconducting coil is housed in a toroidal dewar, the central "hole" of which is open to the atmosphere at room temperature and holds the shim stack and NMR probe. Typically, the dewar is constructed of stainless steel, with high vacuum between dewar sections containing liquid Nitrogen and liquid Helium and also between the liquid Nitrogen dewar and the outer surface of the magnet. Figure 3.2 shows a schematic of a vertical cross-section of a superconducting magnet.

Activation of a superconducting magnet is carried out by using an external power supply to ramp up the current in the superconducting coil (already immersed in liquid He) until the desired current and corresponding magnetic field are achieved. At this point, the external power supply is disconnected from the superconducting coil, but the current is maintained in the coil because there is no resistance. As long as the coil is intact and immersed in liquid helium, the current and corresponding magnetic field can be maintained indefinitely.

Unfortunately, the world has used up most of the easily accessible Helium, so efforts are underway to reclaim Helium whenever possible and to develop liquid Nitrogen superconductors that can sustain the high current needed for NMR magnets.

The NMR sample fits in the probe and is situated at the strongest and most homogeneous part of the magnetic field where all of the magnetic lines of force are nearly perfectly parallel and of equal magnitude. The homogeneity of the magnetic field across the sample is further improved by using small corrective electromagnets called shims, located in the "shim stack" that surrounds the cavity occupied by

---

A Primer of NMR Theory with Calculations in Mathematica®, First Edition. Alan J. Benesi.

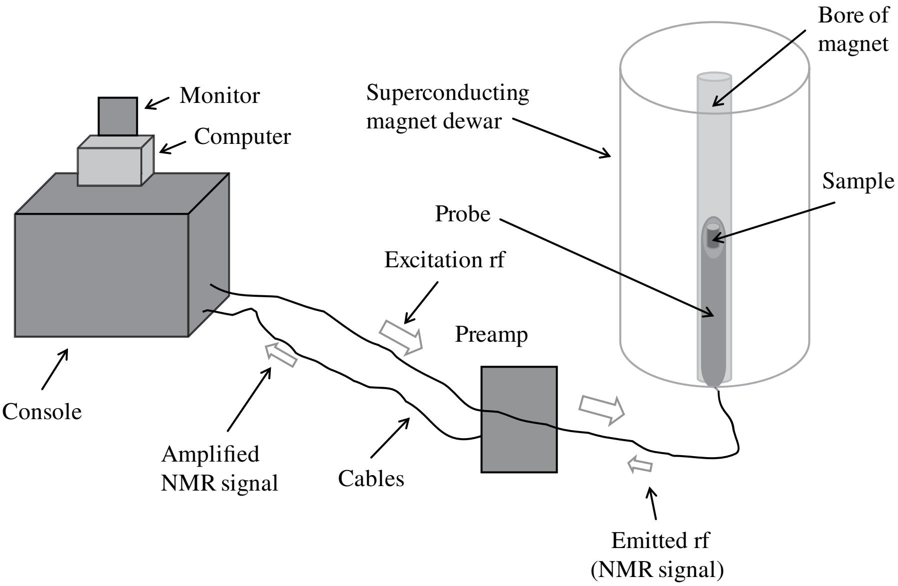

Figure 3.1 Schematic of a modern NMR spectrometer.

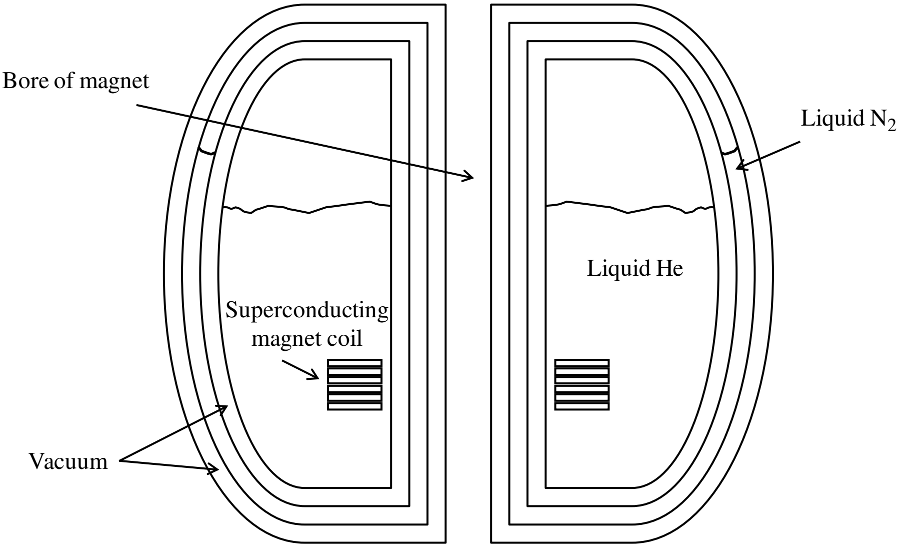

Figure 3.2 Vertical cross-section of a superconducting magnet.

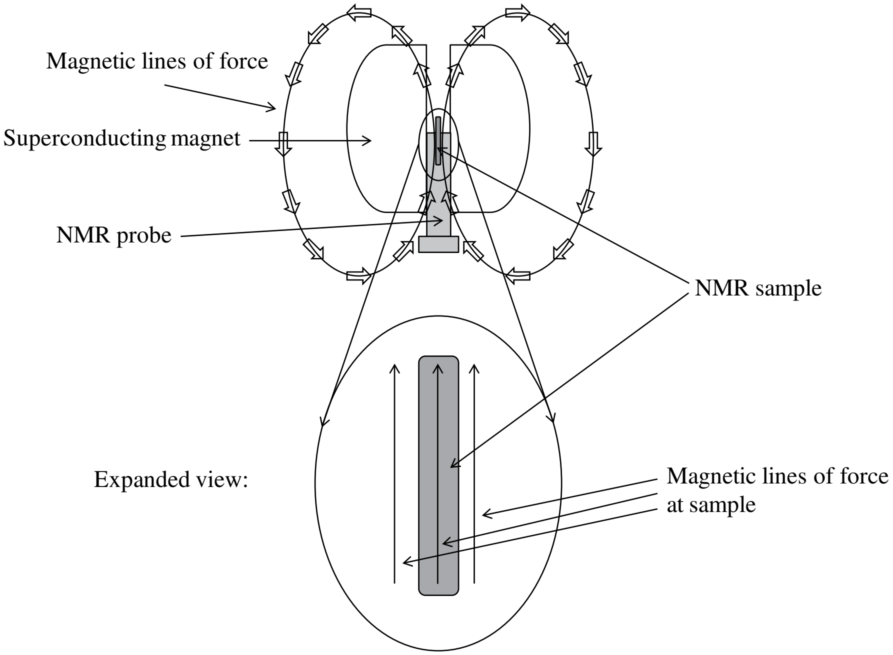

Figure 3.3 NMR sample placement relative to magnetic lines of force, vertical cross-section with expanded view.

the probe. Modest adjustable currents through the shims allow the magnetic field across the sample to be made almost perfectly homogeneous, thereby increasing both resolution and vertical peak intensity in the NMR spectrum. The NMR sample placement relative to the magnetic lines of force is shown in Figure 3.3.

CHAPTER 4

THE NMR EXPERIMENT

The sample is placed in the probe in the magnet. The probe is tuned to the desired resonance frequency(ies) and then shimmed to obtain a homogeneous magnetic field, that is, $\mathbf{B}=\{0,0,B_0\}$,[1] as shown in Figure 3.3. The magnetic field removes the degeneracy of the nuclear spin states—the Zeeman effect. The Zeeman Hamiltonian is $\hat{\mathrm{H}}_Z=-\gamma\, B_0\, \hat{\mathrm{I}}_z$. If the *nuclear spin quantum number* is I, the Zeeman Hamiltonian splits the quantized states into $2I+1$ evenly spaced energy levels, ranging from $m=-I$ to $+I$ in units of 1, corresponding to the different expectation values for $\hat{\mathrm{I}}_z$ ($I=0$ nuclei such as ^{16}O and ^{12}C have only one level and are not NMR observable). Figure 4.1 shows the Zeeman energy levels for an $I=1/2$ spin and an $I=1$ spin.

Transitions are only allowed between adjacent energy levels that are evenly spaced with $\Delta E=h\nu_0$ where ν_0 is the resonance (Larmor) frequency. $2\,\pi\,\nu_0=-\gamma\,B_0$, where γ is the gyromagnetic ratio of the nucleus in radian s^{-1} Tesla^{-1} and B_0 is the magnetic field in Tesla. Gyromagnetic ratios and Larmor frequencies for NMR observable elements are available in the online NMR Periodic Table.[2]

Radio frequency (rf) pulses of frequency ν_0 are generated in the console (see Fig. 3.1). At the probe, the rf pulse generates a linearly oscillating field in the x–y plane perpendicular to the magnetic field. A drawing of a Helmholtz rf coil used for liquid-state NMR samples is shown in Figure 4.2.

The rf is "gated" to create pulse(s), typically of about 1–100 μs duration. With modern spectrometers, it is possible to control the phase of the pulse precisely. The pulses are amplified in the console to 1–1000 W power. The rf pulse(s) propagate at approximately two-thirds the speed of light through the circuitry and coaxial cables to the probe and sample in the magnet. A duplexing or λ/4 arrangement is used to protect the sensitive preamplifier and receiver from the high-power rf pulse(s).

The rf pulses perturb the nuclear spin energy states, creating coherences that contain the energy imparted to the *nuclear spin system*. After the pulses are over, it is necessary to wait for the effects of the high-power rf pulses to dissipate through the electronic components before the NMR signal can be measured, about 5–100 μs depending on the Larmor frequency. Luckily, in most cases, the NMR signal emitted by the sample lasts much longer. Having been excited by the rf pulses into one or

---

[1] In the case of liquid samples, the sample is "locked" to allow compensation for small spontaneous changes in the magnetic field that would otherwise broaden the peaks. Usually the lock nucleus is ^{2}H.

[2] http://www.bruker-nmr.de/guide/eNMR/chem/NMRnuclei.html

A Primer of NMR Theory with Calculations in Mathematica®, First Edition. Alan J. Benesi.

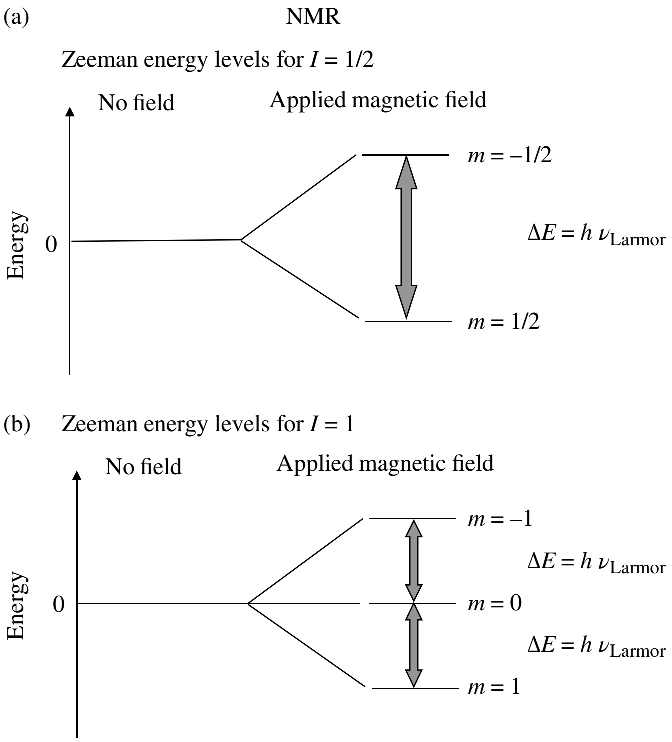

Figure 4.1 Zeeman energy levels for (a) $I = 1/2$ and (b) $I = 1$.

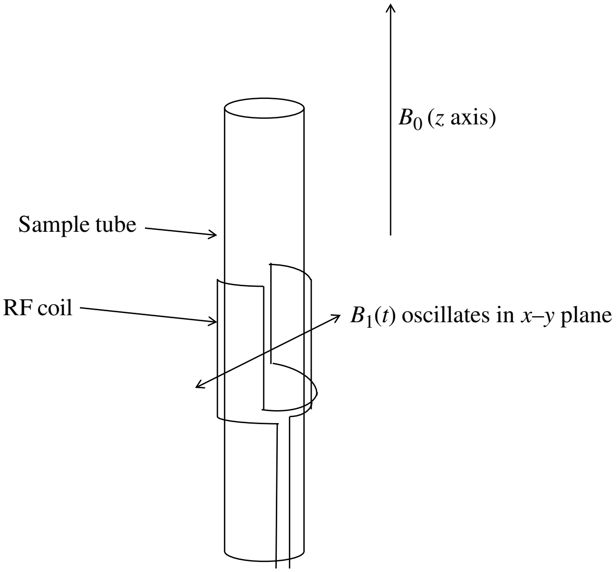

Figure 4.2 A Helmholtz rf coil.

more states of coherence, the NMR sample emits the rf signal, the NMR signal, at $\nu_0 \pm \delta$ kHz. The wavelength of the rf is larger than the size of the NMR sample, so accurate quantum mechanical description requires spatially dependent quantum field theory as opposed to the simpler long-distance excitation/emission theory that applies to radio transmission and reception. The absorption/emission process can also be accurately described with quantum electrodynamics (Feynman, 1985; Hoult and Bhakar, 1997). The easiest description of the absorption/emission process, however, is made with classical electrodynamics (Hoult, 1989). In this case, the NMR signal is modeled as a magnetic dipole moment rotating at the resonance (Larmor) frequency. The changing magnetic field induces an oscillating voltage at this frequency in the rf coil. This is the experimental NMR signal.[3] Do not be fooled by the success of this approach, however. There are very many aspects of NMR that the classical approach does not explain.

The emission of the energy stored in the spin system is not spontaneous. Spontaneous emission would take longer than the lifetime of the universe. In the language of quantum electrodynamics, the emission is *stimulated* by virtual rf photons (photons unobservable to external observers) arising from motions of the molecules containing and adjacent to the observed nuclei (see Chapters 36 and 39). The emission of the NMR signal typically lasts on the order of about 1 s.

The power of the emitted NMR signal is generally in the microwatt to milliwatt range, many orders of magnitude less than the power of the rf pulses used to excite the sample. The intensity of the signal depends on the number of NMR observable nuclei in the sample, the gyromagnetic ratio, and the magnetic field strength B_0. Unless it is increased artificially by isotopic enrichment, the number of NMR observable nuclei depends on the natural abundance of the isotope. The NMR signal is detected as an oscillating voltage on the same coil that delivered the rf pulse(s). It is “duplexed” to the preamplifier where it is amplified, then sent to the console where it is further amplified.

The amplified NMR signal is mixed with the input frequency ν_0 to yield the *difference* frequency $\pm\delta$ kHz in the *audio* frequency range. This signal is equivalent to the NMR signal in the *rotating frame* (see Chapter 7). The NMR signal is detected as an oscillating voltage on *two* receiver channels that are 90° ($\pi/2$ radians) apart in the rotating frame. The x and y components of the NMR signal in the rotating frame, equally real experimentally, are taken to be the “real” and “imaginary” components, respectively. The presence of two channels 90° apart in phase allows discrimination of positive and negative frequencies. The successive complex data points of the signal are separated by dw seconds, where dw is the “dwell” time. The dwell time is the inverse of the full width of the spectrum in s^{-1} (so a 1-MHz spectral width corresponds to a dwell time of 1 μs). Each complex data point is measured by opening the receiver channels for 50–100 ns, depending on the spectrometer. The total time during which the NMR signal is digitized is called the acquisition time. The *complex* time-dependent NMR signal is called the free induction decay (FID).

---

[3] External rf from other NMR spectrometers, computers, or communication devices can significantly distort the observed NMR spectrum.

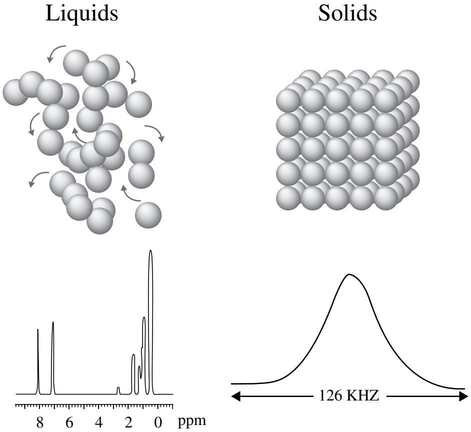

Figure 4.3 Effect of motional averaging on NMR spectra. Reproduced from a talk by Sharon Ashbrook, "The Power of Solid-State NMR," CASTEP Workshop, Oxford, August 2009.

The complex FID is Fourier-transformed and phased to yield the NMR spectrum. Due to the finite lengths of cables and connectors, the phase correction needed for the spectrum is unknown. The phase correction usually consists of a zero-order phase correction that is applied uniformly for all frequencies followed by a first-order phase correction that varies linearly with frequency.

As will be shown in later chapters, the instantaneous frequency observed for any nucleus depends on the instantaneous orientation of the molecule that contains it. This means that for a statistical ensemble of the nuclei, a range of frequencies will be observed due to the dependence on molecular orientation. However, if the molecules containing the observed nuclei reorient quickly compared with the Larmor period ($1/\nu_0$), the receiver only detects the *average* of the range of frequencies. If the angular reorientation is totally random, the frequency or frequencies observed are *isotropic* because the anisotropic orientational dependence has been averaged out. If the molecules reorient slowly, the receiver detects the full range of orientational frequencies, and the spectrum is *anisotropic*. This is illustrated in Figure 4.3. In the liquid state, near room temperature, most molecules exhibit isotropic rotational diffusion[4] with rotational correlation times of 10^{-12} to 10^{-9} seconds, so only the isotropic frequencies are observed. In most solids, near room temperature, the reorientational correlation times are much longer, typically 10^{1} to 10^{-6} seconds, so the range of anisotropic frequencies is apparent in the spectrum.

---

[4] Isotropic rotational diffusion is totally random in direction.

CHAPTER 5

CLASSICAL MAGNETS AND PRECESSION

In some ways, NMR active nuclei behave like classical magnetic dipoles. The classical description of magnetic dipoles in an externally applied magnetic field is therefore presented in this chapter.

In the classical view of NMR, the nucleus is likened to a sphere of charge +**z** (the atomic number, i.e., the number of protons in the nucleus) and mass **m** spinning about its z axis. The spinning mass has spin angular momentum, and the spinning charge generates a magnetic dipole moment proportional to and parallel to the spin angular momentum vector as illustrated in Figure 5.1.

Let Ze be the charge of the nucleus, where Z is the atomic number (number of protons) and e is the proton charge. Let m be the mass of the nucleus, c be the speed of light, **L** be the angular momentum vector, and $\boldsymbol{\mu}$ be the resulting magnetic dipole moment vector chosen arbitrarily to define the z axis. **L** and $\boldsymbol{\mu}$ are vectors, denoted in boldface. The derivation yields the following (Gerstein, 2002):

$$\frac{\mu}{4\pi} = \frac{Ze}{2mc}\mathbf{L} = \gamma\mathbf{L} \tag{5.1}$$

This equation predicts that the magnetic moment is proportional to the nuclear spin angular momentum (*true*) but also predicts that the gyromagnetic ratio γ increases with the spin angular momentum and charge of the nucleus (*false*).

Some other experimental observations are incompatible with the predictions of the classical model. If a classical model held, one would *not* expect the angular momentum to be quantized. Moreover, the classical result predicts a single energy "level" proportional to the dot product of the magnetic moment and the applied magnetic field, disallowing transitions (see Eq. 5.2). Therefore, one would *not* expect to observe interactions at a single Larmor frequency for a given NMR-observable isotope. Despite these shortcomings, the classical model describes some aspects of NMR very accurately, for example, the effect of applied magnetic fields and radio frequency irradiation on nuclei in the liquid state.

In the presence of the external NMR magnetic field $\mathbf{B} = \{0,0,B_0\}$, the classical behavior of the nuclear spin magnetic dipoles $\boldsymbol{\mu}$ is described by the following equation:

$$\frac{d\mu}{dt} = \gamma\mu \times \mathbf{B} \tag{5.2}$$

A Primer of NMR Theory with Calculations in Mathematica®, First Edition. Alan J. Benesi.

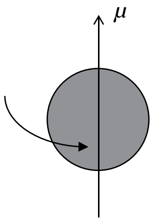

Figure 5.1 Classical magnetic dipole moment μ of a spinning charged particle.

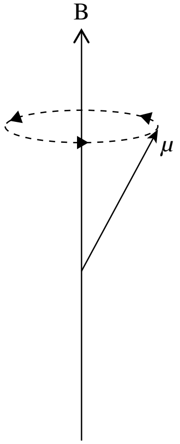

Figure 5.2 Precession of a magnetic dipole moment μ around a magnetic field **B**.

where × represents the vector cross product. The resulting motion is precession of the nuclear magnetic dipole moment **μ** around the magnetic field **B** (see Fig. 5.2), with a positive rotation around the field defined by *the right-hand rule*. The right-hand rule works as follows: Take your right hand. Align your thumb with B pointing toward the north pole of the magnet. The direction of motion of **μ** around your thumb is indicated by your remaining fingers, illustrated in Figure 5.2.

The energy of **μ** in radians s^{-1} (i.e., units of $h/2\pi$) in the magnetic field **B** relative to no magnetic field is as follows:

$$E = -\boldsymbol{\mu} \cdot \mathbf{B} = -\gamma \mathbf{L} \cdot \mathbf{B} \tag{5.3}$$

The problem with this result is that there is only one energy "level," so no transitions can occur.

Equation 5.2 is the basis of the Bloch equation(s), which are widely used in NMR calculations for $I = 1/2$ nuclei and for quadrupolar nuclei in liquids (that behave like $I = 1/2$ nuclei). The Mathematica notebook *magdipoleanimation.nb* goes through the mathematics and provides animation of a classical magnetic dipole precessing in a permanent magnetic field **B**.

EXPLANATION OF MATHEMATICA PROGRAMMING IN *magdipoleanimation.nb*

The first input line of *magdipoleanimation.nb* is a comment of the form (* comment *). On the right-hand side of the Mathematica notebook, the input of the comment is denoted by a closing square bracket with a small diagonal from the upper left-hand side of the bracket to the right-hand vertical part of the bracket. All Mathematica input lines are indicated in this way. Comments are input by typing a left parenthesis and *, typing the comment, then finishing with a * and right parenthesis. All input lines in Mathematica are evaluated by typing shift Enter on the qwertyuiop keypad or typing enter on the numeric keypad (far right-hand-side bottom key).

The next input line demonstrates how a symbol, in this case a vector $\boldsymbol{\mu}$ representing the magnetic dipole moment vector, is defined. In Mathematica, symbols such as $\boldsymbol{\mu}$ are most easily chosen using the Basic Math Input palette. This palette is activated by clicking on Palettes → Other → Basic Math Input. By using the equal sign, $\boldsymbol{\mu}$ is defined as a vector with time-dependent Cartesian coordinates $\mu x[t]$, $\mu y[t]$, and $\mu z[t]$. The vector is indicated by the left- and right-hand squiggly brackets, { and }. In this case, the input line generates an output line, denoted on the right-hand side of the notebook by a closing square bracket, small diagonal from upper left- to the right-hand vertical part, and a small mark projecting left at right angles to the vertical part. All Mathematica output lines are indicated in this way. The output line gives the evaluation result of the input line, in this case a restatement of the input definition. The combination of the input and output lines is called a "cell" and is indicated on the right-hand side of the notebook by the large closing square bracket enclosing the smaller input and output square brackets. Input lines, output lines, and entire cells can be copied by highlighting the respective brackets, then typing ctrl/c. They can be inserted after copying by putting the mouse cursor below another cell, then typing ctrl/v.

The next input line is a comment and generates no output.

The next input line defines the permanent magnetic field vector **B**. It generates an output line that restates the input definition.

Mathematica has a huge number of built-in functions. The next cell demonstrates the function MatrixForm. The input line requests the matrix form of the magnetic dipole vector $\boldsymbol{\mu}$. The built-in function MatrixForm yields the output line showing the three time-dependent elements of the $\boldsymbol{\mu}$ vector as a column vector. This form is more consistent with mathematical convention than the squiggly bracket form.

The next cell generates the matrix form of the permanent magnetic field vector.

The next input line is a comment.

The next cell defines a variable $d\boldsymbol{\mu}dt$ that expresses the rate of change of the magnetic dipole moment. Here, γ is the gyromagnetic ratio of the nucleus, $\boldsymbol{\mu}$ is the magnetic dipole moment vector, × is the cross product operation, and **B** is the permanent magnetic field vector. The output line shows that $d\boldsymbol{\mu}dt$ is a vector with x, y, and z components $B_0\,\gamma\,\mu y[t]$, $-B_0\,\gamma\,\mu x[t]$, and 0 respectively.

The next input line is a comment.

One of the very useful aspects of Mathematica is that the different parts of an expression can be "extracted" by specifying the part number. The next cell extracts the first part (the *x* component) of the vector *d***μ***dt*, yielding $B_0\ \gamma\ \mu y[t]$. Extraction of the parts of an expression is achieved by enclosing the desired part between double square brackets.

The next cell extracts the second part (the *y* component) of the vector *d***μ***dt*, yielding $-B_0\ \gamma\ \mu x[t]$.

The next cell extracts the third part (the *z* component) of the vector *d***μ***dt*, yielding 0.

The next input line is a comment.

The next cell shows how for all built-in Mathematica functions, information about the function can be obtained by typing? function, in this case ?/. . More detailed information can be obtained by clicking on the >> in the output line of the cell. In this book, /. is called the substitution function.

The next cell demonstrates how the substitution function is used in Mathematica. It defines a new symbol, $d\boldsymbol{\mu}dt\omega_0$, that is obtained from *d***μ***dt* by substituting the negative Larmor frequency $-\omega_0$ for the product $B_0\ \gamma$. The substitution is carried out with the built-in /. command. The input line for this cell can be interpreted as "define a new symbol $d\boldsymbol{\mu}dt\omega_0$ that is equal to the symbol *dμdt such that* all occurrences of the product $B_0\ \gamma$ (or $\gamma\ B_0$) are replaced with $-\omega_0$." The resulting output line shows the successful result.

The next input line is a comment.

The next cell introduces the built-in Mathematica function DSolve, which is used to solve differential equations.

The next input line can be read as solve the set of differential equations enclosed in the squiggly brackets given that the time derivative of $\mu x[t]$, denoted by $\mu x'[t]$, is equal to (note the double equals sign) the first (*x*) part of $d\boldsymbol{\mu}dt\omega_0$, that is, $d\boldsymbol{\mu}dt\omega_0[[1]]$, and subject to the initial boundary condition that $\mu x[0]$ is equal to $\text{Sin}[\theta]\ \cos[\phi]$. (Note that double equals signs are used.) Here θ is the nutation angle brought about by the rf pulse, and ϕ is the phase of the rf pulse. The set of differential equations enclosed in squiggly brackets is completed by defining $\mu y'[t]$ as equal to the second part of $d\boldsymbol{\mu}dt\omega_0$, that is, $d\boldsymbol{\mu}dt\omega_0[[2]]$ with the initial condition $\mu y[t] == \sin[\theta]\ \sin[\phi]$ and $\mu z'[t]$ as equal to the third part of $d\boldsymbol{\mu}dt\omega_0$, that is, $d\boldsymbol{\mu}dt\omega_0[[3]]$ with the initial condition $\mu z[t] = \cos[\theta]$. Note that all differential equations and initial (boundary) conditions are separated by commas and enclosed in the squiggly brackets. Following the set of differential equations and initial conditions, the desired set of solutions is identified, again enclosed within squiggly brackets. In this case, the desired solutions are $\mu x[t]$, $\mu y[t]$, and $\mu z[t]$, with *t* identified as the independent variable. The output line of the cell identifies the desired solutions with forward arrows (→). Thus, the solution for $\mu x[t]$ is $\cos[\phi]\ \cos[t\ \omega_0]\ \sin[\theta] - \sin[\theta]\ \sin[\phi]\ \sin[t\ \omega_0]$, the solution for $\mu y[t]$ is $\sin[\phi]\ \cos[t\ \omega_0]\ \sin[\theta] + \sin[\theta]\ \text{Cos}[\phi]\ \sin[t\ \omega_0]$, and the solution for $\mu z[t]$ is $\cos[\theta]$.

The next cell requests information about the := function, which is used to create new functions in Mathematica.

The next cell requests information about the _ function.

The next cell creates a function μtime[t] that is dependent on the input variables θ_, ϕ_, ω_0_, and t_. Notice how the right-hand side is written using the same symbols *without* the _*s* (Blanks). Function definitions generate no output lines.

The next cell shows how the function can be used to calculate the position of the magnetic dipole moment as a function of time. Note that symbols or numerical values can be used.

The next cell requests the numerical value (*N*) of the previous cell output. The previous cell output is denoted by %.

The next cell requests information about *N*.

The next cell is a comment.

The next six cells request information about some important built-in functions: ListAnimate, Table, Graphics3D, AbsoluteThickness, Arrow, and PlotRange.

The next cell incorporates the preceding functions and shows how Mathematica can be used to animate the motion of the dipole moment vector. The ListAnimate function animates the table of 3D graphics created using the Table function. A Table of thick Arrows (AbsoluteThickness 3) with starting point 0,0,0 and ending points defined by μtime are generated by varying t from 0 to 5.0×10^{9} s in increments of 3.0×10^{-11} s. The Plot Range is chosen so that the maximum and minimum values displayed are 1 and −1, respectively, for all three Cartesian axes. A box is automatically drawn to define the plot range limits. In this cell, the μtime nutation value θ is chosen to be $\pi/2$ radians, the rf phase is chosen to be 0 radians, and the Larmor frequency in radians s^{-1} is chosen to be $2\pi\times3.0\times10^{8}$. The animation shows the rotation of the magnetic dipole moment around the z axis.

The next cell is exactly the same as the preceding one, except that the nutation angle θ is only $\pi/4$ radians.

The next cell is the same except that the nutation angle θ is $3\pi/4$.

The next cell is the same except that the nutation angle θ is π. Note that the dipole moment vector (Arrow) μtime remains on the $-z$ axis as time proceeds.

The next cell is the same except that the nutation angle θ is 0. The dipole moment remains on the $+z$ axis as time proceeds.

CHAPTER 6

THE BLOCH EQUATION IN THE LABORATORY REFERENCE FRAME

Consider a NMR sample sitting in the superconducting magnet. The superconducting magnet defines the laboratory reference frame. The laboratory z axis is aligned with the magnetic field, while the x and y axes are fixed arbitrarily within the magnet (Fig. 3.3) (Ernst et al., 1987, pp. 49, 115–125). Adjustable small magnetic fields provided by the shim coils insure that the x and y components of the magnetic field are 0 and the z component is constant over the NMR sample.

In Mathematica the convention is that the components of a vector are enclosed within squiggly brackets, so $\mathbf{B} = \{0, 0, B_0\}$.

There is a statistical ensemble of nuclear magnetic dipole moments μ_i. The individual nuclear magnetic dipole moments μ_i precess about the magnetic field $\mathbf{B}$ as described in the previous chapter. The net magnetic dipole moment $\mathbf{M}$ of the ensemble of nuclear magnetic moments is the vector sum of the individual magnetic moments, i.e. $\boldsymbol{M} = \sum_i \mu_i$. Due to cancellation of the randomly distributed x and y components of the individual nuclear magnetic moments (i.e., random phases of the individual magnetization vectors), the net magnetization vector is aligned with the laboratory z axis as shown in Figure 6.1. We denote this equilibrium magnetization as $\mathbf{M} = \{0,0,M_{\text{zeq}}\}$.

The behavior of the net magnetization $\mathbf{M}$ in the presence of the magnetic field is described by the Bloch equation:

$$\frac{d\boldsymbol{M}}{dt} = \gamma \boldsymbol{M} \times \boldsymbol{B}_{\text{tot}} - \bar{\boldsymbol{R}}(\boldsymbol{M} - \boldsymbol{M}_0) \qquad (6.1)$$

where $\mathbf{M}$ is the instantaneous net magnetization dipole moment for the ensemble of spins, $\mathbf{M}_0 = \{0, 0, M_{\text{zeq}}\}$ is the equilibrium net magnetization aligned with the laboratory (magnet) z axis, and $\bar{\boldsymbol{R}} = \begin{pmatrix} 1/T_2 & 0 & 0 \\ 0 & 1/T_2 & 0 \\ 0 & 0 & 1/T_1 \end{pmatrix}$ is the relaxation matrix. Except for $\bar{\boldsymbol{R}}$, this is identical to the equation of motion for a magnetic dipole in a magnetic field (Chapter 5).

A Primer of NMR Theory with Calculations in Mathematica®, First Edition. Alan J. Benesi.

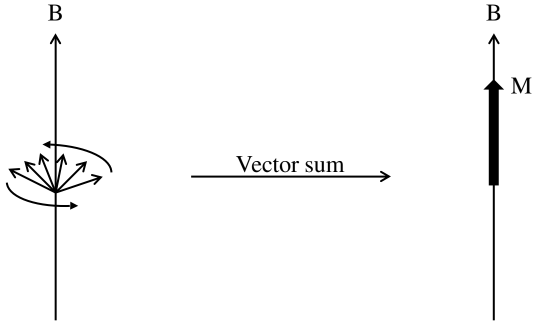

Figure 6.1 The classical net magnetization vector.

In Mathematica, the convention is that a matrix is a set of row vectors enclosed within squiggly brackets, so $\bar{\boldsymbol{R}} = \{\{1/T_2, 0, 0\}, \{0, 1/T_2, 0\}, \{0, 0, 1/T_1\}\}$ is the relaxation matrix, with matrices such as $\bar{\boldsymbol{R}}$ denoted in boldface italic with a horizontal bar on top.

In the presence of rf irradiation, the total magnetic field used in the Bloch equation is given by $\mathbf{B}_{\mathrm{tot}} = \mathbf{B}_0 + \mathbf{B}_{\mathrm{rf}}$, where $\mathbf{B}_{\mathrm{rf}}$ is a linearly oscillating magnetic field at or near the Larmor frequency in the *x–y* plane (Fig. 4.2).

The Bloch equation can be solved for arbitrary initial conditions as shown in the notebook *bloch1.nb*.

EXPLANATION OF *bloch1.nb*

For basic Mathematica instructions and definitions, see the line-by-line analysis of *magdipoleanimation.nb* in Chapter 5.

The first cell is a comment. It is followed by two cells that define two different vectors, **a** and **b**.

After a comment, the scalar product (dot product) of the two vectors is demonstrated, followed by a cell showing that the scalar product is commutative.

After a comment, the vector cross product is demonstrated, followed by a cell that shows that the cross product is *not* commutative.

After a comment, two 3×3 square matrices *A* and *G* are defined. Then the matrix products *A.G* and *G.A* are demonstrated. Matrix multiplication of square matrices yields a square matrix of the same dimensionality, in this case 3×3. Elements of the product matrix are obtained by adding the products of appropriate row elements of the first matrix and elements of the appropriate column of the second matrix.

Matrix multiplication is generally not commutative, as demonstrated in the next several cells.

Products of vectors and matrices yield vectors as shown in the next cells. These products are also generally not commutative.

Scalar multiplication can be represented in several ways and is always commutative.

The next cells introduce the magnetic dipole moment vector **μ**, magnetic field vector **B**, and the rate-of-change vector *d***μ***dt* describing the rate of change of the magnetic dipole moment vector (see *magdipoleanimation.nb*, Chapter 5).

The next cells introduce the vector and matrix components used in the Bloch equation. The magnetization vector at any arbitrary time *t* is denoted by M. The net equilibrium magnetization is aligned with the magnetic field *B* and denoted by *M*0. The relaxation matrix is diagonal[1] and has as components the transverse or spin–spin relaxation rate $1/T_2$ and the longitudinal or spin lattice relaxation rate $1/T_1$.

The next cells define the Bloch equation. The rate of change of the magnetization vector *dMdt* is given by the Bloch equation. Note that the Bloch equation contains a cross product of *M* and *B and* the relaxation rate matrix. The resulting *dMdt* vector contains *x*, *y*, and *z* components, respectively. These can be easily extracted as shown in the following cells.

The next cells show how DSolve is used to solve the Bloch equation for the time dependence of the magnetization *M* given that it is initially on the +*x* axis (as it would be after a 90° +*y* rf pulse). See Chapter 5 for the introduction of DSolve. Note how the *x*, *y*, and *z* components of *dMdt* are used to achieve the solution. The desired solutions *Mx*[*t*], *My*[*t*], and *Mz*[*t*] are also identified as is the independent time variable *t*. The resulting solutions are displayed in the output line with forward arrows.

Next, we use the built-in Mathematica functions ExpToTrig and FullSimplify to simplify the solutions. ExpToTrig converts expressions containing complex exponentials to equivalent expressions containing trigonometric functions. FullSimplify seeks the most compact expression. Remember that % refers to the previous output line. Also note how the two functions are applied successively using // to separate them. Finally, we make the substitution $\gamma B_0 \to -\omega_0$. The *x* and *y* components *Mx*[*t*] and *My*[*t*] oscillate at the Larmor frequency ω_0 radian s^{-1} and decay as $e^{-\frac{t}{T_z}}$. The *z* component decays as $e^{-\frac{t}{T_1}}$ but does not oscillate.

The next few cells solve the Bloch equation for the initial condition that the net magnetization vector **M** is aligned with the—*z* axis (as it would be by the 180° rf pulse in the inversion recovery experiment).

The resulting solution for $M_z[t]$ (the *x* and *y* components are zero) is then used to create the function Mtime, where the value of M_{zeq} is assumed to be 1 for convenience (and for the subsequent animation). The function Mtime is then used in animated form (see Chapter 5) to show the decay of the longitudinal (*z* axis) magnetization back to its equilibrium value of $+M_{zeq}$.

---

[1] The only non-zero elements are along the diagonal from upper left to lower right.

CHAPTER 7

THE BLOCH EQUATION IN THE ROTATING FRAME

Classically, the observable NMR signal is an oscillating voltage generated in the probe coil by the precession of the transverse (*xy* plane) component of **M**. This component decays exponentially due to T_2* and T_1 relaxation.[1] Before digitization, the oscillating voltage is transformed from the laboratory frame to the rotating frame. This is achieved by electronically mixing the input Larmor frequency with the received experimental NMR signal that has frequencies at the Larmor frequency $\nu_0 \pm \delta$ kHz, where δ can range from less than 0 Hz to as much as 1000 kHz (i.e., 1 MHz). This yields both the sum and difference signals, but only the difference signal is retained. The difference signal (±δ kHz) is a decaying oscillation and is called a free induction decay (FID) (see Fig. 7.1). This is the experimental NMR signal that is digitized and Fourier transformed to yield the spectrum. It is these relatively small shifts away from the Larmor frequency (the δ values) that provide useful information in the liquid-state NMR spectrum such as chemical shifts and coupling constants.

The rotating frame is obtained from the laboratory frame by rotating the laboratory frame at the observe frequency[2] in coincidence with the precession of transverse x and y components of the magnetization vector **M**. In this reference frame, the x and y components of a magnetization vector at the observe frequency are fixed. The precession induced by the superconducting magnetic field thus vanishes for an on-resonance magnetization vector in the rotating frame, as if there was no magnetic field, that is, $\mathbf{B}^{\text{rot}} = \{0,0,0\}$. Magnetization vectors that are slightly "off resonance," that is, not at the exact Larmor frequency, precess at their difference frequencies, that is, ±δ kHz. The effective magnetic field for an off-resonance magnetization vector is defined by its difference frequency δ, with $\mathbf{B}^{\text{rot}} = \{0,0,-\delta/\gamma\}$, where γ is the gyromagnetic ratio of the nucleus.

The linearly oscillating radio frequency (rf) magnetic field at the Larmor frequency can be decomposed into two circularly polarized oscillatory magnetic fields, one rotating at the positive Larmor frequency in coincidence with the net magnetic

---

[1] T_2* is the apparent T_2. It is affected by small magnetic field inhomogeneities and the pulse sequence used to measure it. The T_1 is not affected by either and is therefore more reliable experimentally.

[2] The observe frequency is usually the rf transmitter frequency, at or close to the Larmor frequency.

A Primer of NMR Theory with Calculations in Mathematica®, First Edition. Alan J. Benesi.

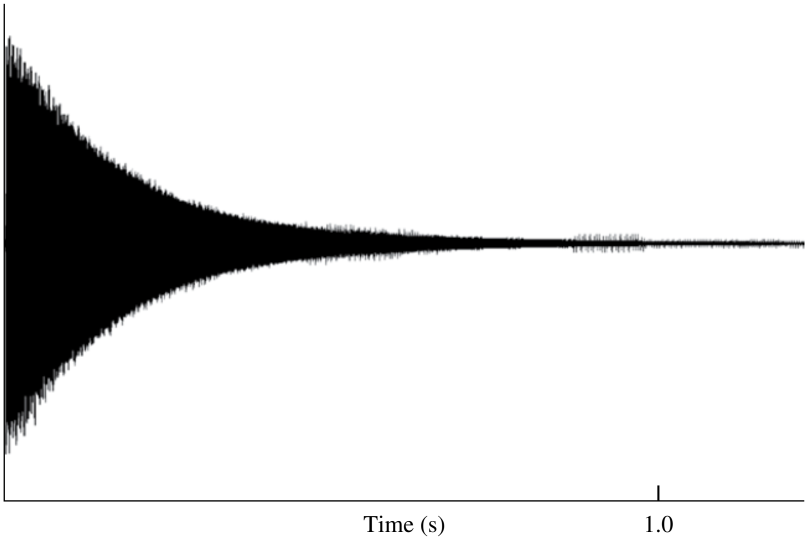

Figure 7.1 A liquid-state NMR signal—the ^{1}H FID obtained at 600.18 MHz for **Δ**^{9}-tetrahydrocannabinol dissolved in deuterated methanol.

moment **M** of the nuclear spins and one rotating in the opposite direction at the negative Larmor frequency. The sum of these counterrotating magnetic fields gives the linearly oscillating rf magnetic field. For the purposes of solving the Bloch equation, we retain only the positive component that oscillates at the same positive Larmor frequency as the net magnetization vector **M**. The other circularly polarized component of the rf field has only small effects on **M** (manifested in Bloch Siegert shifts (Bloch and Siegert, 1940)) and is usually ignored. Therefore, in the rotating frame, the positive circularly polarized component of the rf magnetic field looks like a static magnetic field, with $\mathbf{B}_{\mathbf{rf\_rot}} = B_1$ {Cos[ϕ], Sin[ϕ], 0}, where ϕ is the phase of the rf, with $\phi = 0$ corresponding to the x axis of the rotating frame. When the rf field is on, the *on-resonance* magnetization vector **M** precesses ("nutates") around $\mathbf{B}_{\mathbf{rf\_rot}}$ at $\omega_1 = -\gamma\, \mathbf{B}_1$ radians s^{-1}.

For net magnetization vectors **M** that are *on-resonance* in the rotating frame, the *total* magnetic field in the presence of rf in the rotating frame is therefore $\mathbf{B}_{\mathbf{tot\_rot}} = \{B_1\ \mathrm{Cos}[\phi], B_1\ \mathrm{Sin}[\phi], 0\}$. For *off-resonance* net magnetization vectors, the *total* magnetic field is $\mathbf{B}_{\mathbf{tot\_rot}} = \{B_1\ \mathrm{Cos}[\phi], B_1\ \mathrm{Sin}[\phi], -\delta/\gamma\}$.

The principle of relativity requires that the same laws of physics apply to the rotating frame as the laboratory frame. This means that the Bloch equation has the same form as given in Equation 6.1, except that in the rotating frame $\mathbf{B}^{\mathbf{rot}}$ = {0,0,0} on resonance or $\mathbf{B}^{\mathbf{rot}} = \{0,0,-\delta/\gamma\}$ off resonance, that is,

$$\frac{d\boldsymbol{M}}{dt} = \gamma \boldsymbol{M}^{\mathrm{rot}} \times \boldsymbol{B}_{\mathrm{tot\_rot}} - \bar{\boldsymbol{R}}(\boldsymbol{M}^{\mathrm{rot}} - \boldsymbol{M}_0) \tag{7.1}$$

Examples of solutions in the rotating frame are shown in *bloch2animation.nb* (ω_1 comparable to δ) and *bloch3animation.nb* ($\omega_1 >> \delta$). The behavior is simple as long as $\omega_1 >> \delta$. For example, if $\delta = 0$, a 90° or $\pi/2$ rf pulse has a duration τ_{90} defined by $\pi/2 = \omega_1\, \tau_{90}$.

EXPLANATION OF *bloch2animation.nb*

After a comment, the second cell defines the rotating frame effective magnetic field vector $\mathbf{B}_{\mathbf{tot}}$ in the presence of a rf field B_1 at the Larmor frequency and an offset (e.g., chemical shift) of δ radians s^{-1}. In the next cells, the net magnetization vector $\mathbf{M}_{\mathbf{rot}}$ is introduced, the equilibrium net magnetization vector M_0 and relaxation matrix R are defined. Then the Bloch equation for the rate of change *dMdt* is introduced, expanded with the built-in Expand function, and expressed as a vector using the built-in MatrixForm function.

The same three cells can be written on one line using // as shown in the next cell, where % is used (the previous output line). The substitution command (/.) is used in the following cell and then the assignment of *dMdt* to % semicolon. The semicolon (;) after the % indicates that the output line is suppressed. The first part of *dMdt* (*x* part) is then selected and expanded.

The next cells replace all instances of *Mx*, *My*, and *Mz* with *Mx*[*t*], *My*[*t*], and *Mz*[*t*]. Notice that the collection of desired substitutions is enclosed in squiggly brackets { }. These are necessary whenever multiple replacements are made.

During an rf pulse, there is usually insufficient time for relaxation to affect the results. We therefore make the substitution that both T_1 and $T_2 \rightarrow \infty$ and that $1/T_1$ and $1/T_2$ are zero. This yields a simpler version of *dMdt.*

Next, we use DSolve to obtain the time dependencies *Mx*[*t*], *My*[*t*], and *Mz*[*t*] given that the initial magnetization is along the +*z* axis at equilibrium. The solutions are complicated but are greatly simplified with the built-in FullSimplify function. Next, we convert the simplified expressions into a function Mtime that can be animated (see *magdipoleanimation.nb* in Chapter 5).

The parameter values for the animations in the next cells are, respectively, as follows: (i) $\delta = 0$ radian s^{-1}, $\phi = 0$ radian, $\omega_1 = 2\pi \times 5 \times 10^4$ radian s^{-1}, $t = 0\text{–}2.5 \times 10^{-4}$ s in increments of 1×10^{-6} s; (ii) $\delta = 0$ radian s^{-1}, $\phi = \pi/2$ radian, $\omega_1 = 2\pi \times 5 \times 10^4$ radian s^{-1}, $t = 0\text{–}2.5 \times 10^{-4}$ s in increments of 1×10^{-6} s; (iii) $\delta = 2\pi \times 2.5 \times 10^4$ radian s^{-1}, $\phi = 0$ radian, $\omega_1 = 2\pi \times 5 \times 10^4$ radian s^{-1}, $t = 0\text{–}2.5 \times 10^{-4}$ s in increments of 1×10^{-6} sec; (iv) $\delta = 2\pi \times 2.5 \times 10^4$ radian sec^{-1}, $\phi = \pi/2$ radian, $\omega_1 = 2\pi \times 5 \times 10^4$ radian s^{-1}, $t = 0\text{–}2.5 \times 10^{-4}$ s in increments of 1×10^{-6} s; (v) $\delta = 2\pi \times 2.0 \times 10^5$ radian s^{-1}, $\phi = 0$ radian, $\omega_1 = 2\pi \times 5 \times 10^4$ radian s^{-1}, $t = 0\text{–}5.0 \times 10^{-5}$ s in increments of 1×10^{-6} s; (vi) $\delta = 2\pi \times 2.0 \times 10^5$ radian s^{-1}, $\phi = \pi/2$ radian, $\omega_1 = 2\pi \times 5 \times 10^4$ radian s^{-1}, $t = 0\text{–}5.0 \times 10^{-5}$ s in increments of 1×10^{-6} s.

The animations that greater offsets (δ) reduce the efficiency of rf pulses.

EXPLANATION OF *bloch3animation.nb*

This notebook is similar to the previous one, except that this looks at the net magnetization in the rotating frame after "hard" rf pulses ($\omega_1 >> \delta$). The initial position of the net magnetization after a hard pulse is defined by $\theta = \omega_1\, \tau_{\text{pulse}}$, where τ_{pulse} is the duration of the pulse in s, and by ϕ, the phase of the pulse in the rotating frame. The initial *x*, *y*, and *z* magnetization components are given by Sin[θ] Sin[ϕ], −Sin[θ] Sin[ϕ], and Cos[θ], respectively for $M_{\text{zeq}} = 1$.

It elucidates the time dependence of the net magnetization after the hard pulse and includes the effects of relaxation. The net magnetization M is defined as a vector with $Mx[t]$, $My[t]$, and $Mz[t]$} as elements. After the hard pulse there is no rf irradiation, so $B = \{0,0, -\delta/\gamma\}$. The relaxation matrix R is diagonal with elements of $1/T_2$, $1/T_2$, and $1/T_1$. As in previous notebooks, we introduce the Bloch equation as *dMdt*. We create the time-dependent magnetization functions magx, magy, and magz, then combine them into the net magnetization vector function Mag that is suitable for animation.

Animation of Mag is achieved as in previous notebooks. The parameter values for the animations in the animation cells are, respectively, as follows: (i) $\delta = 10$ radian s^{-1}, $\theta = \pi/2$ radian, $\phi = \pi/2$ radian, $T_1 = 1$ s, $T_2 = 1$ s, $t = 0$–5 s in increments of 0.01 s; (ii) $\delta = 10$ radian s^{-1}, $\theta = \pi$ radian, $\phi = \pi/2$ radian, $T_1 = 1$ s, $T_2 = 1$ s, $t = 0$–5 s in increments of 0.01 s; (iii) $\delta = 10$ radian s^{-1}, $\theta = 3\pi/4$ radian, $\phi = \pi/2$ radian, $T_1 = 1$ s, $T_2 = 1$ s, $t = 0$–5 s in increments of 0.01 s.

HOMEWORK

Homework 7.1: Investigate the effect of ω_1 on the magnetization animation *blochanimation2.nb*. For example, try $\omega_1 = 2\pi \times 10^5$ radian s^{-1} and $\omega_1 = 2\pi \times 10^3$ radian s^{-1} while holding $\delta = 2\pi \times 2.5 \times 10^4$ radian s^{-1}.

Homework 7.2: Assuming that $\omega_1 >> \delta$, what is ω_1 if the 90° pulse is (a) 5.0 μs? (b) 100 μs?

CHAPTER 8

THE VECTOR MODEL

The vector model is the graphical representation of the Bloch equation in the rotating frame. The magnetization **M** only gives an observable NMR signal when it has transverse components in the *x*–*y* plane. Typically, it is assumed that the NMR experiment starts with equilibrium net magnetization **M** along the *z* axis, parallel to $\mathbf{B}_0$. Radio frequency (rf) pulses are usually assumed to be "strong," that is, $|\gamma \mathbf{B}_1| >> |\delta|$.

Figure 8.1 shows the vector model for a single *on-resonance* ($\delta = 0$) 90° pulse along the *x* axis (e.g., $(\pi/2)_x$) of the rotating frame. During the rf pulse, the net magnetization *nutates* around the *x* axis according to the right-hand rule. After completion of the $(\pi/2)_x$ pulse, the net magnetization is on the –*y* axis of the rotating frame. Because the rotating frame is on-resonance, the net magnetization *does not precess* in the *x*–*y* plane around the *z* axis. Only T_1 and T_2 relaxation occurs. The –*y* and *z* components of the decreasing magnetization are shown in gray.

Figure 8.2 shows the vector model for an *on-resonance* single pulse experiment along the +*y* axis of the rotating frame. The behavior and results are identical to Figure 8.1 except that the net magnetization after the $(\pi/2)_y$ rf pulse is on the +*x* axis of the rotating frame.

Figure 8.3 shows the vector model for an *on-resonance* single pulse experiment of phase ϕ. The behavior and results are identical to Figure 8.1 except that the net magnetization after the $(\pi/2)_\phi$ rf pulse is at $+\phi$ radians relative to the –*y* axis. Do not confuse the magnetization vector (thicker arrow) with the $\mathbf{B}_1$ vector (thinner arrow) located at ϕ radians relative to the +*x* axis.

Figure 8.4 shows the vector model for a single *off-resonance* ($\delta \neq 0$) 90° pulse along the *x* axis of the rotating frame. In this case, after the $(\pi/2)_x$ rf pulse, the magnetization precesses in the *x*–*y* plane around the *z* axis at δ radians s^{-1}. Relaxation components are not depicted. See *blochanimation3.nb* for an animation of the precessing and relaxing magnetization.

Figure 8.5 shows the vector model for the inversion recovery experiment that is widely used to measure T_1 relaxation. The π rf pulse can be of any phase. It inverts the net magnetization vector **M** so that it is on the –*z* axis. With time, T_1 relaxation causes the net magnetization to decay back to its equilibrium value along the +*z* axis. Typically, a set of specific time delays are used in separate experiments to monitor the return to equilibrium and hence the T_1 relaxation time. The unobservable *z* magnetization is converted to observable transverse magnetization by the $(\pi/2)_x$ pulse.

A Primer of NMR Theory with Calculations in Mathematica®, First Edition. Alan J. Benesi.

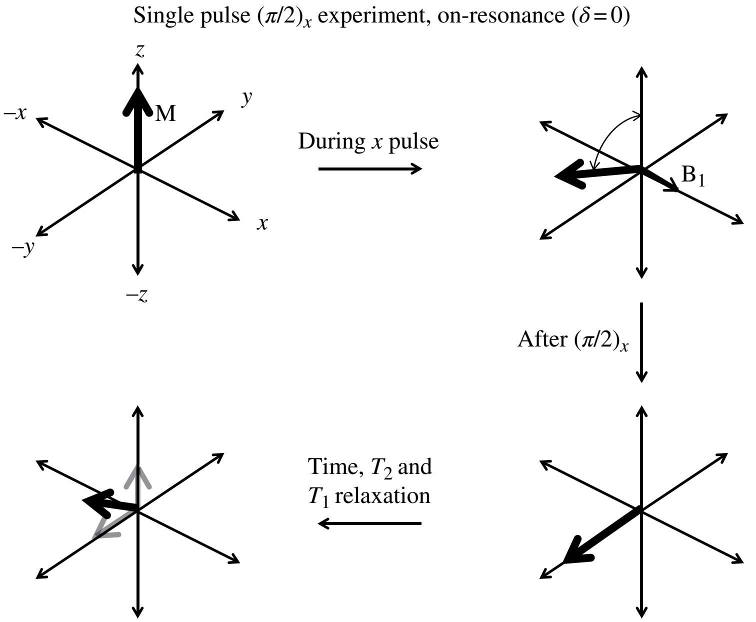

Figure 8.1 Single pulse $(\pi/2)_x$ experiment, on-resonance ($\delta = 0$). Before the pulse, the net magnetization **M** is aligned along the z axis. During the on-resonance pulse, the rf magnetic field $\mathbf{B}_1$ is aligned with the x axis of the rotating frame, and the net magnetization precesses ("nutates") around the $\mathbf{B}_1$ field. After rotating $\pi/2$ radians, the net magnetization **M** ends up on the $-y$ axis of the rotating frame, where it stays because the rf pulse is on resonance. With time, T_2 relaxation causes decay of the magnetization along the $-y$ axis (shown in gray), and T_1 relaxation causes reestablishment of magnetization along the $+z$ axis (shown in gray). The net magnetization has components along the $-y$ axis and $+z$ axis during relaxation.

Figure 8.6 shows the vector model for the spin echo experiment that can be used to measure T_2 relaxation. The $(\pi/2)_x$ rf pulse puts the equilibrium magnetization **M** on the $-y$ axis. With time τ, chemical shift evolution rotates the transverse magnetization in the x–y plane. T_2 relaxation simultaneously reduces the magnitude of the transverse magnetization. The π_y rf pulse puts the residual transverse magnetization on the opposite side of the $-y$ axis. After the second time interval τ, chemical shift evolution returns the remaining transverse magnetization to the $-y$ axis. However, the magnitude of **M** is reduced by T_2 relaxation. A set of different experiments with different τ values is used to measure T_2 relaxation.

Figure 8.7 shows the failure of the vector model to account for experiments involving J-coupled nuclei. We assume here that the coupled nuclei are both ^{1}H spins and that strong $(\pi/2)_y$ pulses nutate the magnetizations of both ^{1}H spins to the x axis. Figure 8.7 shows the magnetization of only the on-resonance ($\delta = 0$) ^{1}H spin. Its coupling partner spin is at a different ($\delta \neq 0$) chemical shift. Its magnetization vector is not shown in the figure. The J-coupling "splits" the magnetization of the on-resonance ($\delta = 0$) spin into two components, one rotating at $+J/2\,\mathrm{s}^{-1}$ and one at $-J/2\,\mathrm{s}^{-1}$. If acquisition would start immediately after the *first* $(\pi/2)_y$ rf pulse, the spectrum

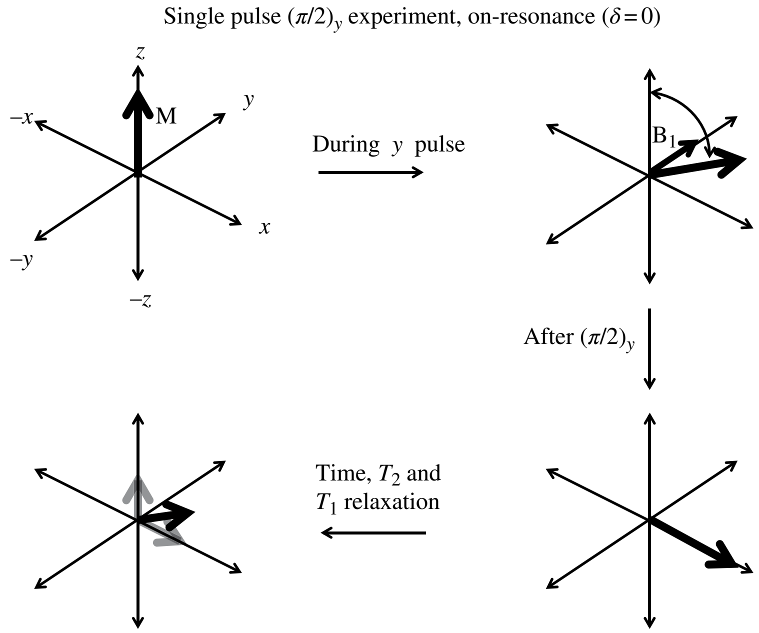
Single pulse $(\pi/2)_y$ experiment, on-resonance $(\delta = 0)$

Figure 8.2 Single pulse $(\pi/2)_y$ experiment, on-resonance ($\delta = 0$). Before the pulse, the net magnetization **M** is aligned along the z axis. During the on-resonance pulse, the rf magnetic field $\mathbf{B}_1$ is aligned with the y axis of the rotating frame, and the net magnetization precesses ("nutates") around the $\mathbf{B}_1$ field. After rotating $\pi/2$ radians, the net magnetization **M** ends up on the $+x$ axis of the rotating frame, where it stays because the rf pulse is on resonance. With time, T_2 relaxation causes decay of the magnetization along the $+x$ axis (shown in gray), and T_1 relaxation causes reestablishment of magnetization along the $+z$ axis (shown in gray). The net magnetization has components along the $+x$ axis and $+z$ axis during relaxation.

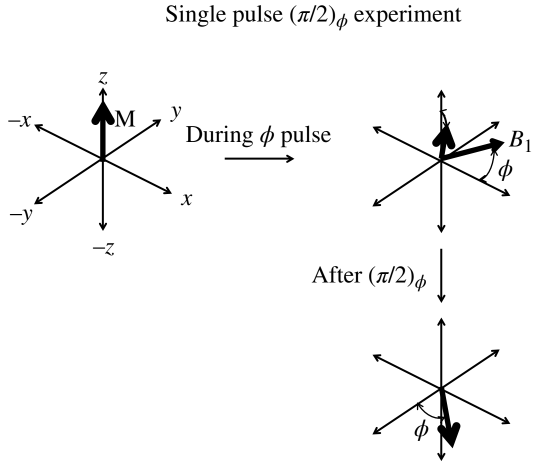
Single pulse $(\pi/2)_\phi$ experiment

Figure 8.3 Single pulse $(\pi/2)_\phi$ experiment, on-resonance ($\delta = 0$). Before the pulse, the net magnetization **M** is aligned along the z axis. During the on-resonance pulse, the rf magnetic field $\mathbf{B}_1$ is aligned in the xy plane at ϕ radians with respect to the x axis. During the pulse, the net magnetization precesses ("nutates") around the $\mathbf{B}_1$ field. After rotating $\pi/2$ radians, the net magnetization **M** ends up in the xy plane at ϕ radians relative to the $-y$ axis of the rotating frame, where it stays because the rf pulse is on resonance. Relaxation is not shown but proceeds as in Figures 8.1 and 8.2.

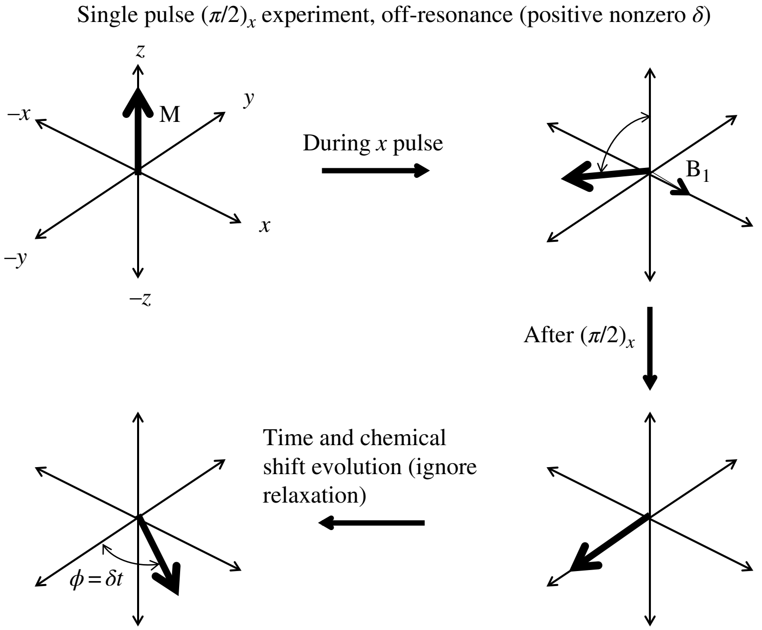

Figure 8.4 Single pulse $(\pi/2)_x$ experiment, off-resonance ($\delta \neq 0$). Before the pulse, the net magnetization **M** is aligned along the *z* axis. During the on-resonance pulse, the rf magnetic field $\mathbf{B}_1$ is aligned with the *x* axis of the rotating frame, and the net magnetization precesses ("nutates") around the $\mathbf{B}_1$ field. After rotating $\pi/2$ radians, the net magnetization **M** ends up on the $-y$ axis of the rotating frame. After the pulse, the net magnetization **M** precesses around the $+z$ axis. Relaxation also occurs but is not shown.

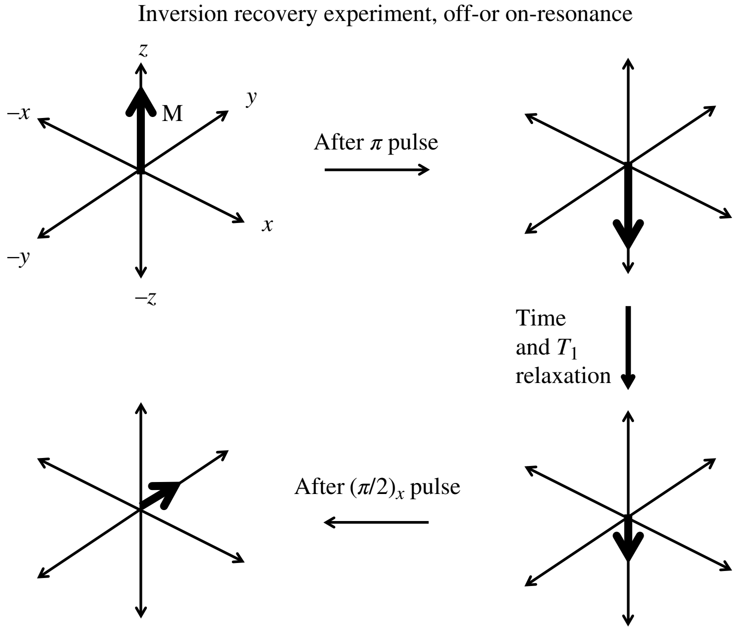

Figure 8.5 Inversion Recovery experiment, on- or off-resonance. Before the pulse, the net magnetization **M** is aligned along the $+z$ axis. After the π pulse, the net magnetization **M** has nutated to the $-z$ axis. With time, T_1 relaxation causes **M** to decay toward the $+z$ axis. The $(\pi/2)_x$ pulse nutates the partially relaxed magnetization to the $+y$ axis if **M** is along the $-z$ axis prior to the pulse and to the $-y$ axis if **M** is along the $+z$ axis prior to the pulse. The experiment is repeated for different relaxation times to obtain data, which are analyzed to measure the quantitative T_1 value.

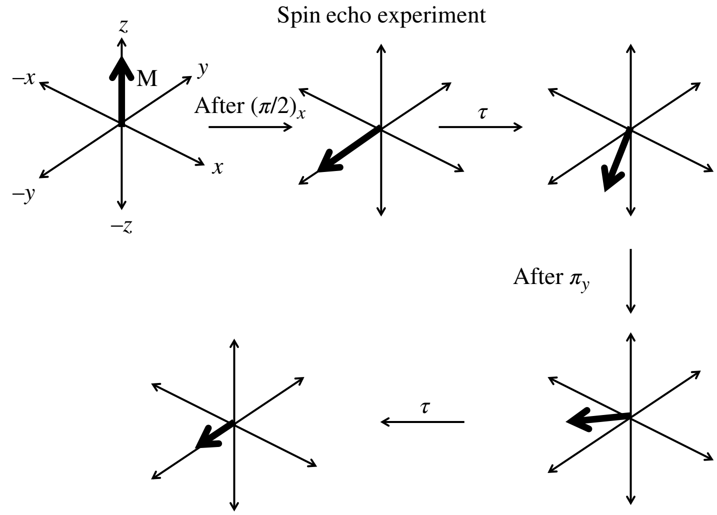

Figure 8.6 Spin Echo experiment, off-resonance ($\delta \neq 0$). Before the pulse, the net magnetization **M** is aligned along the z axis. The $(\pi/2)_x$ rf pulse rotates **M** to the $-y$ axis of the rotating frame. During the first τ delay, the magnetization **M** precesses around the $+z$ axis. The π_y rf pulse rotates the magnetization to the opposite side of the y and $-y$ axes. During the second τ delay, precession returns **M** to the $-y$ axis. T_2 relaxation during the two τ delays reduces the magnitude of **M** in the xy plane, but the magnetization is otherwise unaffected. The experiment is repeated for different τ values, yielding data that can be analyzed to measure the T_2 value.

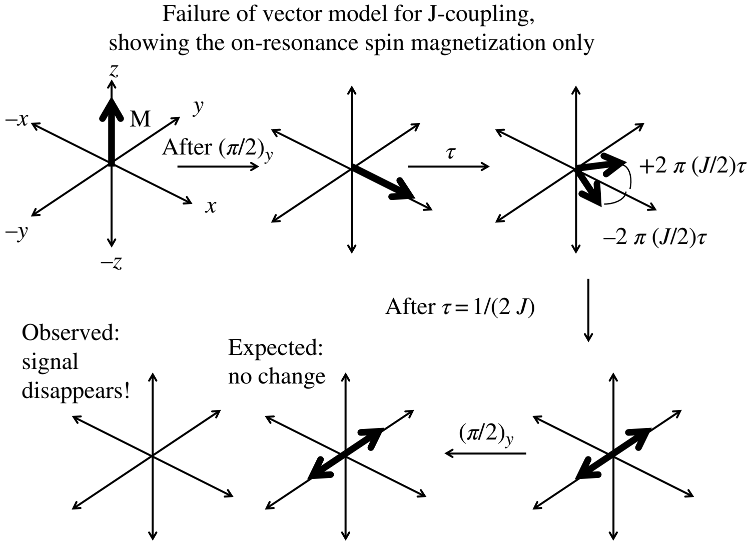

Figure 8.7 Failure of the Vector Model for Two J-coupled $I = 1/2$ Nuclear Spins. One spin is on-resonance ($\delta = 0$) and one is off-resonance ($\delta \neq 0$). Only the magnetization of the on-resonance spin is depicted. Before the $(\pi/2)_y$ rf pulse, the net magnetization **M** is aligned along the z axis. The $(\pi/2)_y$ rf pulse rotates **M** to the $+x$ axis of the rotating frame. During the first τ delay, the magnetization **M** splits into two components, one precessing at $2\pi(+j/2)$ radian s^{-1} and one precessing at $2\pi(-j/2)$ around the $+z$ axis. If τ is set to $1/(2\,j)$, the two components of **M** are aligned with the $+y$ and $-y$ axes, respectively. Based on the vector model (Bloch equation), one *expects* the $(\pi/2)_y$ to bring about no change in the magnetization components. However, experiment and quantum mechanical analysis show that the magnetization "disappears." Why? Because the $(\pi/2)_y$ pulse has created unobservable zero and double quantum coherence.

shows two positive peaks separated by $J\,\text{s}^{-1}$ (see Fig. 22.1). If acquisition would start at $\tau = 1/(2\text{ J})$, the spectrum would show a positive and a negative peak separated by $J\,\text{s}^{-1}$ (see Fig. 22.2). The major problem for the vector model occurs if acquisition starts after the *second* $(\pi/2)_y$. The vector model predicts that the spectrum should still show a positive and a negative peak separated by $J\,\text{s}^{-1}$ as in Figure 22.2. The vector model is incorrect in this prediction. *The experimentally observed spectrum shows no peaks at all.* We will see that this is because we have created *unobservable double and zero quantum coherence*.

CHAPTER 9

FOURIER TRANSFORM OF THE NMR SIGNAL

Here, we follow the treatment of Levitt (2008, pp. 96–105). Fourier transformation is a mathematical method that converts the NMR signal, a function of time, to the NMR spectrum, a function of frequency. It is much easier to "read" and understand the NMR spectrum than the NMR signal or free induction decay (FID). The information content of the spectrum and the signal are, however, equivalent.

The mathematical definition of the Fourier transform used in NMR is:

$$S(\omega) = \int_0^\infty s(t)e^{-i\omega t}\,dt \tag{9.1}$$

where $s(t)$ is the "input" NMR signal, and the "output" $S(\omega)$ is a function of the frequency variable ω.

The NMR signal (FID) corresponding to a spectrum with just one peak can be described with the equation

$$s(t) = \alpha e^{(i\delta-(1/T_2))t} \tag{9.2}$$

where δ is the frequency of the peak relative to the Larmor frequency and T_2 is the transverse relaxation time of the peak. $(1/T_2)$ is the transverse relaxation rate constant.

The integral (Eq. 9.1) is carried out in the notebook *fouriertransform2.nb*.

Phasing of the experimental NMR spectrum corresponds to adjusting the x and y axes of the rotating frame so that the x axis is coincident with the transverse magnetization at the first point ($t = 0$) of the FID. This gives the maximum positive real (x) value for the FID at $t = 0$. This yields data that are purely absorptive and positive.

A very useful fact about the time-dependent NMR signal is that the properly phased FID at $t=0$ gives the integral intensity for all observed spins. With proper calibration, this property can be used to calculate the number of observed spins.

EXPLANATION OF *fouriertransform2.nb*

The notebook starts by explicitly evaluating Equations 9.1 and 9.2. It is convenient to use the Basic Math Input Palette for the evaluation of the integrals. The spectrum is evaluated in the next several cells. It is algebraically manipulated to form a real

---

A Primer of NMR Theory with Calculations in Mathematica®, First Edition. Alan J. Benesi.

absorptive component and a dispersive imaginary component. These are converted, respectively, into an absorption function and a dispersion function in the next cells. The built-in Mathematica function Plot is used to plot the absorption and dispersion spectra for the parameters $a = 1$, $T_2 = 1\ \mathrm{s}^{-1}$, $\delta = 0$ radian s^{-1}. It is shown that identical results are obtained for the same parameters if the spectrum is left in the original imaginary form (see Plots of the function "spec").

Next, the built-in Mathematica function FindRoot is used to find the peak width at half height of the absorption spectrum. The absorptive peak width is found to be $(1/\pi)\ \mathrm{s}^{-1}$, as is expected from the general expression in terms of T_2, confirming that the absorptive peak width at half height $\Delta\nu$ is $1/(\pi\, T_2)$, where T_2 is the transverse relaxation time and $\nu = \omega/(2\,\pi)$.

HOMEWORK

Homework 9.1: (a) Calculate and plot a spectrum with $\delta = 100$ radian s^{-1}. (b) Vary the T_2 value and verify that the peak width at half height $\Delta\nu$ is $1/(\pi\, T_2)$.

CHAPTER 10

ESSENTIALS OF QUANTUM MECHANICS

For a more complete description of the quantum mechanics described in the next several chapters, the reader is referred to Levitt (2008).

The *time-independent* Schrödinger equation is as follows:

$$\hat{\mathrm{H}}\psi = E\psi \tag{10.1}$$

where $\hat{\mathbf{H}}$ is the Hamiltonian operator, ψ is the wavefunction (eigenfunction), and E is the energy eigenvalue (e.g., energy level). In general, there are a number of n quantized energy levels E_n and n different eigenfunctions ψ_n that satisfy this equation. The eigenfunctions ψ_n are the stationary states of the system. In the Dirac bra-ket notation, the aforementioned equation may be written as

$$\hat{\mathrm{H}} \mid \psi > = \mathrm{E} \mid \psi > \tag{10.2}$$

In NMR, the dominant Hamiltonian is the Zeeman Hamiltonian $H_Z = -\gamma\, \hbar\, B_0\, \hat{\mathrm{I}}_z = \hbar\, \omega_0\, \hat{\mathrm{I}}_z$ with the z axis aligned with the magnetic field B_0, where γ is the gyromagnetic ratio of the nucleus, ω_0 is the Larmor frequency of the bare nucleus in radians per second, and $\hbar$ is Planck's constant divided by 2 π radians. NMR spectroscopists usually prefer to work in frequency units (radians s^{-1}) rather than energy units, in which case the Zeeman Hamiltonian is given by $H_Z = -\gamma\, B_0\, \hat{\mathrm{I}}_z = \omega_0\, \hat{\mathrm{I}}_z$. The spin angular momentum wavefunctions have no spatial extent (unlike the wavefunctions for the hydrogen atom) and are completely characterized by the nuclear spin quantum number I (not to be confused with the operator $\hat{\mathrm{I}}$) and quantum number m in the state kets $|I,m>$.

Equation 10.2 for H_Z is as follows:

$$\hat{\mathrm{H}}_Z \mid I, m > = -\gamma\, \hbar B_0 \hat{\mathrm{I}}_z \mid I, m > = -\gamma\, \hbar B_0 m \mid I, m > = \hbar\omega_0 m \mid I, m > \tag{10.3a}$$

In units of radian s^{-1},

$$\hat{\mathrm{H}}_Z \mid I,m >= \omega_0 m \mid I,m > \tag{10.3b}$$

where m can take values from $-I$ to $+I$ in increments of 1. For example, if $I = 3/2$, m can have values −3/2, −1/2, 1/2, 3/2. The energy eigenvalue of the $|I=3/2, m=-3/2>$ state is $-3/2\ \hbar\ \omega_0$, the energy eigenvalue of the $|I=3/2, m=-1/2>$ state is $-1/2\hbar\ \omega_0$, etc. Since transitions are only allowed for $\Delta m = \pm 1$, all transitions have the same

---

A Primer of NMR Theory with Calculations in Mathematica®, First Edition. Alan J. Benesi.

energy $\Delta E = \hbar\,\omega_0 = h\,\nu_0$, where ν_0 is the resonance (Larmor) frequency of the bare nucleus in s^{-1}. It is the perturbations to the Zeeman energy levels and ν_0 that provide information in NMR. The Zeeman eigenstates are used as the basis for quantum mechanical perturbation calculations.

Only the operators $\hat{I}_z$ and $\hat{I}^2$ are eigenoperators for the spin angular momentum wavefunctions. The eigenvalue for $\hat{I}^2$ is, in Dirac bra-ket notation:

$$\hat{I}^2 \left|I,m\right> = I(I+1)\left|I,m\right> \tag{10.4}$$

For example, the eigenvalue of $\hat{I}^2$ for an $I = 5/2$ nuclear spin is 35/4.

Many important operators for observable quantities are not eigenoperators. They do not yield real eigenvalues when acting on ψ. For example, the nuclear spin angular momentum operator $\hat{I}$ is not an eigenoperator. Nor is the operator $\hat{I}^+$, which is used to calculate or simulate the observable NMR signal, or the transverse operators $\hat{I}_x$ and $\hat{I}_y$.

To calculate the expectation value of an arbitrary non-eigenoperator $\hat{O}$p:

$$<\widehat{Op}> = \int \psi^* \widehat{Op}\,\psi\, d\tau \tag{10.5}$$

where the integration is over all space τ.

The same equation in Dirac's bra-ket notation is:

$$<\widehat{Op}> = <\psi\left|\widehat{Op}\right|\psi> \tag{10.6}$$

where $<\psi|$ is called the bra and $|\psi>$ is called the ket.

Because the nuclear spin angular momentum wavefunctions have no spatial extent, there is no need to perform the integration over all space indicated in Equations 10.5 and 10.6. For eigenoperators such as $\hat{I}_z$ and $\hat{I}^2$, the expectation value is the same as the eigenvalue.

The expectation values for the important *non-eigenoperators* $\hat{I}^+$ and $\hat{I}^-$ are as follows (Levine, 1983):

$$\hat{I}^+ \left|I,m\right> = \{I(I+1) - m(m+1)\}^{1/2}\left|I,m+1\right> \tag{10.7}$$

$$\hat{I}^- \left|I,m\right> = \{I(I+1) - m(m-1)\}^{1/2}\left|I,m-1\right> \tag{10.8}$$

These are NOT eigenoperators. They change the eigenstate. The $\hat{I}_x$ and $\hat{I}_y$ operators are derived from the $\hat{I}^+$ and $\hat{I}^-$ operators as follows:

$$\hat{I}_x = (\hat{I}^+ - \hat{I}^-)/2 \tag{10.9}$$

$$\hat{I}_y = (\hat{I}^+ - \hat{I}^-)/(2i) \tag{10.10}$$

One of the more confusing aspects of quantum mechanics is the idea of superposition of states. This confusion arises because a naïve interpretation of Equations 10.1 to 10.3 suggests that a given nuclear spin must be in one of the allowed eigenstates $|\psi> = |I,m>$. *However, it turns out that a linear combination of the different allowed eigenstates* $|I,m>$ *also satisfy these equations and that the linear combination of* *states for each nuclear spin is a function of time.* At any time t, an individual nuclear spin in the presence of a magnetic field will be in the spin angular momentum state

$$|\psi(t)>=c_1(t)\big|I,m_1>+c_2(t)\big|I,m_2>+\cdots \tag{10.11}$$

where $m_n = -I$ to $+I$ in increments of 1, $c_1(t)$, $c_2(t)$, … are complex numbers with $|c_1(t)|^2 + |c_2(t)|^2 + \ldots = 1$, and different individual nuclear spins have different sets of complex coefficients $c_1(t)$, $c_2(t)$, … . *In order to understand NMR experiments, one needs to know the time dependence of the coefficients for the entire ensemble of nuclear spins.*

To paraphrase Levitt, "What is the significance of the pure eigenstates given that the nuclear spins are typically in a superposition of eigenstates?" The answer is that the pure eigenstates are the only states that are stationary. That is, if a system is somehow prepared in a pure eigenstate it will stay there as long as the Hamiltonian does not change. This is indeed the case for electronic eigenstates for atoms and molecules where the eigenstates are separated by energies much greater than the average thermal energy *but not for nuclear spin angular momentum where the eigenstates are separated by energies much less than the average thermal energy*. The motions produced by thermal energy and corresponding fluctuating internal Hamiltonians perturb nuclear spins away from their pure Zeeman eigenstates.

The strange nature of superposition can be appreciated by considering a non-NMR experiment (Sakurai, 1985). Stern and Gerlach generated a beam of neutral silver atoms in a vacuum by evaporating silver from an oven. After collimating the beam of silver atoms by passing it through slits, it was passed through a region with a large nonuniform magnetic field. Because each silver atom contained one unpaired electron with electron spin quantum number $I = 1/2$,[1] each silver atom had a net electron spin magnetic moment. The unpaired electron spin behaves like an $I = 1/2$ nuclear spin but has a much larger magnetic dipole moment μ. The dipole moment is imparted to the silver atom containing the unpaired electron spin.[2] The magnetic field inhomogeneity $\frac{\partial B}{\partial z}$ produces a force on the magnetic moments $\frac{\partial B}{\partial z}\mu_z$ where μ_z is the component of the magnetic moment in the z direction. The silver atoms in the Stern Gerlach experiment were thus deflected and allowed to strike a metallic plate where the silver atoms accumulated with time. The deposit showed two distinct marks showing that the silver atoms had only two allowed components of μ_z. This is different than the classical expectation, where a continuum of values from $+\mu$ to $-\mu$ would be expected.

Quantum mechanically, different silver atoms have different and random complex coefficients (Eq. 10.11), so one might again naively expect a continuous distribution at the detector. Experimentally, however, the beam splits into two distinct "spots," one for the |1/2,1/2> eigenstate and one for the |1/2,−1/2> eigenstate.

---

[1] http://hyperphysics.phy-astr.gsu.edu/hbase/spin.html

[2] The Zeeman eigenstates for an electron spin are separated by energies much less than the thermal energy available at ambient temperature.

Although individual nuclear spins will generally be in a superposition state as described in Equation 10.11, in analogy to the Stern Gerlach experiment the *detectable signal* from the simplest NMR experiments corresponds to a transition between adjacent "pure" eigenstates and therefore can be described (as shown in later chapters) by applying *time-independent perturbation theory* to the Zeeman eigenstates. However, understanding more complicated NMR experiments requires explicit knowledge of the time-dependent coefficients $c_n(t)$ of the superposition of states for the ensemble of nuclear spins.

CHAPTER 11

THE TIME-DEPENDENT SCHRÖDINGER EQUATION, MATRIX REPRESENTATION OF NUCLEAR SPIN ANGULAR MOMENTUM OPERATORS

In energy units, the *time-dependent* Schrödinger wave equation is:

$$\frac{d}{dt}|\psi>(t)=-i\hbar\hat{\mathrm{H}}|\psi>(t) \tag{11.1}$$

or in units of rad s^{-1} as commonly used by NMR spectroscopists,

$$\frac{d}{dt}|\psi>(t)=-i\hat{\mathrm{H}}|\psi>(t) \tag{11.2}$$

If $\hat{\mathrm{H}}$ is the time-independent Zeeman Hamiltonian $\hat{\mathrm{H}}_Z=\omega_0\hat{\mathrm{I}}_z$, Equation 11.2 is easily solved to yield

$$|\psi>(t)=e^{-i\omega_0\hat{\mathrm{I}}_z t}|\psi>(0) \tag{11.3}$$

This indicates that the nuclear spin angular momentum wavefunction rotates about the *z* axis defined by the magnetic field.

If the system is in a pure Zeeman eigenstate $|\psi_n>=|I,m>$ at $t=0$, Equation 11.3 yields (we postpone the discussion of exponential operators to Chapter 17) the following:

$$|I,m>(t)=e^{-im\omega_0 t}|I,m>(0) \tag{11.4}$$

Thus, each spin in a pure eigenstate rotates about the *z* axis at *m* times the Larmor frequency.

As discussed in the previous chapter, a single nuclear spin is hardly ever found in a pure eigenstate. Instead, the vast majority of spins are in a superposition of different eigenstates of the Zeeman Hamiltonian, $\hat{\mathrm{H}}_Z=-\gamma\hbar B_0\hat{\mathrm{I}}_Z$. A convenient way to describe

---

A Primer of NMR Theory with Calculations in Mathematica®, First Edition. Alan J. Benesi.

the superposition state of an individual spin is to list the time-dependent complex coefficients c_n in the form of a *vector*, as shown in the notebook *vector_matrix.nb*.

All of the Hamiltonians encountered in NMR are constructed using spin angular momentum operators. These can be expressed in *matrix form* as shown for several important spin operators here, where it is assumed that the nuclear spin quantum number is $I = 3/2$.

The matrix representation of the operator $\hat{I}_z$ for an $I = 3/2$ spin is:

<3/2,3/2|$\hat{I}_z$|3/2,3/2> <3/2,3/2|$\hat{I}_z$|3/2,1/2> <3/2,3/2|$\hat{I}_z$|3/2,–1/2> <3/2,3/2|$\hat{I}_z$|3/2,–3/2>
<3/2,1/2|$\hat{I}_z$|3/2,3/2> <3/2,1/2|$\hat{I}_z$|3/2,1/2> <3/2,1/2|$\hat{I}_z$|3/2,–1/2> <3/2,1/2|$\hat{I}_z$|3/2,–3/2>
<3/2,–1/2|$\hat{I}_z$|3/2,3/2> <3/2,–1/2|$\hat{I}_z$|3/2,1/2> <3/2,–1/2|$\hat{I}_z$|3/2,–1/2> <3/2,–1/2|$\hat{I}_z$|3/2,–3/2>
<3/2,–3/2|$\hat{I}_z$|3/2,3/2> <3/2,–3/2|$\hat{I}_z$|3/2,1/2> <3/2,–3/2|$\hat{I}_z$|3/2,–1/2> <3/2,–3/2|$\hat{I}_z$|3/2,–3/2>

Because I_z is an eigenoperator, the preceding 4×4 matrix can be expressed in terms of the corresponding scalar eigenvalues:

<3/2,3/2|3/2|3/2,3/2> <3/2,3/2|1/2|3/2,1/2> <3/2,3/2|–1/2|3/2,–1/2> <3/2,3/2|–3/2|3/2,–3/2>
<3/2,1/2|3/2|3/2,3/2> <3/2,1/2|1/2|3/2,1/2> <3/2,1/2|–1/2|3/2,–1/2> <3/2,1/2|–3/2|3/2,–3/2>
<3/2,–1/2|3/2|3/2,3/2> <3/2,–1/2|1/2|3/2,1/2> <3/2,–1/2|–1/2|3/2,–1/2> <3/2,–1/2|–3/2|3/2,–3/2>
<3/2,–3/2|3/2|3/2,3/2> <3/2,–3/2|1/2|3/2,1/2> <3/2,–3/2|–1/2|3/2,–1/2> <3/2,–3/2|–3/2|3/2,–3/2>

The scalar eigenvalues can be moved to precede the brackets:

3/2<3/2,3/2|3/2,3/2> 1/2<3/2,3/2|3/2,1/2> –1/2<3/2,3/2|3/2,–1/2> –3/2<3/2,3/2|3/2,–3/2>
3/2<3/2,1/2|3/2,3/2> 1/2<3/2,1/2|3/2,1/2> –1/2<3/2,1/2|3/2,–1/2> –3/2<3/2,1/2|3/2,–3/2>
3/2<3/2,–1/2|3/2,3/2> 1/2<3/2,–1/2|3/2,1/2> –1/2<3/2,–1/2|3/2,–1/2> –3/2<3/2,–1/2|3/2,–3/2>
3/2<3/2,–3/2|3/2,3/2> 1/2<3/2,–3/2|3/2,1/2> –1/2<3/2,–3/2|3/2,–1/2> –3/2<3/2,–3/2|3/2,–3/2>

At this point, we take advantage of the orthonormality of the bras and kets, that is, <3/2,3/2|3/2,3/2> = 1, but <3/2,3/2|3/2,1/2> = 0, etc., to find the following:

$$\begin{pmatrix} \frac{3}{2} & 0 & 0 & 0 \\ 0 & \frac{1}{2} & 0 & 0 \\ 0 & 0 & -\frac{1}{2} & 0 \\ 0 & 0 & 0 & -\frac{3}{2} \end{pmatrix}$$

This is the matrix representation of the spin angular momentum eigenoperator I_z for an $I = 3/2$ nuclear spin.

The matrix representation of the spin angular momentum operator $\hat{I}^+$ (NOT an eigenoperator) is obtained in the same way (see Eq. 10.7):

$$
\begin{matrix}
<3/2,3/2|\hat{I}^+|3/2,3/2> & <3/2,3/2|\hat{I}^+|3/2,1/2> & <3/2,3/2|\hat{I}^+|3/2,-1/2> & <3/2,3/2|\hat{I}^+|3/2,-3/2> \\
<3/2,1/2|\hat{I}^+|3/2,3/2> & <3/2,1/2|\hat{I}^+|3/2,1/2> & <3/2,1/2|\hat{I}^+|3/2,-1/2> & <3/2,1/2|\hat{I}^+|3/2,-3/2> \\
<3/2,-1/2|\hat{I}^+|3/2,3/2> & <3/2,-1/2|\hat{I}^+|3/2,1/2> & <3/2,-1/2|\hat{I}^+|3/2,-1/2> & <3/2,-1/2|\hat{I}^+|3/2,-3/2> \\
<3/2,-3/2|\hat{I}^+|3/2,3/2> & <3/2,-3/2|\hat{I}^+|3/2,1/2> & <3/2,-3/2|\hat{I}^+|3/2,-1/2> & <3/2,-3/2|\hat{I}^+|3/2,-3/2>
\end{matrix}
$$

Straightforward evaluation yields the following:

$$
\begin{pmatrix}
0 & \sqrt{3} & 0 & 0 \\
0 & 0 & 2 & 0 \\
0 & 0 & 0 & \sqrt{3} \\
0 & 0 & 0 & 0
\end{pmatrix}
$$

In order to easily obtain matrix representations of the spin angular momentum operators with Mathematica, evaluate the notebook *matrep2.nb*, and then go through the notebook *matrixformoperators.nb*. Matrix representations of $\hat{I}_z$, $\hat{I}^2$, $\hat{I}^+$, $\hat{I}^-$, $\hat{I}_x$, $\hat{I}_y$, are available for arbitrary spin angular quantum numbers *I*. The student should also learn and understand the matrix representations of these operators for different values of the nuclear spin angular momentum quantum number *I*.

EXPLANATION OF *vector_matrix.nb*

This notebook starts with a brief review of the vector dot product and cross product, then proceeds to demonstrate the Mathematica built-in function Outer, which yields the outer product of vectors to produce matrices. The cells also show that the Outer product of vectors is not commutative. The next cells introduce two 3 × 3 matrices *X* and *Y*, then show the matrix product and the products of vectors and matrices. The noncommutativity of these operations is also demonstrated.

The next cells show how the wavefunction $|\Psi>$, the "ket" in Dirac nomenclature, for a superposition state can be represented as a vector of complex coefficients and that the vector composed of the complex conjugates of these coefficients $<\Psi^*|$ represents the bra for the superposition state. The next cells define a generic operator Q and show how to evaluate its expectation value, $<\Psi^*|Q|\Psi>$. The expectation value is shown to be a scalar.

The next cells show that the outer product of the ket and bra yield a matrix that represents the density matrix for a single spin. Following cells show that the expectation value for the generic operator Q can be obtained by taking the trace (sum of diagonal elements) of the matrix product of Q and the density matrix or the trace of the product of the density matrix and Q.

EXPLANATION OF *matrep2.nb*

matrep2.nb is used as a “tool” for density matrix calculations in other Mathematica notebooks. It defines functions that calculate matrix representations of spin angular momentum operators and functions for other important matrix operations such as trace, adjoint, dirprod, simtran, etc. Note that all the individual cells of *matrep2.nb* are tied together into one “supercell.” The individual functions were created with the := command. The /: commands add no content to the functions defined with := command and are not necessary. The /: additions appear when the individual cells are united into a supercell.

EXPLANATION OF *matrixformoperators.nb*

The first comment in this notebook sets an important precedent. It is often necessary to evaluate other notebooks in order to evaluate the desired notebook. In this case, *matrep2.nb* must be evaluated in order to evaluate *matrixformoperators.nb*. The comment directs the user to evaluate *matrep2.nb* and close it without saving changes.

The next cells demonstrate how to obtain the matrix representations of spin angular momentum operators. The matrix representations of I^2, I_z, I^+, I^-, I_x, I_y for nuclear spin quantum number I are obtained with the functions $i_{\mathrm{sq}}[I]$, $i_z[I]$, $i_{\mathrm{plus}}[I]$, $i_{\mathrm{min}}[I]$, $i_x[I]$, $i_y[I]$. These functions are used to obtain matrix representations of spin angular momentum operators for $I = 1/2$, 1, and 3/2.

HOMEWORK

Homework 11.1: Use program *matrep2.nb* to calculate the matrix representations of operators I_x, I_y, I_z, I^+, I^-, I^2 for

(a) $I = 1/2$
(b) $I = 1$
(c) $I = 5/2$

CHAPTER 12

THE DENSITY OPERATOR

The solution to the time-dependent Schrödinger equation (Eqs. 11.1 and 11.2) gives the time dependence of the complex coefficients $c_n(t)$ for the superposition of eigenstates of an individual nuclear spin. These coefficients may be represented as a vector of dimension $n = 2I + 1$, as shown in the Mathematica notebook *vector_matrix.nb*. However, another useful way to represent these coefficients is through the density operator in matrix form.

The density operator of an individual nuclear spin k, ρ(k), is the outer product of the ket and bra of that spin (Levitt, 2008, pp. 259–261),

$$\rho(k) = |\psi(k)><\psi(k)| \tag{12.1}$$

where $|\psi(k)>$ and $<\psi(k)|$ are the time-dependent vectors of coefficients $c_n(t)$ and $c_n^*(t)$, respectively, for the Zeeman eigenstates of spin k (see *vector_matrix.nb* and the explanation of it at the end of Chapter 11), that is,

$$\rho(k) = \begin{pmatrix} c_1^* c_1 & \cdots & c_1^* c_n \\ \vdots & \ddots & \vdots \\ c_n^* c_1 & \cdots & c_n^* c_n \end{pmatrix} \tag{12.2}$$

where the diagonal elements are $c_1^* c_1, c_2^* c_2, \ldots, c_n^* c_n$. The diagonal elements are real numbers and represent the populations of the corresponding Zeeman states. The off-diagonal elements are generally complex and represent "coherences" with transverse x and y components. Coherences are the response of the spin system to the energy from the rf pulses. Random, incoherent off-diagonal elements can also be created by thermal fluctuations of the internal Hamiltonians.

The density operator for the entire ensemble of nuclear spins is given by the sum of contributions from the individual nuclear spins:

$$\hat{\rho}_{\text{ensemble}} = \sum_k \hat{\rho}(k) \tag{12.3}$$

A Primer of NMR Theory with Calculations in Mathematica®, First Edition. Alan J. Benesi.

The expectation value for *any* operator $\hat{Q}$ (such as $\hat{I}^{+}$) for the statistical ensemble of nuclear spins is as follows:

$$<\hat{Q}_{\text{ensemble}}> = \text{Tr}[\hat{\rho}_{\text{ensemble}} \cdot \hat{Q}] = \text{Tr}[\hat{Q} \cdot \hat{\rho}_{\text{ensemble}}] \tag{12.4}$$

This is an exceptionally important result because it allows the nuclear magnetic resonance signal to be predicted by calculating the expectation value (Eq. 12.4*) of the spin angular momentum operator* $\hat{I}^{+}$.

CHAPTER 13

THE LIOUVILLE–VON NEUMANN EQUATION

The Liouville–von Neumann equation (von Neumann, 1932) is the equation of motion for the density operator. It applies to the density operator of a single nuclear spin and to the density operator for an ensemble of spins. It follows directly from the time-dependent Schrödinger equation (Eqs 11.1 and 11.2) (Sakurai, 1985, p. 181). In units of energy, it is (we neglect effects of relaxation for now):

$$\frac{d\hat{\rho}}{dt} = -\frac{i}{\hbar}[\hat{\mathrm{H}}, \hat{\rho}] \tag{13.1}$$

where $\hat{\rho}$ is the density operator, $\hat{\mathrm{H}}$ is the Hamiltonian operator, and $[\hat{\mathrm{H}},\ \hat{\rho}] = \hat{\mathrm{H}} \cdot \hat{\rho} - \hat{\rho} \cdot \hat{\mathrm{H}}$ is the commutator of $\hat{\mathrm{H}}$ and $\hat{\rho}$.

In units of rotational frequency (rad s^{-1}), it is:

$$\frac{d\hat{\rho}}{dt} = -i[\hat{\mathrm{H}}, \hat{\rho}] \tag{13.2}$$

When effects of relaxation are included,

$$\frac{d\hat{\rho}}{dt} = -\frac{i}{\hbar}[\hat{\mathrm{H}}, \hat{\rho}] - \Gamma(\hat{\rho} - \hat{\rho}_{\mathrm{eq}}) \tag{13.3}$$

where Γ is the relaxation superoperator. NMR relaxation is the subject of later chapters. However, because NMR relaxation is often relatively slow, it is possible to use Equation 13.2 for the analysis of many pulse sequences.

A Primer of NMR Theory with Calculations in Mathematica®, First Edition. Alan J. Benesi.

CHAPTER 14

THE DENSITY OPERATOR AT THERMAL EQUILIBRIUM

For an ensemble of nuclear spins, the close spacing of the Zeeman energy levels and the Boltzmann distribution guarantee that at thermal equilibrium the populations of the different m levels are nearly equal. At thermal equilibrium, the off-diagonal components of the density matrix[1] for a nuclear spin have random values and average to zero for the ensemble. Therefore $\rho_{rs} = 0$ for $r \neq s$. The populations of the diagonal components ρ_{rr} of the ensemble are given by the Boltzmann distribution:

$$\rho_{\mathrm{eq\_}rr} = \frac{\exp(-m_r \hbar(\omega_0 / k_\mathrm{B} T))}{\sum_s \exp(-m_s \hbar(\omega_0 / k_\mathrm{B} T))} \tag{14.1}$$

where m_r and m_s are the m quantum numbers for the Zeeman eigenstates $|I,m>$, ω_0 is the Larmor frequency in rad s^{-1}, k_B is Boltzmann's constant, and T is the absolute temperature.

Even in the strongest magnetic fields available, $\hbar\omega_0 \ll k_\mathrm{B}T$, and the exponentials can be expanded in a Taylor series that retains only two terms, hence

$$\exp\left(-m_r \hbar \frac{\omega_0}{k_\mathrm{B} T}\right) \cong 1 + m_r \hbar \omega_0 / k_\mathrm{B} T \tag{14.2}$$

This is the so-called *high temperature approximation*, although it is valid as low as 1 K for currently available magnetic fields. The fractional population difference between adjacent m levels is typically less than one part in 10^5, which is one of the reasons that NMR is not an especially sensitive technique.

Each exponential term in the sum in the denominator of Equation 14.1 is almost exactly 1, therefore for the $2I+1$ different values of m_r the sum yields $2I+1$, where I is the nuclear spin quantum number.

---

[1] The off-diagonal elements define the phases of individual nuclear spins.

A Primer of NMR Theory with Calculations in Mathematica®, First Edition. Alan J. Benesi.

Combining Equations 14.1 and 14.2 with the denominator $2I+1$ yields the following:

$$\rho_{\mathrm{eq\_}rr} = \frac{1}{2I+1} + \frac{m_r \hbar \omega_0}{(2I+1)k_\mathrm{B}T} \tag{14.3}$$

Therefore, the equilibrium density matrix for an $I=3/2$ nuclear spin in a magnetic field is as follows:

$$\hat{\rho}_{\mathrm{eq}} = \begin{pmatrix} \frac{1}{4}+\frac{3b}{8} & 0 & 0 & 0 \\ 0 & \frac{1}{4}+\frac{b}{8} & 0 & 0 \\ 0 & 0 & \frac{1}{4}-\frac{b}{8} & 0 \\ 0 & 0 & 0 & \frac{1}{4}-\frac{3b}{8} \end{pmatrix} \tag{14.4}$$

where $b=\hbar\omega_0/k_\mathrm{B}T$.

As shown in the Mathematica notebook *equil_densitymatrix.nb*, the part of the equilibrium density matrix corresponding to the $1/(2I+1)$ term in Equation 14.3 is unaffected by Hamiltonians since it is a constant times the identity matrix. Therefore, it *cannot* be used to generate off-diagonal coherence observable in NMR experiments and can be ignored. Only the difference in population between Zeeman levels can give rise to off-diagonal coherence. *Thus, the effective equilibrium density matrix for each type of nucleus is as follows*:

$$\hat{\rho}_{\mathrm{eq}} = \frac{b}{2I+1}\hat{\mathrm{I}}_z \tag{14.5a}$$

If several different types k of nuclear spin are in the system,

$$\hat{\rho}_{\mathrm{eq}} = \sum_{k=1}^{n} \frac{b_k}{2I_k+1}\hat{\mathrm{I}}_z(k) \tag{14.5b}$$

where $b_k=\hbar\omega_{0k}/k_\mathrm{B}T$.

For a single type of $I=3/2$ nuclear spin, the matrix representation is as follows:

$$\hat{\rho}_{\mathrm{eq}} = \begin{pmatrix} \frac{3b}{8} & 0 & 0 & 0 \\ 0 & \frac{b}{8} & 0 & 0 \\ 0 & 0 & -\frac{b}{8} & 0 \\ 0 & 0 & 0 & -\frac{3b}{8} \end{pmatrix} \tag{14.6}$$

Also as shown in *equil_densitymatrix.nb*, transforming from the laboratory to the rotating frame does not change the equilibrium density matrix. *The effective equilibrium density matrix in the rotating frame is therefore also given by Equation 14.5.* This result is of extreme importance because it is the starting point for all NMR experiments. $\hat{\rho}_{\text{eq}}$ is the only part of the ensemble density operator that can be changed by the Liouville–von Neumann equation (Eqs. 13.1–13.3).

EXPLANATION OF *equil_densitymatrix.nb*

The first cell instructs the user to evaluate and close *matrep2.nb* (without saving). The following cells define the equilibrium density matrix ρ_{eq} for an $I=3/2$ nuclear spin. The next cells illustrate the "propagation" of the lab frame density matrix to the rotating frame. This transformation is discussed more in later chapters. Since the magnetic field defines the z axis, the rotating frame corresponds to a rotation about the z axis. This transformation does not affect ρ_{eq}.

In contrast, the next cells show that rotations around the x or y axes transform ρ_{eq} to forms with non-zero x and y components. We then show that these transverse components (coherences) arise from only the difference term b. The next cells show explicitly that the constant term is unaffected by rotations about any axis and cannot generate off-diagonal coherence. The last cells show that the "difference" part of the equilibrium density matrix ρ_{diff}, equivalent to $\hat{\rho}_{\text{eq}}$ in Equations 14.5 and 14.6, is significantly transformed by rotations around the x and y axes. The final cell, a comment, is worth repeating. All NMR experiments start with $\hat{\rho}_{\text{eq}}$ (ρ_{diff}).

CHAPTER 15

HAMILTONIANS OF NMR: ISOTROPIC LIQUID-STATE HAMILTONIANS

With the effective equilibrium density operator $\hat{\rho}_{eq}$ as the starting point of all NMR experiments (Chapter 14), the time-dependence of the density operator can be calculated with the Liouville–von Neumann equation (Chapter 13) if the Hamiltonians at each time in the experiment are known. Nuclear spins are only weakly coupled to their surroundings and therefore have weak Hamiltonians. The Zeeman Hamiltonian is almost always the strongest Hamiltonian, although it is the other internal Hamiltonians that are important if one wishes to obtain detailed information about atomic structure and dynamics. Conveniently, the smaller magnitudes of the internal Hamiltonians allow the Zeeman eigenstates to be used as the basis set for perturbation calculations in NMR.

The solid-state Hamiltonians will be introduced in Chapter 29. There it is shown that each Hamiltonian encountered in NMR is expressed in terms of a *spin space* part that depends only on spin angular momentum operators and a *real space* part that depends on the orientation of the molecules containing the nuclei (Mehring, 2002; Spiess, 1978). The laboratory reference frame for both spaces is defined by the magnetic field north pole that is aligned by convention with the positive *z* axis (Fig. 3.3). The positions of the *x* and *y* axes are orthogonal and fixed but arbitrary.

The rotating frame is obtained from the *spin space* laboratory frame by rotating it in coincidence with the resonance (Larmor) precession. The *real space* part of the Hamiltonian is unaffected by the transformation to the rotating frame.

It is the "real space" part of the Hamiltonian that determines the observed frequencies in the NMR spectrum. Although $\hat{H}_Z$ and $\hat{H}_{RF}$ are usually uniform across the NMR sample,[1] the real space parts of the other Hamiltonians depend on the *real space* orientations of the atoms and molecules containing the nuclei.

---

[1] Unless magnetic field gradients or radiofrequency field gradients are applied.

A Primer of NMR Theory with Calculations in Mathematica®, First Edition. Alan J. Benesi.

The total Hamiltonian $\hat{H}_{tot}$ acting on nuclear spins can include the following contributions,

$$\hat{H}_{tot} = \hat{H}_Z + \hat{H}_Q + \hat{H}_{RF} + \hat{H}_{SR} + \hat{H}_D + \hat{H}_{CS} + \hat{H}_K + \hat{H}_J \tag{15.1}$$

where $\hat{H}_Z$ is the Zeeman Hamiltonian, $\hat{H}_Q$ is the quadrupolar Hamiltonian, $\hat{H}_{RF}$ is the radiofrequency Hamiltonian, $\hat{H}_{SR}$ is the spin rotation Hamiltonian, $\hat{H}_D$ is the dipolar Hamiltonian,[2] $\hat{H}_{CS}$ is the chemical shift Hamiltonian, $\hat{H}_K$ is the Knight shift Hamiltonian, and $\hat{H}_J$ is the J-coupling Hamiltonian. $\hat{H}_Z$ and $\hat{H}_{RF}$ are *external Hamiltonians* under human control (e.g., the magnet, magnetic field gradients, and radiofrequency pulses), while the others are *internal Hamiltonians* determined by their local atomic level environment.

Although the Zeeman resonance frequency of a bare nucleus is exactly equal to ω_0, the internal Hamiltonians perturb the resonance frequency. In general, each different electronic environment of a given nucleus produces a different internal Hamiltonian and a different perturbation. For example, $\hat{H}_{CS\_C13}$ for a carboxyl group carbon is different than $\hat{H}_{CS\_C13}$ for a methyl group carbon. *The unique values for the internal Hamiltonians of each electronic environment and position in a molecule are the way NMR provides a window into the atomic-level world.*

The magnitude of a Hamiltonian $\hat{H}_X$ is defined as

$$\left\|\hat{H}_X\right\| = (\text{Trace}[\hat{H}_X \cdot \hat{H}_X])^{1/2} \tag{15.2}$$

where the double vertical bars denote the magnitude, $\hat{H}_X \cdot \hat{H}_X$ indicates the matrix product of $\hat{H}_{XX}$ with itself, Trace indicates the sum of diagonal elements of the resulting product matrix from upper left to lower right, of which the square root is taken.

$\hat{H}_Q$ is often the largest of the internal Hamiltonians with a magnitude that can in rare cases exceed that of $\hat{H}_Z$. It is only observed in nuclei with $I > 1/2$, that is, $I = 1$, $I = 3/2$, $I = 2$, $I = 5/2$, $I = 3$, $I = 7/2$, etc. There is a nonuniform distribution of positive charge in nuclei with $I > 1/2$, which means that they have an electric quadrupole moment in addition to a magnetic dipole moment. $\hat{H}_Q$ arises from the *electric coupling* of the nuclear electric quadrupole moment and the electric field gradients from electron orbitals surrounding the nucleus. Reorientation of molecules (hence electron orbitals) in liquids averages it to zero, that is, $\hat{H}_{Q\_liquid} = 0$.

The effects of $\hat{H}_{SR}$ are only observed in polyatomic gases, liquids with very low viscosity, or functional groups with free torsion angles. *Unchanging molecular angular momentum* is required to observe the effects of $\hat{H}_{SR}$, but the collisions in most liquids cause rapid changes in molecular angular momentum. Therefore, in the vast majority of liquid-state samples $\hat{H}_{SR\_liquid} = 0$. In solids, there is rarely unhindered molecular angular momentum, so $\hat{H}_{SR\_solid} = 0$.

---

[2] $\hat{H}_D$ applies to homonuclear, heteronuclear, and paramagnetic (nuclear spin–unpaired electron spin) interactions.

The total dipolar Hamiltonian $\hat{H}_D$ for a nuclear spin *i* is given by $\sum_{j \neq i} \hat{H}_{Dij}$, the sum of the pairwise interactions. These come about from the direct through-space magnetic interaction of the nuclear magnetic dipole moments. The dipolar Hamiltonian is large, internuclear distance–dependent, and orientation-dependent. It is a very useful source of information in solid-state NMR where experiments utilize the dipolar Hamiltonian for coherence transfer between nuclei. Nevertheless, it averages to zero in liquid samples, that is, $\hat{H}_{Dij\_liquid} = 0$.

The Knight shift Hamiltonian $\hat{H}_K$ is observed in conductive samples such as metals and conducting polymers. It arises from circulation of the electron density in open shell (metallic) orbitals.

The chemical shift Hamiltonian $\hat{H}_{CS}$ is observed in nonconductive diamagnetic samples in both the solid state and the liquid state. This constitutes the vast majority of NMR samples. $\hat{H}_{CS}$ has a non-zero isotropic component. It is the major source of information in liquid-state NMR. It arises from the electric currents and magnetic shielding induced in electron orbitals by the magnetic field. $\hat{H}_{CS\_liquid} \neq 0$.

$\hat{H}_J$ is observed in nonconductive diamagnetic samples in both the solid state and the liquid state, which means the vast majority of NMR samples. $\hat{H}_J$ has a non-zero isotropic component. It is used not only for its information content but also for coherence transfer between nuclei. It arises from the indirect coupling of nuclear spins mediated by electron density in orbitals between them. In liquids, $\hat{H}_{J\_liquid} \neq 0$.

Summarizing, in rigid solids, $\|\hat{H}_Z\| \gg \|\hat{H}_Q\| > \|\hat{H}_{RF}\| > \|\hat{H}_{SR}\| > \|\hat{H}_D\| > \|\hat{H}_K\| > \|\hat{H}_{CS}\| > \|\hat{H}_J\|$. However, due to differences in the electronic environment there is variation in the relative magnitudes, so this order does not always apply.

In liquids, the relative magnitudes of the Hamiltonians are very different. *Rapid molecular reorientation in liquids averages the real space parts of the internal Hamiltonians.* With rotational correlation times of 10^{-12} to 10^{-9} s, the Hamiltonians are completely averaged in one Larmor period ($1/\nu_0$). For $\hat{H}_Q$ and $\hat{H}_D$, the average is zero. Therefore, these have no direct effect on the frequencies observed in the NMR spectrum or on the evolution of the density operator. However, the *rapidly fluctuating real space components* from these Hamiltonians cause NMR relaxation and can therefore affect peak linewidths via their effects on T_2. $\hat{H}_{SR}$ has a non-zero real space average but is rarely observed except in gases or for very small molecules in very low–viscosity solvents. $\hat{H}_K$ has a non-zero average but is only observed for conductive metals and conductive polymers. The only remaining important liquid-state Hamiltonians for molecules in liquids are therefore $\hat{H}_{CS}$ and $\hat{H}_J$, which have non-zero isotropic components that determine the frequencies and splitting observed in liquid-state spectra.

Almost all time-dependent theoretical analyses use the rotating frame Hamiltonian. This eliminates the effects of $\hat{H}_Z$ in the Liouville–von Neumann equation. $\hat{H}_Z$ is nevertheless the dominant Hamilton. Its eigenstates are the basis set for the calculations.

The liquid-state Hamiltonians are summarized for convenience in Table 15.1.

A semiquantitative comparison of the relative magnitudes of some solid-state and liquid-state Hamiltonians is shown in Figure 15.1.

TABLE 15.1 Liquid-state Hamiltonians

Hamiltonian[a]	Symbol	Lab frame isotropic component	Lab frame isotropic (rad s^{-1})	Rotating frame isotropic	Comments
Zeeman	$\hat{H}_Z$	$-\gamma B_0 \hat{I}_z$	$\omega_0 \hat{I}_z$	0	Homogeneous B_0, can be inhomogeneous as in pulsed magnetic field gradients
Quadrupolar	$\hat{H}_Q$	0	0	0	Only for $I > 1/2$, has large effects on relaxation times
Spin rotation	$\hat{H}_{SR}$	Usually 0, $-\gamma B_0 \hat{I}_z (1 - C_{iso} \hat{I}.\hat{O})$ when observable	Usually 0, $\omega_0 \hat{I}_z - C_{iso} \hat{I}.\hat{O}$ when observable	Usually 0, $-C_{iso} \hat{I}.\hat{O}$ if observable	Only observed in gases and very low–viscosity liquids
Dipolar	$\hat{H}_{Dij}$	0	0	0	Large effects on relaxation times
Knight shift	$\hat{H}_K$	Usually 0, $-\gamma B_0 \hat{I}_z (1 - K_{iso})$ when observable	Usually 0, $(\omega_0 - \delta_{iso}) \hat{I}_z$ when observable	Usually 0, $-\xi_{iso} \hat{I}_z$ if observable	Observed in metallic solids and liquids
Chemical shift	$\hat{H}_{CS}$	$-\gamma B_0 \hat{I}_z (1 - \sigma_{iso})$	$(\omega_0 - \delta_{iso}) \hat{I}_z$	$-\delta_{iso} \hat{I}_z$	Observed in liquids
J-coupling	$\hat{H}_J$	$-\gamma B_0 \hat{I}_z + 2\pi J_{iso} \hat{I}_1.\hat{I}_2$	$\omega_0 \hat{I}_z + 2\pi J_{iso} \hat{I}_1.\hat{I}_2$	$2\pi J_{iso} \hat{I}_1.\hat{I}_2$	Observed in liquids, $\lvert\delta_1 - \delta_2\rvert \leq$ or $\approx \lvert 2\pi J_{iso}\rvert$
		$-\gamma B_0 \hat{I}_z + 2\pi J_{iso} \hat{I}_{z1}.\hat{I}_{z2}$	$\omega_0 \hat{I}_z + 2\pi J_{iso} \hat{I}_{z1}.\hat{I}_{z2}$	$2\pi J_{iso} \hat{I}_{z1}.\hat{I}_{z2}$	Observed in liquids, $\lvert\delta_1 - \delta_2\rvert \gg \lvert J_{iso}\rvert$
Radio frequency[b]	$\hat{H}_{RF}$	$-\gamma B_1(\cos\phi \hat{I}_x + \sin\phi \hat{I}_y) + -\gamma B_0 \hat{I}_z$	$\omega_1 (\cos\phi \hat{I}_x + \sin\phi \hat{I}_y) + \omega_0 \hat{I}_z$	$\omega_1 (\cos\phi \hat{I}_x + \sin\phi \hat{I}_y)$	Under precise human control

[a] Mehring (2002) and Spiess (1978).

[b] We remember that $\hat{H}_{RF}$ represents a linearly oscillating magnetic field in the x–y laboratory frame (see Fig. 3.2). We “decompose” it into two counter-rotating circularly rotating components at ω_0 and $-\omega_0$. Here, we consider the component of $\hat{H}_{RF}$ that rotates in the same direction as ω_0.

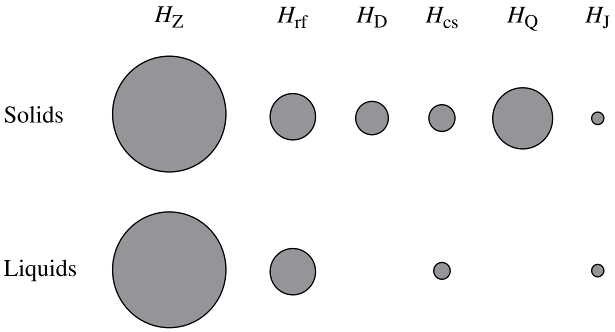

Figure 15.1 A Semiquantitative Comparison of the Effects of Solid- and Liquid-State Hamiltonian Magnitudes on NMR spectra. Levitt, M.H., *Spin Dynamics: Basics of Nuclear Magnetic Resonance*, 2nd Edition, John Wiley & Sons, Ltd, 2008. Adapted from Figure 9.31, page 223.

Rapid molecular reorientation averages the nonisotropic components of the various Hamiltonians to zero. Only the isotropic components of the Hamiltonians survive. H_z and H_{rf} are isotropic and unaffected by rapid molecular reorientation. H_{CS} and H_J are reduced in magnitude but survive because they have non-zero isotropic components in addition to anisotropic components. H_Q and H_D possess only anisotropic components, so their effects on NMR spectra in liquids are eliminated by rapid molecular reorientation.

CHAPTER 16

THE DIRECT PRODUCT MATRIX REPRESENTATION OF COUPLING HAMILTONIANS H_J AND H_D

$\hat{\mathrm{H}}_\mathrm{J}$ and $\hat{\mathrm{H}}_\mathrm{D}$ are both extremely important Hamiltonians for NMR, because they provide the opportunity for coherence transfer between different nuclear spins. These pairwise "coupling" Hamiltonians require modification of the matrix representation of the Hamiltonian and the density operator, illustrated below for the weak J coupling between two homonuclear $I=1/2$ nuclei (e.g., two ^{1}H nuclei) in the liquid state, for which $\hat{\mathrm{H}}_\mathrm{J}=2\pi\ \mathrm{J}_{12}\ \hat{\mathrm{I}}_{z1}.\hat{\mathrm{I}}_{z2}$ and for which $\rho_\mathrm{eq}=\mathrm{const}\ I_{z1}+\mathrm{const}\ I_{z2}$ (Eq. 14.5).

The matrix representation of I_{z1} is obtained by taking the *direct product* of the single spin matrix representation of $\hat{\mathrm{I}}_{z1}$ for $I=1/2$ with the unit (identity) matrix for spin 2,

$$\hat{\mathrm{I}}_{z1}=\hat{\mathrm{I}}_{z1}\,1_2 \tag{16.1a}$$

$$=\begin{pmatrix} \frac{1}{2} & 0 \\ 0 & -\frac{1}{2} \end{pmatrix}\otimes\begin{pmatrix} 1 & 0 \\ 0 & 1 \end{pmatrix} \tag{16.1b}$$

We use streamlined bras and kets to simplify the nomenclature for the resulting matrix. For example, the bra $\langle I_1,m_1,I_2,m_2|$ is simplified to $\langle m_1,m_2|$. With this simplification, the direct product aforementioned for two $I=1/2$ spins can be expressed as follows:

$$\begin{array}{cccc}
\langle 1/2,1/2|\hat{\mathrm{I}}_{z1}|1/2,1/2\rangle & \langle 1/2,1/2|\hat{\mathrm{I}}_{z1}|1/2,-1/2\rangle & \langle 1/2,1/2|\hat{\mathrm{I}}_{z1}|-1/2,1/2\rangle & \langle 1/2,1/2|\hat{\mathrm{I}}_{z1}|-1/2,-1/2\rangle \\
\langle 1/2,-1/2|\hat{\mathrm{I}}_{z1}|1/2,1/2\rangle & \langle 1/2,-1/2|\hat{\mathrm{I}}_{z1}|1/2,-1/2\rangle & \langle 1/2,-1/2|\hat{\mathrm{I}}_{z1}|-1/2,1/2\rangle & \langle 1/2,-1/2|\hat{\mathrm{I}}_{z1}|-1/2,-1/2\rangle \\
\langle -1/2,1/2|\hat{\mathrm{I}}_{z1}|1/2,1/2\rangle & \langle -1/2,-1/2|\hat{\mathrm{I}}_{z1}|1/2,-1/2\rangle & \langle -1/2,1/2|\hat{\mathrm{I}}_{z1}|-1/2,1/2\rangle & \langle -1/2,1/2|\hat{\mathrm{I}}_{z1}|-1/2,-1/2\rangle \\
\langle -1/2,-1/2|\hat{\mathrm{I}}_{z1}|1/2,1/2\rangle & \langle -1/2,-1/2|\hat{\mathrm{I}}_{z1}|1/2,-1/2\rangle & \langle -1/2,-1/2|\hat{\mathrm{I}}_{z1}|-1/2,1/2\rangle & \langle -1/2,-1/2|\hat{\mathrm{I}}_{z1}|-1/2,-1/2\rangle
\end{array}$$

A Primer of NMR Theory with Calculations in Mathematica®, First Edition. Alan J. Benesi.

I_{z1} returns eigenvalues for m_1:

<1/2,1/2|1/2|1/2,1/2> <1/2,1/2|1/2|1/2,–1/2> <1/2,1/2|–1/2|–1/2,1/2> <1/2,1/2|–1/2|–1/2,–1/2>
<1/2,–1/2|1/2|1/2,1/2> <1/2,–1/2|1/2|1/2,–1/2> <1/2,–1/2|–1/2|–1/2,1/2> <1/2,–1/2|–1/2|–1/2,–1/2>
<–1/2,1/2|1/2|1/2,1/2> <–1/2,–1/2|1/2|1/2,–1/2> <–1/2,1/2|–1/2|–1/2,1/2> <–1/2,1/2|–1/2|–1/2,–1/2>
<–1/2,–1/2|1/2|1/2,1/2><–1/2,–1/2|1/2|1/2,–1/2><–1/2,–1/2|–1/2|–1/2,1/2><–1/2,–1/2|–1/2|–1/2,–1/2>

The scalar eigenvalues can be moved to precede the bra-ket, and orthonormality of the bras and kets gives 1 if and only if m_1 and m_2 in the bra are the same as m_1 and m_2 in the ket, otherwise giving 0. This yields to the following:

$$\hat{\mathrm{I}}_{z1} = \begin{pmatrix} \frac{1}{2} & 0 & 0 & 0 \\ 0 & \frac{1}{2} & 0 & 0 \\ 0 & 0 & -\frac{1}{2} & 0 \\ 0 & 0 & 0 & -\frac{1}{2} \end{pmatrix} \tag{16.1c}$$

This result can be understood by examining Equation 16.1b and the result in Equation 16.1c. The 1/2 in the upper left-hand corner of the single spin I_{z1} matrix multiplies the entire unit matrix for spin 2, giving the four upper left-hand values of the matrix in Equation 16.1c. The 0 in the upper right-hand corner of the single spin I_{z1} matrix multiplies the entire unit matrix for spin 2, yielding the four zeroes in the upper right-hand part of the matrix in Equation 16.1c. The 0 in the lower left-hand corner of the single spin I_{z1} matrix multiplies the entire unit matrix for spin 2, yielding the four zeroes in the lower left-hand part of the matrix in Equation 16.1c. The −1/2 in the lower right-hand corner of the single spin I_{z1} matrix multiplies the entire unit matrix for spin 2, yielding the four values in the lower right-hand part of the matrix in Equation 16.1c.

The matrix representation of $\hat{\mathrm{I}}_{z2}$ is obtained by taking the *direct product* of the single spin matrix representation of the unit (identity) matrix for spin 1 with the single spin $\hat{\mathrm{I}}_{z2}$ matrix,

$$\hat{\mathrm{I}}_{z2} = 1_1\, \hat{\mathrm{I}}_{z2} \tag{16.2a}$$

$$= \begin{pmatrix} 1 & 0 \\ 0 & 1 \end{pmatrix} \otimes \begin{pmatrix} \frac{1}{2} & 0 \\ 0 & -\frac{1}{2} \end{pmatrix} \tag{16.2b}$$

The result is as follows:

$$\hat{I}_{z2} = \begin{pmatrix} \frac{1}{2} & 0 & 0 & 0 \\ 0 & -\frac{1}{2} & 0 & 0 \\ 0 & 0 & \frac{1}{2} & 0 \\ 0 & 0 & 0 & -\frac{1}{2} \end{pmatrix} \tag{16.2c}$$

Coupling to a third $I = 1/2$ nucleus in the spin system is obtained by repeating Equations 16.1 and 16.2 using the representations from Equations 16.1c and 16.2c for I_{z1} and I_{z2}. The dimensionality increases from 4×4 to 8×8. Further coupling for 4 $I = 1/2$ coupled spins is carried out the same way, increasing the dimensionality to 16×16. Expressions can be obtained in this way for all spin angular momentum operators for arbitrary numbers of coupled spins, although the complexity of the calculation increases exponentially. Matrix representations for coupling between spins with $I > 1/2$ are carried out in the same way.

Matrix representations of the coupled spin angular momentum operators and Hamiltonian operators are easily carried out using the Mathematica notebook program *matrep2.nb*. This process is illustrated in the Mathematica notebook *directproduct.nb*.

EXPLANATION OF *directproduct.nb*

The first cell tells the user to evaluate *matrep2.nb*, then close it without saving changes. The next cells remind the user how to evaluate the matrix representations of single spin angular momentum operators. The next cells show how the dirprod function is used to calculate the matrix representations of two $I = 1/2$ scalar or dipolar coupled nuclear spins. Note that the matrix representations of each of the two coupled spins are different in the direct product representation. The next cells show how to obtain the matrix representations of spin angular momentum operators for an $I = 1/2$ nuclear spin coupled to an $I = 1$ nuclear spin. The notebook then proceeds to show how to obtain the matrix representations for each of three coupled $I = 1/2$ nuclear spins.

The next cells show how to build the matrix representation of the equilibrium density matrix for three coupled $I = 1/2$ nuclear spins. The next cells show that the same method can be used to obtain matrix representations of "transverse" spin angular momentum operators for coupled spins. The last cells show the matrix representation of the weak J-coupling Hamiltonian H_J for two coupled $I = 1/2$ spins. The final cell comments that the matrix representation can be very large for a system with many couplings.

HOMEWORK

Homework 16.1: Use *matrep2.nb* and the methods described *directproduct.nb* to calculate the direct product matrix representations of spin angular momentum operators I^2, I_z, I^+, I_x, and I_y for each spin in a system of one $I=1$ spin coupled to two $I=1/2$ nuclear spins. Let the $I=1$ spin be spin number 1, and the two $I=1/2$ spins be spins 2 and 3.

CHAPTER 17

SOLVING THE LIOUVILLE–VON NEUMANN EQUATION FOR THE TIME DEPENDENCE OF THE DENSITY MATRIX

If one knows the sequence of Hamiltonian operators that act on a spin system during an NMR pulse sequence, one can solve the Liouville–von Neumann (LVN) equation (Eqs. 13.2 and 13.3) to calculate the time dependence of the density matrix. *The density matrix contains all of the information for the spin system including the observable NMR signal.* In most NMR experiments on diamagnetic samples, the Hamiltonians that must be considered are H_Z, H_{RF}, H_Q, H_{CS}, H_D, and H_J. In most liquid-state NMR experiments, rapid molecular motion averages H_D and H_Q to zero except for their effects on relaxation. It also averages H_{CS} and H_J but to non-zero values characteristic of particular atomic environments in the sample molecules.

All pulse sequences start with the effective equilibrium density operator in the rotating frame at $t=0$ and utilize Hamiltonians that have been transformed to the rotating frame:[1]

$$\hat{\rho}_{eq}(0)=\sum_k \text{const}_k\,\hat{I}_z(k) \tag{17.1}$$

where the sum is taken over all k different nuclear spins in the spin system, and the direct product representation has been used if there is dipolar or J coupling between the spins.

Consider the first interval τ_1 in the pulse sequence with a constant Hamiltonian $\hat{H}_1$ in the rotating frame.[2] The solution to the LVN equation gives the density matrix at time τ_1:

$$\hat{\rho}(\tau_1)=e^{-i\hat{H}_1\tau_1}\cdot\hat{\rho}_{eq}(0)\cdot e^{i\hat{H}_1\tau_1} \tag{17.2a}$$

Equation 17.2 can be evaluated using the matrix representations of the density operator $\rho_{eq}(0)$ and Hamiltonian operator $\hat{H}_1$ in the rotating frame. The complex exponentials are also matrices, and the dots represent the matrix product.

---

[1] The effective equilibrium density matrix in the rotating frame is identical to that found in the laboratory frame.

[2] $\hat{H}_{RF}$ is time independent if the rf is on resonance in the rotating frame.

A Primer of NMR Theory with Calculations in Mathematica®, First Edition. Alan J. Benesi.

Equation 17.2 can also be evaluated by taking advantage of commutation relations between the Hamiltonian and density operators, as discussed in later chapters. Here we focus on the matrix representation methods.

The idea is that the starting density matrix is *propagated* by the sandwich of complex exponentials to yield the density matrix after the interval. If there are *n* different intervals τ_i in the pulse sequence with respective constant Hamiltonian operators $\hat{\mathrm{H}}_i$, the density matrix obtained immediately after the last interval τ_n is given by

$$\hat{\rho}(\tau_n + \cdots + \tau_2 + \tau_1) = e^{-i\hat{\mathrm{H}}_n\tau_n} \ldots e^{-i\hat{\mathrm{H}}_2\tau_2}\, e^{-i\hat{\mathrm{H}}_1\tau_1}\, \hat{\rho}_{\mathrm{eq}}(0)\, e^{i\hat{\mathrm{H}}_1\tau_1}\, e^{i\hat{\mathrm{H}}_2\tau_2} \ldots e^{i\hat{\mathrm{H}}_n\tau_n} \qquad (17.2\mathrm{b})$$

where τ_1 is the duration of the first interval in the pulse sequence with constant Hamiltonian operator $\hat{\mathrm{H}}_1$, τ_2 is the duration of the second interval in the pulse sequence with constant Hamiltonian operator $\hat{\mathrm{H}}_2$, …, and τ_n is the duration of the *n*th interval in the pulse sequence with constant Hamiltonian operator $\hat{\mathrm{H}}_n$. Even if the Hamiltonians are time dependent, sufficiently short intervals can be chosen so that $\hat{\mathrm{H}}$ is approximately constant over the shorter interval (Benesi, 1993).

There are two cases that must be considered in evaluating the propagator sandwich exponentials in Equations 17.2a and 17.2b.

CASE 1 DIAGONAL HAMILTONIAN

If the Hamiltonian $\hat{\mathrm{H}}_i$ acting during the interval τ_i has a diagonal matrix representation, the complex exponentials are evaluated directly as follows, shown here for the typical liquid-state Hamiltonians $\hat{\mathrm{H}}_{\mathrm{CS}}$ and $\hat{\mathrm{H}}_{\mathrm{J}}$ acting on two J-coupled $I = 1/2$ nuclear spins of the same nucleus (e.g., ^{1}H), $\hat{\mathrm{H}}_{\mathrm{CS1}} = \delta_1\,\hat{\mathrm{I}}_{z1}$, $\hat{\mathrm{H}}_{\mathrm{CS2}} = \delta_2\,\hat{\mathrm{I}}_{z2}$ where δ_1 and δ_2 are the rotating frame chemical shifts of the two spins expressed in rad s^{-1} (see *densitymatrix_primer.nb*), and $\hat{\mathrm{H}}_{\mathrm{J12}} = 2\pi\,\mathrm{J}\,\hat{\mathrm{I}}_{z1}\,\hat{\mathrm{I}}_{z2}$ where J_{12} is the coupling constant expressed in s^{-1}:

$$\hat{\mathrm{H}}_{\mathrm{CS}} = \begin{pmatrix} \frac{\delta_1}{2}+\frac{\delta_2}{2} & 0 & 0 & 0 \\ 0 & \frac{\delta_1}{2}-\frac{\delta_2}{2} & 0 & 0 \\ 0 & 0 & -\frac{\delta_1}{2}+\frac{\delta_2}{2} & 0 \\ 0 & 0 & 0 & -\frac{\delta_1}{2}-\frac{\delta_2}{2} \end{pmatrix} \qquad (17.3\mathrm{a})$$

$$\hat{\mathrm{H}}_{\mathrm{J}} = \begin{pmatrix} \frac{\mathrm{J}\pi}{2} & 0 & 0 & 0 \\ 0 & -\frac{\mathrm{J}\pi}{2} & 0 & 0 \\ 0 & 0 & -\frac{\mathrm{J}\pi}{2} & 0 \\ 0 & 0 & 0 & \frac{\mathrm{J}\pi}{2} \end{pmatrix} \qquad (17.3\mathrm{b})$$

$$\hat{\mathrm{H}}_{\mathrm{CS+J}} = \begin{pmatrix} \frac{\mathrm{J}\pi}{2}+\frac{\delta_1}{2}+\frac{\delta_2}{2} & 0 & 0 & 0 \\ 0 & -\frac{\mathrm{J}\pi}{2}+\frac{\delta_1}{2}-\frac{\delta_2}{2} & 0 & 0 \\ 0 & 0 & -\frac{\mathrm{J}\pi}{2}-\frac{\delta_1}{2}+\frac{\delta_2}{2} & 0 \\ 0 & 0 & 0 & \frac{\mathrm{J}\pi}{2}-\frac{\delta_1}{2}-\frac{\delta_2}{2} \end{pmatrix} \tag{17.3c}$$

$$e^{-i\hat{\mathrm{H}}_{\mathrm{CS+J}}t} = \begin{pmatrix} e^{-i\left(\frac{\mathrm{J}\pi t}{2}+\frac{t\delta_1}{2}+\frac{t\delta_2}{2}\right)} & 0 & 0 & 0 \\ 0 & e^{i\left(\frac{\mathrm{J}\pi t}{2}-\frac{t\delta_1}{2}+\frac{t\delta_2}{2}\right)} & 0 & 0 \\ 0 & 0 & e^{i\left(\frac{\mathrm{J}\pi t}{2}+\frac{t\delta_1}{2}-\frac{t\delta_2}{2}\right)} & 0 \\ 0 & 0 & 0 & e^{-i\left(\frac{\mathrm{J}\pi t}{2}-\frac{t\delta_1}{2}-\frac{t\delta_2}{2}\right)} \end{pmatrix} \tag{17.3d}$$

CASE 2 NONDIAGONAL HAMILTONIAN

If the Hamiltonian $\hat{\mathrm{H}}_i$ acting during the interval τ_i is *not* diagonal as is the case when the interval includes an radio frequency (rf) pulse, the complex exponentials are evaluated in a more complicated manner (see *densitymatrix_primer.nb*), although recent versions of Mathematica make the evaluation much easier than it would otherwise be. The process requires that the nondiagonal Hamiltonian be diagonalized using a similarity transform as demonstrated in *densitymatrix_primer.nb*. The similarity transform matrix is constructed from the orthogonalized eigenvectors of the Hamiltonian. The sandwich of similarity transforms results in a diagonalized argument for the complex exponential that can be evaluated as in case 1. After evaluation of the diagonalized complex exponential, the complex exponential must be "*undiagonalized*" *by again using the inverse (adjoint) sandwich of similarity transforms* (see *densitymatrix_primer.nb*).

In many cases $\left\|\hat{\mathrm{H}}_{\mathrm{RF}}\right\| \gg \left\|\hat{\mathrm{H}}_{\mathrm{CS+J}}\right\|$, so that during rf pulses the Hamiltonian $\hat{\mathrm{H}}_{\mathrm{pulse}} = \hat{\mathrm{H}}_{\mathrm{RF}} + \hat{\mathrm{H}}_{\mathrm{CS+J}} \cong \hat{\mathrm{H}}_{\mathrm{RF}}$. In cases where this is not a reasonable approximation, the full Hamiltonian for $\hat{\mathrm{H}}_{\mathrm{pulse}}$ must be used. As shown in *densitymatrix_primer.nb*, the full Hamiltonian $\hat{\mathrm{H}}_{\mathrm{pulse}}$ must be evaluated numerically rather than symbolically.

EXPLANATION OF *densitymatrix_primer.nb*

The first few cells are comments. The user is told to evaluate *matrep2.nb* and close it without saving. The two $I = 1/2$ spins' matrix representations are set up in the following cells. The sample is assumed to be in the liquid state and therefore subject only to $\hat{H}_{CS}$ and $\hat{H}_J$. The presence of J-coupling requires the direct product representation of the coupled spins. The next cells show how the matrix representations of the coupled spins can be added to give the total density matrix for the coupled spins.

The chemical shift Hamiltonians H_{cs1} and H_{cs2} and the weak J-coupling Hamiltonian H_{jweak} ($|\delta_1 - \delta_2| \gg |J|$) are defined. The resulting total Hamiltonian H_{csj} during periods without rf pulses is the sum H_{cs1}, H_{cs2}, and H_{jweak}. It is diagonal, with no non-zero off-diagonal elements.

The equilibrium density matrix ρ_0 for the two coupled $I = 1/2$ spins is constructed. The two spins are assumed to be homonuclear (e.g., ^{1}H spins). Each spin's initial signal magnitude is represented as mh.

The next cells compare the diagonal H_{csj} with nondiagonal H_{rfx}. The latter has only zero diagonal elements. There are only non-zero off-diagonal elements.

In the next cells, the propagators ucsj and ucsjadj are calculated for intervals without rf irradiation. These are used to propagate the equilibrium density operator and have no effect.

The next cells show the effect of a "hard" $\pi/2$ rf pulse ($H_{rf} \gg H_{csj}$) along the x axis of the rotating frame on the equilibrium density operator. First, the propagators u and uadj are calculated using the similarity transform method as described earlier in Case 2 Nondiagonal Hamiltonians. Then the propagators um and umadj are calculated with the built-in Mathematica function MatrixExp. Next, we demonstrate the built-in Mathematica function == is used to test the equivalence of u and um and of uadj and umadj. The equivalence is also obvious by inspection. The equilibrium density operator is then propagated with u and uadj to yield the density operator after the $(\pi/2)_x$ pulse. The resulting density operator ρ_1 has only off-diagonal non-zero elements.

The next cells show how to evaluate the observable NMR signal expectation value immediately after the rf pulse. The NMR signal is obtained by taking the trace of iplustot.ρ_1 and yields 2 i mh. The expectation value for ixtot yields 0. The expectation value for iytot yields −2 mh. This result is identical to what is predicted using the vector model. The "magnetization" for both spins ends up on the $-y$ axis of the rotating frame after the $(\pi/2)_x$ pulse.

The next cells show that one can also obtain the expectation values of operators for the spins separately. For iy1 and iy2, the expectation values are −mh and −mh, respectively.

Next, the Hamiltonian H_{csj} is allowed to act on ρ_1. The operators ucsj and ucsjadj are used to propagate ρ_1. The resulting time-dependent density operator ρ_2 has oscillatory off-diagonal elements and no diagonal elements. The NMR signal is obtained by taking the trace of iplustot.ρ_2. After using the built-in Mathematica function ExpToTrig to convert complex exponentials to trigonometric functions, the NMR signal is saved as sig2.

The next cells calculate the expectation value iy1 for one of the two spins. After ExpToTrig conversion, the NMR signal for spin 1 is simplified to yield (1/2) mh $(\cos[(\delta_1 - \pi \mathrm{j})t + \cos[(\delta_1 + \pi \mathrm{j})t)$. Thus the NMR signal from spin 1, originally of magnitude mh, splits into two positive signals of magnitude mh/2.

The next cells show the effect of a "soft" rf × pulse (H_{rf} and H_{csj} comparable in magnitude) on the equilibrium density operator ρ_0. The built-in MatrixExp function is not able to solve for the symbolic form of usoftx. However, as shown in the subsequent cells, substituting numerical values for the parameters ω_1, δ_1, δ_2, and j in H_{rf} and H_{csj} allows MatrixExp to solve for usoftx and usoftxadj.

Propagating ρ_0 with usoftx and usoftxadj yields ρ1soft. The built-in Mathematica functions FullSimplify and Chop are used to "clean up" the numerical result for ρ1soft. Note that it is numerically almost the same as the result for ρ_1 with the hard pulse, indicating that the "soft" pulse was still pretty hard.

The next cells deal with the density operator ρ1het that is obtained for a heteronuclear two-spin system, here assumed to be ^{1}H (spin 1) and ^{13}C (spin 2), after a hard $(\pi/2)_x$ pulse to the ^{1}H spin only. Only the ^{1}H spin has non-zero off-diagonal elements. The density operator ρ1het is then propagated with ucsj and ucsjadj to yield the time-dependent density operator ρ2het. The next cells show that this signal corresponds to a doublet at $\delta_1 + \pi \mathrm{J}$ and $\delta_1 - \pi \mathrm{J}$ rad s^{-1}.

If we allow ρhetj to evolve for $t = 1/(2\ \mathrm{j})$ and take the trace of iplustot to get the NMR signal for both spins, there is none! This density operator ρ2antiphase corresponds to antiphase magnetization. In later chapters, we will see that the operator 2 ix1.iz2 corresponds to antiphase magnetization of spin 1 with respect to spin 2. When we take the trace of this operator on ρ2antiphase, the result is mh.

CHAPTER 18

THE OBSERVABLE NMR SIGNAL

The calculated complex NMR signal (theoretical free induction decay (FID)) is obtained by taking *the trace of the matrix product of the* $\hat{I}^+$ *operator for the observed spins and the density matrix operator* $\rho(t)$ *in the rotating frame during acquisition*,

$$\mathrm{FID}(t) = \mathrm{Tr}[\hat{I}^+ \cdot \hat{\rho}(t)] = \mathrm{Tr}[\hat{\rho}(t) \cdot \hat{I}^+] \tag{18.1}$$

where FID(t) is the complex time-dependent NMR signal in the rotating frame, Tr is the matrix trace (sum of diagonal elements from upper left to lower right), and it is applied to the matrix product of the $\hat{I}^+$ operator for the observed spins and the time-dependent complex density operator $\hat{\rho}(t)$ of the spin system.

The part of $\hat{\rho}(t)$ that is "extracted" by this process is $\hat{I}^-$, as shown in *ladder_operator.nb*. The trace of the $\hat{I}^+$ operator with itself is zero (see *ladder_operator.nb*). As with the experimental FID(t), the calculated signal can be Fourier transformed to yield the NMR spectrum.

The ladder operators $\hat{I}^+ = \hat{I}_x + i\,\hat{I}_y$ and $\hat{I}^- = \hat{I}_x - i\,\hat{I}_y$ correspond to single quantum coherence of coherence order $p = +1$ and -1, respectively. Because $\hat{I}^+$ selects the $\hat{I}^-$ part of the density operator, an NMR experiment must produce $p = -1$ coherence of the observed nucleus during acquisition. At equilibrium, however, the density operator is proportional to $\hat{I}_z$ and has zero coherence, i.e. no transverse components, and corresponds therefore to coherence order $p = 0$.

If one ignores relaxation, only radio frequency (rf) pulses can produce a change in coherence order (see *ladder_operator.nb*). During intervals when $\hat{H}_{\mathrm{rf}} = 0$, the coherence orders present in the density operator do not change. NMR relaxation, usually ignored in the analysis of NMR pulse sequences, causes all transverse ($p \neq 0$) coherences in the density operator to decay to zero and ultimately return to $p = 0$ at equilibrium.

For two coupled I = 1/2 spins, a combination of rf pulses and delays without rf can create density operator components such as $\hat{I}_{x1}.\hat{I}_{x2}$, $\hat{I}_{x1}.\hat{I}_{y2}$, $\hat{I}_{x1}.\hat{I}_{z2}$, $\hat{I}_{y1}.\hat{I}_{x2}$, $\hat{I}_{y1}.\hat{I}_{y2}$, $\hat{I}_{y1}.\hat{I}_{z2}$, $\hat{I}_{z1}.\hat{I}_{x2}$, $\hat{I}_{z1}.\hat{I}_{y2}$, and $\hat{I}_{z1}.\hat{I}_{z2}$. Using the relationships $\hat{I}_x = 1/2\,(\hat{I}^+ + \hat{I}^-)$ and $\hat{I}_y = (1/(2i))^*\,(\hat{I}^+ - \hat{I}^-)$, one finds (see *ladder_operator.nb*) that the preceding Cartesian two spin operators are composed of ladder operator terms such as $\hat{I}_1^+.\hat{I}_2^+$, $\hat{I}_1^+.\hat{I}_2^-$, $\hat{I}_1^-.\hat{I}_2^+$, $\hat{I}_1^-.\hat{I}_2^-$, $\hat{I}_{z1}.\hat{I}_2^+$, $\hat{I}_{z1}.\hat{I}_2^-$, $\hat{I}_1^+.\hat{I}_{z2}$, $\hat{I}_1^-.\hat{I}_{z2}$, and $\hat{I}_{z1}.\hat{I}_{z2}$ The coherence order of these two-spin coherences is given by the *sum* of the p values of the operators in the product. The range of coherences that can be created for two coupled spins ranges from $p = -2$ to $p = +2$. For three

---

A Primer of NMR Theory with Calculations in Mathematica®, First Edition. Alan J. Benesi.

coupled I = 1/2 spins, the range of possible p values ranges from −3 to +3. For n coupled I = 1/2 spins, the range of p values ranges from $-n$ to $+n$.

As will be shown in later chapters, the *design* of NMR pulse sequences takes advantage of the ladder operator representation. Phase cycling of the rf pulses and/or gradient methods are used to select specific coherence order pathways.

EXPLANATION OF *ladder_operator.nb*

The first cell instructs the user to evaluate *matrep2.nb* then close it without saving. The following cell defines a hypothetical nonequilibrium density operator ρ as the sum of I^+ and I^- spin angular momentum operators. The observable signal is "extracted" from ρ by taking the trace of the matrix product of I^+ and ρ. It is immediately apparent that only the I^- part of the density operator is observable.

This is shown to be true for all nuclear spins with $I \geq 1/2$. The example analyzed is an $I = 5/2$ nuclear spin.

The next cells calculate the direct product matrix representations for spin operators of two coupled $I = 1/2$ spins to construct the density operator ρcoup and show again that only the I^- part of ρcoup contributes to the observable NMR signal.

Then a new hypothetical density operator ρ2spin is defined that contains all possible types of two-spin coherence. Because the density operator contains all of the information about the spin system, the expectation value for *any* spin operator Op is easily obtained by taking the trace[Op.ρ2spin]. This is illustrated for several arbitrary two-spin operators. The next cells assign names such as dqplus, dqmin, zeroq, and twospinx to some of the two-spin coherences. These operators are tested for their expectation values with other operators by taking the trace of their matrix product.

CHAPTER 19

COMMUTATION RELATIONS OF SPIN ANGULAR MOMENTUM OPERATORS

The Liouville–von Neumann equation uses the commutator of the Hamiltonian operator and density operator to propagate the density operator in time. Since both operators are constructed from spin angular momentum operators, it is also possible to use explicit commutation relations between them to propagate the density operator without relying on the matrix representations of the operators. This approach is especially useful in liquid-state NMR, where the only effective internal Hamiltonians are $\hat{H}_{CS}$ and $\hat{H}_J$. This approach is called the "product operator" formalism (Bax, 1982; Sorensen et al., 1983). Evaluation of commutators is also essential for analysis of NMR relaxation in both solids and liquids and for first-order average Hamiltonian theory in solids NMR.

Real and imaginary numbers are commutative, for example, $[3,2]=(3\times 2)-(2\times 3)=0$. Quantum mechanical operators, however, are not necessarily commutative. For example, the commutator of the spin angular momentum operators $\hat{I}_x$ and $\hat{I}_y$ is:

$$[\hat{I}_x, \hat{I}_y] = i\hat{I}_z \tag{19.1}$$

These and other commutation relations between the spin angular momentum operators can be proved by expressing the operators in Cartesian form (Levine, 1974, pp. 70, 71, 82–86) or by using the matrix representations of the operators. The general commutators mentioned later are all are easily verified with simple arithmetic. The Mathematica notebook *commutators.nb* evaluates some of the important commutation relations needed in later chapters. Some others are included in the following equations:

$$[A, A] = 0 \tag{19.2a}$$

$$[A, B] = AB - BA = -[B, A] \tag{19.2b}$$

$$[A, B+C] = [A, B] + [A, C] \tag{19.2c}$$

$$[A+B, C] = [A, C] + [B, C] \tag{19.2d}$$

A Primer of NMR Theory with Calculations in Mathematica®, First Edition. Alan J. Benesi.

$$[AB, C] = A[B, C] + [A, C]B \tag{19.2e}$$

$$[A, BC] = [A, B]C + B[A, C] \tag{19.2f}$$

$$[AB, CD] = A[B, C]D + C[A, D]B + AC[B, D] + [A, C]DB \tag{19.2g}$$

The fundamental spin angular momentum commutators are as follows:

$$[\hat{\mathrm{I}}_x, \hat{\mathrm{I}}_y] = i\hat{\mathrm{I}}_z \tag{19.3a}$$

$$[\hat{\mathrm{I}}_y, \hat{\mathrm{I}}_z] = i\hat{\mathrm{I}}_x \tag{19.3b}$$

$$[\hat{\mathrm{I}}_z, \hat{\mathrm{I}}_x] = i\hat{\mathrm{I}}_y \tag{19.3c}$$

$$[\hat{\mathrm{I}}_\alpha, [\hat{\mathrm{I}}_\alpha, \hat{\mathrm{I}}_\beta]] = \hat{\mathrm{I}}_\beta \quad \text{for } \alpha \neq \beta, \alpha, \beta = x, y, \text{or } z \tag{19.3d}$$

$$[\hat{I}^+, \hat{I}^-] = 2\ \hat{\mathrm{I}}_z \tag{19.3e}$$

$$[\hat{I}_z, \hat{\mathrm{I}}^\pm] = \pm\hat{\mathrm{I}}^\pm \tag{19.3f}$$

Expanding Equation 19.3e in terms of Cartesian operators, it can be shown that

$$\hat{\mathrm{I}}^2 = \{\hat{\mathrm{I}}_x^2 + \hat{\mathrm{I}}_y^2 + \hat{\mathrm{I}}_z^2\} = \hat{\mathrm{I}}_z^2 + \frac{1}{2}(\hat{\mathrm{I}}^+\hat{\mathrm{I}}^- + \hat{\mathrm{I}}^-\hat{\mathrm{I}}^+) \tag{19.4}$$

Using Equations 19.3e and 19.3f, we can derive two important relations that are important for NMR relaxation:

$$\hat{\mathrm{I}}^+\hat{\mathrm{I}}^- = \hat{\mathrm{I}}^2 - \hat{\mathrm{I}}_z^2 + \hat{\mathrm{I}}_z \tag{19.5a}$$

$$\hat{\mathrm{I}}^-\hat{\mathrm{I}}^+ = \hat{\mathrm{I}}^2 - \hat{\mathrm{I}}_z^2 - \hat{\mathrm{I}}_z \tag{19.5b}$$

For two different spins $\hat{\mathrm{S}}$ and $\hat{\mathrm{I}}$ (e.g., ^{13}C nuclei in methane and ^{1}H nuclei in methane),

$$[\hat{\mathrm{S}}_\alpha, \hat{\mathrm{I}}_\beta] = 0 \quad \text{for } \alpha = x,\ y, \text{ or } z,\ \beta = x,\ y, \text{ or } z \tag{19.6}$$

Also,

$$[2\hat{\mathrm{S}}_\alpha\hat{\mathrm{I}}_\beta, [\hat{\mathrm{S}}_\gamma, \hat{\mathrm{I}}_\varepsilon]] = 0 \quad \text{for } \alpha = \gamma \text{ and } \beta = \varepsilon \text{ OR } \alpha \neq \gamma \text{ and } \beta \neq \varepsilon,\ \alpha,\ \beta,\ \gamma,\ \varepsilon = x, y, \text{or } z \tag{19.7}$$

Some other important commutators and relationships between spin operators that occur in calculation of NMR relaxation times are (Abragam, 1983, pp. 290–291):

$$[\hat{\mathrm{I}}^+\hat{\mathrm{S}}^+, \hat{\mathrm{I}}^-\hat{\mathrm{S}}^-] = +2\hat{\mathrm{I}}_z\hat{\mathrm{S}}^+\hat{\mathrm{S}}^- + 2\hat{\mathrm{S}}_z\hat{\mathrm{I}}^-\hat{\mathrm{I}}^+ \tag{19.8}$$

$$[\hat{\mathrm{I}}^-\hat{\mathrm{S}}^+, \hat{\mathrm{I}}^+\hat{\mathrm{S}}^-] = -2\hat{\mathrm{I}}_z\hat{\mathrm{S}}^+\hat{\mathrm{S}}^- + 2\hat{\mathrm{S}}_z\hat{\mathrm{I}}^+\hat{\mathrm{I}}^- \tag{19.9}$$

$$[\hat{\mathrm{I}}^+\hat{\mathrm{S}}_z, \hat{\mathrm{I}}^-\hat{\mathrm{S}}_z] = 2\hat{\mathrm{I}}_z\hat{\mathrm{S}}_z^2 \tag{19.10}$$

$$\frac{1}{2}(\hat{I}^+\hat{S}^- + \hat{I}^-\hat{S}^+) = \hat{I}\hat{S} - \hat{I}_z\hat{S}_z \tag{19.11}$$

As shown in Equations 17.1 and 17.2, the effective equilibrium density operator is propagated during periods with constant Hamiltonians (i.e. pulse and delay periods) by using "sandwiches" of complex exponential operators. When using commutation relations between spin angular momentum operators, the propagation steps are evaluated by using one or more of the following properties. These are similar to the two cases described for matrix propagators in Chapter 17:

Case 1: If the operators $\hat{A}$ and $\hat{B}$ commute, then

$$\hat{A}e^{i\phi\hat{B}} = e^{i\phi\hat{B}}\hat{A} \tag{19.12a}$$

$$e^{i(\phi_1\hat{A}+\phi_2\hat{B})} = e^{i\phi_1\hat{A}}e^{i\phi_2\hat{B}} = e^{i\phi_2\hat{B}}e^{i\phi_1\hat{A}} \tag{19.12b}$$

where ϕ, ϕ_1, and ϕ_2 represent real numbers such as the chemical shift δ, coupling constant 2π J, and/or ±1. For example, consider two different weakly J-coupled $I = 1/2$ nuclear spins (say ^{1}H spins) in the liquid state subject to the Hamiltonians $\hat{H}_{CS} = \delta_1\hat{I}_{1z}$, $\delta_2\hat{I}_{2z}$, and $\hat{H}_J = 2\pi\,J\,\hat{I}_{1z}\hat{I}_{2z}$:[1]

$$[\hat{H}_{CS}, \hat{H}_J] = 2\pi\ J[\delta_1\hat{I}_{1z} + \delta_2\hat{I}_{2z}, \hat{I}_{1z}\hat{I}_{2z}] \tag{19.13a}$$

Using Equations 19.2, this may be written as

$$[\hat{H}_{CS}, \hat{H}_J] = 2\pi J\delta_1[\hat{I}_{1z}, \hat{I}_{1z}\hat{I}_{2z}] + 2\pi\ J\ \delta_2[\hat{I}_{2z}, \hat{I}_{1z}\hat{I}_{2z}] \tag{19.13b}$$

which simplifies to

$$[\hat{H}_{CS}, \hat{H}_J] = 2\pi\ J\ \delta_1([\hat{I}_{1z}, \hat{I}_{1z}] + [\hat{I}_{1z}, \hat{I}_{2z}]) + 2\pi\ J\ \delta_2([\hat{I}_{2z}, \hat{I}_{1z}] + [\hat{I}_{2z}, \hat{I}_{2z}]) \tag{19.13c}$$

All commutators yield zero, so

$$[\hat{H}_{CS}, \hat{H}_J] = 0 \tag{19.13d}$$

Therefore, from Equation 19.12b,

$$\begin{aligned} e^{-i(\delta_1\hat{I}_{1z}+\delta_2\hat{I}_{2z}+2\pi J\hat{I}_{1z}\hat{I}_{2z})\tau} &= e^{-i\delta_1\hat{I}_{1z}\tau}\cdot e^{-i\delta_2\hat{I}_{2z}\tau}\cdot e^{-i2\pi\ J\ \hat{I}_{1z}\hat{I}_{2z}\tau} \\ &= e^{-i2\pi J\hat{I}_{1z}\hat{I}_{2z}\tau}\cdot e^{-i\delta_2\hat{I}_{2z}\tau}\cdot e^{-i\delta_1\hat{I}_{1z}\tau} \\ &= e^{-i2\pi J\hat{I}_{1z}\hat{I}_{2z}\tau}\cdot e^{-i\delta_1\hat{I}_{1z}\tau}\ e^{-i\delta_2\hat{I}_{2z}\tau} \end{aligned} \tag{19.13e}$$

The same applies to the conjugate complex exponentials on the right-hand side of the propagator "sandwich." This result is extremely useful, indicating that chemical shift propagation and weak J coupling propagation of the density operator during a delay can be carried out in arbitrary order. All of the complex exponentials are diagonal, so the propagation in this case is straightforward.

---

[1] Here we switch from *I* and *S* for the different spins to I_1 and I_2.

Case 2: If the operators A and B do NOT commute, that is, $[\hat{A},\hat{B}] \neq 0$ (Sorensen et al., 1983):

$$e^{-i\phi\hat{A}\tau}\,\hat{B}\,e^{i\phi\hat{A}t} = \hat{B}\cos(\phi t) - i[\hat{A},\hat{B}]\sin(\phi t) \tag{19.14}$$

For example, consider the effect of an "*x*" rf pulse in the rotating frame on the effective equilibrium density operator for a single spin:

$$e^{-i\omega_1\tau\hat{I}_x}(\text{const}*\hat{I}_z)e^{i\omega_1\tau\hat{I}_x} = \text{const}*\hat{I}_z\cos(\omega_1 t) - i\,\text{const}*[\hat{I}_x,\hat{I}_z]\sin(\omega_1 t) \tag{19.15a}$$

$$= \text{const}*\hat{I}_z\cos(\omega_1 t) - \text{const}*\hat{I}_y\sin(\omega_1 t) \tag{19.15b}$$

If $\omega_1 t = \pi/2$, Equation 19.15b predicts that the density operator after the $\pi/2$ pulse is given by const $* -\hat{I}_y$, which is the same result that is predicted by the Bloch equation in Chapter 7 or by using matrix representation as in Chapter 17.

EXPLANATION OF *commutators.nb*

The notebook *commutators.nb* is used to evaluate commutators of sums and products of spin angular momentum operators encountered in product operator theory and relaxation theory. The program is far from complete. The user is invited to improve it. The most important aspect to keep in mind is that matrix representations are NOT used for the nuclear spin angular momentum operators. They are left in symbolic form using the terminologies ix, iy, iz, iplus, imin, and isq.

The first cells define the functions comm in terms of the functions commspin.

The commspin functions have single-spin angular momentum operators and constants as arguments. The built-in Mathematica functions MemberQ and /; are introduced. The combination of /; and MemberQ is used to test the density operator term for sums and products of single-spin commutators and constants that can be evaluated by commspin.

Some of the results obtained by the commspin functions are not evaluated fully or in simplest form, so additional commspin functions are created to help overcome this.

The spherical spin space tensor operators used in solid-state NMR and in relaxation theory are defined in the next cells.

Commutators of the spin space tensor operators are then evaluated.

HOMEWORK

Homework 19.1: Prove Equations 19.3e, 19.3f, 19.4, 19.5a, and 19.5b.

Homework 19.2: Starting with an initial density operator of const1 $*\hat{I}_{y1}$ + const2 $*\hat{I}_{z2}$, calculate the time dependence of the density operator subject only to the weak coupling Hamiltonian $2\pi J\hat{I}_{z1}\hat{I}_{z2}$.

CHAPTER 20

THE PRODUCT OPERATOR FORMALISM

The "Product Operator Formalism" (Sorensen et al., 1983; Bax, 1982) for coupled $I = 1/2$ spins in liquid-state NMR is based on the commutator relations presented in Chapter 19. The only Hamiltonian operators that are usually considered are $\hat{H}_{RF}$, $\hat{H}_{CS}$, and $\hat{H}_{J}$.

With the product operator approach, the density operator $\rho(t)$ is expressed as a linear combination of base product operators:

$$\rho(t) = \sum_j b_j(t) B_j \qquad (20.1)$$

where $b_j(t)$ is the time-dependent coefficient for the product operator B_j.

The Cartesian base product operators B_j and corresponding nomenclature for one $I = 1/2$ spin are $\hat{I}_{1z}$, $\hat{I}_{1x}$, and $\hat{I}_{1y}$. It is sometimes advantageous to use base operators incorporating the raising and lowering operators $\hat{I}_1^+$ or $\hat{I}_1^-$ (see Chapter 10).

The Cartesian base product operators B_j and corresponding nomenclature for two $I = 1/2$ spins are given here. Only $\hat{I}_{1x}$, $\hat{I}_{1x}$, $\hat{I}_{2x}$, and $\hat{I}_{2y}$ magnetization is observable in the NMR signal.

the unity operator

$\hat{I}_{1z}$ longitudinal magnetization of spin 1

$\hat{I}_{2z}$ longitudinal magnetization of spin 2

$\hat{I}_{1x}$ observable in phase magnetization of spin 1

$\hat{I}_{1y}$ observable in phase magnetization of spin 1

$\hat{I}_{2x}$ observable in phase magnetization of spin 2

$\hat{I}_{2y}$ observable in phase magnetization of spin 2

$2\hat{I}_{1x}\hat{I}_{2z}$ antiphase x magnetization of spin 1 with respect to spin 2

$2\hat{I}_{1y}\hat{I}_{2z}$ antiphase y magnetization of spin 1 with respect to spin 2

$2\hat{I}_{1z}\hat{I}_{2x}$ antiphase x magnetization of spin 2 with respect to spin 1

$2\hat{I}_{1z}\hat{I}_{2y}$ antiphase y magnetization of spin 2 with respect to spin 1

$2\hat{I}_{1x}\hat{I}_{2x}$ two-spin coherence of spins 1 and 2

$2\hat{I}_{1y}\hat{I}_{2x}$ two-spin coherence of spins 1 and 2

A Primer of NMR Theory with Calculations in Mathematica®, First Edition. Alan J. Benesi.

$2\hat{I}_{1x}\hat{I}_{2y}$ two-spin coherence of spins 1 and 2
$2\hat{I}_{1y}\hat{I}_{2y}$ two-spin coherence of spins 1 and 2
$2\hat{I}_{1x}\hat{I}_{2x}$ two-spin coherence of spins 1 and 2
$2\hat{I}_{1z}\hat{I}_{2z}$ longitudinal two-spin order of spins 1 and 2

For more coupled $I=1/2$ spins, one obtains Cartesian base product operators like the following:

$4\hat{I}_{1x}\hat{I}_{2z}\hat{I}_{3z}$ antiphase magnetization of spin 1 with respect to spins 2 and 3
$4\hat{I}_{1x}\hat{I}_{2z}\hat{I}_{3y}$ two-spin coherence of spins 1 and 3 antiphase with respect to spin 2
$4\hat{I}_{1x}\hat{I}_{2x}\hat{I}_{3y}$ three-spin coherence of spins 1, 2, and 3

Applying the commutation and exponential relations from Chapter 19 to the product operators yields the "rules" of propagation for product operators. For two weakly coupled $I=1/2$ spins, a and x, subject only to "hard" rf pulses (i.e., $\omega_1 \gg \delta$, Chapter 7, *bloch3animation.nb*) the rules are listed explicitly for two J-coupled spins in program *shortspin.nb*. The rules are also used in the program *poma.nb*, where an arbitrary number of J-coupled spins may be considered. Both of these notebooks can be used to analyze pulse sequences. They take advantage of the following simplifications:

1. $[\hat{H}_{CS1}, \hat{H}_{CS2}]=0$. This means that chemical shift propagation during delays can be carried out separately for the spins and in arbitrary order.
2. $[\hat{H}_{CS1}, \hat{H}_J]=0$ and $[\hat{H}_{CS2}, \hat{H}_J]=0$ because only weak coupling is considered ($\hat{H}_J=2\pi\ J\ \hat{I}_{z1}\ \hat{I}_{z2}$). This means that coupling propagation during delays can be carried out separately from chemical shift propagation and in either order.
3. Only "hard" RF pulses are used, so $|\hat{H}_{RF}| \gg |\hat{H}_{CS1}|$, $|\hat{H}_{CS2}|$, or $|\hat{H}_J|$, so that during pulses only the effects of $\hat{H}_{RF}$ are calculated.

EXPLANATION OF *shortspin.nb*

Program *shortspin.nb* is used to analyze pulse sequences for two weakly J-coupled $I=1/2$ nuclear spins subject only to the chemical shift Hamiltonian, the J-coupling Hamiltonian, and the hard rf pulse Hamiltonian in the liquid state. It should be evaluated and closed without saving prior to being used for pulse sequence analysis. The two $I=1/2$ spins are designated as "a" and "x" spins, respectively. Functions are explicitly defined for the effects of rf pulses and delays for all possible two-spin product operators as well as for the individual spins. During delays the chemical shift and the weak J-coupling interaction are active.

The program starts by making trigonometric definitions needed in other expressions.

Then the program defines the effects of hard rf pulses on all possible two-spin product operators with functions like $a0$, $a3$, $x1$, and $ax2$. For example, suppose the pulse sequence starts with the equilibrium density operator ("magnetization") with a $\pi/2$ pulse along the y axis of the rotating frame to only the "a" spin. If the equilibrium magnetization (density operator) is mh iza + mc izx, the syntax of the pulse would be a1[$\pi/2$, mh iza + mc izx]. The a indicates that only the a spin is hit with rf pulse. The

1 indicates that the pulse is along the y axis of the rotating frame (x is 0, y is 1, $-x$ is 2, and $-y$ is 3). The $\pi/2$ indicates that the pulse nutates the magnetization of the a spin only by $\pi/2$ radians around the $+y$ axis. The mh is just a "label" for the magnitude of the equilibrium a spin magnetization. In other notebooks, mh is often used to represent ^{1}H magnetization magnitude. The a1 rf pulse does not affect the x spin's magnetization of magnitude mc (we often use mc to represent ^{13}C magnetization magnitude). Hard rf pulses to the x spin only are designated with x1, etc. Hard rf pulses of the same rf phase to both spins are designated with ax0, ax1, etc.

Hard rf pulses with arbitrary rf phase (not necessarily aligned with one of the rotating frame axes) are designated with ar, xr, or axr depending on whether one or both spins receive the pulse. For example, the pulse xr[$\pi/4$, $\pi/3$, mh ixa + mc izx] causes a nutation of $\pi/4$ radians around an axis that is $+\pi/3$ radians from the x axis of the rotating frame.

Evolution during delays without hard rf pulses is designated with delay. For example, delay[t, j, mh iya + mh iyx] causes chemical shift evolution of the density operator mh iya + mh iyx over time t with chemical shifts wa and wx (rad s^{-1}) and j-coupling evolution with coupling constant j (in s^{-1}).

The density operators encountered during pulse sequences are often sums of product operators. These are easily decomposed into sums of two-spin product operators that can be handled by other rf pulse and delay functions. For example, the function delay[*t*_,*j*_,*x*_+*y*_] decomposes the density operator into delay[*t*,*j*,*x*] + delay[*t*,*j*,*y*]. Note that sums of three or more product operators are also decomposed with the same function.

Some special functions such as trig, mq, and cart are also defined using built-in Mathematica functions that have not been discussed previously. One of these is //., which repeatedly performs replacements until the expression no longer changes (similar to /., which just goes through an expression once). The list of replacements designated between { and } can be long, and uses the built-in Mathematica function :>. The function :> transforms the expression on the left-hand side of :> to the expression on the right-hand side of :>.

EXPLANATION OF *poma.nb*

This Mathematica notebook was developed by the Wüthrich group (Guntert et al., 1993). It is a powerful program for the analysis of liquid-state pulse sequences subject only to hard rf pulses, chemical shift, and weak j-coupling. Unlike *shortpin.nb*, it is not limited to two coupled spins, although too many coupled spins will cause computer crashes. It should be evaluated then closed without saving prior to use.

The programming in *poma.nb* is more detailed than has been used in the other Mathematica notebooks, and would not be discussed in detail here because the goal is understanding NMR, not understanding every subtlety of the Mathematica programming language. Remember that when a Mathematica notebook is running, definitions of functions such as ^= can be obtained by entering ?^=.

The syntax required to use *poma.nb* is demonstrated in several future notebooks (*ineptpoma.nb, hsqc_poma.nb, hmqc_poma.nb, and double_quantum_poma.nb*).

CHAPTER 21

NMR PULSE SEQUENCES AND PHASE CYCLING

Nuclear magnetic resonance (NMR) pulse sequences use "phase cycles" to eliminate the unwanted signals by *destructive interference* and add up the desired signals by *constructive interference*. Many pulse sequences also employ pulsed magnetic field gradients, but these operate in a different manner that will be discussed in later chapters. The simplest modern NMR pulse sequence is the single pulse Bloch decay experiment with a quadrature phase cycle (Fig. 21.1).

The rf pulse phase $\phi_1 = 0° \ 90° \ 180° \ 270° = 0 \ \pi/2 \ \pi \ 3\pi/2$ is the phase of the rf pulse $\mathbf{B}_1$ field in the rotating frame (with the x axis corresponding to $\phi_1 = 0°$ or 0 rad). The phase of the "real" receiver in the rotating frame is the same: $\phi_{\text{recvr}} = 0° \ 90° \ 180° \ 270°$. The phase of the (just as real electronically) imaginary receiver is $\phi_{\text{recvr\_imag}} = 90° \ 180° \ 270° \ 0°$. Both the "real" and "imaginary" signals are saved together as the complex FID. The $\pi/2$ rf pulse is represented as a vertical rectangle. Strong rf pulses ($|-\gamma \mathbf{B}_1| >> |\delta|$) are generally represented as vertical rectangles, and the phase cycling is also listed explicitly. In the actual experiment, a shorter pulse than a 90° pulse is often used to allow more scans with a shorter relaxation delay.

The pulse sequence operates as follows:

1. Pulse and acquire the FID using $\phi_1 = 0°$, $\phi_{\text{recvr}} = 0°$. Save result in memory. Wait for NMR relaxation to return the density operator to thermal equilibrium.
2. Pulse and acquire the FID using $\phi_1 = 90°$, $\phi_{\text{recvr}} = 90°$. Add this FID to previous result in memory. Wait for NMR relaxation to return the density operator to thermal equilibrium.
3. Pulse and acquire the FID using $\phi_1 = 180°$, $\phi_{\text{recvr}} = 180°$. Add this FID to result in memory from step 2. Wait for NMR relaxation to return the density operator to thermal equilibrium.

A Primer of NMR Theory with Calculations in Mathematica®, First Edition. Alan J. Benesi.

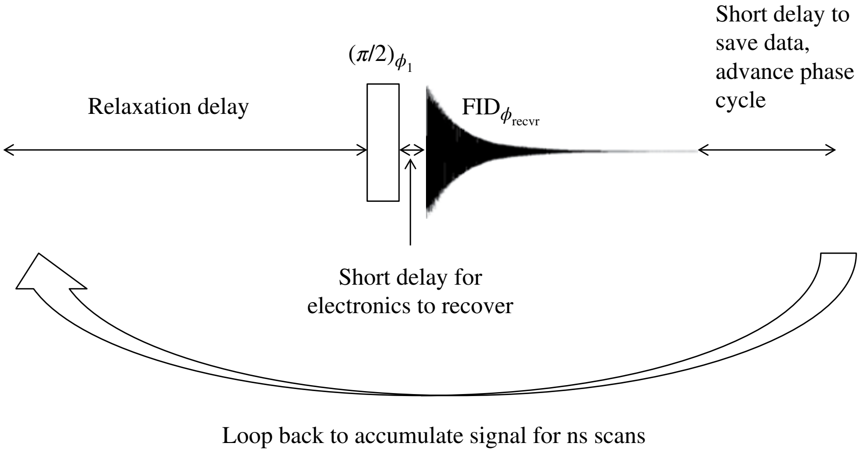

Figure 21.1 The Single Pulse NMR Experiment. The relaxation delay allows the spin system to reach thermal equilibrium. The radio frequency (rf) pulse is represented by the vertical rectangle. In many cases, it is a $\pi/2$ pulse with phase cycle $\phi_1 = 0° \; 90° \; 180° \; 270° = 0 \; \pi/2 \; \pi \; 3\pi/2$. The short delay (typically <30 μs) following the rf pulse allows the spectrometer receiver electronics to recover from the high-power rf. The NMR signal (free induction decay (FID)) is then amplified, digitized, saved, and added to the signal from preceding scans. For each scan, the phase of the spectrometer receiver matches the phase of the rf pulse.

4. Pulse and acquire the FID using $\phi_1 = 270°$, $\phi_{\mathrm{recvr}} = 270°$. Add this FID to result in memory from step 3. Wait for NMR relaxation to return the density operator to thermal equilibrium.
5. Repeat steps 1–4 until sufficient NMR signal is obtained.

The vector model analysis of the single pulse NMR experiment is shown in Figure 21.2.

By moving the receiver phase in concert with the pulse phase, the magnetization is always placed in the same position in the rotating frame relative to the receiver. This does not guarantee, however, that the magnetization is aligned with the axes. Phasing the resulting spectrum after Fourier transformation of the sum FID amounts to moving the receiver so that the magnetization is maximum, absorptive, and positive. The function of this "quadrature" phase cycle is to cancel out any imbalance in the pulse and receiver phases.

After Fourier transformation and phasing of the resultant FID, the one-dimensional NMR spectrum is obtained, as shown in Figure 21.3.

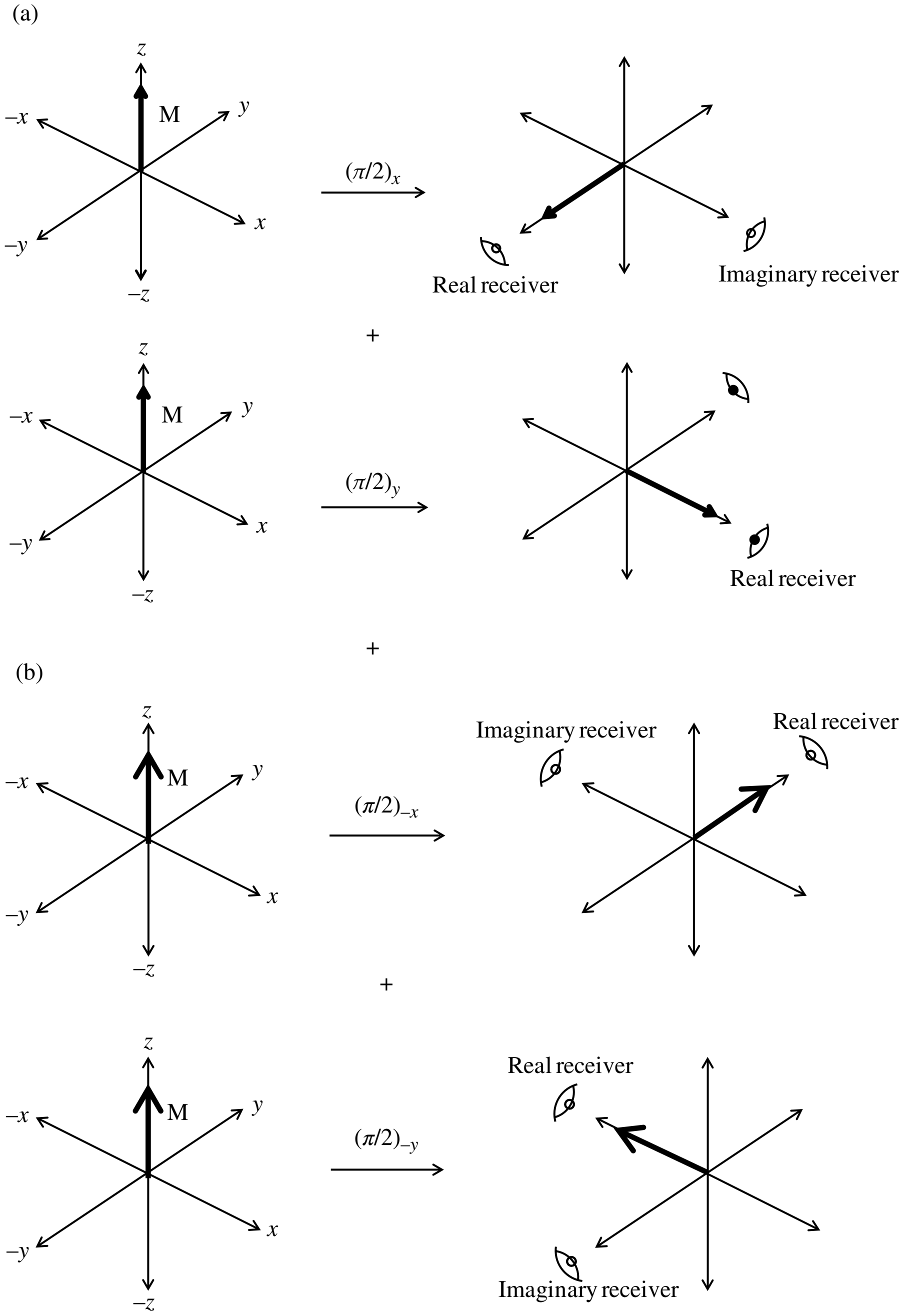

Figure 21.2 (a and b) Vector Model of Cyclops Phase Cycling. The single pulse experiment with quadrature phase cycling from Figure 21.1 is analyzed with the vector model. The receiver real channel is matched to the rf pulse phase in the four depicted scans.

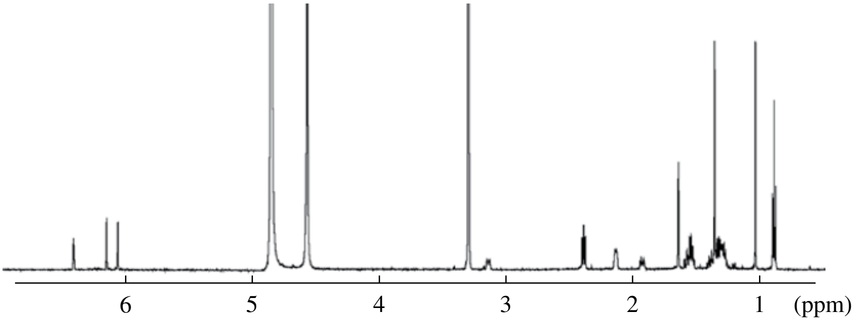

Figure 21.3 The ^{1}H NMR Spectrum of Δ^9-tetrahydrocannabinol dissolved in deuterated methanol, 25°C, Larmor frequency = 600.18 MHz, obtained by Fourier Transformation and Phasing of the NMR Signal (FID) in Figure 7.1. The spectrum *x* axis is presented in ppm units, where 1 ppm represents 1×10^{-6} of the Larmor frequency. In this spectrum, 1 ppm = 600.18 Hz. Note that the NMR frequency increases from right to left rather than left to right. This is typical for modern NMR spectrometers.

CHAPTER 22

ANALYSIS OF LIQUID-STATE NMR PULSE SEQUENCES WITH THE PRODUCT OPERATOR FORMALISM

Two Mathematica notebooks, *shortspin.nb* and *poma.nb* (Guntert et al., 1993), are provided to enable the commutator-based analysis of liquid-state NMR pulse sequences on coupled $I=1/2$ spins, hereafter called the product operator formalism. *Shortspin.nb* is limited to one or two J-coupled $I=1/2$ spins, while *poma.nb* can in principle be used to analyze pulse sequences for an arbitrary number of J-coupled $I=1/2$ spins. With *shortspin.nb*, the analysis *must* be carried out pulse by pulse, delay by delay, and phase by phase (i.e., for each interval with a constant Hamiltonian and for each scan and corresponding pulse phase of the "phase cycle"). This is useful for gaining basic understanding of how pulse sequences work. The calculations in this chapter use program *shortspin.nb.*

When performing calculations with program *Shortspin.nb*, it is necessary to reduce all pulse phases to *constant receiver phase* (i.e., move the receiver to the x axis of the rotating frame). This is achieved by adding $(2\pi-\phi_{\text{recvr}})$ to each pulse phase. For example, for the quadrature phase cycle in the single pulse NMR experiment from the previous chapter, phase cycle used on NMR spectrometer is:

$$\theta_1 = 0 \quad \pi/2 \quad \pi \quad 3\pi/2$$

$$\theta_{\text{recvr}} = 0 \quad \pi/2 \quad \pi \quad 3\pi/2$$

when we add $(2\pi-\phi_{\text{recvr}})$:

$$\theta_1 = 0 \quad 0 \quad 0 \quad 0$$

$$\theta_{\text{recvr}} = 0 \quad 0 \quad 0 \quad 0$$

Example 1:

Analysis of the Single Pulse NMR experiment: Single spin hit with 90° radio frequency (rf) pulse along x axis of rotating frame with no J-coupling during acquisition (see Fig. 21.1).

A Primer of NMR Theory with Calculations in Mathematica®, First Edition. Alan J. Benesi.

After reducing to constant receiver phase, the quadrature 1-pulse sequence is seen to be equivalent to a single $\pi/2$ single pulse along the x axis of the rotating frame to the effective equilibrium density operator, in this case mh iza. The nucleus is assumed to be ^{1}H, and the empirical magnitude of the density operator is designated as mh. The analysis is shown in *1pulseshort.nb*. In shorthand notation, this can be written as

$$\rho_{\mathrm{eq}} \xrightarrow{\left(\frac{\pi}{2}\right)_x} \rho_1 \xrightarrow{t} \rho_2(t)$$

The *1pulseshort.nb* analysis shows that applying a $90_x{}^\circ = (\pi/2)_x$ pulse to the effective equilibrium density operator, mh iza, causes it to become $\rho_1 = -$mh iya. This quantum mechanical result for the density operator is the same one predicted by the Bloch equation for the magnetization vector **M**.

By allowing the density operator ρ_1 to evolve during the acquisition time, *1pulseshort.nb* shows that one obtains the density operator $\rho_2(t) = -$mh iya cos[wa t] + mh ixa sin[wa t], where wa is the offset of the peak relative to the Larmor frequency (i.e., wa is equivalent to δ from Chapter 8) again consistent with the Bloch description of the magnetization vector **M**. The absorptive part of the density operator, expressed in ladder operators, is −1/2 i imina mh cos[t wa].

Example 2:

Single spin hit with 90° pulse with J-coupling during acquisition.

1pulseshort.nb also analyzes the 1-pulse sequence for one of two weakly J-coupled $I = 1/2$ nuclear spins, here assumed to be ^{13}C (spin a) and ^{1}H (spin x). In shorthand notation, this experiment is the same as example a, but in this case the ^{13}C-^{1}H J-coupling Hamiltonian is present during the acquisition time t.

The equilibrium density operator is $\rho_{\mathrm{eq}} =$ mc iza + mh izx. The analysis, shown in *1pulseshort.nb*, shows that the single pulse to the "a" spin yields $\rho_1 = -$mc iya + mh izx. The density operator during the acquisition of the NMR signal is $\rho_2(t) = -$mc iya cos[wa t] cos[πj t] + mc ixa sin[wa t] cos[πj t] − mc 2 iya izx sin[wa t] sin[πj t] + mc 2 ixa izx cos[wa t] sin[πj t] + mh izx, where j is the coupling constant in s^{-1}.

The observable absorptive part of the NMR spectrum for spin a is −¼ i (mc imina cos[wa $t - \pi j$ t] + mc imina cos[wa $t + \pi j$ t]) and corresponds to a positive in-phase "doublet" centered at $\omega_a/(2\pi) = \nu_a$, with the two peaks occurring at $\nu_a + j/2$ and $\nu_a -$ j/2. The J-coupling splits the chemical shift frequency into two peaks at wa ± $j/2$ s^{-1} (Fig. 22.1).

The other parts of the density operator during acquisition for spin a are not directly observable in the phased spectrum and correspond to the $p = 0$, $p = +1$, and $p = -1$ dispersive and antiphase components. Each of these components has sin time dependence that yields zero intensity at $t = 0$, hence zero intensity in the Fourier-transformed spectrum.

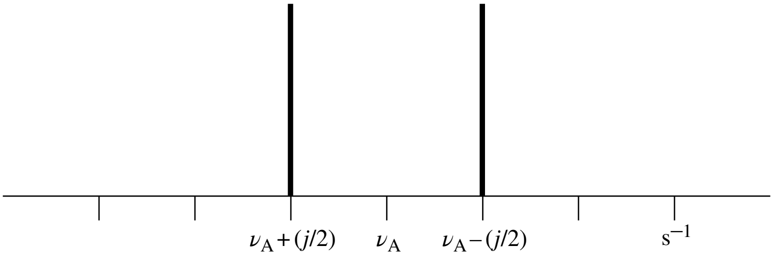

Figure 22.1 Effect of J-coupling of one $I = 1/2$ nucleus (spin A) to one other $I = 1/2$ nucleus (spin X). Only the spectrum of spin A is shown. The frequencies are expressed in s^{-1}. Relative to the chemical shift ν_A of spin A, the frequencies of the two doublet peaks are $+j/2$ and $-j/2\,s^{-1}$, respectively.

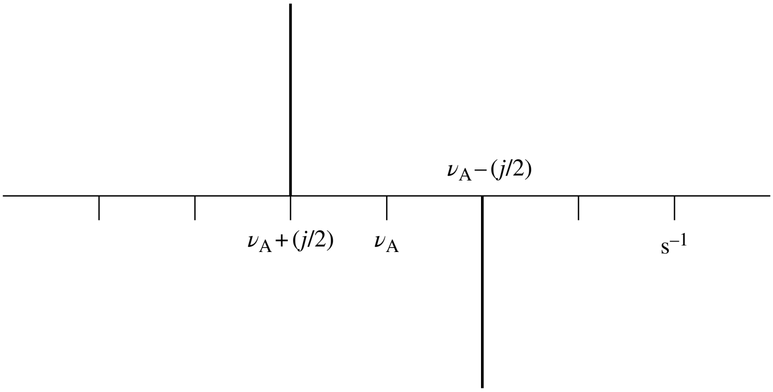

Figure 22.2 Antiphase J-coupling of one $I = 1/2$ nucleus (spin A) to one other $I = 1/2$ nucleus (spin X). Only the antiphase spectrum of spin A is shown. The frequencies are expressed in s^{-1}. Relative to the chemical shift ν_A of spin A, the frequencies of the two antiphase doublet components are $+j/2$ and $-j/2\,s^{-1}$, respectively.

Example 3:

Evolution of antiphase magnetization terms.

As shown in *1pulseshort.nb*, the antiphase components evolve into and out of observable in-phase components if $\hat{H}_J$ is active, giving rise to an antiphase doublet centered at $\omega_a/(2\pi) = \nu_a$, with the two peaks occurring at $\nu_a + j/2$ and $\nu_a - j/2$ (Fig. 22.2).

Antiphase magnetization, especially *heteronuclear antiphase magnetization*, is extremely important in modern liquid-state NMR. The next chapter discusses a pulse sequence that takes advantage of it.

Example 4:

NMR Spin Echoes, a Valuable Tool in NMR Pulse Sequences.

Case A: The echo pulse sequence in Figure 22.3 for two J-coupled ^{1}H spins is analyzed in *echooneortwo.nb*. The critical factor is that *both* coupled spins receive the hard π pulse ($\omega_1 >> \delta$, J). The echo obtained depends only on J and 2τ, NOT on the chemical shifts of the two ^{1}H spins. *The effect of the chemical shift Hamiltonian* $\hat{H}_{CS}$ *is suppressed over the echo period* 2τ.

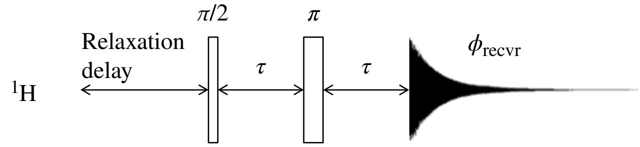

Figure 22.3 The Spin Echo NMR Experiment for two coupled ^{1}H spins. The narrow vertical rectangle represents a $\pi/2$ rf pulse and the thick vertical rectangle represents a π rf pulse. Both J-coupled spins are hit with the rf pulses. As shown in *echooneortwo.nb*, the effect of the chemical shift Hamiltonian is suppressed over the 2τ period.

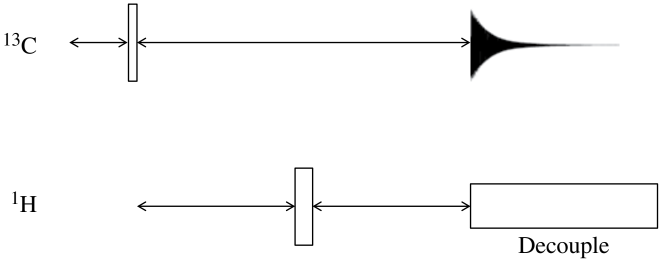

Figure 22.4 Heteronuclear Spin Echo Experiment for a ^{13}C coupled to ^{1}H. The narrow vertical rectangle represents a $\pi/2$ rf pulse to the ^{13}C spin and the thick vertical rectangle represents a π rf pulse to the ^{1}H spin. The effect of the J-coupling Hamiltonian is suppressed over the 2τ period. The chemical shift Hamiltonian is preserved.

Case B: The echo pulse sequence shown later for J-coupled heteronuclei like ^{1}H and ^{13}C is analyzed for two spins in *echooneortwo.nb*. Here only the ^{1}H spin receives a hard π pulse. The echo obtained depends only on the ^{13}C chemical shift δ and 2τ, NOT on the ^{1}H-^{13}C J-coupling. *The effect of the heteronuclear ^{1}H-^{13}C J-coupling Hamiltonian $\hat{H}_J$ is suppressed over the echo period. The ^{1}H has been decoupled from ^{13}C.* The decoupling of ^{1}H during acquisition of the ^{13}C free induction decay consists of the equivalent of a series of π rf pulses (Fig. 22.4).

EXPLANATION OF *1pulseshort.nb*

The user is told to evaluate *shortspin.nb*, then close it without saving. The first case analyzed (Example 1) is of a single spin where the equilibrium density operator is subjected to a strong $\pi/2$ rf pulse ($\omega_1 >> \delta$) along the x axis of the rotating frame. The function a0 identifies the spin as the "a" spin, and the 0 indicates the x axis rf phase. The hard pulse nutates the equilibrium density operator by $\pi/2$ rad around the x axis. The starting equilibrium density operator is designated as mh iza. After the rf pulse, the resulting density operator ρ_1 is −mh iya. The $-y$ axis predicted for the density operator is exactly the same as predicted for the "magnetization" in the Bloch equations.

The next cells demonstrate that the function mq converts from Cartesian to ladder operator representation of the density operator. The −mh iya density operator corresponds to a mixture of iplusa and imina components.

The next cells show the calculation used to obtain the time-dependent acquisition density operator ρ_{acq}. The coupling constant *j* is zero because there is no scalar coupling, so the ρ_{acq} $-y$ and $+x$ components oscillate as cos[*t* wa] and sin[*t* wa], respectively. Converting to ladder operators with the function mq shows that the density operator is an equal mixture of imina and iplusa. The user is then reminded that only the $p=-1$ part, that is, the imina part, is observable. The absorptive peak oscillates as cos[*t* wa]. The dispersive peak oscillates as sin[*t* wa].

(Example 2) The a spin is ^{13}C. The x spin is ^{1}H. There is scalar coupling of $j\,\mathrm{s}^{-1}$ between them. The equilibrium density operator $\rho_0=$ mc iza + mh izx. The a0 rf pulse to the ^{13}C nucleus does not affect the ^{1}H spin, so the resulting density operator ρ_1 contains the equilibrium ^{1}H component mh izx.

The next cells show the time-dependence of the spin density operator $\rho_{2\mathrm{acq}}$ in Cartesian and ladder operator form. The absorptive $p=-1$ component oscillates as cos[*t* wa] cos[*j* π *t*] and corresponds to a positive "doublet" at $(\mathrm{wa}+\pi j)\,\mathrm{rad\,s^{-1}}$ and $(\mathrm{wa}-\pi j)\,\mathrm{rad\,s^{-1}}$. The built-in Mathematica function TrigReduce is used to simplify some of the expressions.

(Example 3) The next cells calculate the time-dependence of the unobservable "antiphase" part 2 mc ixa izx of $\rho_{2\mathrm{acq}}$. The analysis shows that the unobservable antiphase part evolves into an absorptive antiphase doublet with a positive peak at $(\mathrm{wa}+\pi j)$ and a negative peak at $(\mathrm{wa}-\pi j)$.

EXPLANATION OF *echooneortwo.nb*

The user is instructed to evaluate *shortspin.nb*, then close it without saving changes.

(Example 4, Case A) Both spins are ^{1}H, and the equilibrium density operator mh iza + mh izx is nutated by the initial $\pi/2$ rf pulse along the *x* axis of the rotating frame (ax0). The density operator evolves with both chemical shift and J-coupling during the first delay period *t* and then is hit with the π rf pulse along the *x* axis of the rotating frame. A second delay period of the duration *t* allows for further chemical shift and J-coupling evolution. After the second delay, the density operator shows no dependence on chemical shift. Only J-coupling has occurred over the period 2t. The chemical shift evolution has been suppressed.

(Example 4, Case B) The "a" spin is ^{1}H and the "x" spin is ^{13}C. The equilibrium density operator mh iza + mc izx is subjected to $\pi/2$ rf pulses along the *x* axes of the respective rotating frames at both Larmor frequencies to yield the density operator −mc iyx − mh iya. This density operator evolves during the first delay period *t* subject to chemical shift and J-coupling. At this time, the resulting density operator is hit with a π pulse to the ^{1}H spin only along the *x* axis of the rotating frame (a0). Note that %% refers to the output from the cell before last. After the π rf pulse to the density operator, the second delay period *t* allows for both chemical shift and J-coupling evolution. The resulting density operator, mh iya − mc cos[2 *t* wx] iyx + mc sin[2 *t* wx] ixx, shows that the density operator of the x spin has no dependence on J-coupling over the period 2*t*. For the ^{13}C spin, chemical shift evolution has occurred but the J-coupling evolution has been suppressed. This behavior is the basis of "decoupling."

(Example 4, Case C) Here, we again have the “a” spin as ^{1}H and the “x” spin as ^{13}C. This time we hit only the ^{13}C spin with a $\pi/2$ pulse along the x axis of the rotating frame (x0). During the first delay period t, both chemical shift and J-coupling evolution occur. Then the ^{1}H spin only is hit with a π pulse along the x axis of the rotating frame, followed by a second delay period t with both chemical shift and J-coupling evolution. Again the J-coupling between the ^{1}H and ^{13}C spins is suppressed, leaving only the chemical shift dependence.

(Example 4, Case D) Again the “a” spin is ^{1}H and the “x” spin is ^{13}C. Only the ^{1}H spin is hit with a $\pi/2$ rf pulse along the x axis of the rotating frame. This is followed by a delay of duration $1/(4\,j)$ during which the density operator evolves with both the chemical shift and J-coupling. Then a π pulse along the x axes of the respective rotating frames is given to both spins (ax0). Then a second delay of duration $1/(4\,j)$ allows evolution with both chemical shift and J-coupling. The resulting density operator is −mc izx − 2 mh ixa izx. The ^{1}H signal is pure antiphase.

CHAPTER 23

ANALYSIS OF THE INEPT PULSE SEQUENCE WITH PROGRAM SHORTSPIN AND PROGRAM POMA

Figure 23.1 shows the INEPT pulse sequence. INEPT is an acronym for Insensitive Nucleus Enhancement by Polarization Transfer.

In Figure 23.1, the sensitive nucleus is ^{1}H and the insensitive nucleus is ^{13}C. The INEPT sequence also works for many other insensitive $I = 1/2$ nuclei such as ^{15}N. For the case of ^{1}H–^{13}C coupling, $j = {}^1J_{CH}$ is the coupling constant, typically approximately 145 s^{-1} for ^{1}H directly bonded to ^{13}C, and the phase cycle is:

$\phi_1 = 0\ 2\ 3\ 1\ 1\ 3\ 0\ 2\ 2\ 0\ 1\ 3\ 3\ 1\ 2\ 0$ in units of $\pi/2$

$\phi_2 = 0\ 0\ 3\ 3\ 1\ 1\ 0\ 0\ 2\ 2\ 1\ 1\ 3\ 3\ 2\ 2$ in units of $\pi/2$

$\phi_3 = 1\ 1\ 0\ 0\ 2\ 2\ 1\ 1\ 3\ 3\ 2\ 2\ 0\ 0\ 3\ 3$ in units of $\pi/2$

$\phi_4 = 0\ 0\ 3\ 3\ 1\ 1\ 0\ 0\ 2\ 2\ 1\ 1\ 3\ 3\ 2\ 2$ in units of $\pi/2$

$\phi_5 = 0\ 2\ 0\ 2\ 1\ 3\ 1\ 3\ 2\ 0\ 2\ 0\ 3\ 1\ 3\ 1$ in units of $\pi/2$

$\phi_{\text{recvr}} = 0\ 0\ 0\ 0\ 1\ 1\ 1\ 1\ 2\ 2\ 2\ 2\ 3\ 3\ 3\ 3$ in units of $\pi/2$

After adding $(360° - \phi_{\text{recvr}})$ or $(4 - \phi_{\text{recvr}}$ in units of $\pi/2)$ to all pulse phases, the phase cycle simplifies to the following:

$\phi_1 = 0\ 2\ 3\ 1$

$\phi_2 = 0\ 0\ 3\ 3$

$\phi_3 = 1\ 1\ 0\ 0$

$\phi_4 = 0\ 0\ 3\ 3$

$\phi_5 = 0\ 2\ 0\ 2$

$\phi_{\text{recvr}} = 0\ 0\ 0\ 0$

Pulse-by-pulse, delay-by-delay analysis with program *shortspin.nb* in *inept.nb* shows that polarization transfer from ^{1}H to ^{13}C is achieved and that all other coherence is cancelled by destructive interference. The polarization transfer is indicated by the

---

A Primer of NMR Theory with Calculations in Mathematica®, First Edition. Alan J. Benesi.

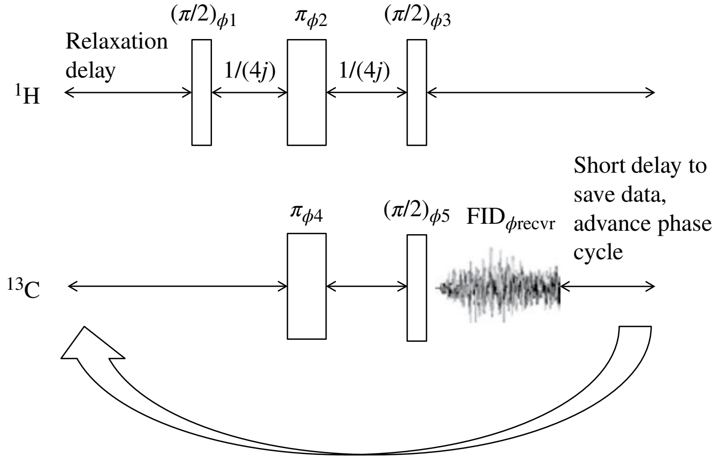

Loop back to accumulate signal for ns scans

Figure 23.1 The INEPT pulse sequence. The narrow vertical rectangles represent $\pi/2$ rf pulses, and the thick vertical rectangles represent π rf pulses. The chemical shift Hamiltonian is suppressed and the J-coupling Hamiltonian is preserved over the 2 (1/4*j*) intervals. The two final $\pi/2$ rf pulses to the ^{13}C and ^{1}H spins transfer the polarization of the ^{1}H spin to the coupled ^{13}C spin, improving sensitivity.

"mh" intensity term of the resulting ^{13}C antiphase coherence. If one allows the antiphase coherence to evolve for a period τ such that $\sin[\pi\, j\, \tau]=1$ or -1, the antiphase coherence becomes in-phase coherence for ^{13}C with magnitude mh. The larger signal from ^{1}H has been transferred to the ^{13}C nucleus. The INEPT method for enhancing the signal of insensitive nuclei like ^{13}C and ^{15}N is widely used in advanced pulse sequences.

The notebook *ineptpoma.nb* shows how the same pulse sequence is analyzed using program *poma.nb*. POMA is more convenient for fast analysis of an entire pulse sequence, but as shown in *ineptpoma.nb* the symbols such as J_{12} cannot be evaluated numerically.

EXPLANATION OF *inept.nb*

The user is instructed to evaluate *shortspin.nb*, then close it without saving changes. After reduction to constant receiver phase as described earlier, the analysis requires evaluation of the INEPT pulse sequence for four different sets of radio frequency (rf) pulse phases.

The first set of pulses starts with a $(\pi/2)_x$ rf pulse to the "a" spin (the ^{1}H spin). This is followed by a delay of duration 1/(4 *j*), where *j* is the ^{1}H–^{13}C J-coupling constant. Then both the ^{1}H and ^{13}C spins receive a π_x rf pulse. This is followed by another delay of duration 1/(4 *j*). Then the ^{1}H spin is hit with a $(\pi/2)_y$ rf pulse at the same time as the ^{13}C spin receives a $(\pi/2)_x$ rf pulse. The resulting density operator is sig1 = mc iyx −2 mh iyx iza.

The second set of pulses and delays are identical in duration and nutation angle to the first but with different phases for the rf pulses. The resulting density operator is saved as sig2 = −mc iyx −2 mh iyx iza.

The third set of pulses and delays are identical in duration and nutation angle to the first and second but with different phases for the rf pulses. The resulting density operator is saved as sig3 = mc iyx −2 mh iyx iza.

The fourth set of pulses and delays are identical in duration and nutation angle to the first, second, and third but with different phases for the rf pulses. The resulting density operator is saved as sig4 = −mc iyx −2 mh iyx iza.

Adding sig1 + sig2 + sig3 + sig4 gives the density operator at $t = 0$ of the acquisition interval. The result is sigtot = −8 mh iyx iza. The important aspect to note is that this is pure antiphase magnetization of the x spin (^{13}C) with respect to the a spin (^{1}H) and that this antiphase signal has the magnitude of the ^{1}H spin.

The resulting antiphase signal is not itself observable but evolves under chemical shift and J-coupling during the acquisition time into in-phase observable ^{13}C coherence with the magnitude of an ^{1}H signal. The observable absorptive part of the signal is the 4 mh ixx cos[t wx] sin[$j\ \pi\ t$].

Finally, to show the effect of ^{1}H decoupling on the observability, we "decouple" the evolution of the sigtot density operator by setting $j = 0$ in the acquisition delay. With $j = 0$, the antiphase magnetization does NOT evolve into observable in-phase coherence.

EXPLANATION OF *ineptpoma.nb*

The user is instructed to evaluate *poma.nb* and then to close it without saving changes. The same phase cycle, reduced to constant receiver phase, is used for this analysis as for the analysis with *shortspin.nb*. The advantage of POMA is that the density operator resulting from the sum of all four sets of rf pulse phases can be calculated with one input line. The spins in *poma.nb* are identified with numbers. In this case, spin 1 is ^{1}H and spin 2 is ^{13}C. The starting equilibrium density operator is mh spin[1,z] + mc spin[2,z]. The // indicates that the subsequent "pulse" command use the preceding output (the equilibrium density operator) as input for the pulse. The first rf pulse is applied to spin 1 (the ^{1}H spin) only, so the command is pulse[90,{x,−x,−y,y},{1}]. Note that it is allowed to identify the nutation angle of the rf pulse in degrees rather than radians. The four allowed pulse phases for the first pulse are identified within squiggly brackets, and the fact that only spin 1 (the ^{1}H spin) is hit with these pulses is indicated by the 1 enclosed in squiggly brackets. The output from this command is used as input for the "delay" command, where the duration of the delay is set to t1 (rather than 1/(4 j)—this will be explained later) and the J-coupling between spins 1 and 2 is indicated by the {{1,2}}. The output from this delay is used as input for the following pulse command where the nutation angle is set to 180°, the four allowed pulse phases are identified within squiggly brackets, and the fact that both spins are hit with the 180° pulse is indicated by {1,2}. The output from this pulse is followed by another delay of duration t1, then a 90° pulse with phases {y,y,x,x} to spin 1 and then a 90° pulse with phases {x,−x,x,−x} to spin 2. The output is then passed on to the receiver, where the receiver phase (which has been "reduced" to constant phase 0 or x) is identified as {0,0,0,0}.

The *poma.nb* density operator result for the whole INEPT pulse sequence is −mh sin[2 π t1 (J12)] i1z i2y. We try to make the substitution t1 → 1/(4 J12), but the program cannot recognize that J12/J12 = 1. Another minor problem with the result is that the coefficient for the resulting antiphase magnetization is 1 rather than 8. With this caveat, the *poma.nb* analysis gives the same result as obtained with *shortspin.nb* in *inept.nb*.

HOMEWORK

Homework 23.1: Considering the natural abundances of ^{13}C and ^{1}H, describe a chemical method that could be used to further improve sensitivity of the INEPT experiment. What additional interaction would have to be considered?

Homework 23.2: Analyze the following pulse sequences (i) DEPT-135 (Doddrell et al., 1982)[1] and (ii) BIRD (Garbow et al., 1982).[2]

---

[1] Use $\theta = 3\pi/4 = 135°$.

[2] Use the pulse sequence in Figure 2 (a) from this paper.

CHAPTER 24

THE RADIO FREQUENCY HAMILTONIAN

In modern NMR spectrometers, the radio frequency (rf) Hamiltonian

$$\hat{\mathrm{H}}_{\mathrm{rf}} = \omega_1(\cos(\phi)\hat{\mathrm{I}}_x + \sin(\phi)\hat{\mathrm{I}}_y) \tag{24.1}$$

is under precise human control. The frequency and amplitude of ω_1 as well as the phase ϕ can be changed quickly and arbitrarily, typically in less than 3 μsec, with maximum nutation frequencies[1] ($\omega_1/2\pi$) up to about $200\times10^3\,\mathrm{s}^{-1}$ achievable. Even higher nutation frequencies are possible with smaller rf coils, but the NMR samples in these contain fewer nuclei. In the preceding examples of liquid-state NMR pulse sequences, it was assumed that the rf pulses were "hard," such that $\|\hat{\mathrm{H}}_{\mathrm{rf}}\| \gg \|\hat{\mathrm{H}}_{\mathrm{internal}}\|$. This is a reasonable approximation for most liquid-state NMR samples where rapid reorientation of the nuclei-containing molecules averages the internal Hamiltonians. In general, the only surviving internal Hamiltonians in liquid-state NMR are the relatively weak isotropic chemical shift and J-coupling Hamiltonians $\hat{\mathrm{H}}_{\mathrm{cs}}$ and $\hat{\mathrm{H}}_{\mathrm{J}}$. In solid-state NMR samples, this approximation often fails because the magnitudes of the dipolar and quadrupolar internal Hamiltonians can be comparable with or greater than $\|\hat{\mathrm{H}}_{\mathrm{rf}}\|$.

An rf pulse applied to an ensemble of nuclear spins at their resonant Larmor frequency almost always has negligible effects on other NMR nuclei with different Larmor frequencies since these are almost always outside the spectral *excitation bandwidth* of the rf pulses.[2] An exception to this occurs when there are heteronuclear internal Hamiltonians such as $\hat{\mathrm{H}}_{\mathrm{D}}$ (in the solid state) or $\hat{\mathrm{H}}_{\mathrm{J}}$ (in the solid or liquid state) that couple nuclei with different Larmor frequencies. In such cases, rf pulses on one NMR-observable isotope can have significant effects on the density operator for other NMR-observable isotopes.

In this chapter, the spectral *excitation bandwidths* of a $\pi/2$ ($\pi/2=\omega_1\,\tau_{\mathrm{pulse}}$) rectangular rf "x" pulse ($\phi=0$ in Eq. 24.2) and of a $\pi/2$ truncated sinc-shaped "x" rf pulse are compared using density matrix theory (see *excitation_bandwidth.nb*) for an

---

[1] The nutation frequency is the rate at which the magnetization rotates around the rf field.

[2] The excitation bandwidth can be defined as the frequency range for which the rf pulse(s) significantly change the density operator for the observed spins.

A Primer of NMR Theory with Calculations in Mathematica®, First Edition. Alan J. Benesi.

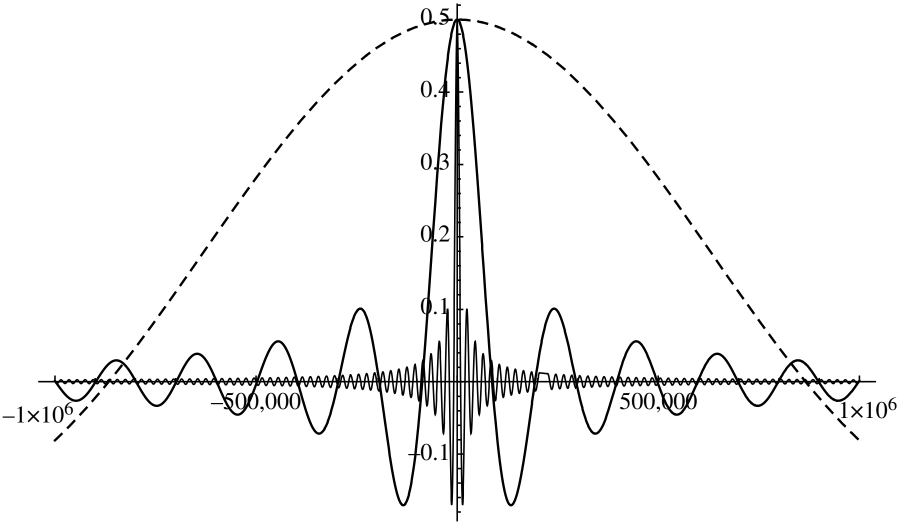

Figure 24.1 Offset dependence of rectangular $(\pi/2)_x$ pulses with different durations ($\tau_{\text{pulse}} = (\pi/2)/\omega_1$) and different rf field strengths ω_1. The imaginary part of the NMR signal $<I^+.\rho(t)>$, $-I_y(t)$ from Equation 24.3 is plotted against the offset $\delta/(2\pi)$ in s^{-1}: Dashed curve: $\omega_1 = 2\pi \times 5 \times 10^5\,\text{rad}\,\text{s}^{-1}$. Thick solid oscillation: $\omega_1 = 2\pi \times 5 \times 10^4$. Thin solid oscillation: $\omega_1 = 2\pi \times 5 \times 10^3\,\text{rad}\,\text{s}^{-1}$. The damped oscillatory response is equivalent to a sinc function. The maximum signal intensity is +0.5 for an on-resonance $(\pi/2)$ pulse.

$I = 1/2$ nuclear spin. In these calculations, it is assumed that the sample is in the liquid state and that the only non-zero internal Hamiltonian is the isotropic chemical shift $\overline{\overline{\text{H}}}_{\text{CS\_iso}} = \delta\hat{\text{I}}_z$ so that in this case the total rotating frame Hamiltonian during the rf pulse is

$$\overline{\overline{\text{H}}}_{\text{pulse}} = \overline{\overline{\text{H}}}_{\text{rf}} + \overline{\overline{\text{H}}}_{\text{CS\_iso}} = \omega_1(t)(\cos(\phi)\hat{\text{I}}_x + \sin(\phi)\hat{\text{I}}_y) + \delta\hat{\text{I}}_z \tag{24.2}$$

where in the case of the rectangular pulse ω_1 is constant and $\phi = 0$. An analytical solution for the observable NMR signal from the combined effects of the $\pi/2$ rf pulse and chemical shift offset δ is obtained by evaluating $\text{Trace}[\hat{\text{I}}^+.\rho]$, Equation 18.1, on the density operator obtained immediately after the rectangular pulse (see *excitation_bandwidth.nb*):

$$(\text{NMR signal})_{\text{rect\_90}} = \frac{\omega_1\left(\delta - \delta\cosh\left[\pi\sqrt{-\delta^2 - \omega_1^2}/2\omega_1\right] + \text{i}\sqrt{-\delta^2 - \omega_1^2}\,\sinh\left[\pi\sqrt{-\delta^2 - \omega_1^2}/2\omega_1\right]\right)}{2(\delta^2 + \omega_1^2)} \tag{24.3}$$

where both ω_1 and δ have units of rad s^{-1}. If $\delta = 0$ (on-resonance), the resulting signal is $-\text{i}/2$ regardless of the value of ω_1, indicating that the equilibrium magnetization has been rotated to the $-y$ axis in the rotating frame as expected for a $(\pi/2)_x$ pulse. For non-zero values of δ the NMR signal is less, as calculated in *excitation_bandwidth.nb* and shown in Figure 24.1.

As shown in *excitation_bandwidth.nb*, the sinc offset dependence is not unexpected, since the Fourier transform of a rectangular pulse yields the sinc function. The Fourier transform of the time-dependence of an rf pulse yields the excitation profile in the frequency domain. In the same way, the Fourier transform of a sinc-shaped pulse has a rectangular excitation profile (see *excitation_bandwidth.nb*). The absolute value of the NMR signal after a sinc pulse has a much wider excitation profile than the equivalent rectangular pulse. For a given pulse, regardless of shape, the excitation bandwidth is proportional to ω_1. The negative values for ω_1 in the sinc pulse are experimentally achieved by switching the rf phase from $+x$ to $-x$ when the sign of the sinc function becomes negative. The sinc function and many other shaped pulses allow for selected regions or individual peaks in the NMR spectrum to be selectively excited (or inverted). Such pulses are called selective or shaped pulses. A special class of shaped pulses called "adiabatic" pulses are also widely employed. These pulses change frequency and phase as a function of time and can give extremely wide excitation bandwidths.

EXPLANATION OF *excitation_bandwidth.nb*

The user is instructed to evaluate *matrep2.nb* and then close it without saving changes. The equilibrium density matrix $\rho 0 = \text{iz}[1/2]$ for an $I = 1/2$ nuclear spin is defined. The chemical shift and rf Hamiltonians $H_{\text{CS}} = \delta\ \text{iz}[1/2]$, $H_{\text{rf}} = \omega_1\ \text{ix}[1/2]$, and $H_{\text{tot}} = H_{\text{CS}} + H_{\text{rf}}$ are defined.

The propagator operators u and $u$adj are calculated using the built-in Mathematica function MatrixExp, then simplified with the built-in function FullSimplify.

These are used to propagate the equilibrium density operator $\rho 0$, yielding the density operator $\rho 1$ after the pulse.

The NMR signal intensity immediately after the pulse, sig, is given by the trace[iplus[1/2].ρ1], and simplified with the built-in function FullSimplify. The resulting maximum signal intensity is –0.5 i, which means that the maximum signal is obtained on the $-y$ axis ($-i$ axis) of the rotating frame.

The next cells substitute $(\pi/2)/\omega_1$ for the duration t of the rf pulse. The resulting expression for the NMR signal is used to create the function sig90[δ,ω_1].

The function sig90 is plotted (built-in Mathematica function Plot) as a function of ν for $\delta = 2\,\pi\,\nu$, $\omega_1 = 2\,\pi\,5 \times 10^4\,\text{rad s}^{-1}$ from $\nu = -100 \times 10^4\,\text{s}^{-1}$ to $100 \times 10^4\,\text{s}^{-1}$.

The function sig90 is then plotted as a function of ν for $\omega_1 = 2\,\pi\,5 \times 10^4\,\text{rad s}^{-1}$, $\omega_1 = 2\,\pi\,5 \times 10^3\,\text{rad s}^{-1}$, and $\omega_1 = 2\,\pi\,5 \times 10^5\,\text{rad}$. The excitation bandwidth is proportional to ω_1. Some variations in the PlotStyle are shown.

The built-in Mathematica function FindRoot is next used to show that the half-bandwidth is proportional to ω_1.

The integral in radians of a rectangular pulse is obtained by multiplying the pulse duration and ω_1. For example, a 5-μs rf pulse with $\omega_1 = 2\,\pi\,10^4\,\text{rad s}^{-1}$ yields an integral of $\pi/2$.

The next cells solve for a *truncated* sinc-shaped pulse with eight nodes that has the same integral as the rectangular pulse. Since the duration of the sinc pulse in the calculation is 4 μs rather than 5 μs, the argument of the sinc function in the integral over 5 μs is $2\ \pi\ (4/5)\ 10^6\ t$. We find that the maximum amplitude of the sinc pulse must be $8.42159 \times 2\ \pi\ 10^4$ rad s^{-1}.

The Fourier transform of a full *nontruncated* sinc pulse excitation profile is calculated by using the built-in Mathematica function FourierTransform. The resulting profile is rectangular. However, keep in mind that this is for a full sinc function, not the truncated one used earlier.

The Fourier transform of the rectangular pulse is calculated next. It yields the sinc function. The Fourier transform of the sinc function conversely yields a positive rectangular pulse shape. The Fourier transform of −sinc function yields a negative rectangular pulse as expected.

The next series of cells uses the density matrix approach to calculate the excitation profile of the eight-node sinc pulse. The function hrfsinc gives the time-dependent rf Hamiltonian that had the same integral as the rectangular pulse with $\omega_1 = 2\ \pi\ 5 \times 10^4$. We calculate a second time-dependent Hamiltonian hrfsinc2 for a pulse with the same integral as a rectangular pulse with $\omega_1 = 2\ \pi\ 5 \times 10^3$.

The Hamiltonians hpulse[t] = δ iz[1/2] + hrfsinc[t] and hpulse2[t] = δ iz[1/2] + hrfsinc2[t] are calculated. Then tables of values of hpulse[t] and hpulse2[t] over the 5-μs duration of the sinc pulse are calculated assuming $\delta = 0$.

The hpulse and hpulse2 tables are then used to calculate the time-dependent propagators needed to calculate the density operator after the pulse. These are then used sequentially with the built-in Mathematica function Do to calculate the density operator after the pulse. We see that the on-resonance ($\delta = 0$) sinc pulse we calculated to be equivalent to the rectangular pulse with $\omega_1 = 2\ \pi\ 5\ 10^4$ fully excites the density operator to −0.5 i. The weaker on-resonance sinc pulse with $\omega_1 = 2\ \pi\ 5\ 10^3$ does not.

We then calculate time-dependent expectation values for −iy[1/2], ix[1/2], and iz[1/2]. After the pulse they yield the expected results of 0.5, 0, and 0, respectively.

Next we look at the offset (δ) dependence of the sinc pulse. We create an offset and time-dependent table of hpulse Hamiltonians that we call htab.

We use the table of time-dependent Hamiltonians to propagate the equilibrium density operator $\rho[0] = \rho 0$ over the duration of the sinc pulse. The resulting set of 1001 different density operators with different δs is called rho. Note that each m value corresponds to a different offset δ and that each offset generates 51 n increments, the last of which gives the density operator after the pulse.

Next the NMR signal for the 51st increment of each of the 1001 offsets is calculated by taking the trace of rho[[m]][[51]].iplus[1/2]. These are used with the built-in Mathematica function ListPlot to plot the offset dependence.

It is clear that the phase of the NMR signal varies with offset, but as shown in the table sincsigabs, the absolute value of the NMR signal gives an approximately rectangular excitation profile. It is approximate because we have used only an eight-node sinc function.

The excitation profile of the rectangular pulse is then compared with that of the sinc pulse. Again the absolute value of the NMR signal is plotted. The subsequent plot shows both excitation profiles and the much broader excitation profile of the sinc pulse.

We then repeat the excitation profile calculations for the sinc and rectangular pulses using a 5-ms rf pulse with $\omega_1 = 2\ \pi\ 50$ rad s^{-1}. We find that the shape of the resulting excitation profile is exactly the same as for $\omega_1 = 2\ \pi\ 5 \times 10^4$ s^{-1} but exactly 1000 times narrower.

CHAPTER 25

COMPARISON OF 1D AND 2D NMR

One-dimensional (1D) NMR experiments consist of a pulse or sequence of pulses and delays immediately preceding the acquisition and digitization of the complex NMR signal (free induction decay (FID)) in the rotating frame (see Chapters 4, 20, and 22). Adjacent complex data points are separated by the “dwell” time. The total time during which the NMR signal is digitized is called the acquisition time, often denoted as t_2 (Fig. 25.1).

Due to the finite lengths of cables and connectors, the exact phase of the absorption spectrum in the electronically determined experimental rotating frame is unknown. A zero-order phase correction is used to rotate the x axis of the frame into coincidence with the on-resonance magnetization immediately after the pulse. A first-order phase correction is then used to correct for phase differences of the magnetization that vary linearly with frequency away from resonance. In some NMR experiments, the phase of the peaks in the spectrum varies, and a “magnitude” spectrum is obtained by squaring each complex data point (i.e. $\mathrm{fid}(n) \times \mathrm{fid}(n)^*$) in the transformed spectrum, then taking the square root, where $\mathrm{fid}(n)$ is the nth complex data point in the FID.

Two-dimensional (2D) NMR experiments operate by repeating the 1D experiment while incrementing or decrementing a nonacquisition delay and saving the data from each 1D experiment in a separate row for each different delay value. This is illustrated in the Figure 25.2. The basic idea is to manipulate the density operator with the pulses, delays, and phase cycle (and perhaps pulsed magnetic field gradients) so that it has the desired form during the t_1 evolution interval and t_2 acquisition interval. For example, by using heteronuclear J-coupling and coherence transfer similar to that described in the preceding chapter, it is possible to manipulate the density operator so that it evolves at the ^{13}C chemical shift during the t_1 interval and at the ^{1}H chemical shift during the t_2 acquisition interval.

It should be apparent that the same principle can be used to create 3D and 4D NMR experiments.

“Tricks” to obtain absorption mode peaks in both the t_1 and t_2 intervals include the time proportional phase incrementation (TPPI) (Marion and Wuthrich, 1983), States (States et al., 1982), and hypercomplex methods (Keeler and Neuhaus, 1985). Another “trick” to obtain an approximate gain of $\sqrt{2}$ in sensitivity is obtained with the aptly named sensitivity improvement method (Palmer et al., 1991). These and other methods are very important experimentally but less so to the theoretical discussion presented here.

A Primer of NMR Theory with Calculations in Mathematica®, First Edition. Alan J. Benesi.

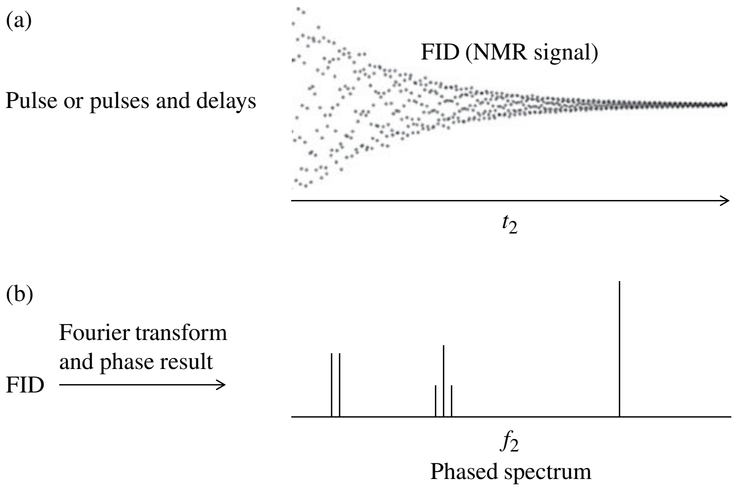

Figure 25.1 1D NMR. (a) The complex NMR signal or FID is saved after the appropriate pulses and phase cycle. Only the real part of the FID is shown. (b) The complex FID is Fourier transformed to yield the 1D spectrum, which is then phased.

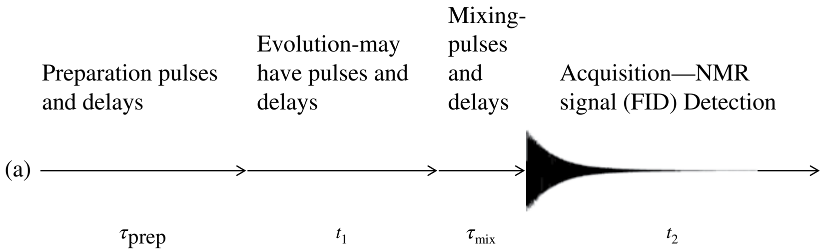

(b) Complete phase cycle for each t_1 value, acquiring the NMR signal during t_2. Save this as FID(t_1, t_2)

(c) Increment or decrement t_1, then repeat step b for the new t_1 value.

(d) Fourier transform the “rows” of the FID(t_1, t_2) with respect to t_2 where each row is defined by its t_1 value. This yields the spectra SPC(f_2, t_1):

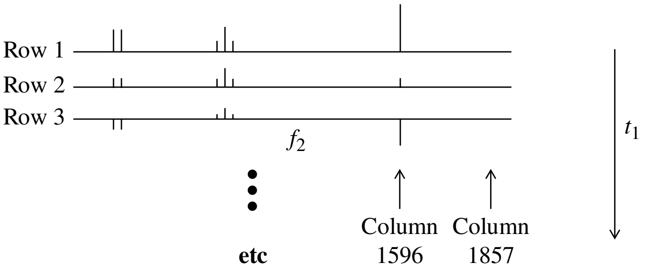

Figure 25.2 (Part 1) Two-dimensional NMR experiments. (a) The radio frequency (rf) pulse sequence and (b) phase cycle generate a complex NMR signal FID(t_1, t_2). (c) The t_1 value is incremented (or decremented) to generate the different FID(t_1, t_2)s. (d) The different FID(t_1, t_2)s are Fourier transformed with respect to t_2, then phased to yield a sequence of 1D NMR spectra in rows, SPC(f_2, t_1).

(e) Now, FT each column of SPC(f_2, t_1) of the spectrum with respect to t_1:

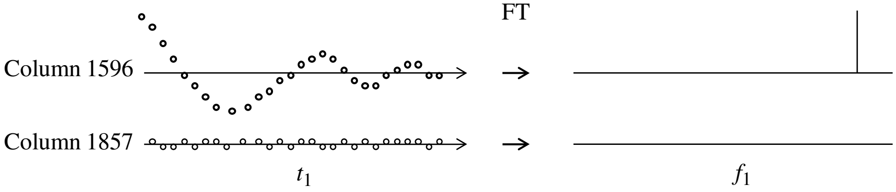

(f) It is useful to represent the 2D spectrum SPC(f_2, t_1) as a topographical map:

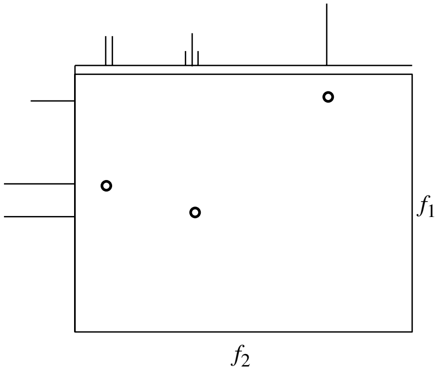

Figure 25.2 (*Continued*) (Part 2) (e) Fourier transform the columns with respect to t_1 to yield the 2D spectrum SPC(f_2,f_1). (f) Contour plots are often used to represent the 2D NMR spectrum.

CHAPTER 26

ANALYSIS OF THE HSQC, HMQC, AND DQF-COSY 2D NMR EXPERIMENTS

Three of the most useful liquid-state two-dimensional (2D) NMR pulse sequences for structural elucidation are the HSQC (heteronuclear single quantum coherence) (Bodenhausen and Ruben, 1980), HMQC (heteronuclear multiple quantum coherence) (Bax et al., 1983), and homonuclear DQF-COSY (double quantum filtered correlation spectroscopy) (Derome and Williamson, 1990). The HSQC sequence is depicted in Figure 26.1 and the HMQC sequence is depicted in Figure 26.2.

The preparation part of the HSQC pulse sequence (before the t_1 evolution time) can be recognized as the Insensitive Nuclei Enhanced by Polarization Transfer (INEPT) pulse sequence (Chapter 23). It is used to transfer the larger ^{1}H signal to the X nucleus (see *hsqc_shortspin.nb*). The 180° pulse on the ^{1}H during the t_1 evolution time decouples the ^{1}H from the ^{13}C, and the INEPT pulse sequence then returns the coherence to in-phase ^{1}H magnetization while the X nucleus is decoupled during the acquisition time t_2. The name of this pulse sequence describes the *single quantum* evolution of the eventually observable antiphase coherence of ^{13}C with respect to ^{1}H during the t_1 interval (see *hsqc_shortspin.nb*). The Mathematica notebook *hsqc_poma.nb* calculates the result for the overall phase cycle and yields the same result.

The preparation part of the HMQC pulse sequence (before the t_1 evolution time) generates a mixture of double and zero quantum coherence (see *hmqc_shortspin.nb*). The 180° pulse on the ^{1}H decouples the ^{1}H from the ^{13}C during t_1, and the final delay for acquisition returns the coherence to in-phase ^{1}H magnetization, which is decoupled from the X nucleus during the acquisition time t_2. The name of this pulse sequence describes the *mixture of double and zero quantum* evolution of the density operator during the t_1 interval (see *hmqc_shortspin.nb*). The Mathematica notebook *hmqc_poma.nb* calculates the result for the overall phase cycle and yields the same result.

After Fourier transformation and phase correction in both dimensions, the experimental ^{1}H-^{13}C HMQC of Δ^9-tetrahydrocannabinol (Δ^9-THC) dissolved in deuterated methanol is shown in Figure 26.3, with the one-dimensional (1D) ^{1}H spectrum along the top and the 1D ^{13}C spectrum along the left-hand side of the 2D spectrum. The large artifact is from the residual ^{1}H signal of CD_3OH solvent.

A Primer of NMR Theory with Calculations in Mathematica®, First Edition. Alan J. Benesi.

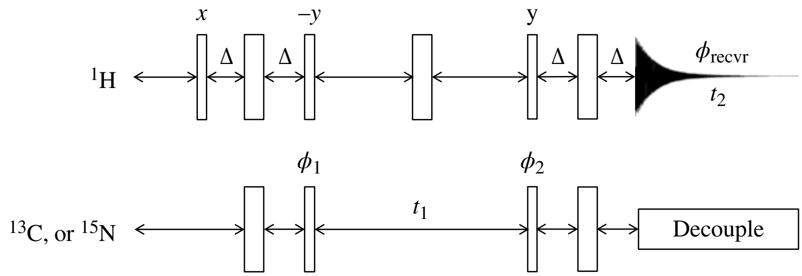

Figure 26.1 The heteronuclear single quantum coherence (HSQC) NMR experiment. The thin and thick vertical rectangles represent 90° and 180° hard pulses ($\omega_1 >> \delta$) applied to the ^{1}H and X (e.g., ^{13}C or ^{15}N) nuclei. The delay Δ is $1/(4\ ^1J_{HX})$. Decoupling of the X spins during t_2 acquisition is achieved with an appropriate decoupling pulse sequence such as WALTZ-16 or Globally Optimized Alternating Phase Rectangular Pulse (GARP) (Shaka et al., 1985). The x, $-y$, and y indicate the phases of the respective ^{1}H pulses in the ^{1}H rotating frame, with $\phi_1 = x\ -x\ x\ -x$ (0 2 0 2 in 90° units) and $\phi_2 = x\ x\ -x\ -x$ (0 0 2 2) the phases of the ^{13}C pulses in the ^{13}C rotating frame, and $\phi_{rcvr} = x\ -x\ -x\ x$ (0 2 2 0) in the ^{1}H rotating frame, and with the phase of the 180° pulse constant and arbitrary. Decoupling sequences are composed of 180 degree pulses applied to one of the heteronuclear spins. The pulses are often shaped rather than rectangular. In modern NMR decoupling is optimized for bandwidth and the degree of suppression of heteronuclear J-coupling.

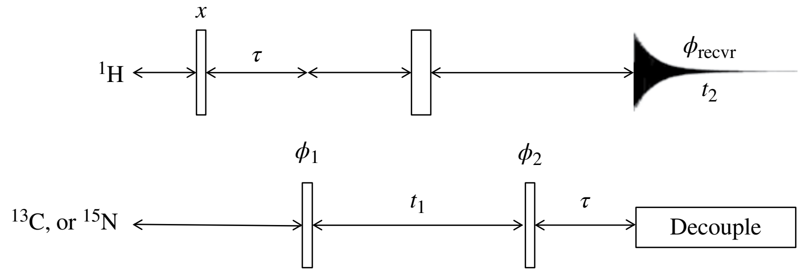

Figure 26.2 The heteronuclear multiple quantum coherence (HMQC) NMR experiment. The thin and thick vertical rectangles represent 90° and 180° hard pulses ($\omega_1 >> \delta$) applied to the ^{1}H and X (e.g., ^{13}C or ^{15}N) nuclei. The delay τ is $1/(2\ ^1J_{HX})$. Decoupling of the X spins during t_2 acquisition is achieved with an appropriate decoupling pulse sequence such as WALTZ-16 or GARP (Shaka et al., 1983, 1985). The phase of the first ^{1}H pulse in the ^{1}H rotating frame is x, $\phi_1 = x\ -x\ x\ -x$ (0 2 0 2), $\phi_2 = x\ x\ -x\ -x$ (0 0 2 2) in the ^{13}C rotating frame, $\phi_{rcvr} = x\ -x\ -x\ x$ (0 2 2 0) in the ^{1}H rotating frame, and the phase of the ^{1}H 180° pulse does not matter as long as it is held constant.

The 2D HSQC experiment gives exactly the same spectrum as the HMQC. The HSQC is better than the HMQC for ^{1}H–^{15}N correlations because during t_1 evolution the $p = +1$ and -1 coherences relax more slowly than $p = +2$, 0, and -2 coherences. The opposite is true for ^{1}H–^{13}C correlations, where the HMQC is advantageous because the $p = +2$, 0, and -2 coherences relax more slowly during the t_1 evolution. Note that *carbon atoms without directly bonded hydrogen atoms do not give cross peaks* in the spectrum. This is evident in the 1D ^{13}C spectrum on the left side of

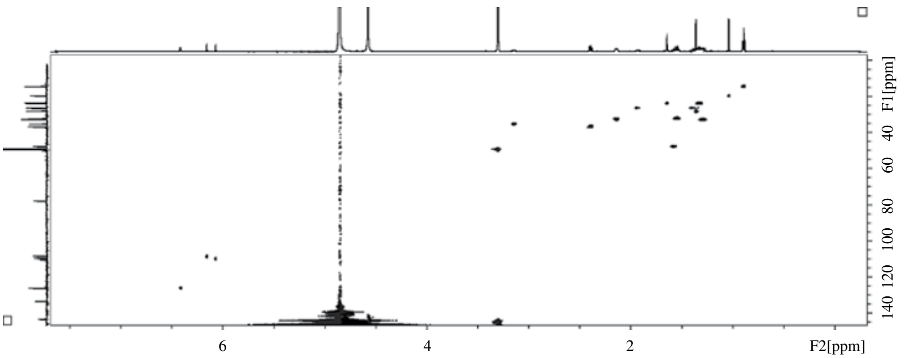

Figure 26.3 The ^{1}H-^{13}C 2D HMQC spectrum of 1 mg of **Δ**^{9}-tetrahydrocannabinol dissolved in deuterated methanol (ideally CD_3OD, where $D = {}^2H$). The 1D ^{1}H NMR spectrum is shown on the top and the 1D ^{13}C spectrum (^{1}H decoupled) is shown on the left side. The three truncated large signals in the 1D ^{1}H NMR spectrum on the top are from methanol OH, water OH, and methanol CH. These large signals give rise to the artifacts toward the bottom of the 2D HMQC spectrum.

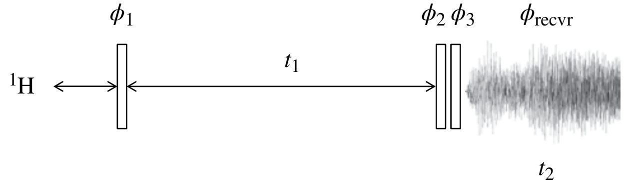

Figure 26.4 The double quantum filtered COSY (DQF-COSY) NMR experiment (Derome and Williamson, 1990). The thin vertical rectangles represent 90° hard pulses ($\omega_1 >> \delta$) applied to the ^{1}H nuclei (or other abundant $I = 1/2$ nuclei such as ^{19}F). The respective phases of the ^{1}H pulses in the rotating frame are $\phi_1 = y\ y\ y\ y\ x\ x\ x\ x$ (1 1 1 1 0 0 0 0), $\phi_2 = x\ x\ x\ x\ y\ y\ y\ y$ (0 0 0 0 1 1 1 1), $\phi_3 = y\ -x\ -y\ x\ -x\ -y\ x\ y$ (1 2 3 0 2 3 0 1), and $\phi_{rcvr} = x\ -y\ -x\ y\ -y\ -x\ y\ x$ (0 3 2 1 3 2 1 0).

Figure 26.3, where the two ^{13}C resonances closest to 140 ppm do not give cross peaks in the HMQC. *Hydrogen atoms with no directly bonded C atoms also give no cross peak.* The largest peaks in the 1D ^{1}H spectrum shown earlier, truncated because they are so large, are those from the OH groups of methanol and water. Neither hydrogen gives rise to a cross peak in the HMQC, although the huge signal from the methanol OH does give rise to a large artifact at the bottom of the spectrum.

A robust experiment for identifying J-coupled pairs of ^{1}H spins is the homonuclear DQF-COSY experiment, shown in Figure 26.4.

The first pulse of the DQF-COSY experiment generates single quantum coherence that evolves with the chemical shifts and J-coupling during t_1, just like a one pulse free induction decay. The next two pulses are given as close to each other in time as possible, typically 3 μs apart on a modern spectrometer. The effect of the two pulses in combination with the phase cycle is to cancel all signals in the final signal except for those that have been through an exclusive $p = +2$ and $p = -2$ (double quantum) coherence level in the short time between the 2D and 3D pulse. The antiphase signal that survives after the phase cycle evolves into observable in-phase

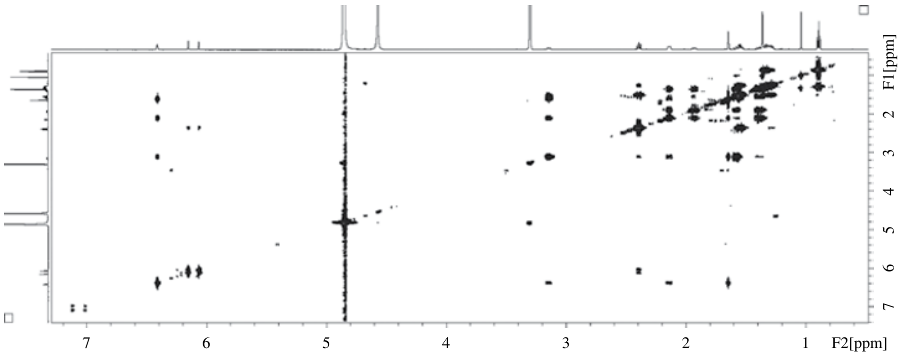

Figure 26.5 The 2D DQF-COSY spectrum of 1 mg of Δ^9-tetrahydrocannabinol dissolved in deuterated methanol. The large vertical ridge in the spectrum is an artifact generated by a large ^{1}H signal from undeuterated methanol OH.

magnetization during the t_2 time interval. The observable signal contains contributions from signals that oscillate at the chemical shift of one spin during t_1 and the coupled spin during t_2, thereby creating off-diagonal cross peaks in the resulting 2D spectrum.

After Fourier transformation and phase correction in both dimensions, the experimental ^{1}H DQF-COSY of Δ^9-THC dissolved in deuterated methanol is shown in Figure 26.5, along with the 1D ^{1}H spectrum along the top and left-hand sides of the 2D spectrum.

The DQF-COSY 2D spectrum gives a clear depiction of the J-coupling between pairs of ^{1}H spins. The double quantum filter removes contributions from coupling between more than two spins, yielding better resolution than other COSY experiments that do not.

EXPLANATION OF *hsqc_shortspin.nb*

The user is instructed to evaluate *shortspin.nb* and then close it without saving changes. The phases of the rf pulses have been reduced to constant (0 or x) receiver phase as described in Chapter 22. The a spin is ^{1}H and the x spin is either ^{13}C or ^{15}N. These are all $I = 1/2$ spins, but only ^{1}H has high natural abundance and high sensitivity and therefore gives a strong NMR signal. The calculation only goes through the first set of rf phases, leaving evaluation of the density operator for the full phase cycle to be completed with program *poma.nb*.

The calculation with *shortspin.nb* proceeds as follows: (i) The first a0 pulse hits the equilibrium density operator mh iza + mc izx with a strong $(\pi/2)_x$ rf pulse (a0) to the ^{1}H spin only. (ii) This is followed by a delay of $(1/(4j))$, where j is the coupling constant in s^{-1}. Both J-coupling and chemical shift Hamiltonians are active during the delay. (iii) Then both the ^{1}H and X spin are hit with simultaneous strong π_x pulses (ax0). (iv) Then there is another delay of $(1/(4j))$. (v) Then the ^{1}H spin is hit with a $(\pi/2)_{-y}$ pulse (a3) while at the same time the X spin is hit with a $(\pi/2)_x$ pulse (x0). (vi) The next step is the first half of incremented delay t_1 (duration $t_{1/2}$). Then a π_x pulse is given to the ^{1}H spin only. (vii) Then the second half of the incremented delay t_1 is applied (duration $t_{1/2}$). (viii) Then the ^{1}H spin is hit with a $(\pi/2)_y$ pulse (a1) while simultaneously hitting the X spin with a $(\pi/2)_x$ pulse (x0). (ix) Then a (1/(4 *j*)) delay is given. Then both the ^{1}H and X spins are hit with respective π_x pulses. (x) Then a second (1/(4 *j*)) delay is given. The resulting density operator is the one of interest because it shows the frequency dependence on the incremented t_1 interval.

Although not included in the calculation, the next step is acquisition of the NMR signal with X-nucleus decoupling. It is shown in the next notebook, *hsqc_poma.nb*, the part of the density operator that survives the destructive interference of the full phase cycle (see *hsqc_poma.nb*) is the mh iya cos[t_1 wx] term. This term is important because it has the magnitude mh of the ^{1}H spin but during the t_1 delay oscillates at the X nucleus chemical shift.

EXPLANATION OF *hsqc_poma.nb*

The user must exit Mathematica, then restart it in order to clear all definitions from the Mathematica kernel. Then the user is told to evaluate *poma.nb,* then to close it without saving.

With *poma.nb*, it is not necessary to reduce the rf phase cycle to constant receiver phase, so the full phase cycle including different receiver phases is included in the analysis.

Spin 1 is assumed to be ^{1}H and spin 2 is assumed to be ^{13}C or ^{15}N. The equilibrium density operators for the two spins have arbitrarily named magnitudes mh and mc to be consistent with the shortspin analysis. It starts by defining the equilibrium density operator mh spin[1,*z*] + mc spin[2,*z*]. The // passes the output of the first function as input to the next function. Thus, the pulse[90,{*x*,*x*,*x*,*x*}] applies a 90° or (π/2) pulse to the ^{1}H spin only (indicated by {1}) with the set of rf phases *x*,*x*,*x*, and *x*. This result is passed on to the function delay that incorporates both J-coupling and chemical shift evolution. The duration of the delay is 1/(4 J12). The {{1,2}} indicates that spins 1 and 2 are J-coupled. This result is passed on to the function pulse. A 180° pulse to both spins with the set of rf phases(*x*,*x*,*x*,*x*) is then applied, followed by a second delay of duration 1/(4 J12). Then a 90° pulse is given to the ^{1}H spin only with rf phase cycle {−*y*,−*y*,−*y*,−*y*}. Simultaneously or immediately after the ^{1}H pulse a 90° pulse is given to the X spin only (indicated by {2}) with rf phase cycle {*x*,−*x*,*x*,−*x*}. This is followed by the first half of the incremented t_1 interval, $t_{1/2}$. The {{1,2}} indicates the active J-coupling between the two spins. This is followed by a π pulse of rf phase cycle {*x*,*x*,*x*,*x*} to the ^{1}H spin only (indicated by {1}), then by another delay of duration $t_{1/2}$. This is followed by 90° pulses to the ^{1}H and X spins. The ^{1}H rf phase cycle for this pulse is {*y*,*y*,*y*,*y*}. The rf phase cycle for the X 90° pulse is {*x*,*x*,−*x*,−*x*}. This is followed by a delay of 1/(4 J12), then a 180° pulse to both spins (hence {{1,2}}) with rf phase cycle {*x*,*x*,*x*,*x*}, then another delay of 1/(4 J12). The receiver function then applies the receiver phase cycle {0,180,180,0}, which is equivalent to {*x*,−*x*,−*x*, *x*}.

The result is the density operator obtained from the full phase cycle immediately before the t_2 acquisition delay. *poma.nb* cannot evaluate the symbolic expression J12/J12, but simple inspection shows that the only surviving density operator term is mh cos[t_1 (w2)] i1y. This is the same result as calculated in *hsqc_shortspin.nb*.

The last cell demonstrates that the result is the same as long as the rf phase of the 180° pulses are held constant.

EXPLANATION OF *hmqc_shortspin.nb*

The user must exit Mathematica, then restart it in order to clear all definitions from the Mathematica kernel. The user is told to evaluate *shortspin.nb*, then to close it without saving. Only the first NMR acquisition of the constant receiver phase version of the HMQC experiment is calculated. Let $a = {}^1$H, $x = {}^{13}$C, or another $I = 1/2$ nucleus. The equilibrium density operator is mh iza + mc izx. A $(\pi/2)_x$ rf pulse is given to the ^{1}H spin. Next there is a delay of duration $1/(2\,j)$ where j is the coupling constant in s^{-1}. This is followed by a $(\pi/2)_x$ pulse to the ^{13}C nuclear spin. Then a delay corresponding to the first half of the t_1 interval is applied, followed by a π_x pulse to the ^{1}H spin. This is followed by a delay corresponding to the second half of the t_1 interval. This yields the density operator immediately before the $\pi/2$ pulse to the ^{13}C spin. It is then converted into an expression composed of ladder operators imina, iminx, iplusa, and iplusx. The latter version shows directly that the density operator consists of in-phase ^{13}C single-quantum iminx and iplusx terms along with a mixture of double quantum iplusa iplusx and imina iminx terms and zero quantum iplusa iminx and imina iplusx terms. The ^{13}C component is cancelled by destructive interference in the full phase cycle as shown in *hmqc_poma.nb*.

EXPLANATION OF *hmqc_poma.nb*

The user must exit Mathematica, then restart it in order to clear all definitions from the Mathematica kernel. Then the user is told to evaluate *poma.nb*, then to close it without saving.

With *poma.nb*, it is not necessary to reduce the rf phase cycle to constant receiver phase, so the full phase cycle including different receiver phases is included in the analysis.

Spin 1 is assumed to be ^{1}H, and spin 2 is assumed to be ^{13}C or ^{15}N. The equilibrium density operators for the two spins have arbitrarily named magnitudes mh and mc to be consistent with the shortspin analysis. It starts with the equilibrium density operator mh spin[1,z] + mc spin[2,z]. The pulse[$\pi/2$,{x,x,x,x},{1}] applies the $(\pi/2)$ pulse of phase cycle x,x,x,x to the ^{1}H spin only. This is followed by a delay of duration $1/(2\,j12)$ where $j12$ is the coupling constant in s^{-1}. Then a $(\pi/2)$ pulse of phase cycle {0,180,0,180}, equivalent to {x,$-x$,x,$-x$}, is given to the ^{13}C spin only. Then a delay corresponding to the first half of the t_1 interval occurs, which is followed by a π pulse of phase cycle {0,0,0,0} to the ^{1}H spin and then the second half of the t_1 interval. This is followed by a $(\pi/2)$ pulse of phase cycle {0,0,180,180}, equivalent to {x,x,$-x$,$-x$}, which is given to the ^{13}C spin only. This is followed by a delay of duration 1/(2*j*12). The resulting density operator is –cos[t_1 w2] i1y, showing that the ^{1}H nucleus signal oscillates at the chemical shift w2 of the ^{13}C spin during the incremented t_1 interval. Finally, we give a delay of duration t_2 to the density operator after the t_1 interval. Since the ^{13}C is decoupled during the t_2 interval, there is no coupling indicated between spins 1 and 2. The t_2-dependent density operator obtained oscillates at w1, the chemical shift of the ^{1}H spin.

The calculations then show that there is no effect of the phase of the π pulse on ^{1}H as long as it is held constant. Further calculations show that there is no effect of reducing the phase cycle to constant receiver phase, that only going through half the phase cycle greatly complicates the density operator, and that leaving out the ^{1}H π pulse allows J-coupling during the t_1 interval.

HOMEWORK

Homework 26.1: Use *shortspin.nb* to analyze the first set of receiver-reduced phases of the homonuclear ^{1}H-^{1}H DQF-COSY experiment. Identify the frequencies observed during the t_1 interval.

Homework 26.2: Use poma.nb to analyze the full phase cycle for the homonuclear ^{1}H-^{1}H DQF-COSY experiment. Verify that there are off-diagonal cross peaks that oscillate at one frequency during the t_1 interval and at another during the t_2 acquisition time.

CHAPTER 27

SELECTION OF COHERENCE ORDER PATHWAYS WITH PHASE CYCLING

The density operator $\hat{\rho}$ and Hamiltonians $\hat{H}_X$ can be constructed using Cartesian spin angular momentum operators $\hat{I}_x$, $\hat{I}_y$, and $\hat{I}_z$, or coherence order (ladder) spin angular momentum operators $\hat{I}^+$, $\hat{I}^-$, and $\hat{I}_z = \hat{I}^0$. The latter approach is usually used to design NMR experiments since NMR experiments such as Insensitive Nuclei Enhanced by Polarization Transfer (INEPT), heteronuclear single quantum coherence, and heteronuclear multiple quantum coherence (HMQC) generate specific coherence orders during different times during the pulse sequence (see Chapters 24 and 26). Coherence order specificity is achieved with either pulsed magnetic field gradients, discussed later, or phase cycling of the radio frequency (rf) pulses and receiver, discussed in this chapter. We follow the treatment by Keeler (2010).

Selection of coherence order pathways with phase cycling is achieved by destructive interference of undesired NMR coherence orders and by constructive interference of desired NMR coherence orders. It is based on the different responses of different coherence orders to rf pulses, illustrated in *phaseshift.nb*. Changing the phase of an rf pulse by ϕ radians in the rotating frame causes a phase change of $-\Delta p\ \phi$ of the coherence produced, where Δp is the change in coherence order of the density operator component due to the pulse. This allows design of experiments that take advantage of destructive and constructive interference. If one ignores NMR relaxation that returns the density operator to thermal equilibrium ($p = 0$), *only rf pulses can cause changes in coherence order*. The coherence order does not change during periods of “free evolution” without rf pulses.

The first step in designing an NMR pulse sequence is to draw out the desired coherence order pathways, illustrated in Figure 27.1 for the homonuclear double quantum 2D experiment.[1]

Once one has identified the desired coherence order pathways, one implements the rules in Table 27.1 to select them.

---

[1] This is NOT the same as the DQF-COSY experiment.

A Primer of NMR Theory with Calculations in Mathematica®, First Edition. Alan J. Benesi.

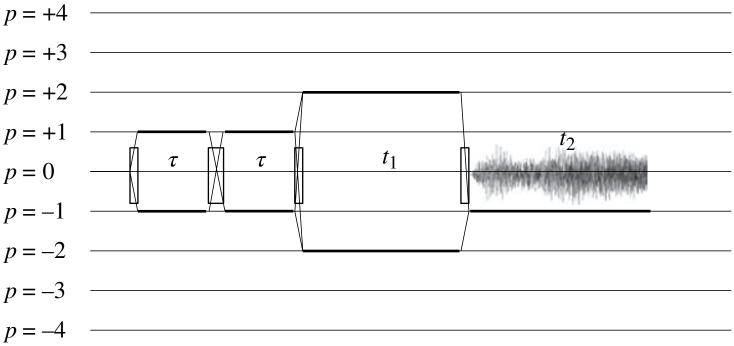

Figure 27.1 Desired coherence levels for the homonuclear double quantum 2D experiment (Mareci and Freeman, 1983). The coherence order is designated by the p level. For compactness, the pulses and resulting NMR signal (after the full phase cycle) have been placed on the $p=0$ coherence level, and the desired coherence orders during the pulse sequence have been highlighted with heavy black horizontal lines. The wider vertical rectangle represents a π pulse. The narrower vertical rectangles represent $\pi/2$ pulses.

The coherence order pathways in the homonuclear double quantum pulse sequence are $\mathbf{p}=\{0,+1,-1,+2,-1\}$, $\{0,+1,-1,-2,-1\}$, $\{0,-1,+1,+2,-1\}$, and $\{0,-1,+1,-2,-1\}$. From these, we can construct the $\Delta\mathbf{p}$ vectors $\{+1,-2,+3,-3\}$, $\{+1,-2,-1,+1\}$, $\{-1,+2,+1,-3\}$, and $\{-1,+2,-3,+1\}$. After the first pulse, we want both the $p=+1$ and $p=-1$ coherences. Since both coherences are created by the first $\pi/2$ pulse, there is no need to phase cycle the first pulse. The 180° pulse simply switches $p=+1$ to $p=-1$ and vice versa and also removes the effect of the shift Hamiltonian over the 2τ interval as discussed in *echooneortwo.nb*. The first three pulses can be "grouped" to generate $p=+2$ and $p=-2$ coherence with an N value of 4 so that $p=1$, 0, and -1 coherences are suppressed and the $p=+2$ and $p=-2$ coherences are retained. The resulting simplified $\Delta\mathbf{p}$ vectors for the group of three pulses and the last pulse are $\{+2,-3\}$ and $\{-2,+1\}$.

The phase cycle for the group of three pulses is $\phi_{\mathrm{grp}}=\{0,\pi/2,\pi,3\pi/4\}$. The last pulse does not need to be phase cycled since only $p=-1$ coherence is observable, so we arbitrarily choose $\phi_4=\{0\}$. The receiver phase cycle, $\phi_{\mathrm{rcvr}}=\{0,\pi,0,\pi\}$ is calculated in *phasecycle.nb*. As shown in *double_quantum_poma.nb*, this unfortunately allows for "passive" double quantum correlations such as spin 1 oscillating during the $t1$ interval at the sum of the spin 2 and spin 3. The desired "active" double quantum correlations for spin 1 occur at the sum of the spin 1 and spin 2 or at the sum of spin 1 and spin 3 chemical shifts. The passive couplings, which arise from higher-order coherences present during the t_1 interval, can be suppressed by using an $N=8$ (45°) additional phase increment for ϕ_{grp} for each increment in $t1$. The calculations in *double_quantum_poma.nb* show that the complexity grows exponentially with the number of coupled spins.

The desired coherence transfer pathway for the double quantum filtered correlation spectroscopy (DQF-COSY) coherence transfer experiment discussed in the previous chapter is shown in Figure 27.2.

TABLE 27.1 Rules for the design of NMR pulse sequences with phase cycles

1. Since changing the phase of an rf pulse by ϕ radians in the rotating frame causes a phase change of $-\Delta p\ \phi$ in the coherence produced, it is most convenient to adjust the *receiver* phase ϕ_{rcvr} to select the desired pathway. In this way, the pulse phases can be implemented independently of each other. Later the pulse phases can be normalized to constant receiver phase if desired.

$$\phi_{\text{rcvr}} = -\Delta\mathbf{p}\cdot\boldsymbol{\phi}_{\mathbf{RF}} \tag{27.1}$$

   where $\Delta\mathbf{p} = \{\Delta p_{1,}\ \Delta p_{2,}\ \Delta p_{3,}\ \ldots,\ \Delta p_n\}$ is a vector of the desired coherence order changes and $\phi_{\mathbf{RF}} = \{\phi_1, \phi_2, \phi_3, \ldots, \phi_n\}$ is a vector of the corresponding pulse phases.
2. The phase cycle *for a particular pulse in the sequence* is chosen such that the phase increments are $2\pi/N$, where N is the desired difference in coherence order between adjacent desired levels produced by the pulse. All N rf phases are given in the full phase cycle for the pulse.
3. The coherence order for the observed nucleus must end on $p=-1$ during the acquisition time t_2 (see Chapter 18). This also means that $\sum_i \Delta p_i = -1$ for the observed nucleus.
4. The coherence order for other nuclei than the observed nucleus must end on $p=0$, hence $\sum_i \Delta p_i = -0$ for the other nuclei.
5. The effect of a 180° pulse on coherence order is to change its value from positive to negative or negative to positive (e.g., from $p=+1$ to $p=-1$ or $p=-2$ to $p=+2$).
6. To obtain absorption peaks in the f_1 dimension of a 2D or 3D NMR experiment, the desired $p=+n$ and $p=-n$ coherence orders must *both* be present during the t_1 evolution interval.
7. Cycle the phase of each pulse independently of the other pulse phases, that is, hold all other pulse phases constant.
8. The first pulse, since it usually applied to $p=0$, generates both $p=+1$ and $p=-1$ coherence. Phase cycling is not needed unless only one of the two is desired.
9. If an unambiguous pathway has been selected before the last pulse, no phase cycling is required. Only the $p=-1$ coherence is observable even if other coherence orders are present.
10. If a group of pulses is supposed to produce a specific Δp, the entire group can be phase cycled together.[a]
11. For $I=1/2$ nuclei, the maximum coherence order possible is determined by the number of different coupled nuclei in the spin system, since at least n coupled $I=1/2$ nuclei are needed to create n-quantum coherence. For quadrupolar nuclei with $I>1/2$ where there are $2I+1$ energy levels, it is possible to create n-quantum coherence for one nucleus if $n \leq 2I$.
12. Additional phase cycling of the preparation pulses preceding the t_1 interval, with phase increments applied for successive t_1 increments, can be used to suppress undesired coherence orders during t_1 evolution.[b]
13. Pulse sequence delays allow T_1 relaxation and regeneration of $p=0$ (I_z) density operator components. Usually, this occurs during the t_1 evolution of a 2D NMR sequence. To suppress these unwanted coherences, an additional phase cycle is used for the last pulse (or group of pulses) before the t_1 interval of $\{0,\pi\}$ with the same additional $\{0,\pi\}$ phase cycle for the receiver. This is called *axial suppression*.
14. CYCLOPS adds an additional phase cycle of $\{0,\pi/2,\pi,3\pi/2\}$ simultaneously to pulse phases and the receiver phase to suppress electronic imbalance in the pulse and receiver phases.

---

[a] In some cases, it is necessary to have different pulses of a group of pulses maintain a fixed phase difference.

[b] See Bruker pulse sequences such as dqsph.

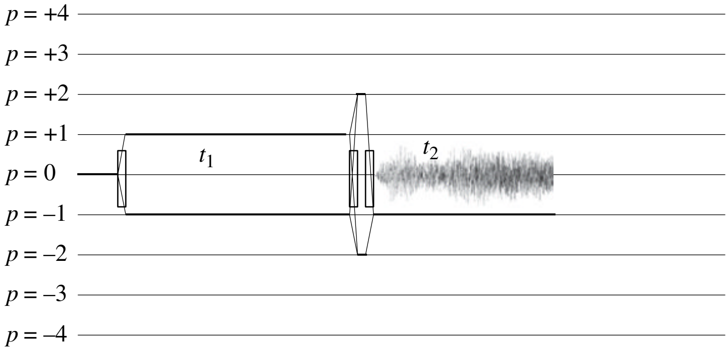

Figure 27.2 Desired coherence levels for the double quantum filtered COSY (DQF-COSY) experiment (Derome and Williamson, 1990). The coherence order is designated by the p level. For compactness, the pulses and resulting NMR signal (after the full phase cycle) have been placed on the $p=0$ coherence level and the desired coherence orders during the pulse sequence have been highlighted with heavy black horizontal lines. The vertical rectangles represent $\pi/2$ pulses.

In this case, there are just three 90° rf pulses. We can group the first two pulses and use $N=4$ to select $p=+2$ and $p=-2$ coherence after the 2'd pulse. There is no need to phase cycle the last pulse. The phase cycle for the group of two pulses is $\phi_{\text{grp}}=\{0,\pi/2,\pi,3\pi/4\}$, identical to that for the double quantum experiment. The last pulse does not need to be phase cycled since only $p=-1$ coherence is observable. We arbitrarily choose $\phi_{\text{last}}=\{0,0,0,0\}$. This yields the same receiver phase cycle, $\phi_{\text{rcvr}}=\{0,\pi,0,\pi\}$, as for the double quantum 2D experiment (see *phasecycle.nb*).

After completion of the phase cycle, the density operator immediately after the last pulse contains pure antiphase coherence of a given spin with respect to itself or one of its J-coupling partner spins (see *double_quantum_poma.nb*). Additional $N=4$ phase cycling of the first pulse phase with successive t_1 increments is used to suppress higher-order coherence that could be created after the second pulse. There are no passive couplings that need to be suppressed. The diagonal peaks in the resulting 2D spectrum represent coherences that oscillate at their own shifts during both the t_1 and t_2 intervals, while the cross peaks represent coherences that oscillate at their own shifts during t_1 and their coupling partner's shift during t_2. See the DQF-COSY 2D spectrum in Chapter 26 (Figure 26.5).

The 2D homonuclear Overhauser experiment has the desired coherence order transfer pathway shown in Figure 27.3. It reveals pairs of spins that are close enough in space (typically 5Å or less) to experience dipolar cross relaxation during the mixing time τ_{mix}.

The first $\pi/2$ pulse does not need to be phase cycled to create the desired $p=\pm1$ coherence pathways. The second pulse does not need to be phase cycled to create $p=0$, so $N=1$. The last pulse does not need to be phase cycled because only $p=-1$ coherence is observable. The calculated phases for the three

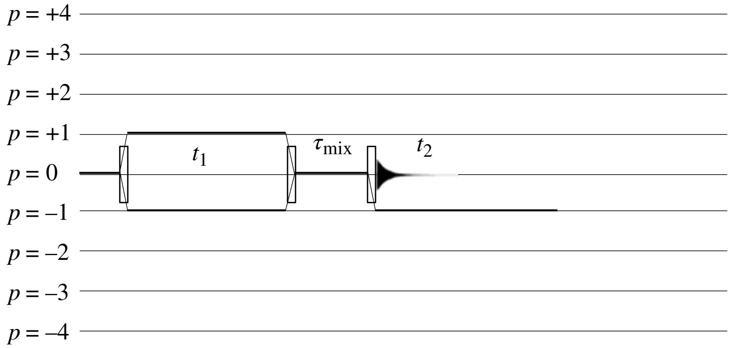

Figure 27.3 Desired coherence levels for the homonuclear overhauser experiment spectroscopy (NOESY) 2D experiment (Jeener et al., 1979). The coherence order is designated by the p level. For compactness, the pulses and resulting NMR signal (after the full phase cycle) have been placed on the $p=0$ coherence level and the desired coherence orders during the pulse sequence have been highlighted with heavy black horizontal lines. The vertical rectangles represent $\pi/2$ pulses.

pulses and receiver are (see *phasecycle.nb*) $\phi_1=\phi_2=\phi_3=\phi_{\text{rcvr}}=\{0\}$. $N=4$ phase incrementation of ϕ_1 for successive t_1 increments is used to suppress the contribution of $p=0$ longitudinal order terms arising from higher-order coherence after the second pulse.

Axial suppression modifies the phase cycle to $\phi_1=\{0,\pi\}$, $\phi_2=\phi_3=\{0,0\}$, and $\phi_{\text{rcvr}}=\{0,\pi\}$. Quadrature phase cycling in addition to axial yields $\phi_1=\{0,\pi,\pi/2,3\pi/2,\pi,0,3\pi/2,\pi/2\}$, $\phi_2=\phi_3=\{0,0,\pi/2,\pi/2,\pi,\pi,3\pi/2,3\pi/2\}$, and $\phi_{\text{rcvr}}=\{0,\pi,\pi/2,3\pi/2,\pi,0,3\pi/2,\pi/2\}$. The NOESY experiment relies on the phenomenon of dipolar cross relaxation to yield correlations between observed spins. The dipolar cross relaxation rates between nuclear spins depend on the identity (usually ^{1}H) of the nuclei and the lengths and rates of reorientation of the internuclear vectors between dipolar coupled spins. For ^{1}H nuclei, the $1/r^6$ dependence limits NOESY cross peaks to H atoms less than about 5Å apart. Because the NOESY cross peaks are very small, it is necessary to minimize artifacts in the 2D spectrum. One of the best methods to do this is with additional gradient selection of the desired coherence orders as described in the next chapter.

The desired coherence order transfer pathways for the heteronuclear multiple quantum 2D experiment are shown in Figure 27.4.

Neither the first $\pi/2$ ^{1}H pulse nor the second π ^{1}H pulse needs to be phase cycled. The first and second ^{13}C $\pi/2$ pulses are grouped to generate $p=0$. This pair of pulses uses $N=2$ to suppress undesired $p=\pm1$ ^{13}C coherences. The ^{1}H Δp vectors are $\{+1,-2\}$. The desired ^{13}C Δp vector is $\{0\}$ for the two grouped ^{13}C pulses. The phase cycle for first ^{1}H pulse is $\phi_1=\{0,0\}$. The phase cycle for the grouped ^{13}C pulses is $\phi_{\text{grp}}=\{0,\pi\}$. The phase cycle for the ^{1}H π pulse is $\phi_2=\{0,0\}$. The calculated receiver cycle is $\phi_{\text{rcvr}}=\{0,0\}$. Adding axial suppression yields $\phi_1=\{0,0,\pi,\pi\}$, $\phi_{\text{grp}}=\{0,\pi,0,\pi\}$, $\phi_2=\{0,0,0,0\}$, and $\phi_{\text{rcvr}}=\{0,0,\pi,\pi\}$.

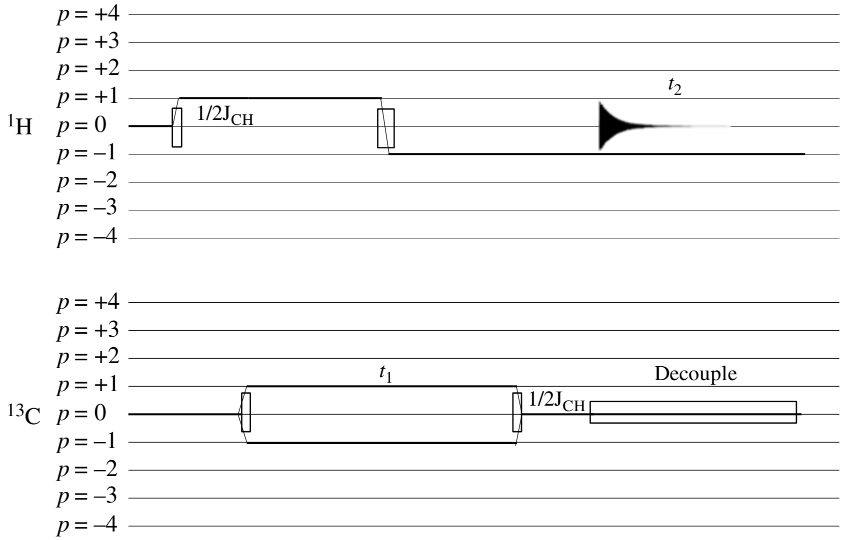

Figure 27.4 Desired coherence levels for the HMQC 2D experiment (Bax et al., 1983). The coherence order is designated by the p level. For compactness, the pulses and resulting NMR signal (after the full phase cycle) have been placed on the $p = 0$ coherence levels and the desired coherence orders during the pulse sequence have been highlighted with heavy black horizontal lines. The narrow vertical rectangles represent $\pi/2$ pulses. The thick vertical rectangle represents a π pulse.

EXPLANATION OF *phaseshift.nb*

The user is told to evaluate *shortspin.nb*, then close it without saving changes. The ar[$\pi/2$, 0, mh iza] command gives a $\pi/2$ rf pulse of phase 0 (x) to the equilibrium density operator mh iza for the a spin. The ar[$\pi/2$, ϕ, mh iza] hits the equilibrium density operator with a $\pi/2$ rf pulse of phase ϕ. The mq command shows that the resulting density operator consists exclusively of single quantum $p = 1$ and $p = -1$ coherences that each have a cos[ϕ] or sin[ϕ] dependence.

Next, $\pi/2$ pulses of phase 0 and ϕ are given to the Cartesian form of the density operator mh iplusa. Remember that % and %% refer to the preceding output and the preceding to the preceding outputs, respectively, so both refer to ixa mh + i iya mh. The built-in Mathematica function TrigReduce is used to simplify the results, and mq is used to express the results in terms of iplusa, imina, and iza. The results show that there is no phase shift for the iplusa produced ($\Delta p = 0$), a phase shift of ϕ for the iza produced ($\Delta p = -1$), and a phase shift of 2ϕ for the imina produced ($\Delta p = -2$).

The next cells show what happens when $\pi/2$ pulses of phase 0 and ϕ are given to both the a and x spins of the density operator 2 mh iza izx. The mq and trig functions, along with the built-in Mathematica function TrigToExp, show that changing the pulse phase by ϕ produces a net phase change of $-\Delta p\ \phi$.

EXPLANATION OF *phasecycle.nb*

This notebook shows how Mathematica can be used to implement Equation 27.1 and Table 27.1 to calculate the phase cycle needed for the double quantum 2D experiment. In the double quantum 2D experiment, the first three rf pulses are grouped, so the desired $\Delta\mathbf{p}$ vectors for the experiment are $\Delta p_{\text{grp1}} = \{+2,-3\}$ and $\Delta p_{\text{grp2}} = \{-2,+1\}$. An $N=4$ "mask" is used to select the $p=+2$ and $p=-2$ pathways simultaneously during $t1$ evolution. Therefore, the phase "vector" for the grouped pulses is $\phi\text{grp} = \{0,\pi/2,\pi,3\pi/2\}$ in radians $= \{0,90,180,270\}$ in degrees. Notice how the built-in Mathematica functions table and mod are used to obtain this result. The phase of the last pulse does not matter, so we arbitrarily choose $\phi\text{last} = \{0,0,0,0\}$.

The receiver phase cycles are calculated using Equation 27.1, Δp_{grp1} and Δp_{grp2} to give $\phi_{\text{recvrgrp1}} = \phi_{\text{recvrgrp2}} = \{0,\pi,0,\pi\}$. Since both the $p=+2$ and $p=-2$ coherence order pathways are selected with the same phase cycle, both pathways can be selected simultaneously.

The phase vectors can be easily converted to constant receiver phase 0 as shown for ϕ_{grp1norm} and ϕ_{lastnorm}.

The receiver phase cycle can also be calculated using the phase cycles for the individual rf pulses. This yields the same result as the "grouped" approach.

The next cells calculate the receiver phase cycle needed for the NOESY 2D experiment. The two desired $\Delta\mathbf{p}$ vectors are $\Delta p_1 = \{+1,-1,-1\}$ and $\Delta p_2 = \{-1,+1,-1\}$. The three phase cycles are $\phi 1 = \phi 2 = \phi 3 = \{0,0,0,0\}$. The resulting $\phi_{\text{rcvr}} = \{0,0,0,0\}$. Using a mask of $N=2$ for the second pulse results in a different $\phi_{\text{rcvr}} = \{0,\pi,0,\pi\}$. Both variations of the experiment should work.

EXPLANATION OF *double_quantum_poma.nb*

The user should exit Mathematica, then restart a fresh session. Then evaluate *poma.nb* and close it without saving changes.

The spin system is homonuclear and J-coupled, for example, two J-coupled ^{1}H spins in a small molecule. The equilibrium density operator is defined simply as spin[1,z] + spin[2,z], to which is given the double quantum pulse sequence derived according the rules for selecting second-order coherence pathways. The resulting density operator immediately prior to the acquisition interval t_2 is pure antiphase single quantum coherence, but *note that the time dependence is* $\cos[t_1 w_1 + t_1 w_2]$*, that is, at the sum of the coupled chemical shifts!*

The next cells show the more complicated t_2 time dependence.

Then three coupled spins are considered, each of which is coupled to the others, and the density operator gets much more complicated. For example, there are now observable signals for spin 1 that oscillate at $w_1 + w_2$ and $w_1 + w_3$ as expected, but also at $w_2 + w_3$. The $w_2 + w_3$ term represents a "passive" coupling cross peak. Extra $N=8$ phase cycling is needed to suppress such peaks since they arise from triple quantum coherence.

The next cells show that the same basic phase cycling used in the double quantum 2D experiment also works for the DQF-COSY 2D experiment. In this experiment, the phases of the first two pulses are grouped. Again, the results for three coupled spins show that the basic phase cycle allows triple quantum coherence to appear in the density operator. Further phase cycling is needed to suppress it.

HOMEWORK

Homework 27.1: Use *shortspin.nb* and/or *poma.*nb to verify that all of the preceding pulse sequences work with the calculated phase cycling.

Homework 27.2: Add: (i) axial suppression phase cycling, (ii) quadrature phase cycling, and (iii) devise a useful increment in phase for successive t_1 values.

CHAPTER 28

SELECTION OF COHERENCE ORDER PATHWAYS WITH PULSED MAGNETIC FIELD GRADIENTS

Although high-resolution NMR requires homogeneous magnetic fields, many modern NMR spectrometers are equipped with probes and amplifiers designed to deliver precisely controlled pulsed magnetic field gradients. These are achieved by adding coils to the probe and turning on DC currents through the coils when magnetic field gradients are required. The purpose of these pulsed magnetic field gradients is to *spatially encode* the observed resonance frequencies. This is illustrated in Figure 28.1.

It is the spatial encoding of resonance frequency (i.e., the Zeeman Larmor frequency) in the presence of linear x, y, and z magnetic field gradients that is the basis of magnetic resonance imaging. More importantly in the context of this chapter, gradients can also be used to select specific coherence order pathways in NMR pulse sequences and to measure translational diffusion coefficients.

In high-resolution NMR experiments, pulsed magnetic field gradients are used to cause dephasing and destructive interference of resonances due to the variation of frequency and phase across the NMR sample. A single pulsed magnetic field gradient of sufficient strength can totally eliminate the NMR signal, as shown in Figure 28.2a. Exact but opposite pulsed gradients applied sequentially restore the NMR signal since the opposite polarity gradient pulse exactly "undoes" the dephasing caused by first gradient pulse, Figure 28.2b. The NMR signal can also be restored by changing the sign of the coherence order with a π pulse after the first gradient pulse, Figure 28.2c, then applying the same polarity and magnitude of gradient pulse.

The amount of dephasing θ in rad m^{-1} caused by a pulsed magnetic field gradient of duration t_g is given by (Hull, 1994)

$$\theta = \gamma\, g\, t_g\, p \tag{28.1}$$

where γ is the gyromagnetic ratio of the nucleus in rad s^{-1} Tesla^{-1}, g is the gradient strength in Tesla m^{-1}, t_g is the duration of the gradient pulse in s, and p is the desired coherence order.

A Primer of NMR Theory with Calculations in Mathematica®, First Edition. Alan J. Benesi.

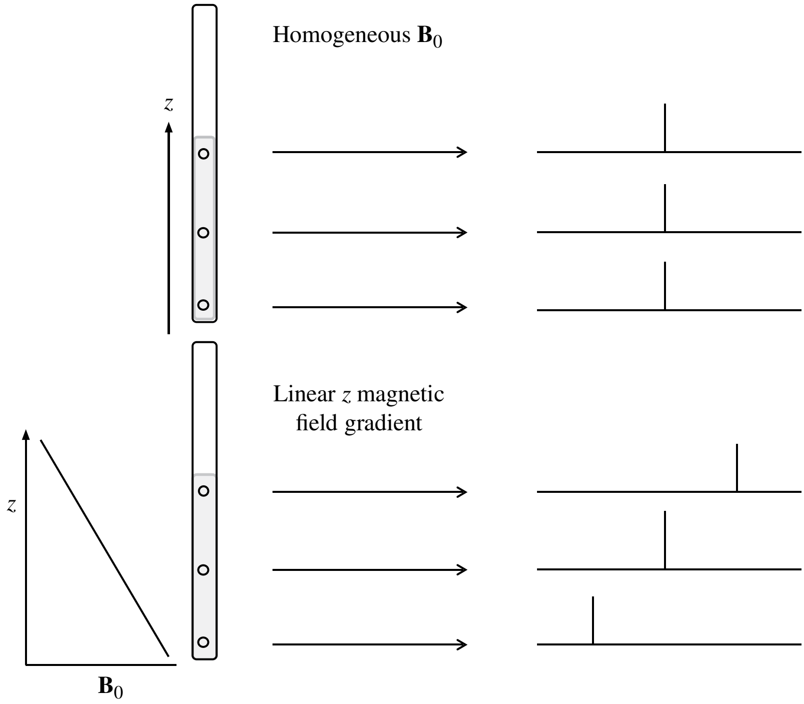

Figure 28.1 Spatial encoding in a magnetic field gradient (For convenience, the peaks in the presence of the magnetic field gradient are shown as positive and phased. In reality, the phase of the peak as well as the frequency will depend on position.) In a homogeneous magnetic field $\mathbf{B}_0$, an NMR resonance occurs at the same frequency for every position in the sample. In the presence of a linear z magnetic field gradient, the frequency of an NMR resonance reflects its z position. For convenience, the peaks in the presence of the magnetic field gradient are shown as positive and phased. In reality, the phase of the peak as well as the frequency will depend on its z position.

The pulsed magnetic field gradients are given during periods of free precession when there are no radio frequency (rf) pulses. Any gradient shape can be used as long as it is reproducible. To account for the variation of the amplitude $g(t)$ during the gradient pulse, that is, the gradient shape, the effective gradient strength G of the gradient pulse in Tesla m^{-1} is calculated:

$$G = \int_0^{t_g} g(\tau)d\tau \tag{28.2}$$

The dephasing in rad m^{-1} is then

$$\theta = \gamma G p \tag{28.3}$$

The rule used to select coherence orders with pulsed magnetic field gradients is based on the *rephasing* necessary to form gradient echoes shown in Figures 28.2b and 28.2c:

$$\sum_i \gamma_i G_i p_i = 0 \tag{28.4}$$

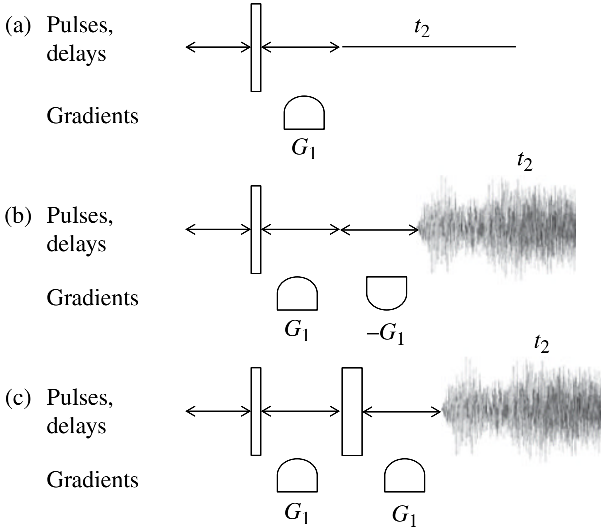

Figure 28.2 Effects of Pulsed Magnetic Field Gradients on NMR Signals. (a) Effect of a single gradient pulse (b) Effect of equal but opposite polarity gradients (c) Effect of equal gradients bracketing a 180 (π) pulse.

where i covers *all* nuclei in the desired coherence pathway and *all* gradient pulses.

Several examples of gradient-selected 2D NMR experiments are discussed later. The gradient-selected correlation spectroscopy (COSY) 2D experiment is shown in Figure 28.3.

The exact placement of the gradient pulses in the free precession periods is not important, although the correct gradient must occur during the correct free precession period. To select the solid coherence order pathway, $\mathbf{p}=\{0,+1,-1\}$, use the gradient ratio $G_1/G_2=1$ during the first and second precession periods. The $p=1$ to $p=-1$ coherence order change is called the "echo" or "N" type pathway. To select the $\mathbf{p}=\{0,-1,-1\}$ dotted coherence order pathway, use the gradient ratio $G_1/G_2=-1$. The $p=-1$ to $p=-1$ coherence order change is called the "antiecho" or "P" type pathway (Ernst et al., 1987). Because one of the gradient pulses occurs during the t_1 interval, it is not possible to select both the $p=1$ and $p=-1$ coherence orders simultaneously. For this reason, the resulting 2D spectrum is not phase sensitive. A second drawback of this experiment is that the signal intensity is reduced by a factor of $\sqrt{2}$ because only one of the two possible coherence order pathways yields an NMR signal.

The advantage of the gradient selection technique is that no phase cycling is required. This allows the total suppression of large signals in ^{1}H–^{13}C 2D experiments such as the heteronuclear multiple quantum coherence (HMQC) of natural abundance samples, where about 99% of the carbon is unobservable ^{12}C ($I=0$) and only 1% is observable ^{13}C ($I=1/2$). This means that the 99% of the ^{1}H signal (for H bonded to ^{12}C) must be suppressed in the HMQC. If only phase cycling is used, huge ^{1}H signals are acquired in each scan of the phase cycle. Imperfect destructive interference of these large signals often yields artifacts. Gradient selection suppresses the large signals in every scan, allowing the smaller desired signals to undergo more amplification,

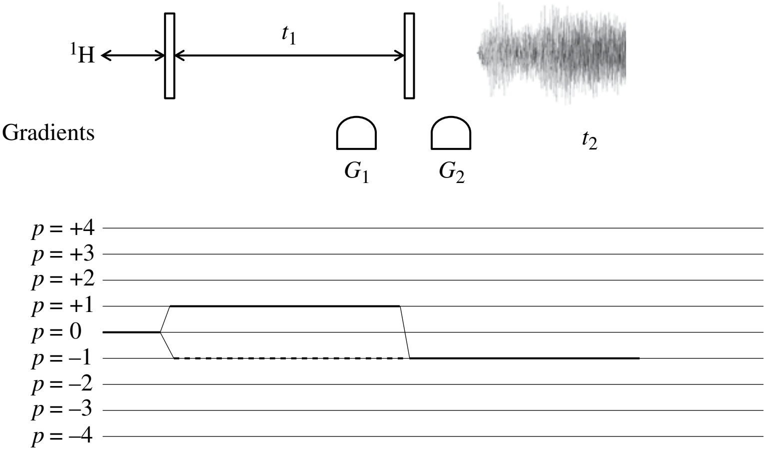

Figure 28.3 Desired Coherence Levels for the Gradient-Selected COSY Experiment, showing its relation to the rf pulses and pulsed magnetic field gradients. The coherence order is designated by the p level. The vertical rectangles represent $\pi/2$ rf pulses.

thereby reducing artifacts. The best quality 2D spectra are obtained using a combination of gradient and phase cycle selection.

The gradient-selected double quantum filtered (DQF) COSY experiment is shown in Figure 28.4.

We solve for G_1, G_2, and G_3 as follows (Eq. 28.4):

$$\gamma_H G_1(+1) + \gamma_H G_2(+2) + \gamma_H G_3(-1) = 0$$

Dividing both sides by γ_H yields $G_1 + 2G_2 - G_3 = 0$. One solution is $G_1 = +1$, $G_2 = +1$, and $G_3 = +3$. The gradient strengths are in arbitrary units. Again, the drawbacks are the loss of signal intensity and the lack of phase sensitivity. The advantage is the destruction of unwanted coherence pathways with each scan.

The heteronuclear gradient-selected HMQC 2D experiment is shown in Figure 28.5.

We solve for G_1, G_2, and G_3 as follows (Eq. 28.4):

$$\gamma_H G_1(+1) + \gamma_C G_1(+1) + \gamma_H G_2(-1) + \gamma_C G_2(+1) + \gamma_H G_3(-1) + \gamma_C G_3(0) = 0$$

Dividing both sides by γ_C, and using $\gamma_H/\gamma_C = 3.98$, this becomes as follows:

$$4.98G_1 - 2.98G_2 - 3.98G_3 = 0$$

One solution is $G_1 = +100$, $G_2 = +60$, and $G_3 = +80.2$. The disadvantages and advantage are the same as for the previous two examples.

Higher-quality 2D and 3D spectra can be obtained with a combination of phase cycle selection and gradient selection. Changing the sign of one or more of the gradient(s) used, or using cleverly placed π pulses to allow for "echo–antiecho" processing that is used to detect both coherence pathways during the t_1 interval, allows for full signal intensity and pure absorption mode peaks (Jacobsen, 2007).

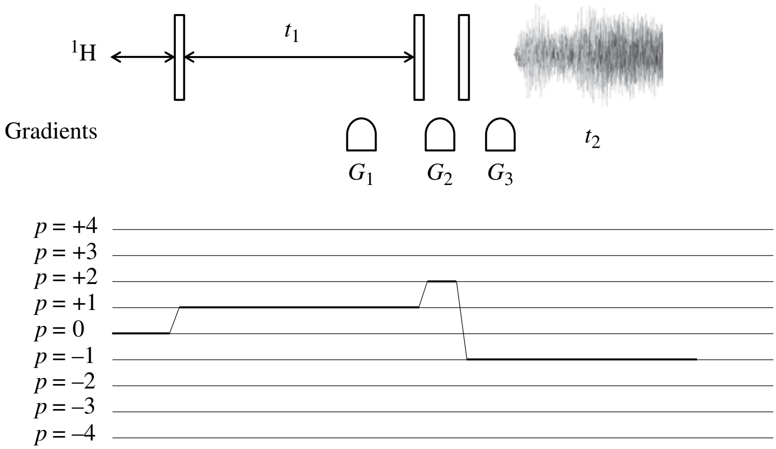

Figure 28.4 Desired Coherence Levels for the Gradient-Selected DQF-COSY Experiment, showing their relation to the rf pulses and magnetic field gradients. The coherence order is designated by the p level. The vertical rectangles represent $\pi/2$ rf pulses.

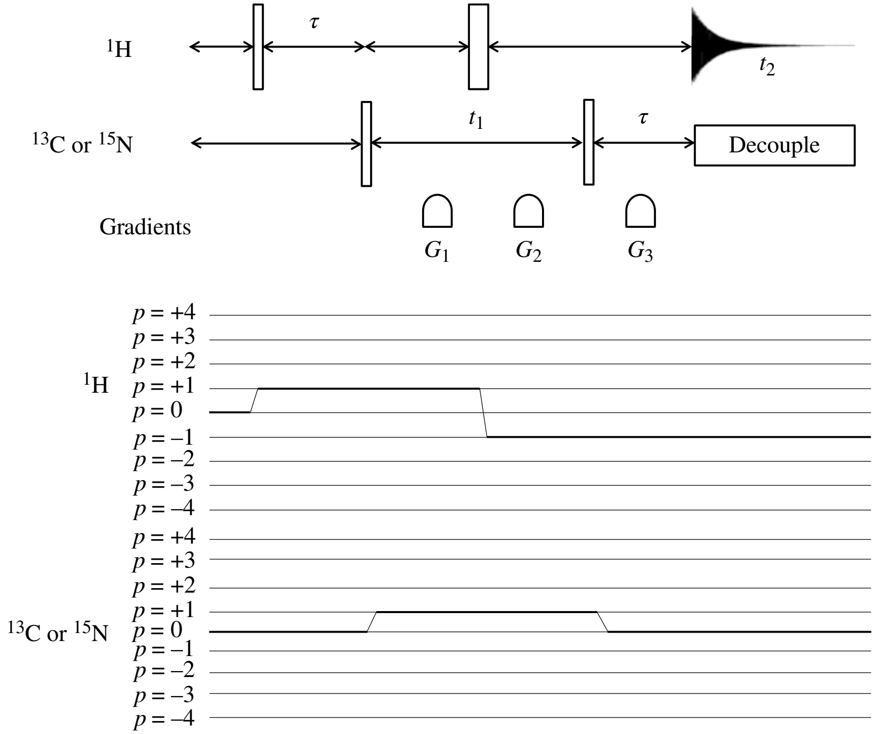

Figure 28.5 Desired Coherence Levels for The Gradient-Selected HMQC Experiment and their relation to the rf pulses and magnetic field gradients. The thin vertical rectangles represent $\pi/2$ rf pulses. The thick vertical rectangle represents a π rf pulse.

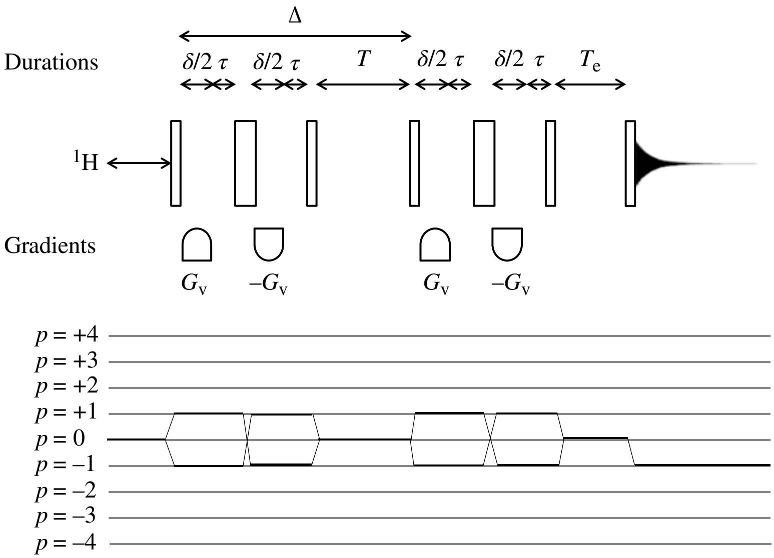

Figure 28.6 Desired Coherence Levels for The BPP-LED Pulse Sequence used to measure translational diffusion coefficients (Wu et al., 1995), showing their relation to the rf pulses and magnetic field gradients. The thin vertical rectangles represent $\pi/2$ rf pulses. The thick vertical rectangles represent π rf pulses.

Gradient pulses are also extremely useful for the measurement of translational diffusion. The bipolar pulse pair longitudinal eddy current delay (BPP-LED) pulse sequence for measurement of translational diffusion coefficients is shown in Figure 28.6.

The first $\pi/2$ pulse creates both $p=1$ (solid line) and $p=-1$ coherence (dashed line). The first positive gradient pulse G_v causes *dephasing* of this coherence. The first π pulse switches $p=1$ to $p=-1$ coherence and vice versa. The second (negative) gradient pulse $-G_v$ therefore causes further *dephasing* of the coherence. This combination of rf and gradient pulses constitutes the bipolar pulse pair (BPP). The combination of equal positive and negative gradient pulses significantly reduces artifacts in the spectra. Translational diffusion and T_2 relaxation occur throughout the BPP. The next $\pi/2$ pulse converts *both* the $p=1$ and $p=-1$ coherence levels to $p=0$ coherence (with appropriate phase cycling), and translational diffusion is allowed to during the relatively long interval of time T before *rephasing* brought about by the second BPP. During the time T only T_1 relaxation occurs. This helps conserve the NMR signal because the T_1 relaxation rate is less than or equal to the T_2 relaxation rate. Rephasing and formation of a gradient echo requires that the second BPP have the opposite phase coherence pathway than the first. Thus, as indicated in the Figure 28.6, if the first BPP is $p=0 \rightarrow +1 \rightarrow -1$, the second must be $p=0 \rightarrow -1 \rightarrow +1$. For this pathway, the gradient echo requires

$$\gamma_H G_V(+1)+\gamma_H(-G_V)(-1)+\gamma_H G_V(-1)+\gamma_H(-G_V)(+1)=0$$

The other pathway must have

$$\gamma_H G_V(-1) + \gamma_H(-G_V)(+1) + \gamma_H G_V(+1) + \gamma_H(-G_V)(-1) = 0$$

The fourth $\pi/2$ pulse converts the coherence ($p=1$ or $p=-1$) to $p=0$ to allow for a short "settling" time of residual eddy currents induced by the application of the pulsed magnetic field gradients.

The BPP-LED pulse sequence is usually run as a 2D NMR experiment with 16 or more rows corresponding to different values of G_v. There is no variation in time of any of the intervals, so there are no relaxation effects of T_2 or T_1, only variation in the strength of the pulsed magnetic field gradient G_v. Only translational diffusion attenuates the observed signal intensities as G_v is varied.

The peak intensities and peak integrals vary as (Wu et al., 1995)

$$S(q) = S(0) \times e^{\left[-Dq^2\left(\Delta - \frac{\delta}{3} - \frac{\tau}{2}\right)\right]} \tag{28.5}$$

where D is the translational diffusion coefficient obtained by best fit of the experimental data, $q = \gamma G_v \delta$, γ is the gyromagnetic ratio of the observed nucleus, δ is the sum of the durations of the two gradient pulses during the BPP (see Fig. 28.6), τ is a short delay for electronic recovery, and G_v is the gradient amplitude for the given row of the 2D spectrum (Eq. 28.3).

HOMEWORK

Homework 28.1: What rf phase cycle should be used for the BPP-LED phase cycle to suppress unwanted coherence pathways and relaxation artifacts?

CHAPTER 29

HAMILTONIANS OF NMR: ANISOTROPIC SOLID-STATE INTERNAL HAMILTONIANS IN RIGID SOLIDS

Each individual nuclear spin has its own specific internal Hamiltonians that determine its evolution in spin space during pulse sequences and its observed frequency relative to the resonance frequency ν_0 in the spectrum. Each of these nuclear spin Hamiltonians has a *principal axis system (PAS) that is fixed for rigid solids with respect to a molecule-fixed reference frame.*[1] This connection provides information about the chemical environment of the nucleus as well as the reorientational dynamics of the molecule. In this chapter, we focus on the Hamiltonians of rigid solids, where reorientational dynamics are too slow to affect the observed spectrum. This is the case for many solids at room temperature. The internal Hamiltonian operators of rigid solids can be represented as Cartesian tensors. The definitions are based on those of Mehring and the numerical simulation program Gamma (Mehring, 2002, pp. 2585–2602).[2,3]

$$\begin{aligned}\hat{\mathrm{H}}_{\mathrm{int}} &= \hat{\mathrm{I}}\cdot\overline{\overline{\mathrm{A}}}(\mathrm{lab})\cdot\hat{\mathrm{O}} = (\hat{\mathrm{I}}_x \quad \hat{\mathrm{I}}_y \quad \hat{\mathrm{I}}_z)\cdot\begin{pmatrix}\mathrm{A}_{xx} & \mathrm{A}_{xy} & \mathrm{A}_{xz}\\ \mathrm{A}_{yx} & \mathrm{A}_{yy} & \mathrm{A}_{yz}\\ \mathrm{A}_{zx} & \mathrm{A}_{zy} & \mathrm{A}_{zz}\end{pmatrix}\cdot\begin{pmatrix}\hat{\mathrm{O}}_x\\ \hat{\mathrm{O}}_y\\ \hat{\mathrm{O}}_z\end{pmatrix}\\ &= \mathrm{A}_{xx}\hat{\mathrm{I}}_x\hat{\mathrm{O}}_x + \mathrm{A}_{xy}\hat{\mathrm{I}}_x\hat{\mathrm{O}}_y + \mathrm{A}_{xz}\hat{\mathrm{I}}_x\hat{\mathrm{O}}_z + \mathrm{A}_{yx}\hat{\mathrm{I}}_y\hat{\mathrm{O}}_x + \mathrm{A}_{yy}\hat{\mathrm{I}}_y\hat{\mathrm{O}}_y\\ &\quad + \mathrm{A}_{yz}\hat{\mathrm{I}}_y\hat{\mathrm{O}}_z + \mathrm{A}_{zx}\hat{\mathrm{I}}_z\hat{\mathrm{O}}_x + \mathrm{A}_{zy}\hat{\mathrm{I}}_z\hat{\mathrm{O}}_y + \mathrm{A}_{zz}\hat{\mathrm{I}}_z\hat{\mathrm{O}}_z\end{aligned} \tag{29.1}$$

where $\hat{\mathrm{I}}$ is a nuclear spin operator in spin space; $\overline{\overline{\mathrm{A}}}(\mathrm{lab})$ is the Cartesian interaction tensor in the real space laboratory frame; and $\hat{\mathrm{O}}$ may be a magnetic field (real space

---

[1] In rigid solids, the internal Hamiltonians for all of the nuclear spins are constant during the course of the NMR experiment.

[2] Notes on spherical tensors, program Gamma. Program Gamma is an extremely powerful numerical simulation program.

[3] There are minor differences in the definitions used. These are tested in the Mathematica notebook *solid_hamiltonians.nb* and corrected accordingly.

A Primer of NMR Theory with Calculations in Mathematica®, First Edition. Alan J. Benesi.

and spin space), nuclear spin operator (spin space), or molecular angular momentum operator (real space). See *solid_hamiltonians.nb*.

If $\|\hat{\mathrm{H}}_{\mathrm{int}}\| \ll \|\hat{\mathrm{H}}_{\mathrm{Z}}\|$, the real space laboratory frame Cartesian interaction matrix $\overline{\overline{\mathrm{A}}}(\mathrm{lab})$ can be well approximated as a sum of rank 0, rank 1, and rank 2 tensors:

$$\overline{\overline{\mathrm{A}}}(\mathrm{lab}) = \begin{pmatrix} A_{xx} & A_{xy} & A_{xz} \\ A_{yx} & A_{yy} & A_{yz} \\ A_{zx} & A_{zy} & A_{zz} \end{pmatrix} \cong A_{\mathrm{iso}} \begin{pmatrix} 1 & 0 & 0 \\ 0 & 1 & 0 \\ 0 & 0 & 1 \end{pmatrix} + \begin{pmatrix} 0 & \alpha_{xy} & \alpha_{xz} \\ -\alpha_{xy} & 0 & \alpha_{yz} \\ -\alpha_{xz} & -\alpha_{yz} & 0 \end{pmatrix} + \begin{pmatrix} \delta_{xx} & \delta_{xy} & \delta_{xz} \\ \delta_{xy} & \delta_{yy} & \delta_{yz} \\ \delta_{xz} & \delta_{yz} & \delta_{zz} \end{pmatrix} \tag{29.2}$$

where $A_{\mathrm{iso}} = 1/3\,\mathrm{Trace}[\overline{\overline{\mathrm{A}}}] = 1/3(A_{xx} + A_{yy} + A_{zz})$, $\alpha_{xy} = 1/2\,(A_{xy} - A_{yx})$, $\alpha_{xz} = 1/2\,(A_{xz} - A_{zx})$, $\alpha_{yz} = 1/2\,(A_{yz} - A_{zy})$, $\delta_{xy} = 1/2\,(A_{xy} + A_{yx} - 2\,A_{\mathrm{iso}})$, $\delta_{xz} = 1/2\,(A_{xz} + A_{zx} - 2A_{\mathrm{iso}})$, and $\delta_{yz} = 1/2\,(A_{yz} + A_{zy} - 2A_{\mathrm{iso}})$. The rank of a tensor is determined by how it is affected by rotations. The first matrix on the right-hand side of Equation 29.2 is the rank 0 isotropic interaction that determines the spectrum observed in liquids. The second represents the antisymmetric rank 1 tensor that rarely contributes to the NMR spectrum of solids or liquids. It can, however, contribute to NMR relaxation. The third matrix represents the symmetric rank 2 tensor. It is the source of the orientational dependence of the NMR spectrum as well most NMR relaxation.

Rank 0 tensors are scalar, isotropic, and unaffected by rotations. Rank 1 tensors are affected by rotations like vectors. Rank 2 tensors are affected as matrices. Rotations are discussed in the next chapter. As shown in *solid_hamiltonians.nb*, the sum of isotropic, antisymmetric, and symmetric tensors is *approximately* but not exactly equal to the Cartesian tensor.

The *PAS* of a given internal Hamiltonian is obtained by diagonalizing the symmetric rank 2 tensor component of $\overline{\overline{\mathrm{A}}}(\mathrm{lab})$ (see *solid_hamiltonians.nb*). The same transformation is also applied to the rank 0 and rank 1 tensors. In this reference frame, the $\overline{\overline{\mathrm{A}}}(\mathrm{PAS})$ tensor is given by

$$\begin{aligned} \overline{\overline{\mathrm{A}}}(\mathrm{PAS}) = \mathrm{S}\cdot\overline{\overline{\mathrm{A}}}(\mathrm{lab})\cdot\mathrm{S}^{\cdot} &= \begin{pmatrix} A_{xx\_\mathrm{pas}} & A_{xy\_\mathrm{pas}} & A_{xz\_\mathrm{pas}} \\ A_{yx\_\mathrm{pas}} & A_{yy\_\mathrm{pas}} & A_{yz\_\mathrm{pas}} \\ A_{zx\_\mathrm{pas}} & A_{zy\_\mathrm{pas}} & A_{zz\_\mathrm{pas}} \end{pmatrix} \\ &\cong A_{\mathrm{iso}} \begin{pmatrix} 1 & 0 & 0 \\ 0 & 1 & 0 \\ 0 & 0 & 1 \end{pmatrix} + \begin{pmatrix} 0 & \alpha'_{xy} & \alpha'_{xz} \\ -\alpha'_{xy} & 0 & \alpha'_{yz} \\ -\alpha'_{xz} & -\alpha'_{yz} & 0 \end{pmatrix} + \begin{pmatrix} \delta'_{xx} & 0 & 0 \\ 0 & \delta'_{yy} & 0 \\ 0 & 0 & \delta'_{zz} \end{pmatrix} \end{aligned} \tag{29.3}$$

where S is the similarity transform of the symmetric rank 2 matrix in Equation 29.2 and $\mathrm{S}^{\cdot}$ is the adjoint (inverse) matrix of S. The Cartesian tensor is brought to the PAS of the Hamiltonian by this transformation and all its elements are changed. The rank 0 tensor is unaffected by the transformation, while the elements of the rank 1 and rank 2 tensors are changed (see *solid_hamiltonians.nb*). The traces of the rank 1 (zero trace) and rank 2 tensors are preserved in the transformation. The convention used in

TABLE 29.1 δ'_{zz}(rad s^{-1}), η, and rank properties for solid-state Hamiltonians in their principal axis systems

$\hat{H}_{CS}$	$\delta'_{zz} = (\sigma_{zz} - \sigma_{iso})\gamma B_0$	$\delta'_{xx} + \delta'_{yy} + \delta'_{zz} = 3\sigma_{\text{iso}}\gamma B_0$	$\eta > 0$ possible Rank 1 asymmetry possible
$\hat{H}_{\text{dipolar}}$[4]	$\delta'_{zz\_ij} = d_{ij} = \left(\frac{\mu_0}{4\pi}\right)\frac{\gamma_i\gamma_j\hbar}{r_{ij}^3}$	$\delta'_{xx} + \delta'_{yy} + \delta'_{zz} = 0$	$\eta = 0$ No rank 1 asymmetry
$\hat{H}_{Q}$	$\delta'_{zz} = \frac{2\pi\, qcc}{2I(2I-1)} = \frac{e^2qQ}{2I(2I-1)\hbar}$	$\delta'_{xx} + \delta'_{yy} + \delta'_{zz} = 0$	$\eta > 0$ possible No rank 1 asymmetry
$\hat{H}_{J}$	$\delta'_{zz\_ij} = 2\pi J_{ij}$	$\delta'_{xx} + \delta'_{yy} + \delta'_{zz} = 6\pi J_{\text{iso}}$	$\eta > 0$ possible Rank 1 asymmetry possible

this book is $|\delta'_{zz}| > |\delta'_{yy}| > |\delta'_{xx}|$ (Levitt, 2008, p. 199), consistent with the convention used by Mehring and program Gamma.

Equation 29.3 may be rewritten in terms of the *asymmetry parameter* $\eta = (\delta'_{xx} - \delta'_{yy})/\delta'_{zz}$:

$$\overline{\overline{\text{A}}}(\text{PAS}) \cong A_{\text{iso}}\begin{pmatrix} 1 & 0 & 0 \\ 0 & 1 & 0 \\ 0 & 0 & 1 \end{pmatrix} + \begin{pmatrix} 0 & \alpha'_{xy} & \alpha'_{xz} \\ -\alpha_{xy} & 0 & \alpha'_{yz} \\ -\alpha'_{xz} & -\alpha'_{yz} & 0 \end{pmatrix} + \delta'_{zz}\begin{pmatrix} (-1/2)(1-\eta) & 0 & 0 \\ 0 & (-1/2)(1+\eta) & 0 \\ 0 & 0 & 1 \end{pmatrix} \tag{29.4}$$

In most cases, the asymmetric rank 1 tensor has no observable effect on the spectrum, relaxation, or evolution of the density operator. This is rigorously true for the dipolar and quadrupolar Hamiltonians $\hat{H}_D$ and $\hat{H}_Q$ where $A_{\text{iso\_D}}$, $A_{\text{iso\_Q}}$, and all elements in the asymmetric tensors are zero. This is *not* the case for $\hat{H}_{CS}$, $\hat{H}_J$, $\hat{H}_K$, and $\hat{H}_{SR}$.

The most important parameters in the expansion of $\overline{\overline{\text{A}}}(\text{PAS})$ are A_{iso} and δ'_{zz}. The latter term dominates NMR relaxation and solid-state NMR powder patterns. Table 29.1 provides a list of δ'_{zz} definitions for different internal Hamiltonians.

For an arbitrary orientation of an internal Hamiltonian PAS, the observed frequency in the spectrum depends on the angles required to bring the second rank tensor PAS *x*, *y*, and *z* axes into coincidence with the laboratory *x*, *y*, and *z* axes. To complicate the issue, there are often multiple Hamiltonians for a given nuclear spin, and these will in general have *different* PASs, so in order to calculate the observed spectrum or evolution of the density operator it is necessary to know the angles that are required to bring the different Hamiltonian PAS coordinate systems into coincidence before transforming all of them into coincidence with the laboratory reference frame.

Example: $\hat{H}_{CS}$

$\hat{H}_{CS}$ of a given nucleus depends on its location within the molecule. The external magnetic field $\hat{B} = \{0, 0, B_0\}$ induces currents in the electron orbitals of the molecule that vary in different positions of the molecule and with the orientation of the

---

[4] Not only nuclear spins with respective gyromagnetic ratios γ_I and γ_j can be dipole-dipole coupled. Electron spins with gyromagnetic ratio γ_e can also dipole-dipole couple to nuclear spins. $\gamma_e = 1.7608597 \times 10^{11}$ radian sec^{-1} tesla^{-1}. By comparison, γ_p for ^{1}H is 2.6751×10^8 radian sec^{-1} tesla^{-1}.

molecule relative to the magnetic field. The induced currents generate an anisotropic magnetic field at the nucleus that is much smaller than the external magnetic field yet has observable effects on the frequency. The strength of the induced magnetic field is directly proportional to the external magnetic field, so the chemical shift frequency is usually reported in parts per million (ppm) relative to a standard sample (e.g., tetramethylsilane for ^{1}H, ^{13}C, and ^{29}Si, defined as 0 ppm for all three $I=1/2$ nuclei). The standard sample frequency substitutes for the bare nucleus Larmor frequency since it is easy to measure experimentally.

We ignore the antisymmetric rank 1 contribution to $\bar{\bar{\sigma}}(\text{PAS})$ because it has negligible effects on the spectrum[5] and make the approximation:

$$\bar{\bar{\sigma}}(\text{PAS}) \cong \sigma_{\text{iso}} \begin{pmatrix} 1 & 0 & 0 \\ 0 & 1 & 0 \\ 0 & 0 & 1 \end{pmatrix} + \begin{pmatrix} \delta'_{xx} & 0 & 0 \\ 0 & \delta'_{yy} & 0 \\ 0 & 0 & \delta'_{zz} \end{pmatrix} \tag{29.5}$$

where σ_{iso} is the isotropic chemical shift (in ppm).

In a single crystal, all molecules have the same orientation with respect to the laboratory reference frame, and therefore each nucleus in the same chemical environment has the same chemical shift. Different single crystals have different orientations and different chemical shifts (Fig. 29.1). Powder samples contain millions of single crystals with different orientations. This results in a broad powder pattern lineshape since all possible angles are present. The principal axis components δ'_{xx}, δ'_{yy}, δ'_{zz} can be obtained directly from the observed NMR powder spectrum or by observing the variation in chemical shifts for a single crystal as its angles relative to the magnetic field are varied (see *Hcsstatlineshape.nb* and Fig. 29.1). It is demonstrated in *Hcsstatlineshape.nb* that the sign of η does not affect the powder spectrum or single crystal NMR spectra.

Figure 29.1a shows a set of superimposed theoretical single crystal NMR spectra that vary in frequency as the orientation of the crystal is varied in β increments of $\pi/18$ (i.e., 10°) for two α values, 0 or $\pi/2$ ($\delta'_{zz}=-2\pi 300$, $\delta'_{xx}=-2\pi 150$, $\delta'_{yy}=-2\pi 150$, $\eta=0$). Figure 29.1c shows the powder spectrum for the same parameters. Figures 29.1c, 29.1d, 29.1e, and 29.1f show the effect of changing the sign of δ'_{zz}. Figure 29.1g shows the powder spectrum for $\eta=1$. As shown in *Hcsstatlineshape.nb*, there is no effect observed in the spectra when the sign of η is changed. It is evident that the principal values can be "read off" directly from the powder spectrum or calculated empirically from angular dependence of single crystal spectra. When the z axis of the PAS is parallel to the laboratory z axis (external magnetic field axis), the observed frequency in the NMR spectrum is $A_{\text{iso}}+\delta'_{zz}$. When the x axis of the PAS is parallel to the laboratory z axis, the observed frequency is $A_{\text{iso}}+\delta'_{xx}$. When the y axis of the PAS is parallel to the laboratory z axis, the observed frequency is $A_{\text{iso}}+\delta'_{yy}$.

The notebook *hcs_cartesian.nb* starts with the Hamiltonian in the laboratory reference (see Eq. 29.1):

$$\hat{\text{H}}_{\text{CS}}(\text{lab}) = \gamma\, \hat{\text{I}} \cdot \bar{\bar{\sigma}} \cdot \hat{\text{B}} = (\hat{\text{I}}_x \quad \hat{\text{I}}_y \quad \hat{\text{I}}_z) \cdot \begin{pmatrix} \sigma_{xx} & \sigma_{xy} & \sigma_{xz} \\ \sigma_{yx} & \sigma_{yy} & \sigma_{yz} \\ \sigma_{zx} & \sigma_{zy} & \sigma_{zz} \end{pmatrix} \cdot \begin{pmatrix} 0 \\ 0 \\ B_0 \end{pmatrix} \tag{29.6}$$

---

[5] but does effect relaxation rates.

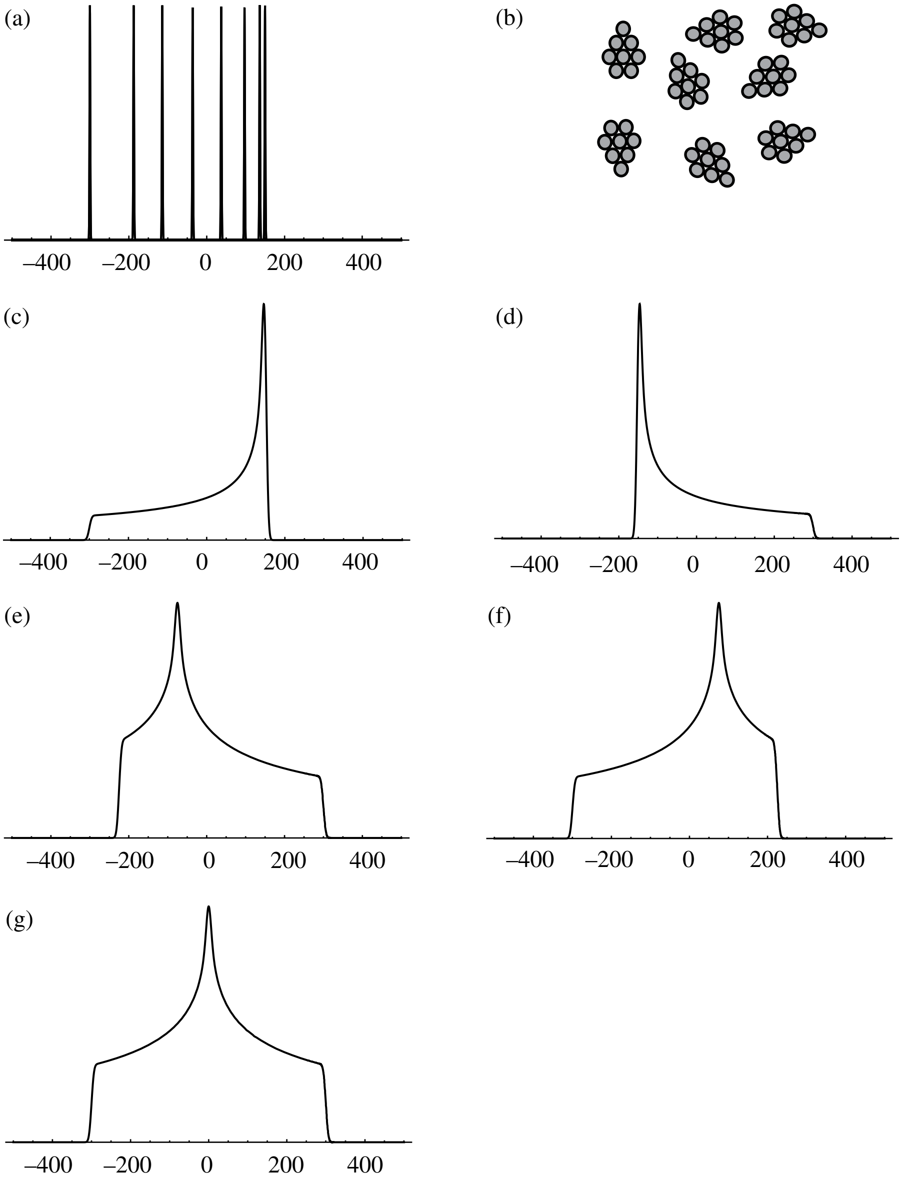

Figure 29.1 Single crystal and powder spectra. The spectra were calculated in the Mathematica notebooks *hcs_cartesian.nb* and *Hcsstatlineshape.nb*. (a) $\delta_{zz} = 2\pi\ 300\,\mathrm{rad\,s^{-1}}$, $\eta = 0$, $\beta = 0$ to $\pi/2$ in increments of $\pi/18$, $\alpha = 0$ or $\pi/2$; (b) schematic representation of eight different single crystals; (c) powder spectrum for $\delta_{zz} = 2\pi\,300\,\mathrm{rad\,s^{-1}}$, $\eta = 0$; (d) powder spectrum for $\delta_{zz} = -2\pi\ 300\,\mathrm{rad\,s^{-1}}$, $\eta = 0$; (e) powder spectrum for $\delta_{zz} = -2\pi\ 300\,\mathrm{rad\,s^{-1}}$, $\eta = 0.5$; (f) powder spectrum for $\delta_{zz} = 2\pi\ 300\,\mathrm{rad\,s^{-1}}$, $\eta = 0.5$; (g) powder spectrum for $\delta_{zz} = \pm 2\pi\ 300\,\mathrm{rad\,s^{-1}}$, $\eta = 1$. Adapted from Levitt (2008, fig. 9.9, 9.10, and 9.11).

where γ is the gyromagnetic ratio of the nucleus in rad s^{-1} Tesla^{-1}, the $\bar{\bar{\sigma}}$ tensor elements are expressed in unitless ppm (10^{-6}), and $\hat{B}$ is the external magnetic field and therefore defines the laboratory reference frame for both spin space and real space, with $\hat{B} = \{0, 0, B_0\}$. The result is $\hat{H}_{CS}(\text{lab}) = \gamma B_0 (\sigma_{xz}\hat{I}_x + \sigma_{yz}\hat{I}_y + \sigma_{zz}\hat{I}_z)$.

As shown in *hcs_cartesian.nb*, transforming $\hat{H}_{CS}$(lab) to the rotating frame in *spin space* causes the $\hat{I}_x$ and $\hat{I}_y$ components to oscillate at the Larmor frequency. When integrated over the Larmor period ($2\pi/\omega_0$), these terms average to zero. Only the *secular* part of $\hat{H}_{CS}$(lab) survives in the rotating frame, where $\hat{H}_{CS}(\text{rot}) = \sigma_{zz}\gamma B_0 \hat{I}_z$.

It is necessary to calculate σ_{zz} in the PAS reference frame where the frequencies σ_{iso}, δ'_{xx}, δ'_{yy}, and δ'_{zz} correspond directly to the observed experimental spectrum (Fig. 29.1). This is done using Cartesian rotations in *hcs_cartesian.nb* and using Wigner rotations in *Hcsstatlineshape.nb* to calculate the single crystal and powder spectra shown in Figure 29.1. The two methods yield the same angular dependence. Rotations are discussed in the next chapters.

EXPLANATION OF *solid_hamiltonians.nb*

The first cells define the Cartesian representation of a generic Hamiltonian H=i. acart.o, where i represents the spin-space nuclear spin angular momentum vector, acart represents the Cartesian real space interaction tensor, and o represents either a spin-space nuclear spin angular momentum vector, the magnetic field vector in spin space and real space, or the molecular angular momentum vector in real space.

The Hamiltonian i.acart.o is composed of nine terms, H=axx ix ox+ayx iy ox+azx iz ox+axy ix oy+ayy iy oy+azy iz oy+axz ix oz+iyz iy oz+izz iz oz.

The next cells introduce the spherical tensor version of the real space tensor elements A[*l*,*m*] according to the definitions of Mehring's book (Mehring, 1983). Another version of these elements (AA[*l*,*m*]) is reproduced using the definitions from the Encyclopedia of NMR. The real space spherical tensor elements are postponed in the text until Chapter 31.

The next cells introduce the spherical tensor versions of the spin space elements T[l,m] (Mehring, 1983). Again, these are not discussed in the text until Chapter 31. The next cells introduce the slightly different spherical tensor versions of the spin space elements as TT[*l*,*m*] (Mehring, 2002).

The evaluation of the Hamiltonian with these according to Equation 31.1 should match the Cartesian Hamiltonian but does not if using the A[*l*,*m*] and T[*l*,*m*] from Mehring's book or the AA[*l*,*m*] and TT[*l*,*m*] from the Encyclopedia of NMR.

This problem is easily solved in the next cells, yielding the correct set of spherical tensor spin space elements, Tconv[*l*,*m*] with the function convertcart. The resulting spin space elements yield the same expression for the Hamiltonian as the Cartesian version. The correct set of spherical spin space elements is also summarized in Table 31.2a.

The next cells use the same approach to express the spherical tensor spin space elements in terms of iz, oz, and the ladder operators ipl, imn, opl, and omin. After clearing the previous definition of the TTs with the built-in Mathematica function Clear, we then redefine the TTs using the versions from Mehring's book (Mehring, 1983). Again, these do not yield the same result as the Cartesian version but are transformed with the function convert to into the correct versions, the TTT[*l*,*m*]. The correct set of spherical spin space elements is also summarized in Table 31.2b.

The next cells compare the Cartesian real space tensor acart with the sum of the rank 0 (aiso), rank 1 (aanti), and rank 2 (asym) spherical tensor versions. *Evaluation shows that stopping the expansion at* $l=2$ *is an approximation.* This is not unexpected since mapping of complicated distributions on the surface of a sphere requires the sum from $l=0$ to $l=\infty$.

The next cells show how a numerical arbitrary symmetric $l=2$ tensor designated test can be diagonalized by using the simtran function to obtain its similarity transformation S, then using the built-in Mathematica function Inverse to obtain the matrix inverse of S, called S2. The adjoint function can also be used to obtain the matrix inverse, called S3. The built-in Mathematica functions Conjugate, Transpose, and Chop are introduced. S.test.S2 yields the diagonalized matrix. The diagonalized matrix has the same trace as the original matrix.

The next cells move the elements of the diagonalized matrix to fit the NMR convention that the largest deviation from aiso is for $\delta_{33}=\delta_{zz}$(pas), that the next largest deviation is $\delta_{22}=\delta_{yy}$(pas), and the smallest deviation is $\delta_{11}=\delta_{xx}$(pas). With this change, the axes change from x to z, from y to x, and from z to y. The resulting diagonal form of asym is designated asympas.

The next cells apply the same transformation to aanti, that is, S.aanti.S3. The results also need to have the elements readjusted according to the convention that is described in the preceding paragraph, but this process is left for the user as a homework problem later. The trace of aantipas is zero just as for the lab frame aanti.

The last cells show that the same transformation has no effect on aiso or its trace.

EXPLANATION OF *hcs_cartesian.nb*

The user is told to evaluate *matrep2.nb,* then close it without saving changes, and to do the same for *wigrot.nb*. The notebook *wigrot.nb* is a program used to carry out rotations using either Cartesian or spherical tensor methods. We will be using it extensively in the rest of the book.

The next cells define the chemical shift tensor σ in the laboratory reference frame, the nuclear spin angular momentum vector I, the magnetic field vector B, and the laboratory frame chemical shift Hamiltonian hcslab.

The next cell substitutes the I = 1/2 matrix representation of the spin angular momentum into hcslab. The lab frame hcslab is taken to the rotating frame by propagating it around the z axis (defined by magnetic field) at the Larmor frequency ω_0. Only the average over the Larmor period survives the transformation, yielding hcsrotavg.

hcsrotavg is the I = 1/2 version of the general expression for the rotating frame, hcsrotgen.

We note that σ_{zz} is in the lab frame, so we want to see what it is in terms of the observable PAS components. In order to do this, we use Cartesian rotation operators (available in *wigrot.nb*).

The next cells introduce the symmetric $l=2$ rank chemical shift tensor σ_{sym} in the PAS frame. The Cartesian rotation operators are used to rotate σ_{sym} to the lab frame, that is, R. σ_{sym}.$\mathrm{R}_{\mathrm{inv}}$, yielding σsymlab. The component needed for the Hamiltonian hcsrotavg is δ_{zz}lab, the [[3,3]] component of σ_{sym}lab.

This is simplified to yield the angular dependence of hcsrotavg in rad s^{-1}.

The last cells compare the angular dependence of hcsrotavg calculated by the Cartesian method with the same Hamiltonian calculated with the spherical tensor method in *hcsstatlineshape.nb*. Other than a factor of $\sqrt{3/2}$ arising from the $l=2$ spherical tensor definitions, the Hamiltonians are shown to be identical (except for a sign change in η that has no effect).

EXPLANATION OF *wigrot.nb*

Program *wigrot.nb* is used as a program in most of the remaining Mathematica notebooks. It contains the definitions of the Wigner rotation elements and spherical tensor real space PAS definitions as given in Mehring (Mehring, 1983). It also contains the Cartesian rotation matrices and Cartesian representations of the real space PAS.

Note that *wigrot.nb* is evaluated in one "supercell." *D*0 is the $l=0$, $m=0$ Wigner rotation element. The *d*1 definitions are for the $l=1$, $m=-1$, 0, and 1 Wigner rotation elements. Note that only the β dependence is given in the *d*1s.[6] *D*1 incorporates the α and γ dependence using complex exponentials. The *d*2 definitions are for the $l=2$, $m=-2$, -1, 0, 1 and 2 Wigner rotation elements. Note that only the β dependence is given in the *d*2s. *D*2 incorporates the α and γ dependence using complex exponentials. apas[*l,m*] gives the expressions for 9 corresponding spherical tensor PAS elements in terms of σ_{iso}, δ_{zz}, and η (and σ_{yz}, σ_{xy}, σ_{xz}, and σ_{yz} for the rarely used antisymmetric $l=1$ PAS elements). cart is a function that converts from spherical tensor to Cartesian representation. Next come the definitions for R, the Cartesian rotation matrix, and Rinv, its inverse and adjoint. rhocart is the Cartesian representation of the $l=2$ symmetric spherical tensor in the PAS.

EXPLANATION OF *hcsstatlineshape.nb*

The user is told to evaluate the notebook *wigrot.nb,* then close it without saving changes, and to do the same for the notebook *matrep2.nb*. In this notebook, chemical shift single crystal and powder spectra are calculated using the spherical tensor method. The calculation requires the chemical shift Hamiltonian Hcs = alab00 t00 + alab20 *t*20 (see Eq. 31.7).

The next cells take the PAS real space spherical tensor components from the PAS to the lab frame, yielding alab00 and alab20. The spin space spherical tensor components *t*00 and *t*20 are introduced. The chemical shift Hamiltonian is calculated. The I = 1/2 matrix representation of Hcs, called Hcsmat, is defined.

---

[6] *wigrot.nb* was translated from an earlier version of Mathematica, so the α, β, and γ symbols were converted to their alphabetic forms. The user is welcome to rewrite it in terms of the symbols.

As will be shown in Chapter 33, the $m = 1/2$ to $m = -1/2$ observable transition in rad s^{-1} is given by Hcsmat[[1,1]] – Hcsmat[[2,2]]. The angular dependence of the $l = 2$ anisotropic frequency is given by the function ωcsangular. The powder average (see Chapter 35) of ωcsangular is shown to be 0, explaining why only the isotropic chemical shift is observed in liquids. The substitution $\delta_{\text{rad}} = \delta_{zz}\ \omega_0$ is made, and then the orientationally dependent function ω is created.

Because a finite number of spherical polar angles (θ, ϕ) are used for the powder average in this calculation (see Chapter 35), each spectral component must be broadened. The gauss and Lorentz lineshape functions are introduced and plotted in the following cells.

The next cells calculate a table of powder average angles (θ and ϕ angles) with 1 degree increments (delthet) in θ and 2° increments (delphi) in ϕ. The weight of each angle (wtthet) is shown by integration to be 2 Sin[delthet] Sin[θ]. The table of angles and weights is called angles.

The functions boogie and boogieg are created to give the Lorentzian and Gaussian broadened lines, respectively, their variables δ_{rad}_, η_, and the angles α_ and β_. Remember that variables like α_ and β_ can take arbitrary symbolic or numerical values. The functions intensity and intensityg calculate the numerical values of boogie and boogieg, respectively.

The next cells calculate the theoretical single crystal spectra for $\delta_{\text{rad}} = 2\pi$ 300 rad s^{-1}, $\eta = 0$, 0.5, or 1, ten different 10° ($\pi/18$) increments of the latitudinal angle β, for each of which there are eight different 45° ($\pi/4$) increments in the longitudinal angle α.

The theoretical single crystal spectra plots show how the distribution of peaks changes with the value of η but that the distribution is *not affected by the sign of* η.

The next cells use the methods described in Chapter 35 to calculate the powder spectra (powder function) for a sample composed of a statistical ensemble of randomly oriented microcrystals. The powder spectrum is obtained from the line spectra (intensity or intensityg functions) by adding the properly weighted contributions of peaks obtained for all the possible angles α and β.

Plots of the powder spectra are obtained for $\delta_{\text{rad}} = \pm 2\pi$ 300 rad s^{-1}, $\eta = 0$, 0.5, 1, -0.5, and -1. Changing the sign of δ_{rad} causes the powder spectrum to “reflect” across 0 s^{-1}. Changing the value of $|\eta|$ changes the appearance of the powder spectrum dramatically. However, changing the sign of η is shown to have no effect.

HOMEWORK

Homework 29.1: Express the generic Hamiltonian in terms of the AA[*l*,*m*] and TT[*l*,*m*] defined early in *solid_hamiltonians.nb*. Compare with the Cartesian result for the Hamiltonian. If the two forms do not match, write a correction function to fix the TT[*l*,*m*] or AA[*l*,*m*].

Homework 29.2: Swap the elements of aantipas to match the NMR convention that the largest deviation from aiso is for $\delta_{33} = \delta_{zz}$(pas), that the next largest deviation is $\delta_{22} = \delta_{yy}$(pas), and the smallest deviation is $\delta_{11} = \delta_{xx}$(pas). You do not have to use Mathematica to carry out the swap.

CHAPTER 30

ROTATIONS OF REAL SPACE AXIS SYSTEMS—CARTESIAN METHOD

Specific rotation angles are needed to bring the real space principal axis system (see $\overline{\overline{\mathrm{A}}}$(PAS) Eq. 29.3) into coincidence with the real space laboratory axis system (see $\overline{\overline{\mathrm{A}}}$(lab) Eq. 29.2). $\overline{\overline{\mathrm{A}}}$(lab) is necessary to calculate the orientation-dependent frequencies in the NMR free induction decay or spectrum and to calculate NMR relaxation rates. There are often intermediate axis systems that are necessary to consider, for example, the molecular axis system.

These transformations are carried out by applying a sequence of three rotations with the unique set of angles called Euler angles that bring the coordinate system of one reference frame into exact coincidence with the next.[1] Two conventions can be used to carry out the transformation.

Convention 1: We can rotate around the original z axis by α radians, followed by a rotation around the *new* y' axis by β radians and finished by a rotation around the *new* z'' axis by γ radians (Levitt, 2008, appendix A.1; Mehring, 2002), This is easy to verify by creating your own labeled coordinate system to play with by putting three skewers at right angles through a styrofoam sphere and labeling the skewer axes. You will find that you can bring the coordinate system to any arbitrary new position with the right choice of α, β, and γ.

Convention 2: The same final result is obtained if the rotations occur first by a rotation of γ (same γ as in convention 1) radians around the *original* z axis, followed by a rotation of β radians (same β as in convention 1) around the *original* y axis, and finished by a rotation of α radians (same α as in convention 1) around the *original* z axis. The latter method is harder to visualize with the ball and skewers but easy to visualize in Mathematica as shown in *euler.nb*.

Regardless of the convention used, the first two rotations bring the z axis of the first reference frame into coincidence with the z axis of the second. The final rotation brings the x and y axes into coincidence. These may be visualized by considering a globe. The first two rotations bring the north poles, that is, the "latitudes," of the two reference frames into coincidence. The last brings the "longitudes" into coincidence.

---

[1] The translational superposition has been assumed.

A Primer of NMR Theory with Calculations in Mathematica®, First Edition. Alan J. Benesi.

Convention 1 Cartesian Rotations:

The Cartesian rotation matrix $\overline{\overline{\mathrm{R}}}$ and its inverse $\overline{\overline{\mathrm{R}_{\mathrm{inv}}}}$ corresponding to *convention 1* are available in the notebook *wigrot.nb*:

$$\overline{\overline{\mathrm{R}}}=\begin{pmatrix} \mathrm{Cos}[\alpha]\mathrm{Cos}[\beta]\mathrm{Cos}[\gamma]-\mathrm{Sin}[\alpha]\mathrm{Sin}[\gamma] & \mathrm{Cos}[\beta]\mathrm{Cos}[\gamma]\mathrm{Sin}[\alpha]+\mathrm{Cos}[\alpha]\mathrm{Sin}[\gamma] & -\mathrm{Cos}[\gamma]\mathrm{Sin}[\beta] \\ -\mathrm{Cos}[\gamma]\mathrm{Sin}[\alpha]-\mathrm{Cos}[\alpha]\mathrm{Cos}[\beta]\mathrm{Sin}[\gamma] & \mathrm{Cos}[\alpha]\mathrm{Cos}[\gamma]-\mathrm{Cos}[\beta]\mathrm{Sin}[\alpha]\mathrm{Sin}[\gamma] & \mathrm{Sin}[\beta]\mathrm{Sin}[\gamma] \\ \mathrm{Cos}[\alpha]\mathrm{Sin}[\beta] & \mathrm{Sin}[\alpha]\mathrm{Sin}[\beta] & \mathrm{Cos}[\beta] \end{pmatrix} \tag{30.1a}$$

$$\overline{\overline{\mathrm{R}_{\mathrm{inv}}}}=\begin{pmatrix} \mathrm{Cos}[\alpha]\mathrm{Cos}[\beta]\mathrm{Cos}[\gamma]-\mathrm{Sin}[\alpha]\mathrm{Sin}[\gamma] & -\mathrm{Cos}[\gamma]\mathrm{Sin}[\alpha]-\mathrm{Cos}[\alpha]\mathrm{Cos}[\beta]\mathrm{Sin}[\gamma] & \mathrm{Cos}[\alpha]\mathrm{Sin}[\beta] \\ \mathrm{Cos}[\beta]\mathrm{Cos}[\gamma]\mathrm{Sin}[\alpha]+\mathrm{Cos}[\alpha]\mathrm{Sin}[\gamma] & \mathrm{Cos}[\alpha]\mathrm{Cos}[\gamma]-\mathrm{Cos}[\beta]\mathrm{Sin}[\alpha]\mathrm{Sin}[\gamma] & \mathrm{Sin}[\alpha]\mathrm{Sin}[\beta] \\ -\mathrm{Cos}[\gamma]\mathrm{Sin}[\beta] & \mathrm{Sin}[\beta]\mathrm{Sin}[\gamma] & \mathrm{Cos}[\beta] \end{pmatrix} \tag{30.1b}$$

Cartesian rotations of matrices such as any of the component matrices of $\overline{\overline{\mathrm{A}}}(\mathrm{PAS})$ (Eqs. 29.3 and 29.4) are achieved by using a sandwich of rotation operators, as shown in *rotations.nb*:

$$\overline{\overline{\mathrm{A}}}(\mathrm{new})=\overline{\overline{\mathrm{R}}}\cdot\overline{\overline{\mathrm{A}}}(\mathrm{PAS})\cdot\overline{\overline{\mathrm{R}_{\mathrm{inv}}}} \tag{30.2}$$

Although not generally used in calculations of NMR Hamiltonians, Cartesian rotations of vectors such as $\mathrm{V}_1=\{v_x, v_y, v_z\}$ are achieved using $\overline{\overline{\mathrm{R}}}$ as follows (see *rotations.nb*):

$$\mathrm{V}_{\mathrm{new}}=\overline{\overline{\mathrm{R}}}\cdot\mathrm{V}_1 \tag{30.3}$$

In the older NMR literature, Cartesian rotations or direction cosines are used to transform coordinate systems. However, as shown in the next chapter, there is a more efficient way to transform coordinate systems based on the properties of spherical tensors.

EXPLANATION OF *euler.nb*

This notebook uses built-in Mathematica functions to illustrate rotations of objects in three dimensions. The Graphics3D function is used to create a set of three arrows, colored black, red, and green, that are in alignment with the Cartesian axis system in the first rendering. The arrows' endpoints and directions are specified with coordinates. For example, the green arrow has the "rear" endpoint at {0,–1,0}, that is, $x=0$, $y=-1$, $z=0$. The "head" endpoint is {0,1,0}, that is, $x=0$, $y=1$, $z=0$. The axis system is also defined via the AxesOrigin, Axes→True, PlotRange→ {{−1,1}, {−1,1},{−1,1}}, that is, the x axis goes from −1 to 1, the y axis does the same, and the z axis does the same.

The "object" composed of the three arrows is rotated in the following cells with the built-in Rotate function. In the first cell, the object is rotated by 45° around the $+z$ axis defined by {0, 0, 1}. The next graphics cell carries out two rotations, one of 45° around the $+z$ axis *and* another one of 30° around the $+y$ axis. The last graphics cell carries out three rotations, one of 45° around the $+z$ axis, one of 30° around the $+y$ axis, *and* one of 60° around the $+z$ axis.

The last comment cell tells the user to try using convention 1 with a styrofoam ball containing orthogonal skewers to achieve the same final orientation.

EXPLANATION OF *rotations.nb*

The user is told to evaluate *wigrot.nb*, then to close it without saving changes. This notebook uses the functions R and R_{inv} to carry out Cartesian rotations of vectors and of the second rank ($l=2$) symmetric principal axis system (PAS) tensor. $R.R_{\mathrm{inv}}$ and $R_{\mathrm{inv}}.R$ are shown to yield the 3×3 unit matrix {{1,0,0},{0,1,0},{0,0,1}}.

Rotation of arbitrary vector1 is implemented using the dot product R.vector1 and yields a new vector, vectornew. Rotation of the PAS spherical tensor asympas is carried out using the "sandwich" product $R.\mathrm{asympas}.R_{\mathrm{inv}}$ and yields a new tensor, anew. The same Cartesian sandwich is also used to rotate the symmetric spherical tensor asympas2, which is expressed in terms of δ_{zz} and η.

HOMEWORK

Homework 30.1: Verify by observation with a Cartesian axis labeled ball that the spherical polar angles θ and φ correspond to the Euler angles $\beta=\theta$ and $\gamma=\pi-\varphi$.

CHAPTER 31

WIGNER ROTATIONS OF IRREDUCIBLE SPHERICAL TENSORS

An internal Hamiltonian can be expressed using the Cartesian representation, $\hat{\mathrm{H}}_{\mathrm{int}} = \hat{\mathrm{I}} \cdot \overline{\overline{\mathbf{A}}} \cdot \hat{\mathrm{O}}$ (Eq. 29.1) and can be transformed to or from other reference frames using Euler angles and Cartesian rotations. This requires matrix multiplication (Eq. 30.2). A more efficient way to express the same internal Hamiltonian and carry out the reference frame transformations is with spherical tensors (Mehring, 2002).

The spherical tensors $\mathrm{T}^{\mathrm{I}}_{l,m}$ used to represent individual nuclear spin angular momentum are used in the calculation of NMR relaxation rates (Spiess, 1978, eqs. 2.14 and 2.15). These are given in Table 31.1.

The *Hamiltonian*-based spin angular momentum operators $\hat{\mathrm{T}}^{l,m}$ are necessary for the calculation and simulation of NMR signals and spectra. These are given in Tables 31.2A and 31.2B. Note that they are different than those in Table 31.1:

Using spherical tensors and units of rad s^{-1}, an internal Hamiltonian is expressed in terms of the real space tensors $\overline{\overline{\mathrm{A}}}^{l,m}$ and the spin space Hamiltonian spherical tensor operators $\hat{\mathrm{T}}^{l,m}$ as

$$\hat{\mathrm{H}}_{\mathrm{int}} = \sum_{l=0}^{2} \sum_{m=-l}^{+l} (-1)^m \, \overline{\overline{\mathbf{A}}}^{l,m} \, \hat{\mathrm{T}}^{l,-m} \tag{31.1}$$

where $\hat{\mathrm{H}}_{\mathrm{int}}$ is the interaction Hamiltonian in an arbitrary reference frame (e.g., lab frame), $\overline{\overline{\mathrm{A}}}^{l,m}$ is the *l*,*m* component of the real space interaction tensor, and $\hat{\mathrm{T}}^{l,-m}$ is the *l*,–*m* component of the Hamiltonian spin space spherical tensor operator (Table 31.2). The real space tensors $\overline{\overline{\mathrm{A}}}^{l,m}$ are given in Table 31.3:

Irreducible spherical tensors have mathematically convenient rotational properties. Transformation between reference frames does not require matrix multiplication, as demonstrated in Equation 31.2:

$$\overline{\overline{\mathrm{A}}}^{l,m} = \sum_{q=-l}^{+l} \overline{\overline{\mathrm{A}}}^{l,q} \, D^{l}_{qm}(\alpha\beta\gamma) \tag{31.2}$$

A Primer of NMR Theory with Calculations in Mathematica®, First Edition. Alan J. Benesi.

TABLE 31.1 Spin Angular Momentum Operators $\mathrm{T}^{\mathrm{I}}_{l,m}$ for Single Nuclear Spins Expressed as Spherical Tensors

$$\mathrm{T}^{\mathrm{I}}_{1,0} = \hat{\mathrm{I}}_0 = \hat{\mathrm{I}}_z$$

$$\mathrm{T}^{\mathrm{I}}_{1,\pm1} = \hat{\mathrm{I}}_{\pm1} = \mp\frac{1}{\sqrt{2}}\hat{\mathrm{I}}^{\pm}$$

$$\mathrm{T}^{\mathrm{I}}_{2,0} = \frac{1}{\sqrt{6}}(3\hat{\mathrm{I}}_z^2 - I(I+1))$$

$$\mathrm{T}^{\mathrm{I}}_{2,1} = \frac{-1}{2}(\hat{\mathrm{I}}_z\hat{\mathrm{I}}^+ + \hat{\mathrm{I}}^+\hat{\mathrm{I}}_z)$$

$$\mathrm{T}^{\mathrm{I}}_{2,-1} = \frac{1}{2}(\hat{\mathrm{I}}_z\hat{\mathrm{I}}^- + \hat{\mathrm{I}}^-\hat{\mathrm{I}}_z)$$

$$\mathrm{T}^{\mathrm{I}}_{2,2} = \frac{1}{2}\hat{\mathrm{I}}^+\hat{\mathrm{I}}^+$$

$$\mathrm{T}^{\mathrm{I}}_{2,-2} = \frac{1}{2}\hat{\mathrm{I}}^-\hat{\mathrm{I}}^-$$

Do not confuse the spherical tensor representation of single nuclear spin angular momentum $\mathrm{T}^{\mathrm{I}}_{l,m}$ given in this table with the Hamiltonian spherical tensors $\hat{\mathrm{T}}^{l,m}$ given in Table 31.2.

where $\overset{=}{\mathrm{A}}^{l,q}$ is the real space interaction tensor in the *original* axis system, $\overset{=}{\mathrm{A}}^{l,m}$ is the real space interaction tensor in the *new* axis system, and $D^l_{qm}(\alpha\beta\gamma)$ is the *Wigner rotation element* (Mehring, 2002) used to carry out rotations by the Euler angles relating the two axis systems. Ultimately, to express the Hamiltonian for simulations of spectra and propagation of the density operator, the real space axis system must be expressed in the laboratory reference frame, that is, $\overset{=}{\mathrm{A}}^{l,m}(\mathrm{lab})$.

The notebook *wigrot.nb* contains the $D^l_{qm}(\alpha\beta\gamma)$ elements for $l=0$, 1, and 2. These can be expressed in even more compact form as

$$D^l_{qm}(\alpha\beta\gamma) = e^{-iq\alpha}\, d^l_{qm}(\beta)e^{-im\gamma} \tag{31.3}$$

where the $d^l_{qm}(\beta)$ elements are real. The orthogonality properties of the Wigner rotation elements are demonstrated in *wigner_orthogonality.nb*:

$$\int_0^{2\pi}\int_0^{\pi}\int_0^{2\pi} D^{l1*}_{q1m1}\times D^{l2}_{q2m2}\sin[\beta]d\gamma d\beta d\alpha = 0 \text{ if } q1\neq q2 \text{ or } m1\neq m2 \text{ or } l1\neq l2$$

$$\text{and} = \frac{8\pi^2}{2l1+1} \text{ if } q1=q2 \text{ and } m1=m2 \text{ and } l1=l2 \tag{31.4}$$

TABLE 31.2 Spin Angular Momentum Operators $\hat{T}^{l,m}$ for Hamiltonians Expressed as Spherical Tensors

(A) In terms of Cartesian Spin Angular Momentum Operators[a]

$$\hat{T}^{0,0} = -\frac{\hat{I}_x\hat{O}_x + \hat{I}_y\hat{O}_y + \hat{I}_z\hat{O}_z}{\sqrt{3}}$$

$$\hat{T}^{1,-1} = \frac{1}{2}(\hat{I}_z\hat{O}_x - \hat{I}_x\hat{O}_z + i(-\hat{I}_z\hat{O}_y + \hat{I}_y\hat{O}_z))$$

$$\hat{T}^{1,0} = -\frac{i(\hat{I}_y\hat{O}_x - \hat{I}_x\hat{O}_y)}{\sqrt{2}}$$

$$\hat{T}^{1,1} = \frac{1}{2}(\hat{I}_z\hat{O}_x - \hat{I}_x\hat{O}_z - i(-\hat{I}_z\hat{O}_y + \hat{I}_y\hat{O}_z))$$

$$\hat{T}^{2,-2} = \frac{1}{2}(\hat{I}_x\hat{O}_x - \hat{I}_y\hat{O}_y - i(\hat{I}_y\hat{O}_x + \hat{I}_x\hat{O}_y))$$

$$\hat{T}^{2,-1} = \frac{1}{2}(\hat{I}_z\hat{O}_x + \hat{I}_x\hat{O}_z - i(\hat{I}_z\hat{O}_y + \hat{I}_y\hat{O}_z))$$

$$\hat{T}^{2,0} = \frac{-\hat{I}_x\hat{O}_x - \hat{I}_y\hat{O}_y + 2\hat{I}_z\hat{O}_z}{\sqrt{6}}$$

$$\hat{T}^{2,1} = \frac{-1}{2}(\hat{I}_z\hat{O}_x + \hat{I}_x\hat{O}_z + i(\hat{I}_z\hat{O}_y + \hat{I}_y\hat{O}_z))$$

$$\hat{T}^{2,2} = \frac{1}{2}(\hat{I}_x\hat{O}_x - \hat{I}_y\hat{O}_y + i(\hat{I}_y\hat{O}_x + \hat{I}_x\hat{O}_y))$$

(B) In terms of Spin Space Angular Momentum Ladder Operators[b]

$$\hat{T}^{0,0} = -\frac{\hat{I}_+\hat{O}_- + \hat{I}_-\hat{O}_+ + 2\hat{I}_z\hat{O}_z}{2\sqrt{3}}$$

$$\hat{T}^{1,-1} = \frac{1}{2}(\hat{I}_z\hat{O}_- - \hat{I}_-\hat{O}_z)$$

$$\hat{T}^{1,0} = \frac{-\hat{I}_+\hat{O}_- + \hat{I}_-\hat{O}_+}{2\sqrt{2}}$$

$$\hat{T}^{1,1} = \frac{1}{2}(\hat{I}_z\hat{O}_+ - \hat{I}_+\hat{O}_z)$$

$$\hat{T}^{2,-2} = \frac{\hat{I}_-\hat{O}_-}{2}$$

$$\hat{T}^{2,-1} = \frac{1}{2}(\hat{I}_z\hat{O}_- + \hat{I}_-\hat{O}_z)$$

$$\hat{T}^{2,0} = -\frac{\hat{I}_+\hat{O}_- + \hat{I}_-\hat{O}_+ - 4\hat{I}_z\hat{O}_z}{2\sqrt{6}}$$

$$\hat{T}^{2,1} = \frac{-1}{2}(\hat{I}_z\hat{O}_+ + \hat{I}_+\hat{O}_z)$$

$$\hat{T}^{2,2} = \frac{\hat{I}_+\hat{O}_+}{2}$$

---

[a] Do not confuse the Hamiltonian Spherical Tensor Operators $\hat{T}^{l,m}$ (Table 31.2) with the Single Spin Angular Momentum operators $T^{I}_{l,m}$ (Table 31.1). The $\hat{T}^{l,m}$ in this table have been corrected for the swap of Î and Ô operators as shown in *solid_hamiltonians.nb.*

[b] Mehring (2002, pp. 2585–2602).

TABLE 31.3 Real Space Tensors $\overset{=}{A}^{l,m}$ in terms of Cartesian Real Space Components

$$\overset{=}{A}^{0,0} = -\frac{A_{xx} + A_{yy} + A_{zz}}{\sqrt{3}}$$

$$\overset{=}{A}^{1,-1} = \frac{1}{2}(A_{xz} - A_{zx} + i(-A_{yz} + A_{zy}))$$

$$\overset{=}{A}^{1,0} = -\frac{i(A_{xy} - A_{yx})}{\sqrt{2}}$$

$$\overset{=}{A}^{1,1} = \frac{1}{2}(A_{xz} - A_{zx} - i(-A_{yz} + A_{zy}))$$

$$\overset{=}{A}^{2,-2} = \frac{1}{2}(A_{xx} - i(A_{xy} + A_{yx}) - A_{yy})$$

$$\overset{=}{A}^{2,-1} = \frac{1}{2}(A_{xz} + A_{zx} - i(A_{yz} + A_{zy}))$$

$$\overset{=}{A}^{2,0} = \frac{-A_{xx} - A_{yy} + 2A_{zz}}{\sqrt{6}}$$

$$\overset{=}{A}^{2,1} = \frac{1}{2}(-A_{xz} - A_{zx} - i(A_{yz} + A_{zy}))$$

$$\overset{=}{A}^{2,2} = \frac{1}{2}(A_{xx} + i(A_{xy} + A_{yx}) - A_{yy})$$

Via Equation 31.2 and as demonstrated in *wigner_orthogonality.nb*, the orthogonality is imparted to the $\overset{=}{A}^{l,m}$:

$$\int_0^{2\pi}\int_0^{\pi}\int_0^{2\pi} \overset{=}{A}^{l1,m1*} \times \overset{=}{A}^{l2,m2} \sin[\beta]d\gamma d\beta d\alpha = 0 \text{ if } m1 \neq m2 \text{ or } l1 \neq l2 \text{ or both} \tag{31.5a}$$

and

$$\int_0^{2\pi}\int_0^{\pi}\int_0^{2\pi} -1^{l+m}\overset{=}{A}^{l1,m1} \times \overset{=}{A}^{l2,m2} \sin[\beta]d\gamma d\beta d\alpha = 0 \text{ if } m1 \neq m2 \text{ or } l1 \neq l2 \text{ or both} \tag{31.5b}$$

Averaging the $\hat{T}^{l,m}$ over the Larmor period (see *hcs_cartesian.nb* and *spherical_tensors_wigner.nb* for examples) in *spin space* yields another simplification in the internal Hamiltonian. All terms vanish except those with m =0, yielding the *secular interaction Hamiltonian in the rotating frame*:

$$\hat{H}_{\text{int}} = \overset{=}{A}^{0,0}\hat{T}^{0,0} + \overset{=}{A}^{1,0}\hat{T}^{1,0} + \overset{=}{A}^{2,0}\hat{T}^{2,0} \tag{31.6}$$

The antisymmetric term $\overset{=}{A}^{1,0}\hat{T}^{1,0}$ is irrelevant for the spectrum or propagation of the density operator but can be important for NMR relaxation (Spiess, 1978).

We conclude that the relevant Hamiltonian for spectral simulations and propagation of the density operator in pulse sequences is as follows:

$$\hat{\mathrm{H}}_{\mathrm{int}} = \overset{=}{\mathrm{A}}^{0,0}\,\hat{\mathrm{T}}^{0,0} + \overset{=}{\mathrm{A}}^{2,0}\,\hat{\mathrm{T}}^{2,0} \tag{31.7}$$

where the $\overset{=}{\mathrm{A}}^{2,0}$ is expressed in the laboratory reference frame ($\overset{=}{\mathrm{A}}^{0,0}$ is unaffected by real space axis system transformations). Calculation of the chemical shift Hamiltonian corresponding to Equation 31.5a is shown in *spherical_tensors_wigner.nb*. The results obtained using the spherical tensor method are identical to those obtained with the Cartesian method except for a factor of $\sqrt{3/2}$ and a change in sign of η that do not affect the spectrum or relaxation (see *spherical_tensors_wigner.nb* and *Hcsstatlineshape.nb*).

The spin space tensors $\hat{\mathrm{T}}^{l,m}$ vary with the particular interaction Hamiltonian, $\hat{\mathrm{H}}_{\mathrm{int}}$ (see *spherical_tensors_wigner.nb*). For example, in the case of $\hat{\mathrm{H}}_{\mathrm{CS}}$, the $\hat{\mathrm{T}}_{\mathrm{CS}}^{1,\mathrm{m}}$ tensors are given by (using the definitions in *wigrot.nb* and $\omega_0 = -\gamma B_0$, $\hat{\mathrm{T}}_{\mathrm{CS}}^{0,0} = -\sqrt{1/3}\omega_0\hat{\mathrm{I}}_z$ and $\hat{\mathrm{T}}_{\mathrm{CS}}^{2,0} = \sqrt{2/3}\omega_0\hat{\mathrm{I}}_z$).

EXPLANATION OF *wigner_orthogonality.nb*

The purpose of this notebook is to show what is meant by orthogonality of the Wigner rotation elements *D*[*l*,*m*] and the real space spherical tensors A[*l*,*m*]. The user is told to evaluate *wigrot.nb*, then to close it without saving changes. The next cells tell Mathematica to recognize that α, β, γ, δzz, η, and the antisymmetric spherical tensor elements ρxy, ρxz, and ρyz are real with no imaginary components.

The next cells evaluate apas[2,0]^2 and apas[2,2]*apas[2,2].

The next cells integrate products of *D*1 and the complex conjugate of *D*1 over all possible Euler angles α, β, and γ with sin[β] weighting (see Chapter 35). It is shown that the triple integrals (obtained using the Basic Math Input palette) yield $8\pi^2/3$ for the product of *D*1[1,–1] and its complex conjugate of *D*1[1,–1], 0 for the product of *D*1[1,–1] with itself, 0 for the product of *D*1[1,1] and *D*1[1,–1], 0 for the product of *D*1[1,–1] and *D*1[–1,–1], $8\pi^2/3$ for the product *D*1[1,–1] and *D*1[–1,1], 0 for the product Conjugate[*D*1[1,–1]] and *D*[–1,1], 0 for the product *D*0[0,0]**D*1[–1,1], $8\pi^2/5$ for the product of *D*2[2,1] and its conjugate, 0 for the product Conjugate[*D*2[2,1]]. *D*2[2,–1], and 0 for the product *D*2[2,1]**D*2[1,2]. These findings are consistent with Equation 31.4.

The next cells evaluate the triple integrals of some of the real space lab frame products of alab[*l*1,*m*1] and alab[*l*2,*m*2] with results that are consistent with Equations 31.5a and 31.5b. Built-in Mathematica functions ExpToTrig and TrigExpand are used to simplify some of the resulting expressions.

EXPLANATION OF *spherical_tensors_wigner.nb*

The purpose of this notebook is to demonstrate the use of the spherical tensors and the equivalence of rank 2 real space Cartesian tensors and spherical tensors. The user is told to evaluate *wigrot.nb*, then close it without saving changes. Then the user is told to do the same for *matrep2.nb*.

The next cells define the spin space spherical tensors as determined in *solid_Hamiltonians.nb* and in Table 31.2A. A generic Hamiltonian Hpas is evaluated using Equation 31.1.

The chemical shift Hamiltonian spin space tensors Tcs[*l*,*m*] are then defined. Then the quadrupolar Hamiltonian spin space tensors Tq[*l*,*m*] are defined, then reexpressed in terms of ladder operators.

The next cells reexpress the spin angular momentum operators in matrix form for $I=1/2$. The resulting full generic Hamiltonian is called Hhpas. Then Hhpas is taken to the rotating frame to yield Hhpasrot. Then Hhpasrot is averaged (integrated) over the Larmor period $2\pi/\omega_0$. Only the secular (diagonal) part of the Hamiltonian survives.

The next cells define expressions for the spherical spin space operators TT[*l*,*m*] based on ladder operators as in Table 31.2B. The chemical shift and quadrupolar versions of these are defined as TTcs[*l*,*m*] and TTq[*l*,*m*], respectively. A new generic Hamiltonian based on Equation 31.1 is then created, Hhpas2.

The next cells define alab20, alab10, and alab00. The generic Hamiltonian Hlab is then defined. Then the alab20 calculated with spherical tensors is compared with the alab20 calculated in hcs_cartesian.nb. They are identical except for a factor of $\sqrt{3/2}$ that arises from the definitions of the $l = 2$ spherical tensors. The angular dependence is the same in both cases.

HOMEWORK

Homework 31.1: Verify Equation 31.4 for all possible products of Wigner rotation elements with $l=0$, $l=1$, and $l=2$.

Homework 31.2: Verify Equation 31.5 for all possible products of the alab[2,*m*] with $l=0$, $l=1$, and $l=2$.

CHAPTER 32

SOLID-STATE NMR REAL SPACE SPHERICAL TENSORS

Here, the methods described in the last chapter are used to calculate real space spherical interaction tensors for some commonly encountered solid-state NMR internal Hamiltonians (Mehring, 2002, 1983). In subsequent chapters, the methods used to calculate spectra with these tensors will be described.

STATIC SAMPLES OF POWDERED SOLIDS

Most solid-state NMR samples are in the form of powders composed of millions of microscopic crystals. There is no preferred orientation of the microscopic crystals relative to the laboratory reference frame and therefore no preferred orientation of the principal axis systems (PASs) of internal Hamiltonians relative to the laboratory reference frame. Every possible random orientation of the PAS relative to the laboratory frame occurs with equal probability, hence every possible Euler angle. In this case, the rotational transformation required to bring the PAS of an arbitrary nuclear internal Hamiltonian into coincidence with the laboratory axis system is shown in Scheme 32.1 and Equations 32.2 and 32.3 below (see *real_tensor_solid.nb)*:

$$\overline{\overline{\mathrm{A}}}_{\mathrm{int}}[\mathrm{pas}] \xrightarrow{\alpha\beta\gamma} \overline{\overline{\mathrm{A}}}_{\mathrm{int}}[\mathrm{laboratory}] \tag{32.1}$$

$$\begin{aligned}\overline{\overline{\mathrm{A}}}^{2,0}(\mathrm{lab}) &= \sum_{q=-2}^{+2} \overline{\overline{\mathrm{A}}}^{2,q}(\mathrm{PAS}) D^{2}_{q0}(\alpha\beta\gamma)\\ &= \frac{1}{4}\sqrt{\frac{3}{2}}(1+3\cos[2\beta]-2\eta\cos[2\alpha]\sin[\beta]^{2})\delta'_{zz}\end{aligned} \tag{32.2}$$

In the rare occasions where $\overline{\overline{\mathrm{A}}}^{1,0}(\mathrm{lab})$ is necessary,

$$\begin{aligned}\overline{\overline{\mathrm{A}}}^{1,0}(\mathrm{lab}) &= \sum_{q=-1}^{+1} \overline{\overline{\mathrm{A}}}^{1,q}(\mathrm{PAS}) D^{1}_{q0}(\alpha\beta\gamma)\\ &= -i\sqrt{2}(\cos[\beta]\rho'_{xy} + \sin[\beta](-\sin[\alpha]\rho'_{xz} + \cos[\alpha]\rho'_{yz}))\end{aligned} \tag{32.3}$$

A Primer of NMR Theory with Calculations in Mathematica®, First Edition. Alan J. Benesi.

where we have used ρ'_{xy}, ρ'_{xz}, and ρ'_{yz} to replace α'_{xy}, α'_{xz}, and α'_{yz} from Equation 29.3 to avoid confusion with the Euler angle α used in Equation 32.2.

The isotropic component is unchanged by the transformation, that is,

$$\overset{=}{\mathrm{A}}{}^{0,0}(\mathrm{lab}) = \overset{=}{\mathrm{A}}{}^{0,0}(\mathrm{PAS}) \tag{32.4}$$

Because there are no preferred orientations, every possible value of each Euler angle occurs. $\overset{=}{\mathrm{A}}{}^{2,0}(\mathrm{lab})$ varies with the Euler angles according to Equation 32.2. There is no γ dependence in $\overset{=}{\mathrm{A}}{}^{2,0}(\mathrm{lab})$.

STATIC SINGLE CRYSTALS

In a single crystal, the PAS of a given internal Hamiltonian is the same for equivalent nuclei. This means that a *single set of unique and specific Euler angles* is sufficient to bring the PAS into coincidence with the crystal axis system. Another set of specific Euler angles are needed to transform from the crystal axis system to the goniometer[1] axis system. Finally, the goniometer axis system has a third set of specific Euler angles that relate it to the laboratory axis system (see *real_tensor_solid.nb*). The transformation from the PAS of the internal Hamiltonian via the intermediate axis systems to the laboratory axis system can be represented as shown in Scheme 32.5 and Equation 32.6

$$\overset{=}{\mathrm{A}}[\mathrm{pas}] \xrightarrow{\alpha\beta\gamma} \overset{=}{\mathrm{A}}[\mathrm{crystal}] \xrightarrow{\xi\psi\zeta} \overset{=}{\mathrm{A}}[\mathrm{goniometer}] \xrightarrow{\varphi\theta\kappa} \overset{=}{\mathrm{A}}[\mathrm{laboratory}] \tag{32.5}$$

$$\overset{=}{\mathrm{A}}{}^{2,0}(\mathrm{lab}) = \sum_{s=-2}^{+2} D^{2}_{s0}(\phi\theta\kappa) \sum_{r=-2}^{+2} D^{2}_{rs}(\xi\psi\zeta) \sum_{q=-2}^{+2} \overset{=}{\mathrm{A}}{}^{2,q}(\mathrm{PAS}) D^{2}_{qr}(\alpha\beta\gamma) \tag{32.6}$$

where the sums are nested and each Euler angle has a singular and unique value, for example, $\alpha=\pi/3$, $\beta=\pi/2$, $\gamma=3\pi/2$; $\xi=\pi$, $\psi=\pi/2$, $\zeta=0$; $\phi=\pi/7$, $\theta=0$, $\kappa=\pi/5$ as for the example shown in *real_tensor_solid.nb.*

MULTIPLE HAMILTONIANS AND REAL SPACE TENSORS FOR STATIC POWDERED SOLID SAMPLES

It is often true for solid samples that a given nucleus has multiple internal Hamiltonians. This is generally true for quadrupolar nuclei, where both $\hat{\mathrm{H}}_{\mathrm{Q}}$ and $\hat{\mathrm{H}}_{\mathrm{CS}}$ (and sometimes $\hat{\mathrm{H}}_{\mathrm{D}}$) can have significant effects on spectra and on evolution of the density operator. In this case, it is necessary to choose *one* of the interaction PASs as the one from which the powder average to the laboratory reference frame is generated. Here, we consider the case where $\hat{\mathrm{H}}_{\mathrm{Q}}$ and $\hat{\mathrm{H}}_{\mathrm{CS}}$ are active, and we choose the

---

[1] A goniometer is a device that allows an object, in this case a single crystal, to be rotated to a precise angular orientation.

$\hat{H}_Q$ PAS as the one from which the powder average to the laboratory reference frame is calculated as shown in Schemes 32.7a and 32.7b:

$$\overline{\overline{A_{CS}}}[\text{pas}] \xrightarrow{\zeta\psi\xi} \overline{\overline{A_{CS}}}[\text{quadpas}] \xrightarrow{\alpha\beta\gamma} \overline{\overline{A_{CS}}}[\text{laboratory}] \tag{32.7a}$$

$$\overline{\overline{A_Q}}[\text{quadpas}] \xrightarrow{\alpha\beta\gamma} \overline{\overline{A_Q}}[\text{laboratory}] \tag{32.7b}$$

where unique values of the Euler angles ζ, ψ, and ξ relate the $\hat{H}_{CS}$ PAS to the $\hat{H}_Q$ PAS, and the powder average angles α, β, and γ relate the $\hat{H}_Q$ PAS to the laboratory axis system (see *real_tensor_solid.nb*).

MAGIC ANGLE SPINNING OF POWDERED SOLID SAMPLES

In many solid-state NMR experiments, a powdered solid sample is placed in a cylindrical rotor and spun at the "magic angle" relative to the laboratory reference frame z axis. The magic angle is the smallest angle θ for which $3\cos^2[\theta]-1=0$. In degrees, this angle is 54.736° (see *real_tensor_solid.nb*). The experimental advantage of magic angle spinning is that the powder spectrum integral is concentrated into a sharp peak or peaks,[2] greatly increasing the signal to noise ratio and resolution of peaks from nuclei in different environments. For all internal Hamiltonians in which $\|\hat{H}_{int}\| \ll \|\hat{H}_Z\|$[3], spinning the sample at the magic angle yields sharp peaks rather than powder spectra.

The real space interaction tensor for spinning at an arbitrary angle with respect to the laboratory axis system is obtained by using the transformations in Scheme 32.8:

$$\overline{\overline{A_{int}}}[\text{pas}] \xrightarrow{\alpha\beta\gamma} \overline{\overline{A_{int}}}[\text{rotor}] \xrightarrow{\phi\theta\chi} \overline{\overline{A_{int}}}[\text{laboratory}] \tag{32.8}$$

where α, β, and γ are powder average Euler angles that relate the internal Hamiltonian PAS to the rotor axis system, and $\phi=\omega_{rot}\,t$, θ, and χ are the Euler angles that relate the rotor axis system to the laboratory axis system. ϕ is time-dependent because the rotor is spinning at ω_{rot}, and χ is arbitrary and can be assigned any single value. θ is usually chosen to be the magic angle. The transformation in Equation 32.9 is illustrated in *real_tensor_solid.nb.*

$$\overline{\overline{A}}{}^{20}_{lab}(t) = \sum_{r=-2}^{+2} D^2_{r0}(\omega_{rot}\,t,\theta,\chi) \sum_{q=-2}^{+2} \overline{\overline{A}}{}^{2,q}(\text{PAS}) D^2_{qr}(\alpha,\beta,\gamma) \tag{32.9}$$

Unlike static powder samples where only the α and β angles are sufficient to align the $\hat{H}_{int}$ PAS with the laboratory frame, a powder average over all three Euler angles α, β, and γ is necessary to align not only the PAS z axis with the rotor spinning axis but also the PAS x and y axes with the rotating x and y axes of the rotor. If γ is not

---

[2] Magic angle spinning spectra contain spinning sidebands separated by the spinning rate in s^{-1}.

[3] For quadrupolar nuclei with odd half integer spin quantum numbers the magnitudes of $\|H_Q\|$ and $\|H_Z\|$ can be comparable, and magic angle spinning does not yield sharp peaks.

included in the powder average, there are phase anomalies observed in the theoretical NMR signal calculated from the time-dependent density operator.

EXPLANATION OF *real_tensor_solid.nb*

The purpose of this notebook is to demonstrate coordinate system transformations of real space spherical tensors using Wigner rotations. The user is told to evaluate *wigrot.nb,* then close it without saving changes.

The first noncomment cell calculates the real space symmetric tensor alab20 for a static sample of a powdered solid according to Scheme 32.1 and Equation 32.2.

The next sequence of transformations takes the PAS apas[2,0] to the single crystal axis system, then to the goniometer axis system, and finally to the lab axis system (see Eqs. 32.5 and 32.6). First the new function acrystal is created. It gives the transformation of a single crystal real symmetric tensor from the PAS to the single crystal axis system characterized by the fixed angles $\alpha 1$, $\beta 1$, and $\gamma 1$. As an example and to illustrate the subsequent calculations, a new function acrystaln is created by substituting $\alpha 1=\pi/3$, $\beta 1=\pi/2$, and $\gamma 1=3\pi/2$ in acrystal.

The next cell creates a new function agoni, which gives the transformation from the crystal fixed axis system to the goniometer axis system characterized by the fixed angles $\alpha 2$, $\beta 2$, and $\gamma 2$. Again, for a numerical example the function agonin is created with fixed angles of $\alpha 2=\pi$, $\beta 2=\pi/2$, and $\gamma 2=0$ rad. The final transformation to the lab axis system is achieved by the function alab[2,0, α3_, β3_, γ3_], where the angles are fixed and relate the goniometer axis system to the lab axis system.

The next cells deal with the frequently encountered case of two or more internal Hamiltonians in a static powder sample. The necessary transformations are shown in Schemes 32.7a and 32.7b. Here there are assumed to be two active internal Hamiltonians, the chemical shift and the quadrupolar. In order to calculate the powder spectrum, we need to calculate the angular dependence of the lab frame alabcs[2,0] and alabQ[2,0] real space symmetric tensors. Since the magnitude of the quadrupolar Hamiltonian $\|H_Q\|$ is usually much greater than the magnitude of the chemical shift Hamiltonian $\|H_{CS}\|$, we arbitrarily choose to powder average to the laboratory frame from the quadrupolar Hamiltonian PAS. Therefore, we need to bring the chemical shift PAS into coincidence with the quadrupolar PAS before we can do the powder average for H_{CS}. This requires specific angles $\alpha 1$, $\beta 1$, and $\gamma 1$. The function acsQ[2,q_] gives the $l=2$ *chemical shift tensor in the quadrupolar* PAS. The lab frame $l=2$ chemical shift real space tensor is given by alabcs[2,0].

The real space quadrupolar tensor alabQ[2,0] only needs the powder average Euler angles α, β, and γ.

Magic Angle Spinning is a widely employed NMR technique. Typically, powder samples are spun rapidly in a cylindrical rotor at the magic angle θ, which is one of the solutions to the equation $3(\cos[\theta])^2-1=0$. In the following cells, we designate the magic angle as magang. The necessary transformations are shown in Scheme 32.8. We assume that there is a single dominant internal Hamiltonian, typically H_{CS} for an $I=1/2$ spin. The function arot[2,q_] is obtained by doing the powder average from the H_{CS} PAS to the rotor axis system using angles $\alpha 1$, $\beta 1$, and $\gamma 1$. Then the time-dependent specific angles ω_{rot} t and magang bring the sample from the rotor reference frame to the lab frame, yielding the desired alab20.

In anticipation of the discussion of average Hamiltonian theory in Chapter 34, we create the function f[t_] from alab20. Taking the *first-order* average over the *rotor period* averages $\overline{\overline{\mathrm{A}_{\mathrm{lab}}^{20}}}(t)$ yields zero, leaving only the isotropic component $\overline{\overline{\mathrm{A}_{\mathrm{lab}}^{00}}}$ to determine the frequency. However, experiment, second-order evaluation, or explicit propagation of the density operator with $\hat{\mathrm{H}}_{\mathrm{int}}$ shows the presence of spinning sidebands separated from the isotropic peak at integer multiples of the spin rate ω_{rot}.

HOMEWORK

Homework 32.1: Calculate the free induction decay (FID(t)) and then by Fourier Transformation the Spectrum obtained with magic angle spinning of a powder sample with

a. Chemical shift Hamiltonian, $I = 1/2$, $\delta_{zz} = 2\pi\ 20 \times 10^3$ rad s^{-1}, $\eta = 0$
b. Quadrupolar Hamiltonian, $I = 1$, $\delta_{zz} = 2\pi\ 100$ rad s^{-1}, $\eta = 0$
c. Homonuclear dipolar Hamiltonian, 2 coupled $I = 1/2$ spins, $\delta_{zz} = 2\pi\ 30 \times 10^3$ rad s^{-1}, $\eta = 0$

CHAPTER 33

TIME-INDEPENDENT PERTURBATION THEORY

Although individual nuclear spins will generally be in a superposition of states as described in Equation 10.11, the *detectable signal* from simple NMR experiments corresponds to a transition between adjacent “pure” eigenstates. Like the results from the Stern–Gerlach experiment , the observed NMR spectrum and corresponding FID can be calculated with *time-independent perturbation theory. More complicated NMR experiments where unobservable coherence orders are necessary in the course of the pulse sequence require explicit knowledge of the time-dependence of the density operator.* With this limitation, time-independent perturbation theory is useful for calculation of solid-state NMR powder spectra.

In the high field limit where $\left\|\hat{\mathrm{H}}_Z\right\| \gg \left\|\hat{\mathrm{H}}_{\mathrm{int}}\right\|$, the *first-order* corrections $\Delta E_{I,m}^{\mathrm{int}}(1)$ to the Zeeman energy levels $E_{I,m}$ are given by (Levine, 1974, pp. 178–185)

$$\Delta E_{I,m}^{\mathrm{int}}(1) = \left\langle I, m \middle| \hat{\mathrm{H}}_{\mathrm{int}} \middle| I, m \right\rangle \tag{33.1}$$

The *second-order* corrections $\Delta E_{I,m}^{\mathrm{int}}(2)$ are given by

$$\Delta E_{I,m_1}^{\mathrm{int}}(2) = \sum_{m_2 \neq m_1} \frac{\left|\left\langle I, m_1 \middle| \hat{\mathrm{H}}_{\mathrm{int}} \middle| I, m_2 \right\rangle\right|^2}{E_{I,m_1} - E_{I,m_2}} \tag{33.2}$$

Care must be taken to use consistent energy or frequency units. Since $E_{I,m_1} = \hbar\,\omega_{I,m_1}$, we use units of rad s^{-1} because these are most convenient for theoretical calculations.

Example 1 $\Delta E_{I,m}^{\mathrm{CS}}(1)$, first-order perturbation theory for the chemical shift, $I = 1/2$ spin

For the $m = 1/2$ Zeeman level, the perturbation is (see Equation 29.5):

$$\begin{aligned}\Delta E_{\frac{1}{2},\frac{1}{2}}^{\mathrm{CS}}(1) &= \left\langle \frac{1}{2},\frac{1}{2} \middle| \hat{\mathrm{H}}_{\mathrm{CS}} \middle| \frac{1}{2},\frac{1}{2} \right\rangle = \left\langle \frac{1}{2},\frac{1}{2} \middle| \overline{\overline{\mathrm{A}}}{}^{0,0}_{\mathrm{CS}}\, \hat{\mathrm{T}}^{0,0}_{\mathrm{CS}} + \overline{\overline{\mathrm{A}}}{}^{2,0}_{CS}\, \hat{\mathrm{T}}^{2,0}_{\mathrm{CS}} \middle| \frac{1}{2},\frac{1}{2} \right\rangle \\ &= \left\langle \frac{1}{2},\frac{1}{2} \middle| \overline{\overline{\mathrm{A}}}{}^{0,0}_{\mathrm{CS}}\, \hat{\mathrm{T}}^{0,0}_{\mathrm{CS}} \middle| \frac{1}{2},\frac{1}{2} \right\rangle + \left\langle \frac{1}{2},\frac{1}{2} \middle| \overline{\overline{\mathrm{A}}}{}^{2,0}_{\mathrm{CS}}\, \hat{\mathrm{T}}^{2,0}_{\mathrm{CS}} \middle| \frac{1}{2},\frac{1}{2} \right\rangle \end{aligned} \tag{33.3a}$$

A Primer of NMR Theory with Calculations in Mathematica®, First Edition. Alan J. Benesi.

where $\hat{\mathrm{T}}_{\mathrm{CS}}^{0,0} = -\sqrt{1/3}\,\omega_0\,\hat{\mathrm{I}}_z$ and $\hat{\mathrm{T}}_{\mathrm{CS}}^{2,0} = \sqrt{2/3}\,\omega_0\,\hat{\mathrm{I}}_z$. $\overset{=0,0}{\mathrm{A}_{\mathrm{CS}}}$ and $\overset{=2,0}{\mathrm{A}_{\mathrm{CS}}}$ are in the laboratory frame. Evaluating the eigenvalues of $\hat{\mathrm{I}}_z$ (see Chapter 10), using the orthonormality of the Zeeman eigenstates, and evaluating $\overset{=2,0}{\mathrm{A}_{\mathrm{CS}}}$ as shown in *real_tensor_solid.nb* and Table 31.2,

$$\Delta E^{\mathrm{CS}}_{\frac{1}{2},\frac{1}{2}}(1) = -\frac{1}{2}\sqrt{\frac{1}{3}}\,\overset{=0,0}{\mathrm{A}_{\mathrm{CS}}}\,\omega_0 + \frac{1}{2}\sqrt{\frac{2}{3}}\,\overset{=2,0}{\mathrm{A}_{\mathrm{CS}}}\,\omega_0$$

$$= \frac{1}{2}\rho_{\mathrm{iso}}\omega_0 + \frac{1}{2}\frac{1}{4}(1 + 3\cos[2\beta] - 2\eta\cos[2\alpha]\sin[\beta]^2)\delta_{zz}{}'\omega_0 \qquad (33.3\mathrm{b})$$

where ρ_{iso} is the isotropic chemical shift (in ppm) and $\delta_{zz}{}'$ is defined in Equations 29.3 and 29.5. For the $m = -1/2$ Zeeman level, the perturbation is

$$\Delta E^{\mathrm{CS}}_{\frac{1}{2},-\frac{1}{2}}(1) = -\frac{1}{2}\rho_{\mathrm{iso}}\omega_0 + -\frac{1}{2}\frac{1}{4}(1 + 3\cos[2\beta] - 2\eta\cos[2\alpha]\sin[\beta]^2)\delta_{zz}{}'\omega_0 \quad (33.3\mathrm{c})$$

The perturbation to the transition between the $m = 1/2$ and $m = -1/2$ Zeeman levels is given by the difference

$$\Delta E^{\mathrm{CS}}_{\frac{1}{2},\frac{1}{2}}(1) - \Delta E^{\mathrm{CS}}_{\frac{1}{2},-\frac{1}{2}}(1) == \rho_{\mathrm{iso}}\omega_0 + \frac{1}{4}(1 + 3\cos[2\beta] - 2\eta\cos[2\alpha]\sin[\beta]^2)\delta_{zz}{}'\omega_0$$

$$(33.3\mathrm{d})$$

In Figure 29.1, Equation 33.3d was used along with the simplifying assumption that $\rho_{\mathrm{iso}} = 0$ to generate the spectra (see *Hcsstatlineshape.nb*).

Example 2 $\Delta E^{\mathrm{Q}}_{I,m}(1)$, first-order perturbation theory for the quadrupolar Hamiltonian, $I = 1$ spin

The quadrupolar Hamiltonian $\hat{\mathrm{H}}_Q$ is a single spin interaction that occurs for nuclei with spin angular momentum quantum numbers $I > 1/2$. Unlike $I = 1/2$ nuclear spins, which have an even distribution of positive charge in the nucleus, $I > 1/2$ nuclear spins have a nonuniform distribution of positive charge in the nucleus. Over 2/3 of the NMR-observable nuclei in the periodic table are quadrupolar. $\hat{\mathrm{H}}_Q$ arises from the *electrical* interaction between the nonuniform electric field gradient tensor $\overset{=}{\mathrm{A}_{\mathrm{Q}}}$ due to electron orbitals near the nuclear spin and the nonspherical distribution of positive charge within the nucleus itself. $\hat{\mathrm{H}}_Q$ can have a magnitude larger than the Zeeman Hamiltonian.

In Cartesian tensor form, $\hat{\mathrm{H}}_{\mathrm{Q}} = \hat{\mathrm{I}}\cdot\overset{=}{\mathrm{Q}}\cdot\hat{\mathrm{I}}$, where $\overset{=}{\mathrm{Q}}$ has units rad s^{-1}, $\overset{=}{\mathrm{Q}} = K_{\mathrm{Q}}\overset{=}{\mathrm{A}_{\mathrm{Q}}} = \dfrac{eQ_{\mathrm{nuc}}}{2I(2I-1)\hbar}\overset{=}{\mathrm{A}_{\mathrm{Q}}}$, where $\overset{=}{\mathrm{A}_{\mathrm{Q}}}$ is the real space electric field gradient tensor, e is the electron charge, Q_{nuc} is the nuclear quadrupole moment, and I is the nuclear spin angular momentum quantum number. In the quadrupolar PAS, $\delta_{zz}{}' = Q_{zz}{}' = K_{\mathrm{Q}}A^{Q'}_{zz} = \dfrac{e^2 qQ_{\mathrm{nuc}}}{2I(2I-1)\hbar} = \omega_{\mathrm{Q}} = 2\pi\,\mathrm{qcc}$ (Gerstein and Dybowski, 1985, pp. 124–128). The qcc in s^{-1} is called the quadrupole coupling constant.

As the first example, we consider the first-order quadrupolar perturbation for. an $I=1$ nuclear spin. Because the real space electric field gradient tensor $\overline{\overline{\mathrm{A}}}_{\mathrm{Q}}$ must satisfy Laplace's equation, $\nabla^2 \overline{\overline{\mathrm{A}}}_{\mathrm{Q}} = 0$, $\overline{\overline{\mathrm{A}}}_{\mathrm{Q}}$ is traceless and $\overline{\overline{\mathrm{A}}}_{\mathrm{Q}}^{00}(\mathrm{lab}) = \overline{\overline{\mathrm{A}}}_{\mathrm{Q}}^{00}(\mathrm{PAS}) = 0$. Therefore

$$\hat{\mathrm{H}}_{\mathrm{Q}} = \overline{\overline{\mathrm{A}}}_{\mathrm{Q}}^{00} \cdot \hat{\mathrm{T}}_{\mathrm{Q}}^{00} + \overline{\overline{\mathrm{A}}}_{\mathrm{Q}}^{20} \cdot \hat{\mathrm{T}}_{\mathrm{Q}}^{20} = \overline{\overline{\mathrm{A}}}_{\mathrm{Q}}^{20} \cdot \hat{\mathrm{T}}_{\mathrm{Q}}^{20} \tag{33.4}$$

and the first-order perturbations to the different m levels are as follows:

$$\Delta E_{1,1}^{\mathrm{Q}}(1) = \left\langle 1,1 \middle| \hat{\mathrm{H}}_{\mathrm{Q}} \middle| 1,1 \right\rangle = \left\langle 1,1 \middle| \overline{\overline{\mathrm{A}}}_{Q}^{2,0}\ \hat{\mathrm{T}}_{\mathrm{Q}}^{2,0} \middle| 1,1 \right\rangle = \left\langle 1,1 \middle| \overline{\overline{\mathrm{A}}}_{\mathrm{Q}}^{2,0}\ \sqrt{\frac{1}{6}}(3I_z^2 - I^2) \middle| 1,1 \right\rangle \tag{33.5a}$$

where, as shown in *spherical_tensors_wigner.nb*, $\hat{\mathrm{T}}_{\mathrm{Q}}^{2,0} = \sqrt{1/6}\,(3I_z^2 - I^2)$, and

$$I_z^2 \mid I,m> = m^2 \mid I,m> \tag{33.5b}$$

$$I^2 \mid I,m> = I(I+1) \mid I,m> \tag{33.5c}$$

The orthonormality of the Zeeman eigenstates yields the following:

$$\Delta E_{1,1}^{Q}(1) = \sqrt{\frac{1}{6}}\,\overline{\overline{\mathrm{A}}}_{\mathrm{Q}}^{2,0} \tag{33.5d}$$

$$\Delta E_{1,0}^{\mathrm{Q}}(1) = -2\sqrt{\frac{1}{6}}\,\overline{\overline{\mathrm{A}}}_{\mathrm{Q}}^{2,0} \tag{33.5e}$$

$$\Delta E_{1,-1}^{\mathrm{Q}}(1) = \sqrt{\frac{1}{6}}\,\overline{\overline{\mathrm{A}}}_{\mathrm{Q}}^{2,0} \tag{33.5f}$$

Transitions are only allowed between adjacent energy levels, with

$$\Delta E_{1,1}^{\mathrm{Q}}(1) - \Delta E_{1,0}^{\mathrm{Q}}(1) = 3\sqrt{\frac{1}{6}}\,\overline{\overline{\mathrm{A}}}_{\mathrm{Q}}^{2,0} \tag{33.5g}$$

$$\Delta E_{1,0}^{\mathrm{Q}}(1) - \Delta E_{1,-1}^{\mathrm{Q}}(1) = -3\sqrt{\frac{1}{6}}\,\overline{\overline{\mathrm{A}}}_{\mathrm{Q}}^{2,0} \tag{33.5h}$$

The powder spectra obtained for these transitions are calculated in *rigiddeutlineshapes.nb*. The methods used to calculate powder lineshapes are discussed in Chapter 35.

Example 3 $\Delta E_{I,m}^{\mathrm{Q}}(1)$, first-order perturbation theory for the quadrupolar Hamiltonian, $I=3/2$ spin

For I = 3/2 spins,

$$\Delta E_{\frac{3}{2},\frac{3}{2}}^{\mathrm{Q}}(1) = 3\sqrt{\frac{1}{6}}\,\overline{\overline{\mathrm{A}}}_{\mathrm{Q}}^{2,0} \tag{33.6a}$$

$$\Delta E_{\frac{3}{2},\frac{1}{2}}^{\mathrm{Q}}(1) = -3\sqrt{\frac{1}{6}}\,\overline{\overline{\mathrm{A}}}_{\mathrm{Q}}^{2,0} \tag{33.6b}$$

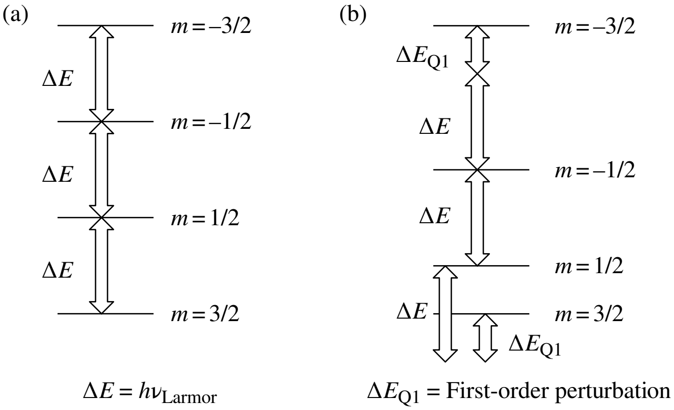

Figure 33.1 $\hat{\mathrm{H}}_{\mathrm{Q}}$ First-Order Perturbation of Zeeman Energy Levels for an $I=3/2$ nuclear spin (a) Unperturbed Zeeman energy levels for $I=3/2$ nuclear spin (b) First-order quadrupolar perturbations of Zeeman levels. The central transition ($m=1/2$ to $m=-1/2$) is unaffected to first order.

$$\Delta E^{\mathrm{Q}}_{\frac{3}{2},\frac{-1}{2}}(1) = -3\sqrt{\frac{1}{6}}\,\bar{\bar{\mathrm{A}}}_{\mathrm{Q}}^{2,0} \tag{33.6c}$$

$$\Delta E^{\mathrm{Q}}_{\frac{3}{2},\frac{-3}{2}}(1) = 3\sqrt{\frac{1}{6}}\,\bar{\bar{\mathrm{A}}}_{\mathrm{Q}}^{2,0} \tag{33.6d}$$

Transitions are only allowed between adjacent energy levels, with

$$\Delta E^{\mathrm{Q}}_{\frac{3}{2},\frac{3}{2}}(1) - \Delta E^{\mathrm{Q}}_{\frac{3}{2},\frac{1}{2}}(1) = 6\sqrt{\frac{1}{6}}\,\bar{\bar{\mathrm{A}}}_{\mathrm{Q}}^{2,0} \tag{33.6e}$$

$$\Delta E^{\mathrm{Q}}_{\frac{3}{2},\frac{1}{2}}(1) - \Delta E^{\mathrm{Q}}_{\frac{3}{2},\frac{-1}{2}}(1) = 0 \tag{33.6f}$$

$$\Delta E^{\mathrm{Q}}_{\frac{3}{2},\frac{-1}{2}}(1) - \Delta E^{\mathrm{Q}}_{\frac{3}{2},\frac{-3}{2}}(1) = -6\sqrt{\frac{1}{6}}\,\bar{\bar{\mathrm{A}}}_{\mathrm{Q}}^{2,0} \tag{33.6g}$$

The $m=3/2$ to $m=1/2$ and $m=-1/2$ to $m=-3/2$ transitions are called "satellite" transitions. The $m=1/2$ to $m=-1/2$ transition is called the "central" transition and is unaffected to first order. The corresponding energy levels are shown in Figure 33.1.

Example 4 $\Delta \mathrm{E}^{\mathrm{Q}}_{I,m}(1)$, second-order perturbation theory for the quadrupolar Hamiltonian, $I=3/2$ spin

$\left\|\hat{\mathrm{H}}_{\mathrm{Q}}\right\|$ can be sufficiently large that the high field assumption, $\left\|\hat{\mathrm{H}}_{\mathrm{Z}}\right\| \gg \left\|\hat{\mathrm{H}}_{\mathrm{Q}}\right\|$ is no longer valid. In this case, the full Hamiltonian (Eq. 31.1) must be used, and second-order perturbation theory is required to predict the observed spectra of the $m=1/2$ to $m=-1/2$ "central" transitions of odd-half-integer quadrupolar nuclei. It

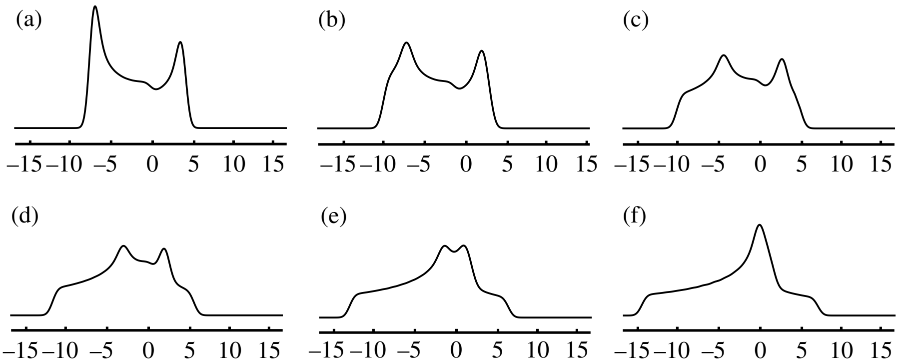

Figure 33.2 Second -order quadrupolar spectra of the central transition ($m = 1/2$ to $m = -1/2$) of an $I = 3/2$ spin, qcc $= 2.5 \times 10^6\,\mathrm{s}^{-1}$, $\nu_0 = 75 \times 10^6\,\mathrm{s}^{-1}$ calculated in *Hq2pert2.nb*. (a) $\eta = 0$ (b) $\eta = 0.2$ (c) $\eta = 0.4$ (d) $\eta = 0.6$ (e) $\eta = 0.8$ (f) $\eta = 1$. Frequency is expressed in kHz ($10^3\,\mathrm{s}^{-1}$). Note that most NMR spectrometers "reverse" the frequency axis to increase from right to left rather than left to right.

also affects the satellite transitions, but the static spectra of the latter are dominated by the first-order $\hat{H}_Q$.

Unlike the first-order perturbations, the second-order perturbations, Equation 33.2, require that the contributions come from Zeeman spin space terms with $m_1 \neq m_2$. Since the real space electric field gradient tensor $\overset{=}{A}_Q$ is traceless, only $l = 2$ terms contribute to $\hat{H}_Q$. The only way that the $m_1 \neq m_2$ requirement can yield non-zero values for $I, m_1 | \hat{H}_Q | I, m_2$ in Equation 33.2 is if the spin space terms in $\hat{H}_Q$ contain $\hat{I}_+$ or $\hat{I}_-$. Therefore, the only spin space tensors that can contribute are $\hat{T}_Q^{2,1} = -\frac{1}{2}(\hat{I}_z\hat{I}_+ + \hat{I}_+\hat{I}_z)$, $\hat{T}_Q^{2,-1} = \frac{1}{2}(\hat{I}_z\hat{I}_- + \hat{I}_-\hat{I}_z)$, $\hat{T}_Q^{2,2} = \frac{1}{2}\hat{I}_+^2$, and $\hat{T}_Q^{2,-2} = \frac{1}{2}\hat{I}_-^2$. Hence the effective second-order quadrupolar Hamiltonian $\hat{H}_Q(2)$ is (compare with Eq. 33.4):

$$\hat{H}_Q(2) = -\overset{=}{A}{}_Q^{2,1}\,\hat{T}_Q^{2,-1} - \overset{=}{A}{}_Q^{2,-1}\,\hat{T}_Q^{2,1} + \overset{=}{A}{}_Q^{2,2}\,\hat{T}_Q^{2,-2} + \overset{=}{A}{}_Q^{2,-2}\,\overset{=}{A}{}_Q^{2,2} \tag{33.7}$$

The second-order quadrupolar perturbations for the central and satellite transitions from Equation 33.2 are calculated in the notebook *Hq2pert.nb*. For the central transition, $|\frac{3}{2},\frac{1}{2}> \to |\frac{3}{2},\frac{-1}{2}>$, the perturbation is

$$\Delta E^{Q}_{\frac{3}{2},\frac{1}{2}}(2) - \Delta E^{Q}_{\frac{3}{2},\frac{-1}{2}}(2) = -\frac{3}{\nu_0}\overset{=}{A}{}_Q^{2,1}\overset{=}{A}{}_Q^{2,1*} + \frac{3}{2\nu_0}\overset{=}{A}{}_Q^{2,2}\overset{=}{A}{}_Q^{2,2*} - \frac{3}{2\nu_0}\overset{=}{A}{}_Q^{2,-1}\overset{=}{A}{}_Q^{2,-1*} + \frac{3}{2\nu_0}\overset{=}{A}{}_Q^{2,-2}\overset{=}{A}{}_Q^{2,-2*} \tag{33.8}$$

The powder spectra corresponding to these first- and second-order perturbations are calculated in *Hq2pert2.nb*, shown in Figure 33.2, and discussed in Chapter 35.

EXPLANATION OF *rigiddeutlineshapes.nb*

This notebook calculates rigid deuterium powder lineshapes using the results from time-independent perturbation theory. The user is told to evaluate *wigrot.nb*, then close it without saving. The user must also open and evaluate the file *repangwt5253* and SHOW THE FULL OUTPUT. This is not a Mathematica notebook but a list of 5253 REPULSION-calculated random powder average (α, β) angle pairs and their respective weights in the powder average (Bak and Nielsen, 1997).

The first noncomment cell calculates the real space spherical tensor responsible for the powder spectrum, alab[2,0]. Using the relationship (see Table 29.1) $\delta_{zz}=e^2qQ/(2I\,(2I-1)\ \nabla=\omega_Q/(2I\,(2I-1)=2\pi$ qcc/(2I (2I−1), π qcc is substituted for δ_{zz} (rad s^{-1}) for $I=1$ deuterium.

Using Equations 33.5g and 33.5h functions ν_1 and ν_2 are created for the frequency-dependence of the two transitions. The function gauss is created for Gaussian broadening needed for each of the finite number of frequencies calculated with the finite number of powder average angles used in the powder average (see Chapter 34). Next we create the functions boogie1 and boogie2. Next the intensity and powder functions are created.

Next, eleven different powder spectra (temp0–temp10) are calculated using lb = 5000 s^{-1}, qcc = 200,000 s^{-1}, and η values ranging from 0 to 1 in increments of 0.1. These are then plotted. If one examines the $\eta=0$ plot, it is easy to understand what is meant by the “horns” in the powder spectrum. These correspond to the most likely value for the Euler angle β, which is 90° for each of the two transitions. The least intense parts of the powder spectrum are the “parallel edges,” which occur at $\beta=0°$ for each of the transitions.

EXPLANATION OF *Hq2pert.nb*

This notebook calculates the expressions obtained from Equations 33.7 and 33.8 for an $I=3/2$ nuclear spin subject only to the quadrupolar Hamiltonian. The user is told *not* to evaluate *matrep2.nb* because *Hq2pert.nb* creates rules that would conflict with those from *matrep2.nb*. The first cells define functions that calculate the effects of the operators iz, iplus, imin on the spin angular momentum eigenstate “kets” |*l,m*>. These functions are necessary to evaluate the second-order time-independent quadrupolar perturbations of the energy levels. The functions *t*22, *t*2*m*2, *t*21, and *t*2*m*1 are in turn created from the functions iz, iplus, and imin.

The spin is assumed to be $I=3/2$.

The next cell gives the second-order quadrupolar Hamiltonian hq2 (see Eq. 33.7).

The second-order perturbation to the |3/2, 1/2>energy level, ΔE[3/2,1/2] is calculated first (in rad s^{-1}). Only terms that end up in the |3/2, 1/2>energy level contribute. The inverse $\pm\omega$0 and inverse $\pm 2\omega$0 factors arise from single quantum and double quantum transitions, respectively. These are caused by the action of the *t*21 and *t*22 functions on the |3/2, −1/2>and |3/2, −3/2>eigenstates.

The second-order perturbation to the |3/2,−1/2>energy level, ΔE[3/2,−1/2], is calculated in the same way.

The second-order central transition perturbation, ΔEcen, is given by the difference of ΔE[3/2,1/2] and ΔE[3/2,−1/2].

The second-order perturbations, ΔE[3/2,3/2] and ΔE[3/2,−3/2], are calculated in the same way as for the other energy levels. The second-order satellite transition, ΔEsat1, is given by the difference of ΔE[3/2,3/2] and ΔE[3/2,1/2]. The second-order satellite transition, ΔEsat2, is given by the difference of ΔE[3/2,−1/2] and ΔE[3/2,-3/2].

The central transition and satellite transition perturbations calculated here are used in the next notebook, *Hq2pert2.nb*.

EXPLANATION OF *Hq2pert2.nb*

This notebook calculates powder lineshapes corresponding to the second-order quadrupolar perturbations calculated in *Hq2pert.nb*. The user must exit Mathematica after having finished *Hq2pert.nb*. After starting a fresh Mathematica session, the user must evaluate *wigrot.nb*, then close it without saving changes. Then the user must open *repangwt5253* (it is NOT a notebook), evaluate it, choose show full output, then close it without saving changes.

The first noncomment cell reproduces the definition of ΔEcen from *Hq2pert.nb*. The next cells calculate the lab frame real space terms needed to evaluate the powder lineshape, *a*21, *a*2*m*1, *a*22, and *a*2*m*2. These give the angular dependence of the perturbation ΔEcen.

For $I=3/2$, we make the substitution $\delta_{zz}=\dfrac{2\pi\,\mathrm{qcc}}{2I(2I-1)}=\dfrac{2\pi\,\mathrm{qcc}}{6}$, where qcc is the quadrupolar coupling constant in s^{-1} (see Table 29.1). We then convert the resulting expression into the frequency function $\nu 1$. Then we introduce the function gauss and plot it. The function boogie1 applies the gauss function to the function $\nu 1$. The intensity function gives the numerical value of the boogie1 function.

Next, examples of the angles and weights contained in *repangwt5253* are shown. For example, repangwt[[5253]] consists of three values, $\alpha=3.13156$ rad, $\beta=1.90438$ rad, and a weight of 1.00136.

The next cells create the powder function that adds all the different Gaussian broadened intensities for all 5253 of the *repangwt5253* Euler angles.

Next, the powder function is used to create powder spectra (temp through temp5) for the following parameters: $\mathrm{lb}=500\,\mathrm{s}^{-1}$, $\mathrm{qcc}=2.5\times10^{6}\,\mathrm{s}^{-1}$, and the Larmor frequency $2\pi\,75\times10^{6}\,\mathrm{rad\,s}^{-1}$, and a range of η values from 0 to 1.0. These are then plotted.

Next, the same process is repeated to calculate powder spectra corresponding to ΔEsat1. Using the same parameters as for the central transition, the plots are shown to depend on the Euler angle γ. If, however, the average over all possible γ angles is taken, the spectra obtained are simpler.

HOMEWORK

Homework 33.1: Calculate the first-order quadrupolar perturbations for an $I=5/2$ nuclear spin.

Homework 33.2: Calculate the second-order quadrupolar perturbations for the central transition of an $I=5/2$ nuclear spin.

CHAPTER 34

AVERAGE HAMILTONIAN THEORY

Nuclear magnetic resonance Hamiltonians are often time-dependent. One way to deal with the time-dependence is to propagate the density operator with sufficiently small time increments that the Hamiltonian is approximately constant during the increment (see Eq. 17.2b). If the Hamiltonian has a periodic time-dependence (such as internal Hamiltonians in the rotating frame), an alternative approach is to calculate the average Hamiltonian over the period τ_p of the oscillation (Ernst et al., 1987, pp. 72–75; Gerstein and Dybowski, 1985, pp. 137–152).

In average Hamiltonian theory, the time-dependent Hamiltonian is approximated with a sum of time-independent Hamiltonians:

$$\hat{\mathrm{H}}(\tau_p) = \bar{\mathrm{H}}^0 + \bar{\mathrm{H}}^1 + \bar{\mathrm{H}}^2 + \cdots \tag{34.1}$$

where

$$\bar{\mathrm{H}}^0 = \frac{1}{\tau_p}\int_0^{\tau_p} \hat{\mathrm{H}}(t)dt \tag{34.2}$$

$$\bar{\mathrm{H}}^1 = \frac{-i}{2\tau_p}\int_0^{\tau_p} dt_1 \int_0^{t_1} [\hat{\mathrm{H}}(t_1), \hat{\mathrm{H}}(t_2)]\,dt_2 \tag{34.3}$$

$$\bar{\mathrm{H}}^2 = \frac{1}{6\tau_p}\int_0^{\tau_p} dt_1 \int_0^{t_1} dt_2 \int_0^{t_2} \{[[\hat{\mathrm{H}}(t_1), \hat{\mathrm{H}}(t_2)], \hat{\mathrm{H}}(t_3)] + [[\hat{\mathrm{H}}(t_3), \hat{\mathrm{H}}(t_2)], \hat{\mathrm{H}}(t_1)]\,dt_3 \tag{34.4}$$

etc.

$\bar{\mathrm{H}}^2$ and higher orders are not necessary for internal Hamiltonians $\hat{\mathrm{H}}_{\mathrm{int}}$ if $\|\hat{\mathrm{H}}_{\mathrm{int}}\| \ll \left|\|\hat{\mathrm{H}}_Z\right|\|$.

We have already encountered the zeroth-order average Hamiltonian $\bar{\mathrm{H}}^0$ when the nine terms obtained for the laboratory frame internal Hamiltonian in Equation 31.1 are propagated to the rotating frame by the unitary transformation

$$\hat{\mathrm{H}}_{\mathrm{rot}} = e^{-i\gamma B_0 \hat{\mathrm{I}}_z t}\,\hat{\mathrm{H}}_{\mathrm{lab}}\,e^{i\gamma B_0 \hat{\mathrm{I}}_z t} = e^{i\omega_0 \hat{\mathrm{I}}_z t}\,\hat{\mathrm{H}}_{\mathrm{lab}}\,e^{-i\omega_0 \hat{\mathrm{I}}_z t} \tag{34.5}$$

$\bar{\mathrm{H}}^0$ is calculated by integrating over the Larmor period $\tau_p = 2\pi/\omega_0$. Only the secular, time-independent terms survive, yielding Equation 31.6.

A Primer of NMR Theory with Calculations in Mathematica®, First Edition. Alan J. Benesi.

$\bar{\mathrm{H}}^1$ can be calculated using Equation 34.3 and the matrix representation of spin operators as shown in *Hqavg2.nb* or by commutation relations between spin angular momentum operators as shown in *Hqavg2new.nb.*

EXPLANATION OF *Hqavg2*

This notebook calculates the first-order average quadrupolar Hamiltonian for an $I=3/2$ nuclear spin using matrix representation of the spin space spherical tensors. The user is told to evaluate matrep2.nb, then close it without saving the changes. The nuclear spin is $I=3/2$. The matrix representations of the density operator, the spin angular momentum, and the Hamiltonians are used.

The matrix representations *T*[*l*,*m*] of the quadrupolar spin space spherical tensors are defined.

The quadrupolar Hamiltonian is the only (or dominant) internal Hamiltonian. hqlab is calculated using Equation 31.1.

Next, the propagators u1, u1adj, u2, and u2adj are evaluated. u1 and u1adj are used to propagate Hqlab to the rotating frame, yielding hqrot1.

The zeroth-order average Hamiltonian (Eq. 34.2) is evaluated by integration to yield h1rotavg0. The result is shown to be identical to *A*[2,0]**T*[2,0].

Since we need it for the first-order average Hamiltonian, we calculate hqrot2 using u2 and u2adj.

Next, we calculate the matrix representation of the commutator of hqrot1 and hqrot2, yielding hqcomm. The first-order average Hamiltonian, $\overline{H_{Q1}}$ (Eq. 34.3), is then evaluated by double integration over the time variables $t1$ and $t2$. The secular (diagonal) part is then selected to yield Hq1avg. Next, we remember that the $l=1$ terms (i.e., *A*[1,1], etc) are zero, simplifying the expression for Hq1avg. Next, the real space spherical tensors *A*[2,*m*] are calculated, yielding a21, a2m1, a22, and a2m2. With these, Hq1avg is calculated in matrix representation.

The central transition is given by Hq1avg[[2,2]]–Hq1avg[[3,3]] and called hqcen. 2 π qcc/6 is substituted for δ_{zz} since $I=3/2$. We then compare this with ΔEcen calculated in hq2pert2.nb using time-independent perturbation theory. Although they look superficially different, they are identical!

EXPLANATION OF *Hqavg2new.nb*

This notebook calculates the first-order average quadrupolar Hamiltonian for an $I=3/2$ nuclear spin but leaves all the spin operators in symbolic form until the end of the notebook when they are evaluated in matrix form for the purpose of comparison with the results in *Hqavg2.nb*. If the user has just evaluated *Hqavg2.nb*, he or she must exit and then restart Mathematica. Next, the user must evaluate *commutators.nb* and close it without saving. Next, the user must evaluate *matrep2.nb,* then close it without saving.

The first-order average Hamiltonian is calculated using commutator relations (see Chapter 19).

First, the *T*[2,*m*] are expressed in symbolic form (e.g., *T*[2,2] = (iplus.iplus)/2).

Then the lab frame quadrupolar Hamiltonian Hqlab is defined.

Hqlab is then propagated into the rotating frame with the time variable *t*1 to yield hqrot1. Hqlab is also propagated into the rotating frame with time variable *t*2 to yield hqrot2. Both propagations take advantage of Equation 41.8, $\hat{T}^{l,m}_{\mathrm{rot}}(t) = e^{-i\omega_0 \hat{I}_z t}\,\hat{T}^{l,m} e^{i\omega_0 \hat{I}_z t} = \hat{T}^{l,m}\, e^{\mathrm{i m}\omega_0 \mathrm{t}}$.

Next, the zeroth-order average Hamiltonian is calculated (Eq. 34.2) to yield *A*[2,0] *T*[2,0], the same as for the first-order time-independent perturbation theory result.

Next, the expressions for hqrot1 and hqrot2 are calculated.

Then the commutator of hqrot1 and hqrot2 is calculated, yielding hqcomm. The parts that were unable to be evaluated by the commspin function were then reevaluated by manually replacing the function commspin with the function comm, then reevaluating. This yields an extremely complicated mess. However, Mathematica is able to perform the double integration of hqcomm over the time variables *t*1 and *t*2 to yield the first-order average Hamiltonian $\overline{\mathrm{H}}_{\mathrm{Q1}}$ (see Eq. 34.3). This is also extremely complicated, even after several simplifications yield the result temp.

The next cells substitute the *I* = 3/2 matrix representations for the spin angular momentum operators iplus, imin, and iz. After full simplification, this is defined as $\overline{\mathrm{H}}_{\mathrm{Q1}}$, the secular part of which is extracted to yield Hq1avg. Except for a sign change, the result is identical to the one from time-independent perturbation theory.

HOMEWORK

Homework 34.1: Calculate $\overline{\mathrm{H}}^0$ and $\overline{\mathrm{H}}^1$ for an *I* = 1/2 spin undergoing magic angle spinning, using $\tau_p = \tau_{\mathrm{rotor}}$. Assume that only $\hat{\mathrm{H}}_{\mathrm{CS}}$ is active.

Homework 34.2: Does the sign change obtained in the expression for Hq1avg in *Hqavg2new.nb* affect the powder spectrum? Can you detect the origin of the change in sign?

CHAPTER 35

THE POWDER AVERAGE

In a powdered static sample of a *rigid solid*, the principal axis systems (PASs) of internal Hamiltonians do not change their orientations with respect to the laboratory reference frame during the course of the NMR experiment. This means that the $l = 2$ real space tensors $\overline{\overline{\mathrm{A}}}{}^{2,q}_{\mathrm{int}}$ keep the same Euler angles throughout the NMR experiment for each microcrystal in the powder sample. In this case, the powder spectrum is obtained by adding the appropriately weighted contributions from all possible Euler angles. In the case of static powder samples, the β Euler angle corresponds to the "latitude" in spherical polar coordinates and must be weighted according to $\sin(\beta)$. The α Euler angle corresponds to the longitude. The γ Euler angle is not required for static NMR samples except in the case of the satellite transitions of quadrupolar nuclei. In some simple cases where first-order perturbation theory can be used, the powder spectrum can be calculated analytically for each allowed transition with $\Delta m = 1$ using the complete elliptic integral of the first kind (Mehring, 2002). But in most cases it is more convenient to calculate the powder spectrum numerically using one of the following numerical strategies:

TIME-INDEPENDENT PERTURBATION THEORY POWDER SPECTRA

Time-independent perturbation theory (Chapter 33) gives spectral frequencies corresponding to a given Hamiltonian PAS with specific Euler angles relative to the laboratory reference frame. The powder spectrum is "built" using the following sequence of steps:

1. Choose new Euler angles (typically α and β).
2. Weight the angles appropriately, that is, by $\sin(\beta)$.
3. Apply line broadening so that addition of a finite number of α and β angles yields the powder spectrum.
4. Save and add to sum saved from previous α and β angles.
5. Loop back to 1. Repeat until entire set of Euler angles has been evaluated.

One example of this type of calculation was shown in *Hcsstatlineshape.nb*. In this case, 1° increments in β and 2° increments in α were used, with the β increments weighted by $\sin(\beta)\, d\beta$.

A Primer of NMR Theory with Calculations in Mathematica®, First Edition. Alan J. Benesi.

A more efficient way to calculate a minimal set of powder average Euler angles α and β is to use the repulsion method (Bak and Nielsen, 1997), in which each of a finite set of points on a sphere is allowed to experience repulsive forces from the others and move accordingly. After a sufficient number of increasingly small displacements, the points arrange themselves into an almost perfectly even distribution on the spherical surface. After motion is stopped, corrections are made to adjust the "weight" of each point on the sphere. An example of the repulsion calculation of these points is shown in *repulsionbook.nb*. A set of 5253 repulsion points was also calculated numerically and is used in many of the Mathematica notebooks, including *Hq2pert2.nb*.

POWDER AVERAGE DENSITY OPERATOR

Time-independent perturbation theory only works for the simplest NMR experiments. More complicated NMR experiments require calculation of the time-dependent density operator $\rho(t)$ with the Liouville–von Neumann (LVN) equation (Eqs. 13.1 and 13.2). The *detected* NMR signal in an NMR experiment is the free induction decay or $\mathrm{FID}(t_2)=\mathrm{Trace}[I^+ \rho(t_2)]$ (see Eq. 18.1). The observed NMR signal $\mathrm{FID}_{\mathrm{powder}}(t_2)$ for a static powder sample of a rigid solid is calculated using the following steps:

1. Choose new Euler angles (typically α and β).
2. Weight the angles appropriately (e.g., by $\sin(\beta)$).
3. Use LVN equation to calculate $\rho(t_2)$ for each scan.
4. Calculate $\mathrm{FID}(t_2)=\mathrm{Trace}[I^+ \rho(t_2)]$.
5. Add $\mathrm{FID}(t_2)$ to sum of previous $\mathrm{FID}(t_2)$.
6. Repeat steps 3 through 6 until full phase cycle has been completed.
7. Save sum from 6 and add to sum saved from previous α and β angles.
8. Loop back to 1. Repeat until entire set of Euler angles has been evaluated. This yields $\mathrm{FID}_{\mathrm{powder}}(t_2)$.
9. Apply time-dependent line broadening and Fourier transform the powder NMR signal $\mathrm{FID}_{\mathrm{powder}}(t_2)$ (see Chapter 9) to obtain the 1D spectrum.

In the case of 2D NMR experiments, an additional loop is used to repeat steps 3 through 6 for each value of the t_1 interval and save the calculated FID separately. This yields $\mathrm{FID}(t_2, t_1)$. Each $\mathrm{FID}(t_2, t_1)$ can be added in the outer powder average loop (steps 1 through 8) to obtain $\mathrm{FID}_{\mathrm{powder}}(t_2, t_1)$. One can also save $\rho_{\mathrm{powder}}(t_2)$ or the set of $\rho_{\mathrm{powder}}(t_1, t_2)$'s and obtain expectation values for other operators as a function of t_2 (or t_1, t_2).

EXPLANATION OF *repulsionbook.nb*

This notebook calculates optimal pairs of Euler angles (α,β) by letting an arbitrary initial distribution of points on a sphere undergo small displacements due to repulsive forces (Bak and Nielsen, 1997). After a sufficient number of sufficiently small displacements, the distribution converges to an uniform arrangement of points on the sphere. For static powdered solid samples, the α Euler angle corresponds to the "longitudinal" angle ϕ (or $\pi-\phi$) (Torchia and Szabo, 1982) and the β angle corresponds to the "latitudinal" angle θ.

The initial distribution of points on a sphere is defined in several steps. The starting θ values are distributed in increments of $\pi/20$ from the "north pole," $\theta=0$, to the "south pole," $\theta=\pi$. The next cells calculate the initial distribution of ϕ values for each θ value. The number of ϕ points for a given θ should vary as sin[θ], as defined in the function nphi[*x*_]. The function ϕ[*x*_] is created so that a slightly randomized set of ϕ points can be calculated for each value of θ. Some examples are given for a couple of θ values. Next, the initial distribution of points p is calculated.

The function cart is created to convert from spherical polar to Cartesian coordinates. It is assumed that the repulsive forces and resulting displacements between the points on the sphere surface can be approximated by Cartesian forces and displacements. Using cart, the initial distribution of points in Cartesian coordinates, pcart, is created.

Next the functions cosdel, delang, dp, and dist are created. These functions are used in the function dpn to calculate the displacements. The function union is created to give the numerical values of all of the points.

The union of all of the initial points in Cartesian coordinates is designated as upcart. The initial Cartesian positions are then plotted with the built-in Mathematica function ListPointPlot3D. The resulting graphics object is designated pgraph. The total number of points plotted is 269.

We then show the initial set of points on a sphere using the built-in Mathematica functions Show and Graphics3D. It is clear the points are not evenly distributed.

Next the function bigdp is created to calculate the displacements. The size of the displacements is controlled with the variable inc. The function newp and bignewp are created to keep the points on a unit sphere.

The next cells show how to make an arbitrary number of successive displacements using the built-in Mathematica function Nest. The next cells show that if inc = 0.0005, 100 iterations do not yield a reasonable distribution. A subsequent calculation with inc = 0.0001 gives much better results.

CHAPTER 36

OVERVIEW OF MOLECULAR MOTION AND NMR

The connection between angular motions and NMR is fundamental. Assuming that the samples are not reacting and that the magnetic field is homogeneous, the source of photons that stimulate NMR relaxation is the reorientation of the internal NMR Hamiltonian principal axis systems (PASs) in real space. If the allowed angles and reorientation rates are known*, it is possible to predict the observed NMR spectrum and NMR relaxation times*. Conversely, the experimental NMR spectrum and experimental NMR relaxation times can be used to assess the allowed orientations and reorientation rates. This relationship makes NMR a powerful tool for the elucidation of molecular dynamics.

The simplifying effect of angular reorientation on liquid-state NMR spectra was discussed briefly in earlier chapters. In liquids, rapid rotational diffusion in real space, generally assumed to be *small-step* rotational diffusion (Diezemann and Sillescu, 1999), averages the anisotropic real space $\overset{=2,0}{\mathrm{A}}_{\mathrm{int}}$ part of the Hamiltonians to zero, leaving only the isotropic real space $\overset{=0,0}{\mathrm{A}}_{\mathrm{int}}$ parts to determine the spectrum (Eq. 29.5). This averaging can be understood in semiquantitative terms. Each complex data point of the rotating frame experimental free induction decay is collected as a single voltage value acquired in an approximately 100-nanosecond window, while the rotational correlation time τ_c of small molecules is on the order of 0.1 nanosecond or less. All possible orientations of the molecule and nuclear PASs are explored during the 100-nanosecond collection interval. In *Hcsstatlineshape.nb,* it is shown that $\int_0^{2\pi}\int_0^{\pi} \overset{=2,0}{\mathrm{A}}_{int}(\alpha,\beta)\sin[\beta]d\beta\, d\alpha = 0\cdot$

Angular reorientation also affects solid-state NMR spectra. The main difference between solid-state reorientation and liquid-state reorientation is that the former usually occurs by a combination of librations and discrete jumps over fixed angles while the latter usually occurs by isotropic small-step rotational diffusion. Because in solids only certain angles of the PASs are allowed relative to a molecule or crystal-fixed reference frame (and thence to the laboratory frame), the effects of the jumps on the NMR spectrum do not necessarily average $\overset{=2,0}{\mathrm{A}}_{\mathrm{int}}$ to zero. An example is shown in Figure 36.1 for the deuterium quadrupole echo spectrum for fast 180° phenyl ring flips about the flip axis of a phenyl ring labeled at the meta or ortho positions with ^{2}H:

A Primer of NMR Theory with Calculations in Mathematica®, First Edition. Alan J. Benesi.

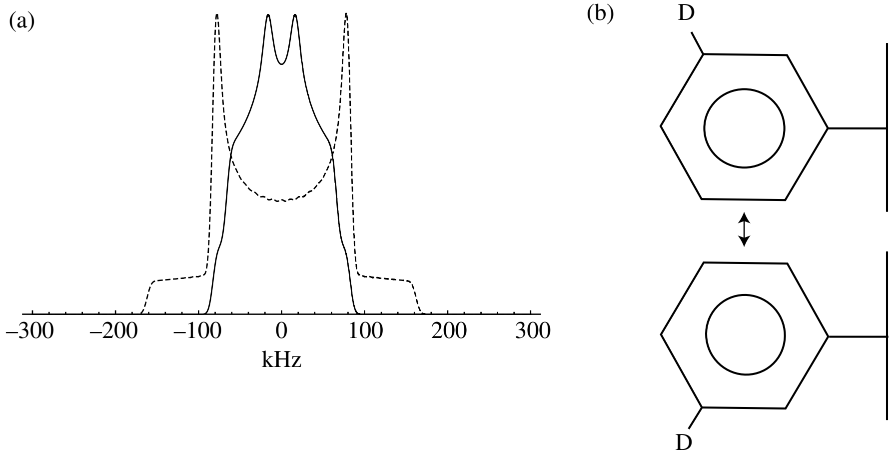

Figure 36.1 (a) 180° fast phenyl ring flip deuterium powder lineshape (solid line) compared with the rigid deuterium powder lineshape (dashed line). In both cases, qcc = 240 kHz and $\eta = 0$. (b) The 180° ring flip motion is responsible for the narrower powder spectrum. The dark vertical line represents a surface or macromolecule to which the phenyl ring is covalently bonded. D represents the deuterium nucleus.

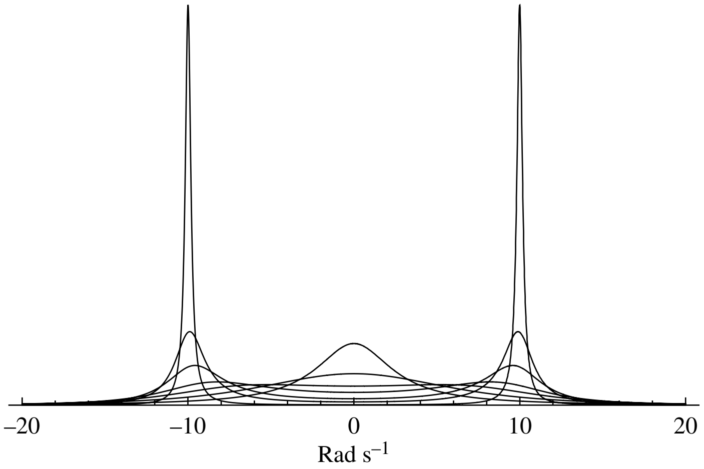

Figure 36.2 Two-Site Exchange in Liquid-State NMR. The Exchanging Resonances observed in slow exchange are of equal intensities with $\delta_A = -10\,\mathrm{rad\,s^{-1}}$, $\delta_B = +10\,\mathrm{rad\,s^{-1}}$, $T_{2A} = T_{2B} = 1\,\mathrm{s^{-1}}$, and $k = 0.1\,\mathrm{s^{-1}}$ to $200\,\mathrm{s^{-1}}$. See *twosite exchange.nb* for details.

In Figure 36.1, the wider powder lineshape corresponds to the rigid deuterium powder pattern with qcc = 240 kHz and $\eta = 0$. The narrower powder lineshape corresponds to the fast phenyl ring flip spectrum with qcc = 240 kHz and $\eta = 0$. Angular motion of any kind always narrows the powder lineshape.

The simplest examples of the effects of motion on NMR spectra are observed in liquid-state “chemical exchange” spectra where the isotropic chemical shift of a nucleus in one chemical environment is changed by conformational motion or reaction to a different isotropic chemical shift corresponding to a different chemical environment. One example is the equatorial to axial conformation changes of the hydrogen atoms in cyclohexane. The mathematics of simple two-site exchange in liquid-state NMR is shown in Figure 36.2 (Mehring, 2002, pp. 2597–2598). The methods used are discussed in the next chapter.

Angular motions are also the source of NMR relaxation. The changing orientations of the internal Hamiltonian PASs cause frequency changes at the resonance frequency for the nuclei, thereby stimulating NMR relaxation. Without stimulated emission, NMR relaxation by spontaneous emission would require the lifetime of the universe! NMR relaxation will be discussed in detail in later chapters.

HOMEWORK

Homework 36.1: Why does $A_{20}=0$ yield a peak at the isotropic chemical shift?

Homework 36.2: K. Schmidt-Rohr and Spiess (1994) have shown that the jump angles can be empirically determined using 2D-exchange spectroscopy. Based on this reference, describe in words and in mathematics how the pulse sequence works.

CHAPTER 37

SLOW, INTERMEDIATE, AND FAST EXCHANGE IN LIQUID-STATE NMR SPECTRA

The effects of molecular motion and chemical reaction on NMR spectra are most clearly evident in liquid-state NMR. In the absence of reaction or conformational exchange in a liquid-state NMR sample, the behavior of the net magnetization $\mathbf{M}_j$ for spins of type j in the presence of the magnetic field is described by the Bloch equation in the rotating frame (Eq. 7.1):

$$\frac{d\mathbf{M}_j}{dt} = \gamma \mathbf{M}_j \times \mathbf{B}_{\text{tot}} - \bar{\mathbf{R}}_j(\mathbf{M}_j - \mathbf{M}_{j0}) \tag{37.1}$$

where $\mathbf{M}_j$ is the instantaneous net magnetization dipole moment for the ensemble of spins j, and $\mathbf{M}_{j0} = \{0, 0, \mathrm{M}_{\mathrm{jzeq}}\}$ is the equilibrium net z magnetization dipole of spins j, and $\bar{\mathbf{R}}_j = \begin{pmatrix} \frac{1}{T_{2j}} & 0 & 0 \\ 0 & \frac{1}{T_{2j}} & 0 \\ 0 & 0 & \frac{1}{T_{1j}} \end{pmatrix}$ is the relaxation matrix for spins j.

A chemical reaction or conformational exchange converts the magnetization $\mathbf{M}_j$ of species j and its corresponding peak in the spectrum to another species k with magnetization vector $\mathbf{M}_k$ and its corresponding peak. If the reaction or exchange is at chemical equilibrium, the reverse reaction or conformational change also creates species j and corresponding magnetization $\mathbf{M}_j$. These changes are reflected in modified Bloch equations in the rotating frame for the observable transverse magnetization of the different spins (Mehring, 2002, p. 2597):

A Primer of NMR Theory with Calculations in Mathematica®, First Edition. Alan J. Benesi.

$$\begin{aligned}\frac{d\mathrm{M}_A^+}{dt} &= \left(i\delta_A - \left(\frac{1}{T_{2A}}\right) - k_{AB} - k_{AC} - \cdots\right)\mathrm{M}_A^+ + k_{BA}\mathrm{M}_B^+ + k_{CA}\mathrm{M}_C^+ + \cdots \\ \frac{d\mathrm{M}_B^+}{dt} &= \left(i\delta_B - \left(\frac{1}{T_{2B}}\right) - k_{BA} - k_{BC} - \cdots\right)\mathrm{M}_B^+ + \mathrm{k}_{AB}\mathrm{M}_A^+ + \mathrm{k}_{CB}\mathrm{M}_C^+ + \ldots \\ &\vdots \\ &\text{etc.}\end{aligned} \tag{37.2}$$

where $\mathrm{M}_A^+ = \mathrm{M}_x + i\mathrm{M}_y$ is the observable transverse magnetization of spins A, δ_A is the chemical shift of spins A in rad s^{-1}, T_{2A} is the T_2 of spins A, k_{AB} is the first-order rate constant (in s^{-1}) for conversion of species A to species B, k_{BA} is the first-order rate constant for conversion of species B to species A (i.e., the reverse reaction), etc.

For the transverse magnetization of N exchanging sites, we create a column vector containing the N different transverse magnetization vectors $\mathrm{M}_X^+(t)$. This is illustrated for three exchanging sites in Equation 37.3:

$$\mathrm{M}^+(t) = \begin{pmatrix} \mathrm{M}_A^+(t) \\ \mathrm{M}_B^+(t) \\ \mathrm{M}_C^+(t) \end{pmatrix} \tag{37.3}$$

If we were looking at longitudinal (z) magnetization, we would construct a column vector $\mathrm{M}_z(t)$ composed of $\mathrm{M}_{zA}(t)$, $\mathrm{M}_{zB}(t)$, and $\mathrm{M}_{zC}(t)$.

Next, we construct a diagonal matrix

$$\bar{\Omega} = \begin{pmatrix} \delta_A & 0 & 0 \\ 0 & \delta_B & 0 \\ 0 & 0 & \delta_C \end{pmatrix} \tag{37.4}$$

where δ_A, δ_B, and δ_C are the respective frequencies in rad s^{-1} (chemical shifts) of spins A, B, and C in the rotating frame.

Next, a rate/relaxation matrix is constructed from the respective relaxation times and rate constants:

$$\bar{\Gamma} = \begin{pmatrix} \left(-\frac{1}{T_{2A}} - k_{AB} - k_{AC}\right) & k_{BA} & k_{CA} \\ k_{AB} & \left(-\frac{1}{T_{2B}} - k_{BA} - k_{BC}\right) & k_{CB} \\ k_{AC} & k_{BC} & \left(-\frac{1}{T_{2C}} - k_{CA} - k_{CB}\right) \end{pmatrix} \tag{37.5}$$

If we are looking at longitudinal z magnetization, we would use the corresponding inverse T_1 values $\frac{1}{T_{1A}}$, $\frac{1}{T_{1B}}$, and $\frac{1}{T_{1C}}$.

Using these definitions, Equation 37.2 may be rewritten as

$$\frac{d\mathrm{M}^+}{dt} = (\mathrm{i}\,\bar{\Omega} + \bar{\Gamma})\mathrm{M}^+(t) \tag{37.6}$$

The free induction decay (time domain NMR signal) from all three components is given by

$$g(t) = \bar{1}\, e^{(i\bar{\Omega}+\bar{\Gamma})t}\, \bar{\mathrm{p}} \tag{37.7}$$

where $\bar{1} = \begin{pmatrix} 1 \\ 1 \\ 1 \end{pmatrix}$ is a unit vector and $\bar{\mathrm{p}} = (p_A \quad p_B \quad p_C)$ is a row vector composed of the equilibrium probabilities of the exchanging sites. For example, if the equilibrium favors B, the probability p_B will be larger than p_A or p_C, with $p_A + p_B + p_C = 1$. Note also that microscopic reversibility requires $k_{AB}\, p_A = k_{BA}\, p_B$.

The NMR spectrum for the exchanging spins is given by the Fourier transform of $g(t)$:

$$I(\omega) = -\mathrm{Re}(\bar{1}\,\bar{\mathrm{A}}^{-1}(\omega)\,\bar{\mathrm{p}}) \tag{37.8a}$$

where

$$\bar{\mathrm{A}}(\omega) = i(\omega\bar{\mathrm{E}} - \bar{\Omega}) + \bar{\Gamma} \tag{37.8b}$$

and

$$\bar{\mathrm{E}} = \begin{pmatrix} 1 & 0 & 0 \\ 0 & 1 & 0 \\ 0 & 0 & 1 \end{pmatrix} \tag{37.8c}$$

is the unit matrix. $\bar{\mathrm{A}}^{-1}(\omega)$ is the matrix inverse of $\bar{\mathrm{A}}(\omega)$ such that $\bar{\mathrm{A}}^{-1}(\omega)\,\bar{\mathrm{A}}(\omega) = \bar{\mathrm{E}}$. As shown in *twosite exchange*.nb, Mathematica is able to directly evaluate the matrix inverse $\bar{\mathrm{A}}^{-1}(\omega)$. The extension to N exchanging sites is self-evident.

The $N=2$ application is shown in *twosite exchange.nb*. The results show three "regimes" of exchange: (i) When the frequency difference $|\delta_A - \delta_B| \gg k_{AB}$ or k_{BA}, separate resolvable peaks are obtained at the chemical shifts δ_A and δ_B. This situation defines "*slow exchange*." (ii) Conversely, when $|\delta_A - \delta_B| \ll k_{AB}$ or k_{BA}, a resolvable single peak is obtained at $p_A\ \delta_A + p_B\ \delta_B$. This situation defines "*fast exchange*." (iii) Finally, when $|\delta_A - \delta_B| \approx k_{AB}$ or k_{BA}, the spectrum changes with increasing exchange rate from two broad peaks to a single very broad peak at the average frequency. This defines "*intermediate" exchange*. There is no loss of integrated signal intensity for liquid-state NMR spectra in going from slow exchange through intermediate exchange to fast exchange.

EXPLANATION OF *twosite exchange.nb*

This notebook calculates the spectra for two-site chemical or conformational exchange between two environments with different frequencies for a single nuclear spin. The user is told to evaluate *matrep2.nb* and then close it without saving changes. A unit vector of dimension 2 is created, called one. The 2×2 identity matrix *e* is then defined. The 2×2 frequency matrix Ω is created. The diagonal elements are the chemical shifts δ_A and δ_B in rad s^{-1}. The rate constant matrix Γ is created according to Equation 37.5 using the rate constant *k* (in s^{-1}) and the transverse relaxation rates $1/T2A$ and $1/T2B$. Since we assume that the equilibrium constant for exchange is 1, the probability vector *p* is {1/2,1/2}.

The next cells use the obsolete Mathematica package Algebra ‘ReIm’ to declare that the rate constant *k* and relaxation times are real.

The next cells evaluate Equations 37.8a and 37.8b. The built-in Mathematica function Inverse is able to calculate the matrix inverse needed in Equation 37.8a.

The next cells create the function *h*, from which the real part is extracted in the function intensity. A plot of the intensity function is inverted but easily corrected with a sign change.

The next cells plot the intensity function for different rate constants *k*, showing the effects of the exchange rate on the spectrum.

In the last set of cells, it is shown that there is no change in integrated intensity regardless of the exchange rate. There is only broadening.

HOMEWORK

Homework 37.1: Calculate the time-dependence of a slow two-site exchange spectrum for a selective inversion recovery experiment in which the *A* peak is selectively inverted with a π pulse at $t=0$ followed by exchange for time τ. Assume that the system is at chemical equilibrium and that the equilibrium constant for the A to B reaction is 4.

CHAPTER 38

EXCHANGE IN SOLID-STATE NMR SPECTRA

The phenomenon of chemical and conformational exchange in solid-state NMR is not fundamentally different than in liquid-state NMR, although destructive interference can distort the resulting powder spectra and attenuate the integrated intensity as the reorientational rates go through the intermediate exchange regime. In most solids, small angular vibrations, called librations, around otherwise fixed orientations occur at frequencies near 10^{13}–$10^{14}\,s^{-1}$. This is much higher than the resonant Larmor frequencies of nuclear spins. For this reason only the averaged behavior of librations affects NMR spectra and relaxation (Lang and Ludemann, 1984). However, there are also occasional large angular jumps to new fixed orientations. These occur at much lower frequencies that are similar to the magnitudes of internal Hamiltonians (Lang and Ludemann, 1984). These jump motions have dramatic effects on the observed solid-state NMR spectrum and NMR relaxation, just as isotropic rotational diffusion dominates the NMR spectra and relaxation observed in liquids.

The accessible jump angles in solid samples are most conveniently described in a crystal-fixed axis system. The crystal-fixed axis system must therefore be related to the principal axis system(s) (PASs) of the internal Hamiltonian(s) and to the laboratory axis system. For a powdered solid sample, the final transformation from the crystal-fixed to the laboratory reference frame is achieved with a powder average of the $\phi\theta\psi$ Euler angles as shown in Scheme 38.1.

$$\overline{\overline{\mathrm{A}}}[\mathrm{pas}] \xrightarrow{\alpha\beta\gamma} \overline{\overline{\mathrm{A}}}[\mathrm{crystal}] \xrightarrow{\phi\theta\psi} \overline{\overline{\mathrm{A}}}[\mathrm{laboratory}] \tag{38.1}$$

In many cases, the jump angles (set of specific allowed $\alpha\,\beta\,\gamma$ angles) can be identified by simple inspection of the pertinent internal Hamiltonian PAS in the crystal reference frame. The quadrupolar Hamiltonian H_Q of deuterium, ^2H, is particularly convenient in this regard. Because hydrogen only forms a single covalent bond (except for boron hydrides), the deuterium quadrupolar PAS z axis is aligned with the covalent bond, with η usually less than or equal to 0.1 (see Eq. 29.4).

The pulse sequence that is used to obtain 1D deuterium NMR spectra of powdered solid samples is the quadrupole echo pulse sequence (Fig. 38.1).

A Primer of NMR Theory with Calculations in Mathematica®, First Edition. Alan J. Benesi.

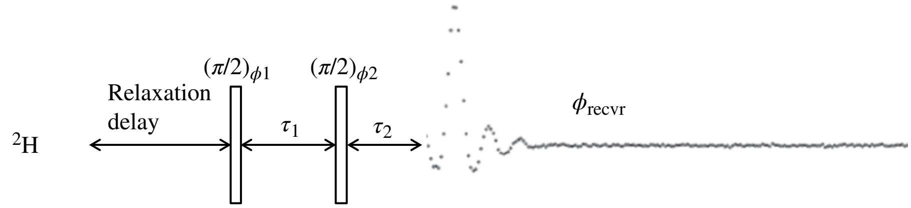

Figure 38.1 The quadrupole echo pulse sequence used extensively in ^{2}H solid-state NMR. The vertical rectangles represent $\pi/2$ rf pulses. The deuterium quadrupolar Hamiltonian magnitude is on the order of $||\bar{H}_Q|| \approx 250\text{kHz}$, so high-power $\pi/2$ pulses must have durations of 2.5 μs or less in order to excite the full powder pattern. τ_1 and τ_2 are typically 25–35 μs with $\tau_2 < \tau_1$, and a dwell time of 1 μs or less (corresponding to a spectral width of 1 MHz or more) must be used. For clarity, only the signal from the phased "real" receiver channel is shown in the FID. $\phi_1 = x$, $\phi_2 = +y, -y$, and $\phi_{\text{recvr}} = x$ (quadrature phase cycling can be added if desired).

We use as our first example the angular jumps of covalent O–H bonds in the most common phase of ice, ice I_h. ^{2}H NMR was instrumental in the elucidation of these motions (Wittebort et al., 1988). Ice I_h is called hexagonal ice because the water molecules are arranged in hydrogen-bonded hexagons. Locally around each individual water molecule, however, the hydrogen bonding arrangement is tetrahedral as shown in Figure 38.2. Unstable hydrogen bonding arrangements called Bjerrum defects propagate rapidly through the ice, causing the O–H covalent bonds to undergo angular jumps between the four tetrahedrally coordinated H-bonding possibilities (Figure 38.3). The tetrahedral angle jumps cause quantitatively predictable changes in the spectrum and relaxation of ^2H_2O ice I_h. More detailed studies show that *translational* motion of individual water molecules occurs through "tunnels" in the Ice I_h lattice (Geil et al., 2005).

Mathematica simulations of the effect of tetrahedral jumps of the O–^{2}H bond tetrahedral jump frequency are demonstrated in the notebooks *tetrahedral jumps wignerology.nb, tetrahedron.nb, tetrahedraljumpspowder.nb* (direct calculation of the powder spectrum) and *tetjumpspowderfid.nb* (calculation of the powder free induction decay (FID) followed by Fourier transformation). The calculated spectra are shown in Figure 38.4. The powder lineshapes closely match those obtained experimentally (Wittebort et al., 1988).

The major differences between the spectra obtained with these calculations and those in *twosite exchange.nb* are as follows: (i) the powder average must be calculated and (ii) the effects of motion during τ_1 and τ_2 of the quadrupole echo pulse sequence must be accounted for (Vega and Luz, 1987) and (iii) intermediate jump rates can yield highly attenuated NMR spectra as shown in Figure 38.4. In comparison, for liquid-state exchange, (i) no powder averaging is needed and (ii) the NMR signal is collected immediately after a single radio frequency (rf) pulse so there is no need to consider effects of delays and (iii) there is no attenuation of the integrated intensity in liquid-state intermediate-exchange spectra.

The effects of fast exchange (i.e., fast reorientation) on solid-state NMR spectra are also considerably different than for liquid-state fast exchange. In the case of fast

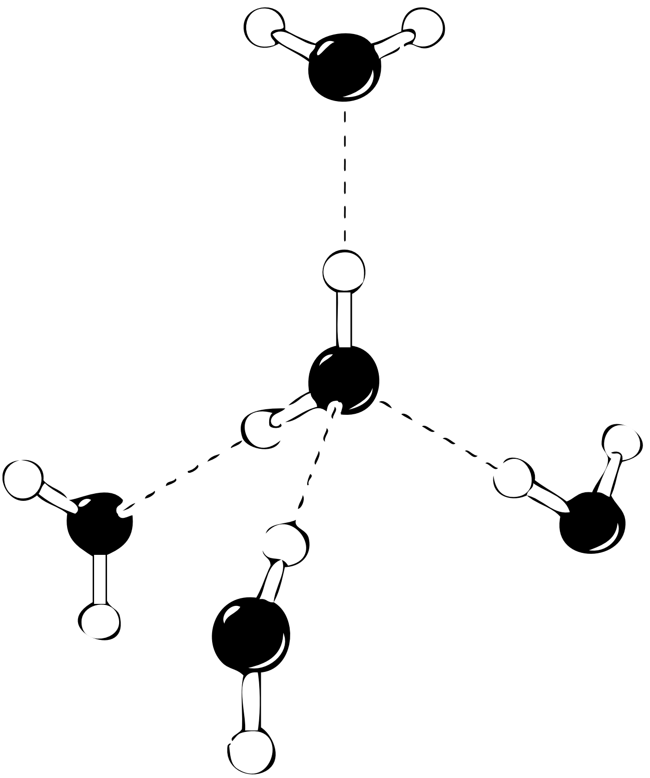

Figure 38.2 Local arrangement of water molecules in Ice I_h. Hydrogen bonds are indicated by single dashed lines. Covalent bonds are double lines. H atoms are indicated by small white spheres. O atoms are indicated by larger black spheres.

angular jumps in solids, the spectrum only averages to a single peak at the isotropic frequency if the angular jumps possess "high symmetry," that is, they are tetrahedral, octahedral, or icosahedral. In the case of tetrahedral jumps of the O–^{2}H bond in ice I_h, the jumps are high symmetry, and fast motion yields a single sharp peak (see *tetrahedral fast jump wignerology.nb*). But in the case of C_2 symmetry jumps of the O–^{2}H bond as observed in ^2H_2O-gypsum, the "low" symmetry jumps do *not* average the rigid powder spectrum to a single peak but instead to a reduced width powder pattern as calculated in *c2jumpfast.nb* and shown in Figure 38.5.

The method used to calculate fast-exchange solid-state spectra is simple. Suppose there are N different sets of Euler angles $(\alpha_j\, \beta_j\, \gamma_j)$, Equation 38.1, between which the angular jumps occur in the crystal-fixed reference frame, each with a respective probability p_j. Then we calculate the corresponding fast average crystal-fixed real space tensor $\overset{=2,m}{\mathrm{A}}_{\mathrm{avg\_crystal}}$ as follows:

$$\overset{=2,m}{\mathrm{A}}_{\mathrm{avg\_crystal}} = \sum\nolimits_j p_j \overset{=2,m}{\mathrm{A}}_j \tag{38.2}$$

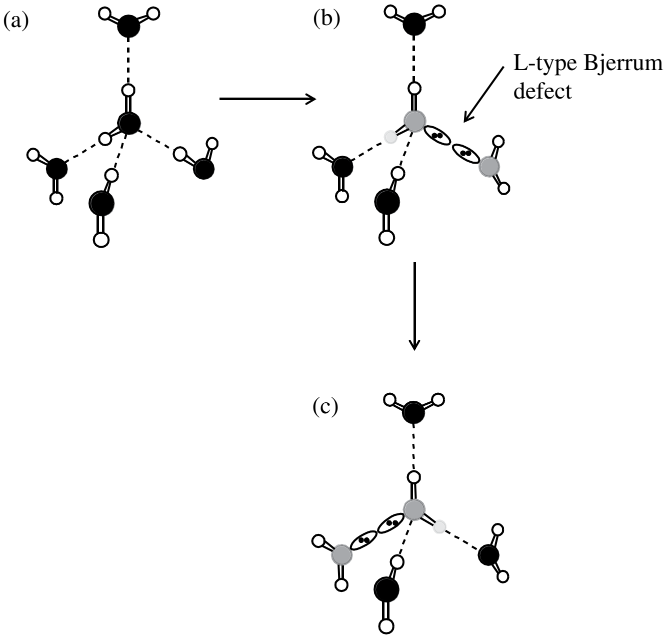

Figure 38.3 Diffusion of Bjerrum Defects Causes Tetrahedral Jumps. ^{2}H and ^{1}H NMR experiments show that the H atoms experience tetrahedral jumps around the oxygen atoms in the crystal lattice. The jump rate at 267 K is $6.5\times10^4\,\mathrm{s}^{-1}$.[111,112] Oxygen atoms are black spheres, except for those involved in a defect, which are dark gray. Hydrogen atoms are small white spheres, except for those that make a tetrahedral jump due to a defect, which are shown in light gray. (a) Water coordination without defects. (b) A Bjerrum L-type defect. Note that oxygen lone-pair electrons are in close proximity, an unstable state. The H atom that will make a tetrahedral jump is indicated in light gray. (c) In response to the instability, the central water molecule experiences a tetrahedral jump that brings the light gray H atom into a stable H-bonding arrangement. Bjerrum defects move quickly through the ice lattice, leaving the water molecules at the same place in the crystal lattice but forcing tetrahedral jumps.

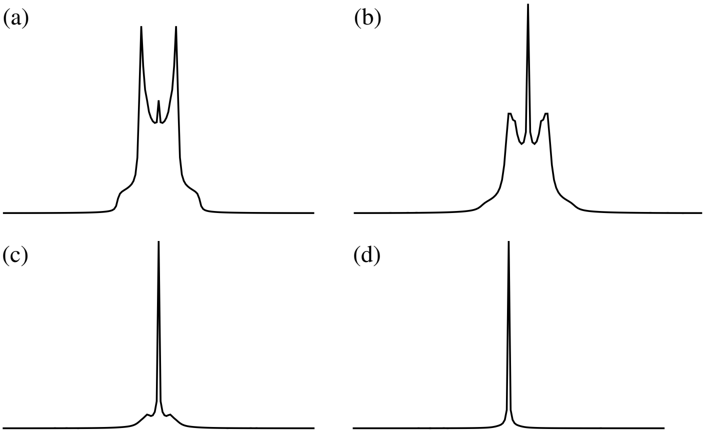

Figure 38.4 Attenuation of the ^{2}H NMR signal by Intermediate-Exchange Tetrahedral Jumps (see *tetrahedraljumpspowder.nb* and *tetjumpspowderfid.nb*). qcc = 216 kHz, $\eta = 0$, and the quadrupole echo delays are $\tau_1 = \tau_2 = 20\,\mu\mathrm{s}$ (see Fig. 38.1). The tetrahedral jump rate constant k and integral intensity for each calculated spectrum: (a) $1\times10^4\,\mathrm{s}^{-1}$, 0.3657 (b) $2.5\times10^4\,\mathrm{s}^{-1}$, 0.1015 (c) $5\times10^4\,\mathrm{s}^{-1}$, 0.0303 (d) $1\times10^5\,\mathrm{s}^{-1}$, 0.0283.

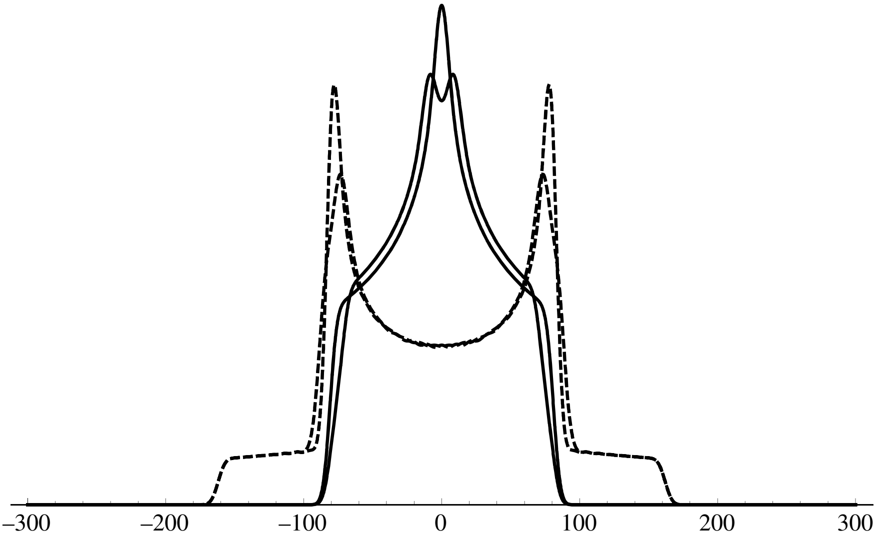

Figure 38.5 Effects of Fast C_2 Symmetry Jumps on ^{2}H Quadrupole Echo Spectrum, qcc = 216 kHz. The dashed black powder spectrum with wider horns is the rigid solid with $\eta = 0$. The dashed black powder spectrum with slightly narrower horns is the rigid solid with $\eta = 0.1$. The solid black spectrum with a single central maximum shows the effects of fast C_2 jumps with θ = magic angle, and the solid black spectrum with two central maxima shows the effects of fast C_2 jumps with $\theta = 52.5°$. Both of the fast C_2 jump spectra were calculated assuming $\eta = 0$. The frequency axis is in units of kHz.

Having calculated the five $\overset{=2,m}{\mathrm{A}}_{\mathrm{avg\_crystal}}$ real space tensors in the crystal-fixed reference frame, we use these to calculate the fast average real space tensor $\overset{=2,0}{\mathrm{A}}_{\mathrm{avg\_lab}}$ in the laboratory frame, using the powder average angles $\phi\theta\psi$ (Eq. 38.1) in Equation 31.2:

$$\overset{=2,0}{\mathrm{A}}_{\mathrm{avg\_lab}} = \sum_{m=-2}^{+2} \overset{=2,m}{\mathrm{A}}_{\mathrm{avg\_crystal}} \, D^{2}_{m0}(\phi\theta\psi) \tag{38.3}$$

This process is shown in the notebooks *tetrahedral fast jump wignerology.nb* and *c2jumpfast.nb*.

EXPLANATION OF *tetrahedral jump wignerology.nb*

This notebook calculates the angular dependence of the real space tensor alab20 needed to simulate the NMR spectrum of a rigid powdered solid. The user is told to evaluate *wigrot.nb,* then close it without saving changes. Jumps take the PAS to specific new angles relative to a molecule- or crystal-fixed axis system.

First, it is necessary to calculate the expressions corresponding to $\overset{=}{\mathrm{A}}$[crystal] in Equation 38.1. Here, they are called the amol[2,*m*]. We only need the $l = 2$ real space tensors to calculate the powder spectrum. For $\eta = 0$, the amol[2,*m*] depend only on β and γ. The function amol2[2,*q*_] is created to substitute θ for β and ϕ for γ. By doing this, we allow the transformation to the lab frame in Equation 38.1 to use the powder average angles α, β, and γ.

Next alab[2,0] is calculated. This is necessary for simulation of powder spectra as shown in subsequent notebooks. The function alab20[α_,β_,θ_,ϕ_] is created.

EXPLANATION OF *tetrahedron.nb*

The purpose of this notebook is to obtain the tetrahedral jump angles. This notebook uses built-in Mathematica packages and functions to calculate the tetrahedral angles. The user must evaluate the Mathematica package *PolyhedronOperations*. This is done by typing ≪PolyhedronOperations' on the input line of the notebook.

Next, the Cartesian coordinates of the vertices of a tetrahedron are obtained by using the package function PolyhedronData. The Cartesian coordinates are then normalized (so that all vertices are unit distance from the origin) by using the built-in Mathematica function Normalize.

Next, the user opens the package VectorAnalysis. Using the package function CoordinatesFromCartesian, the coordinates are converted from Cartesian to spherical polar with components $\{r, \theta, \phi\}$. In this case, $r = 1$ and we *define* the *molecular (crystal)-axis system* to have its z axis aligned with one of the allowed PAS jump angles. The important concept to keep in mind is that the *most convenient crystal-fixed axis system can be arbitrarily chosen*. The function CoordinatesFromCartesian finds that the allowed jump angles are $\{\theta = 0, \phi = 0\}$, $\{\theta =$ thetatet,0$\}$, $\{\theta =$ thetatet, 2π/3$\}$, $\{\theta =$ thetatet, 4π/3$\}$, where thetatet = *N*[Arccos[−1/3]].

EXPLANATION OF *tetrahedraljumpspowder.nb*

This notebook calculates intermediate-exchange powder spectra for the deuterium quadrupolar echo experiment (Vega and Luz, 1987).

The user is told to evaluate *repangwt5253*, evaluate it, choose full output, and then close it without saving changes.

The real space tensor needed to calculate the deuterium quadrupolar powder lineshape is alab20 as calculated in *tetrahedral jump wignerology.nb*. The allowed jump angles are designated with θ and ϕ spherical polar angles as in *tetrahedron.nb*. It is shown that thetatet is exactly twice the magic angle, Arccos $\left[1/\sqrt{3}\right]$. The powder average to the lab frame utilizes the Euler angles α and β.

For deuterium, $I = 1$ and $\delta_{zz} = \pi$ qcc (see Table 29.1).

The one vector and One identity matrix are created for the four tetrahedral jump sites. We assume that the probabilities for each of the four sites are equal (1/4) and create the probability vector p accordingly. The jump rate function Γ[*k*_] is created. It is assumed that each site can jump to any of the three other sites. The jump rate from a site to any of the other sites is assumed to be $k\,\mathrm{s}^{-1}$.

We let qcc = 216 kHz. The expression for alab20 assumes also that $\eta = 0$. Frequency functions $\delta1$, $\delta2$, $\delta3$, and $\delta4$ (in rad s^{-1}) are created using the function alab20. The diagonal matrix function $\delta[\alpha\_,\beta\_]$ is created. It is necessary to take the real part only (Re) because roundoff errors yield a minute imaginary component.

The function $R[\alpha\_, \beta\_, k\_]$ is created. The function gtvec2[α_, β_, k_, t_] is created. It accounts for the echo delay and its effect on the echo intensity.

The functions $A[\alpha\_, \beta\_, k\_]$, Ainv[α_, β_, k_], intimag[α_, β_, k_, τ_], and intensity[α_, β_, k_, τ_] are created.

As an example, for the powder average angle repangwt[[1111]], a Plot of the intensity for $k = 10^4\,s^{-1}$ and echo delay of $\tau = 20\,\mu s$ shows four peaks for one of the two transitions ($m = 1$ to $m = 0$). The other transition ($m = 0$ to $m = -1$) is given by reversing the sign of the frequency ν. The sum of the two plots gives the expected deuterium spectrum for that specific powder angle.

The powder spectrum is obtained with the function powderintensity[k_, τ_], which adds the contributions from all the specific powder angles for one of the transitions ($m = 1$ to $m = 0$). The powder spectrum for the other transition is again obtained by reversing the sign of the frequency ν. The sum yields the full deuterium powder spectrum.

The built-in Mathematica function NIntegrate is used to show that there is destructive interference and intensity loss during the echo period. The evaluation for $\tau_1 = \tau_2 = 20\,\mu s$ yields .05183. The evaluation for $\tau_1 = \tau_2 = 0$ yields 0.4999 regardless of the jump rate.

EXPLANATION OF *tetjumpspowderfid.nb*

For real space PASs experiencing tetrahedral jumps in the intermediate-exchange regime, this notebook calculates the theoretical FID (NMR signal) obtained from the deuterium quadrupole echo NMR experiment and Fourier transforms it to obtain the theoretical spectrum (Vega and Luz, 1987). The user is told to evaluate *repangwt5253*, show full output, then close it without saving changes.

Exactly as in *tetrahedraljumpspowder.nb,* the first cells introduce alab20 calculated in *tetrahedral jump wignerology.nb*. The allowed jump angles are designated with θ and ϕ spherical polar angles as in *tetrahedron.nb*. The powder average to the lab frame utilizes the Euler angles α and β. For deuterium, $I = 1$ and $\delta_{zz} = \pi$ qcc (see Table 29.1). The one = {1,1,1,1} vector and the One identity matrix are created. The probability vector $p = \{1/4,1/4,1/4,1/4\}$ is defined. The jump rate matrix Γ is defined. The frequency functions $\delta1$, $\delta2$, $\delta3$, and $\delta4$ are created. The repulsion angles and weights in repangwt5253 are reviewed. The R function is created, essentially identical (except for the inclusion of qcc as a variable) to the R function in *tetrahedraljumpspowder.nb*.

From here on, the calculations in this notebook and *tetrahedraljumpspowder.nb* differ. The echo[qcc_,α_,β_,k_,τ_] function is created to give the first point in the FID (i.e., the echo maximum) when $\tau1 = \tau2 = \tau$. Then, the powderecho[qcc_,k_,τ_] function is created using the sum of the intensities for all of the repulsion angles.

The angle-dependent real and/or complex NMR signal points are then calculated using the fid and complexfid functions, respectively. The τ variable is the echo delay in the quadrupole echo experiment. The t variable is the time after the echo maximum for which the complex NMR signal point is needed.

Next, the real and/or complex powder average NMR signal points are calculated as a function of the time variable *t* after the echo maximum in the functions powderfid and powdercomplexfid, respectively.

In order to Fourier transform the calculated signals, the functions ft1, ftcorr, ftcorr2, fttot, gaussap, bc, and fttotbc are created. Note that the built-in Mathematica function Fourier does not calculate the spectrum properly.

The theoretical complex FID for a quadrupolar echo experiment is obtained by creating a Table of powdercomplexfid points as a function of t after the echo maximum. The complex FID data2 is calculated in this way; 160 complex data points with a dwell time of 1 μs are calculated assuming that qcc = 216 kHz, the jump rate is $2.5 \times 10^4\,\mathrm{s}^{-1}$, and $\tau = 20\,\mu\mathrm{s}$.

The theoretical FID data1 is then Fourier transformed with the function fttot to yield ftdata1. The spectrum is plotted using the built-in Mathematica function ListPlot.

The theoretical FID data1b is created by using the gaussap function to process the theoretical FID data1. The Fourier transform of data1b is then plotted with ListPlot. The baseline-corrected Fourier transform of data1b is calculated with the function fttotbc.

Theoretical FIDs and corresponding spectra are then calculated and plotted for the same parameters but with different tetrahedral jump rates in data2, data3, data4, and data5. The respective jump rates (*k*) for these are $5 \times 10^4\,\mathrm{s}^{-1}$, $1 \times 10^5\,\mathrm{s}^{-1}$, $1 \times 10^4\,\mathrm{s}^{-1}$, and $5.0 \times 10^3\,\mathrm{s}^{-1}$.

The spectra obtained vary from a single sharp peak when $k = 1 \times 10^5\,\mathrm{s}^{-1}$ to an "almost rigid" powder pattern when $k = 5.0 \times 10^3\,\mathrm{s}^{-1}$.

EXPLANATION OF *tetrahedral fast jump wignerology.nb*

This notebook calculates $\overset{=2,0}{A}_{\mathrm{avg\_lab}}$ or amolfastavg[*l*,*m*] in the terminology of this notebook (see Eq. 38.2 and 38.3) for a nuclear spin experiencing fast tetrahedral jumps. The user is told to evaluate *wigrot.nb,* then close it without saving.

The molecular frame (or crystal frame) amol[2,*m*] are calculated according to Equation 38.2 assuming that $\eta = 0$, a good approximation for deuterium nuclei. The substitution $\beta \rightarrow \theta$ and $\gamma \rightarrow \phi$ is made for the amol[2,*m*]'s when the fast average is calculated. θ and ϕ are the latitudinal and longitudinal angles in spherical polar coordinates. The Euler angle α is not in the expressions obtained for the amol[2,*m*].

For perfect tetrahedral jumps, *all* of the amolfastavg[2,*m*] terms average to 0.

EXPLANATION OF *c2jumpfast.nb*

This notebook calculates the real space tensor for fast C_2 symmetry jumps, then uses it to simulate the spectra of deuterium PASs undergoing fast C_2 symmetry jumps. The user is told to evaluate *wigrot.nb,* then close it without saving changes, then to evaluate *repangwt5253*, show full output, then close it without saving changes.

The function amolfastavgC2[2,*m*] is calculated for C_2 symmetry jumps (Eq. 38.2). In the case of water molecules in gypsum, for example, the symmetry axis is the bisector of the H–O–H (or D–O–D) bond angle, which is somewhat less than the tetrahedral angle. The C_2 jumps rotate the H (or D) atoms 180° about this axis. This interchanges the positions of the H (or D) atoms. The bisector half angle is designated as the latitudinal angle θ, and the two possible ϕ jump angles are 0 and π.

Next, the lab frame alabC2[2,0] is calculated according to Equation 38.3. The result is *not* zero and shows an angular dependence on the powder average Euler angles α and β and on the angle bisector angle θ.

Next, the functions ν1C2[α_,β_,qcc_,θ_] and ν2C2[α_,β_,qcc_,θ_] are calculated assuming $I=1$, as for deuterium. We also copy the functions ν1rigid[α_,β_,qcc_,η_] and ν1rigid[α_,β_,qcc_,η_] from *rigiddeutlineshapes.nb*.

The Gaussian broadening function gauss, as are the expressions for the "boogies" and intensities, are calculated as in *rigiddeutlineshapes.nb*.

The powder spectrum functions powderC2 and powderrigid are defined.

Plots of the rigid deuterium spectra for qcc = 216 kHz, $\eta=0$, and qcc = 216 kHz, $\eta=0.1$ are made and compared with the C_2 symmetry fast jump spectra obtained for qcc = 216 kHz, $\eta=0$, $\theta=52.5°$ and qcc = 216 kHz, $\eta=0$, θ = magic angle (half of tetrahedral angle).

Next, a series of calculations and plots are made for fast C_2 symmetry jumps with qcc = 216 kHz, $\eta=0$, and θ varied in 1° increments from 50 to 55°.

Several other calculations and plots are made to explore the variation of the C_2 fast jump lineshape with θ.

HOMEWORK

Homework 38.1: Use the density matrix approach to show that the quadrupole echo yields full refocusing of the NMR signal for an $I=1$ nucleus such as ^{2}H. Include the anisotropic effects of $\overline{\overline{\mathrm{A}_{\mathrm{Q}}^{2,0}}}$ in your analysis. Hint… $\overline{\overline{\mathrm{A}_{\mathrm{Q}}^{2,0}}}$ may be represented as $\omega_Q(\alpha,\beta,\gamma)$. It is nothing more than a scalar function of the Euler angles.

Homework 38.2: Calculate the fast average lineshape for fast C_3 symmetry jumps of a deuterated methyl group.

CHAPTER 39

NMR RELAXATION: WHAT IS NMR RELAXATION AND WHAT CAUSES IT?

Nuclear magnetic resonance (NMR) relaxation describes the return of the nuclear spin system to thermal equilibrium after radio frequency (rf) perturbation. At thermal equilibrium, there is no coherence, and the populations of the nuclear spin angular momentum energy levels are given by the Boltzmann distribution (Levitt, 2008, p. 543). As pointed out by Abragam (1983, p. 264), spontaneous transitions between the energy levels occur at a negligible rate. It would take longer than the known lifetime of the universe for relaxation to occur by spontaneous transitions. Only stimulated emission and absorption of rf photons at or near the resonant Larmor frequency(ies) brings about NMR relaxation. Thus, just as rf photons at the Larmor frequency(ies) are necessary to stimulate the perturbation of the nuclear spin system, they are necessary to stimulate its relaxation.

The rate of return to thermal equilibrium depends on the nature of the coherence (or population perturbation). In the absence of rf irradiation, the rate of return of the expectation value of $p=-1$ spin coherence $(< I^+(t) >)$ to its equilibrium value of zero is called transverse, spin–spin or simply T_2 relaxation and is characterized by the first-order rate constant $1/T_2\,\mathrm{s}^{-1}$, where T_2 is the relaxation time in seconds. The vector model analysis for the T_2 relaxation experiment is shown in Chapter 8. The rate of return of the expectation value of $p=0$ population $(< I_z(t) >)$ to equilibrium magnetization $(< I_{z\_\mathrm{eq}} >)$ is called longitudinal, spin-lattice, or simply T_1 relaxation and is characterized by the first-order rate constant $1/T_1\,\mathrm{s}^{-1}$. The vector model for the inversion recovery experiment used to measure T_1 relaxation is also shown in Chapter 8.

It is also possible to design multidimensional NMR experiments that measure multiple quantum coherence relaxation. The relaxation of zero and multiple quantum coherence (i.e. $< I_1^- I_2^+(t) >$ or $< I_1^+ I_2^+(t) >$) each have characteristic relaxation rate constants (i.e. relaxation times). In general for spin systems with coupled spins, NMR relaxation is more complicated and one needs more relaxation rate constants (or relaxation times) to characterize it.

NMR relaxation can also occur in the presence of rf irradiation. For example, the rate of return of the expectation value of $p=-1$ spin coherence $(< I^+(t) >)$ to zero

---

A Primer of NMR Theory with Calculations in Mathematica®, First Edition. Alan J. Benesi.

during an rf "spin-lock"[1] is characterized by the first-order rate constant $1/T_{1\rho}$ s^{-1}. Another example is $1/T_{\text{CP}}$, the rate constant for cross polarization (CP) *buildup* during the heteronuclear spin-locks of a CP or Cross Polarization with Magic Angle Spinning (CPMAS) experiment.

In the absence of rf irradiation provided by humans or other external sources, fluctuations in the internal NMR Hamiltonians provide the necessary rf photons at the correct Larmor frequency(ies) to stimulate relaxation. For all internal NMR Hamiltonians except H_J and H_{SR}, the fluctuations are caused by changes in the scalar $A_{\text{lab}}^{l,m}$ real space Hamiltonian components brought about by reorientation of the molecule containing the observed nucleus (Spiess, 1978). This connection can be used to obtain information about the reorientational motions, but the complexity of the connection depends on the Hamiltonian. In the case of H_J, fluctuations in both the $A_{\text{lab}}^{l,m}$ and $T_{\text{rot}}^{l,m}$ occur, making the connection with reorientational motion more difficult to analyze. Luckily, H_J is usually too small in magnitude compared with other internal Hamiltonians to significantly affect NMR relaxation. In the case of H_{SR}, fluctuations in $T_{\text{rot}}^{l,m}$ cause relaxation, but the effects of H_{SR} on relaxation are limited to gases and extremely low-viscosity liquids. In our examples, the focus is on the other internal Hamiltonians.

The mean of the deviations of the $A_{\text{lab}}^{l,m}$ from their equilibrium values is zero, but it is not the mean of the deviations that determines the NMR relaxation rates. Rather, it is the *ensemble average rate of change* of the $A_{\text{lab}}^{l,m}$'s as embodied in their autocorrelation functions that determines the NMR relaxation rates (Torchia and Szabo, 1982): The *unnormalized* autocorrelation functions are (see *wigner_orthogonality.nb*) as follows (Spiess, 1978, equation 4.33):

$$g_{l,m}(t) = < A_{\text{lab}}^{l,m*}(0) A_{\text{lab}}^{l,m}(t) > = -1^{l+m} < A_{\text{lab}}^{l,-m}(0) A_{\text{lab}}^{l,m}(t) > \tag{39.1a}$$

and the *normalized* autocorrelation functions are as follows:

$$G_{l,m}(t) = \frac{< A_{\text{lab}}^{l,m*}(0) A_{\text{lab}}^{l,m}(t) >}{(A_{\text{PAS}}^{2,0\,2})} \tag{39.1b}$$

where the angle brackets denote the ensemble average and * indicates the complex conjugate. Except for the autocorrelation function $G_{0,0}$, which is constant, the $G_{l,m}(t)$ start at a positive value close to 1 at $t = 0$ and decay to 0 for long times τ. As will be shown in subsequent chapters, it is often the case that the autocorrelation function is a simple *monoexponential*, for example,

$$G_{l,m}(t) = \text{const} * e^{-t/\tau} \tag{39.2}$$

where τ is the corresponding autocorrelation time and $\text{const} = \dfrac{< A_{\text{lab}}^{l,m*}(0) A_{\text{lab}}^{l,m}(0) >}{(A_{\text{PAS}}^{2,0\,2})}$.

---

[1] A spin-lock is usually created by giving a $(\pi/2)_x$ pulse to the equilibrium spin system followed immediately by a prolonged rf pulse along the ± y axis. This "locks" the magnetization along the $-y$ axis of the rotating frame, where it decays back to zero at a rate of $1/T_{1\rho}$.

The so-called "spectral density" is given by the Fourier transform of the corresponding autocorrelation function (see *spectraldensity.nb)*: Since the imaginary component of $e^{i\,m\,\omega_0\,t} = \cos(m\,\omega_0\,t) + i\,\sin(m\,\omega_0\,t)$ can be ignored (Abragam, 1983, p. 279),[2] the *unnormalized* spectral density is given by

$$j_{l,m}(m\,\omega) = \int_0^\infty g_{l,m}(t)\cos(m\,\omega t)\,dt \tag{39.3a}$$

and the *normalized* spectral density is given by

$$J_{l,m}(m\,\omega) = \int_0^\infty G_{l,m}(t)\cos(m\,\omega t)\,dt \tag{39.3b}$$

Because $\cos[x] = \cos[-x]$ and $G_{l,m}(t) = G_{l,m}(-t)$, it also follows that $J_{l,m}(m\,\omega) = J_{l,-m}(-m\,\omega)$.

If $G_{l,m}(t)$ is monoexponential[3] as in Equation 39.2, the spectral density is given by (see *spectraldensity.nb)*

$$J_{l,m}(m\,\omega) = \text{const}\,\frac{\tau}{1 + m^2\,\tau^2\,\omega^2} \tag{39.4}$$

where $\text{const} = \dfrac{< A_{\text{lab}}^{l,m*}(0)\,A_{\text{lab}}^{l,m}(0) >}{(A_{\text{PAS}}^{2,0\;2})}$ and $J_{l,m}(\omega)$ has units of s rad^{-2}.

Despite the misleading name, the spectral density is *not* determined by the real space "density" of photons. Due to the short range of internal Hamiltonians, the reorientation-induced "emission" and "absorption" of rf photons occurs over distances much less than the Larmor wavelength, λ_{Larmor}. The distances are sufficiently small that there is considerable uncertainty in position and momentum of the photons as well as their energy and time due to the Heisenberg Uncertainty Principle (Heisenberg, 1927). Quantum field theory or quantum electrodynamics is necessary to understand the exchange of rf photons over such short distances (Feynman, 1985). The perspective of quantum electrodynamics is especially attractive since it is not difficult to visualize exchange of virtual rf photons[4] between nuclei or between a nucleus and the thermal energy "lattice." Quantum electrodynamics allows photons to be emitted and absorbed forward and backward in time. A photon "emitted" backward in time corresponds to an absorption forward in time, and a photon absorbed backward in time corresponds to an emission forward in time. All of the exchanges in energy are mediated by photons. Further speculations are fascinating but beyond the scope of this book. Here, the focus is the physics that works and successfully explains NMR relaxation, not the intriguing scientific questions that derive from it.

---

[2] *spectraldensity.nb*

[3] A "model-free" approach has been developed by Lipari and Szabo to deal with more complicated autocorrelation functions. It is widely used to characterize angular motions of fast-moving side groups that are covalently bound to slow-moving macromolecules.

[4] A virtual photon is one that is exchanged between particles and cannot be detected directly by an external observer.

As will be discussed in the next chapter, the NMR relaxation rates in s^{-1} are given by the appropriate spectral densities $J_{l,m}(m\ \omega)$ multiplied by the *square* of the appropriate constant for the given internal Hamiltonian. The constant is proportional to the magnitude of the internal Hamiltonian, $\|H_{\text{int}}\|$.

EXPLANATION OF *spectraldensity.nb*

This notebook explicitly evaluates Equations 39.3a and 39.3b assuming that the autocorrelation function is given by a monoexponential decay (Eq. 39.2).

The half-sided complex Fourier transform obtained for the first cells is evaluated by explicit integration from $t=0$ to $t=\infty$. It yields the conditional expression $i\tau/(i+\tau\omega)$. Since ω is real and τ is real positive, this condition is met.

The sum of the half-sided cosine transform and i times the half-sided sin transform yield the conditional expression $\tau/(1+\tau^2\omega^2)+i\omega/((1/\tau^2)+\omega^2)$. Again, the conditions are met because τ is positive real and ω is real.

The half-sided cosine transform yields the expression $\tau/(1+\tau^2\omega^2)$.

The half-sided cosine transform yields the same result whether the integration is from $-\infty$ to 0 or from 0 to ∞.

The half-sided sine transform yields $\omega/((1/\tau^2)+\omega^2)$. Unlike the half-sided cosine transform, the integral from $-\infty$ to 0 yields the negative of the result from 0 to ∞.

The isotropic rotational diffusion autocorrelation function for $l=2$ is $\frac{1}{5}e^{-6D_{\text{rot}}t}$. Its half-sided cosine transform yields $\frac{6D_{\text{rot}}}{5(36D_{\text{rot}}^2+m^2\omega^2)}$.

The half-sided complex Fourier transform of an integer multiple m of the Larmor frequency yields $i\tau/(i+m\tau\omega)$. The half-sided cosine transform of an integer multiple m of the Larmor frequency yields $\tau/(1+m^2\tau^2\omega^2)$. The half-sided sin transform of an integer multiple m of the Larmor frequency yields $m\omega/((1/\tau^2)+m^2\omega^2)$.

Next, we create functions $f[\tau\_,\omega\_]$ and fnu[$\tau\_,\nu\_$] for the half-sided cosine transform result and $g[\tau\_,\omega\_]$ and gnu[$\tau\_,\nu\_$] for the half-sided sin transform result.

Several plots of these functions are made in the following cells.

Next, a logarithmic table logfreq is made of frequency values ν.

Then, semilogarithmic plots are made of the functions fnu for autocorrelation times τ of 10^{-10} and 10^{-6} seconds. These plots show essentially a constant spectral density up to a well-defined frequency, followed by a steep drop to zero. It is important to realize that the label for the x axis in these plots is the point number, not the frequency. For example, the first solid black line plot of fnu for $\tau=10^{-10}$ seconds has a half maximum at about point 83 of the table logfreq, at $\nu\cong 1.6\times10^9\ s^{-1}$. The second dashed line plot for $\tau=10^{-6}$ s has a half maximum at about point 43 of table logfreq, at $\nu\cong 1.6\times10^5\ s^{-1}$.

Semilogarithmic plots of the function gnu at the same τ values show the much narrower range of Larmor frequencies affected. The maxima in these plots occur at the same frequency as the half maxima in the plots of fnu.

Plots showing both fnu and gnu show that gnu affects a much smaller range of Larmor frequencies than fnu.

HOMEWORK

Homework 39.1: Write an essay analyzing NMR relaxation based on the exchange of virtual photons caused by reorientation of molecules in real space.

CHAPTER 40

PRACTICAL CONSIDERATIONS FOR THE CALCULATION OF NMR RELAXATION RATES

The connection between angular motion and NMR relaxation rates can be complicated if care is not taken in the choice of observed nuclei and NMR experiments. For example, if one is interested in the angular jump motions of atoms in a crystalline organic solid containing carbon, hydrogen, and nitrogen, one *could* choose to measure the NMR relaxation of ^{1}H, ^{14}N, ^{13}C, ^{15}N, or ^{2}H. For a given nucleus, the internal Hamiltonians with the largest magnitudes dominate NMR relaxation. Since the Hamiltonians with the largest magnitudes for ^{1}H, ^{13}C, and ^{15}N are H_{CS}, $H_{\text{dipolar\_hetero}}$, and $H_{\text{dipolar\_homo}}$, these Hamiltonians must all be included in the relaxation calculations. The magnitude of H_J is considerably less and usually can be ignored.

In the absence of radio frequency (rf) irradiation at the Larmor frequency(ies), the NMR relaxation rate $(1/T_n)_i$ for a given nucleus i is given by the sum of the contributions from each internal Hamiltonian $\hat{H}_{\lambda i}$ that affects the nucleus:

$$\left(\frac{1}{T_n}\right)i = \sum\nolimits_{\lambda}\left(\frac{1}{T_{n\lambda i}}\right) \tag{40.1}$$

where $(1/T_{n\lambda i})$ is the relaxation rate of the nucleus i due to Hamiltonian $\hat{H}_{\lambda i}$. Methods for calculation of $(1/T_{n\lambda i})$ are described in the following chapters.

The dipolar contributions to relaxation are particularly complicated. The pairwise $\hat{H}_{Di}$ contributions to relaxation must include all nuclei close enough to yield significant dipolar couplings. Often, intermolecular as well as intramolecular dipolar couplings must be considered. For *each* pairwise dipolar coupling, the allowed jump angles of the principal axis system (PAS) in the crystal-fixed reference frame and the appropriate transformation angles to the laboratory reference frame must be known. The Euler angles relating different Hamiltonian PASs must also be known. The number of interactions and angles required can be daunting in some cases. The situation is worst for ^{1}H since it is 100% abundant and requires consideration of both homonuclear ^{1}H–^{1}H dipolar coupling Hamiltonians as well as heteronuclear ^{1}H–X dipolar coupling Hamiltonians. The one simplification for ^{1}H is that the ^{1}H chemical shift Hamiltonian can be omitted since its magnitude $\|H_{CS}\|$ is much less than the magnitudes of the dipolar Hamiltonians, $\|H_{\text{dipolar\_hetero}}\|$ and $\|H_{\text{dipolar\_homo}}\|$. The situation

---

A Primer of NMR Theory with Calculations in Mathematica®, First Edition. Alan J. Benesi.

is considerably better for observation of dilute natural abundance nuclei such as ^{13}C and ^{15}N, where homonuclear dipolar couplings are rare and may be ignored, although in both cases H_{CS} must be included in the calculations at high magnetic fields where $\|H_{\mathrm{CS}}\|$ becomes comparable with $\|H_{\mathrm{dipolar\_hetero}}\|$.

The nuclei ^{14}N and ^{2}H, both $I = 1$, have quadrupolar Hamiltonian magnitudes $\|H_{\mathrm{Q}}\|$ that are considerably larger than those of their other internal Hamiltonians. $\|H_{\mathrm{Q}}\|$ for ^{14}N in the form of the quadrupole coupling constant $\mathrm{qcc} = e^2qQ/h$ is usually 1–6 MHz (Moniz and Gutowsky, 1963), much greater than $\|H_{\mathrm{dipolar}}\|$ or $\|H_{\mathrm{CS}}\|$. Unfortunately, this also means that the full quadrupolar powder pattern cannot be uniformly excited by rf pulses. In contrast, $\|H_{\mathrm{Q}}\|$ for ^{2}H in the form of the quadrupole coupling constant e^2qQ/h is usually 200–275 kHz, and the full powder pattern can be uniformly excited by high-power rf pulses.[1] Also, the dipolar coupling and chemical shift for the ^{2}H nucleus are 6.51 times smaller than for the ^{1}H nucleus because $\gamma_{H1}/\gamma_{H2} = 6.51$. For the same reason, the ^{2}H–^{2}H homonuclear dipolar couplings are 42.4 times smaller than ^{1}H–^{1}H homonuclear dipolar couplings. This means that other Hamiltonians such as H_{CS}, $\mathrm{H}_{\mathrm{dipolar\_hetero}}$, and $\mathrm{H}_{\mathrm{dipolar\_homo}}$ may be ignored in ^{2}H relaxation calculations. Thus, in this case, $(1/T_n)_i \cong 1/T_{nQi}$, greatly simplifying the analysis of experimental deuterium NMR relaxation data.

Deuterium (^{2}H) has other advantages. The $I = 1$ deuterium quadrupolar PAS z axis, which is characterized by $\delta'_{zz} = (e^2qQ/2\hbar)$ (in radian s^{-1}, see Table 29.1), is parallel to the single X–H (e.g., C–H or O–H) covalent bond formed by hydrogen,[2] with $\eta \leq 0.1$. Therefore, the analysis of ^{2}H relaxation yields direct information about the angular motions of the covalent bond. For this reason, it is particularly useful in studies of chemical dynamics.

---

[1] 275 kHz is about the upper limit for uniform excitation by rf pulses in commercially available NMR spectrometers.

[2] Except in the case of boranes, where H can form two “half” covalent bonds.

CHAPTER 41

THE MASTER EQUATION FOR NMR RELAXATION—SINGLE SPIN SPECIES I

To understand NMR relaxation, it is necessary to understand the rather difficult derivations in the next two chapters. They are not trivial, and some effort is necessary to go through them. In this chapter, the derivations of Spiess are verified and reproduced for relaxation of the density operator of a *single nuclear spin species I* due to a fluctuating internal Hamiltonian $\hat{\mathrm{H}}_\lambda(t)$ (Abragam, 1983, Chapter 8, Equations 28.33 and 40, 42, pp. 276–279; Spiess, 1978, Chapter 4), Although our main interest is in $\hat{\mathrm{H}}_{\mathrm{Q}}(t)$ for $I=1$ deuterium because of its advantages, the analysis given here encompasses the pairwise homonuclear dipolar coupling Hamiltonian $\hat{\mathrm{H}}_{\mathrm{D-homo}}(t)$, the pairwise homonuclear J-coupling Hamiltonian $\hat{\mathrm{H}}_{\mathrm{J-homo}}(t)$, and the chemical shift Hamiltonian $\hat{\mathrm{H}}_{\mathrm{CS}}(t)$. Each of these Hamiltonians is different and therefore has different commutators, leading to different expressions for NMR relaxation rates.

GENERAL DERIVATION

Like the analysis of NMR pulse sequences, the relaxation derivation starts with the density operator $\rho(t)$ and fluctuating internal Hamiltonian $\hat{\mathrm{H}}_\lambda(t)$ in the rotating frame:

$$\rho_{\mathrm{rot}}(t) = e^{-i\omega_0 \hat{\mathrm{I}}_z t}\, \rho(t)\, e^{i\omega_0 \hat{\mathrm{I}}_z t} \tag{41.1}$$

$$\hat{\mathrm{H}}_\lambda^{\mathrm{rot}}(t) = e^{-i\omega_0 \hat{\mathrm{I}}_z t}\, \hat{\mathrm{H}}_\lambda(t) e^{i\omega_0 \hat{\mathrm{I}}_z t} \tag{41.2}$$

where ω_0 is the resonance (Larmor) frequency of the nucleus.

Using these, the resulting form of the Liouville–von Neumann (LVN) equation is as follows:

$$\frac{d\rho_{\mathrm{rot}}}{dt} = -i[\hat{\mathrm{H}}_\lambda^{\mathrm{rot}}(t), \rho_{\mathrm{rot}}] \tag{41.3}$$

A Primer of NMR Theory with Calculations in Mathematica®, First Edition. Alan J. Benesi.

Because the internal Hamiltonian $\hat{\mathrm{H}}_{\lambda}^{\mathrm{rot}}(t)$ is *not* constant but instead fluctuates due to molecular reorientation, it is necessary to integrate the LVN equation to second order:

$$\rho_{\mathrm{rot}}(t) = \rho_{\mathrm{rot}}(0) - i\int_{0}^{t}[\hat{\mathrm{H}}_{\lambda}^{\mathrm{rot}}(t), \rho_{\mathrm{rot}}(0)]\,dt' - \int_{0}^{t}dt'\int_{0}^{t'}dt''[\hat{\mathrm{H}}_{\lambda}^{\mathrm{rot}}(t'), [\hat{\mathrm{H}}_{\lambda}^{\mathrm{rot}}(t''), \rho_{\mathrm{rot}}(0)]] \qquad (41.4)$$

We take the time derivative to obtain the following:

$$\frac{d\rho_{\mathrm{rot}}}{dt} = -i[\hat{\mathrm{H}}_{\lambda}^{\mathrm{rot}}(t), \rho_{\mathrm{rot}}(0)] - \int_{0}^{t}dt'[\hat{\mathrm{H}}_{\lambda}^{\mathrm{rot}}(t), [\hat{\mathrm{H}}_{\lambda}^{rot}(t'), \rho_{\mathrm{rot}}(0)]] \qquad (41.5)$$

We make the substitution $\tau = t - \mathrm{t}'$ and rearrange it to $t' = t - \tau$ to obtain the following:

$$\frac{d\rho_{\mathrm{rot}}}{dt} = -i[\hat{\mathrm{H}}_{\lambda}^{\mathrm{rot}}(t), \rho_{\mathrm{rot}}(0)] - \int_{0}^{t}d\tau[\hat{\mathrm{H}}_{\lambda}^{\mathrm{rot}}(t), [\hat{\mathrm{H}}_{\lambda}^{\mathrm{rot}}(t-\tau), \rho_{\mathrm{rot}}(0)]] \qquad (41.6)$$

Because $\hat{\mathrm{H}}_{\lambda}^{\mathrm{rot}}(t)$ is random and fluctuating, its ensemble average $\overline{\hat{\mathrm{H}}_{\lambda}^{rot}(t)}$ is zero. This means that the ensemble average of $\left\langle[\hat{\mathrm{H}}_{\lambda}^{\mathrm{rot}}(t), \rho_{\mathrm{rot}}(0)]\right\rangle$ of Equation 41.6 is also zero for the ensemble of spins.

Five other assumptions are ultimately required to yield the master equation: (i) That $\hat{\mathrm{H}}_{\lambda}^{\mathrm{rot}}(t)$ and $\rho_{\mathrm{rot}}(0)$ are uncorrelated. (ii) That $\rho_{\mathrm{rot}}(0)$ can be replaced by $\rho_{\mathrm{rot}}(t)$. (iii) That the range of integration can be lengthened from t to $+\infty$. (iv) That terms of higher order than 2 in Equations 41.4–41.6 can be neglected. (v) That the part of the density operator that deviates from equilibrium is $\rho^{\S} = \rho_{\mathrm{rot}} - \rho_{\mathrm{eq}}$. It is often stated that relaxation toward ρ_{eq} is an "ad hoc" assumption but more likely it reflects a very slight favoring of angular motions that yield the lower Zeeman energy level(s), since this is required energetically.

With these assumptions, Equation 41.6 can be rewritten as *the master equation*:

$$\frac{d\rho^{\S}}{dt} = -\int_{0}^{t}d\tau\left\langle[\hat{\mathrm{H}}_{\lambda}^{\mathrm{rot}}(t), [\hat{\mathrm{H}}_{\lambda}^{\mathrm{rot}}(t-\tau), \rho^{\S}(t)]]\right\rangle \qquad (41.7)$$

where $\rho^{\S} = \rho_{\mathrm{rot}} - \rho_{\mathrm{eq}}$, $\hat{\mathrm{H}}_{\lambda}^{\mathrm{rot}}(t)$ is the rotating frame internal Hamiltonian λ at some arbitrary time t, and $\hat{\mathrm{H}}_{\lambda}^{\mathrm{rot}}(t-\tau)$ is internal Hamiltonian λ at time τ before. The angle brackets indicate the ensemble average. The two sets of square brackets indicate the double commutator.

The internal Hamiltonian is most simply expressed in spherical tensor form with the $\hat{\mathrm{T}}^{l,m}$ in the rotating frame (as verified using matrix representation of the $\hat{\mathrm{T}}^{l,m}$ in *spintensors_matrix.nb*)[1]:

$$\hat{\mathrm{T}}_{\mathrm{rot}}^{l,m}(t) = e^{-i\omega_0\hat{\mathrm{I}}_z t}\,\hat{\mathrm{T}}^{l,m}e^{i\omega_0\hat{\mathrm{I}}_z t} = \hat{\mathrm{T}}^{l,m}\,e^{im\omega_0 t} \qquad (41.8)$$

---

[1] The *laboratory* frame $\hat{\mathrm{T}}^{l,m}$'s are *time dependent* for $\hat{\mathrm{H}}_{\mathrm{J}}$ and $\hat{\mathrm{H}}_{\mathrm{SR}}$ but are time independent for the other internal Hamiltonians.

The fluctuating real space tensors $\overset{=}{\mathrm{A}}^{l,m}(\mathrm{t})$ are unaffected by the spin space rotating frame transformation.

$\hat{\mathrm{H}}_{\lambda}^{\mathrm{rot}}(t)$ is given by Equation 31.1, that is,

$$\hat{\mathrm{H}}_{\lambda}^{\mathrm{rot}}(t)=\textstyle\sum_{l=0}^{2}\sum_{m=-l}^{+l}(-1)^{m}\,\overset{=}{\mathrm{A}}^{l,m}(\mathrm{t})\,\hat{\mathrm{T}}_{\mathrm{rot}}^{l,-m}=\sum_{l=0}^{2}\sum_{m=-l}^{+l}(-1)^{m}\,\overset{=}{\mathrm{A}}^{l,m}(\mathrm{t})\;\hat{\mathrm{T}}^{l,m}\,e^{-im\omega_0 t} \qquad (41.9)$$

where $\hat{\mathrm{T}}^{l,m}$ and $\hat{\mathrm{T}}_{\mathrm{rot}}^{l,m}$ are the spin space tensors in the laboratory and rotating reference frames, respectively.

With the exception of $\hat{\mathrm{H}}_{\mathrm{J}}^{\mathrm{rot}}(t)$ and $\hat{\mathrm{H}}_{\mathrm{SR}}^{\mathrm{rot}}(t)$, which usually have negligible relaxation effects in solids and most liquids, the time-dependence in $\hat{\mathrm{H}}_{\lambda}^{\mathrm{rot}}(t)$ arises exclusively from the time-dependence of $\overset{=}{\mathrm{A}}^{l,m}(\mathrm{t})$. Substituting Equations 41.8 and 41.9 in the master equation (Eq. 41.7) and extending the limit of integration to infinity yields the following (Spiess, 1978, p. 108):

$$\frac{d\rho^{\S}}{dt}=-\sum_{l1=0}^{2}\sum_{l2=0}^{2}\sum_{m1=-l}^{l}\sum_{m2=-l}^{l}(-1)^{m1+m2}\,e^{i(m1+m2)\omega_0 t}[\hat{\mathrm{T}}^{l1,m1},[\hat{\mathrm{T}}^{l2,m2},\rho^{\S}(0)]]$$
$$\times\int_0^{\infty}\left\langle\overset{=}{\mathrm{A}}^{l1,m1}(\mathrm{t})\;\overset{=}{\mathrm{A}}^{l2,m2}(t-\tau)\right\rangle e^{-im2\,\omega_0\tau}\,d\tau \qquad (41.10)$$

The deviation of the density operator from equilibrium, $\rho^{\S}$, is zero in the absence of the perturbing Hamiltonian $\hat{\mathrm{H}}_{\lambda}^{\mathrm{rot}}(t)$. Since $\left\|\hat{\mathrm{H}}_{\lambda}^{\mathrm{rot}}\right\|(t)$ is small compared with the magnitude of the Zeeman Hamiltonian $\|\hat{\mathrm{H}}_{\mathrm{Z}}\|$, the variation of $\rho^{\S}$ with time is slow and the rapidly varying terms with $m1\neq -m2$ can be ignored. Only the time-independent secular terms with $m1=-m2$ are included in the summation. In addition, the orthogonality of the Wigner rotation elements and of the $\overset{=}{\mathrm{A}}^{l,m}$ require $l1=l2$ *and* $m1=-m2$ (see *wigner_orthogonality.nb*) (Spiess, 1978, p. 108). With these stipulations, the *master equation* can be written as

$$\frac{d\rho^{\S}}{dt}=-\textstyle\sum_{l=0}^{2}\sum_{m=-l}^{l}[\hat{\mathrm{T}}^{l,m},[\hat{\mathrm{T}}^{l,-m},\rho^{\S}(0)]]\times\displaystyle\int_0^{\infty}\left\langle\overset{=}{\mathrm{A}}^{l,m*}(\mathrm{t})\;\overset{=}{\mathrm{A}}^{l,m}(t-\tau)\right\rangle e^{im\omega_0\tau}\,d\tau \qquad (41.11)$$

where $\overset{=}{\mathrm{A}}^{l,m*}(\mathrm{t})$ is the complex conjugate of $\overset{=}{\mathrm{A}}^{l,m}(\mathrm{t})$ (see *wigner_orthogonality.nb*).

The term $\left\langle\overset{=}{\mathrm{A}}^{l,m*}(\mathrm{t})\overset{=}{\mathrm{A}}^{l,m}(t-\tau)\right\rangle$ is the autocorrelation function in the real space tensor $\overset{=}{\mathrm{A}}^{l,m}$. The time-dependence is caused by the angular reorientation of the internal Hamiltonian PAS relative to the laboratory frame. *Because the angular reorientation is random with no preferred direction or origin in time*, the arguments t and τ can be changed to yield the autocorrelation function $g_{l,m}(t)$:

$$g_{l,m}(t)\equiv\left\langle\overset{=}{\mathrm{A}}^{l,m*}(t)\overset{=}{\mathrm{A}}^{l,m}(t-\tau)\right\rangle=\left\langle\overset{=}{\mathrm{A}}^{l,m*}(0)\overset{=}{\mathrm{A}}^{l,m}(\tau)\right\rangle \qquad (41.12)$$

As shown in Equation 39.1a, the complex conjugate $\overset{=}{\mathrm{A}}^{l,m*}(0)$ can be replaced with $-1^{l+m}\,\overset{=}{\mathrm{A}}^{l,-m}$.

It is customary to factor out δ'_{zz} and η from $\overset{=}{\mathrm{A}}^{l,m}$ for $l=2$ and α'_{xy}, α'_{xz}, and α'_{yz} for $l=1$ in which case the "reduced" correlation function $G_{l,m}(t)$ is used (Eq. 39.1b), that is,

$$G_{l,m}(\tau)=\frac{\left\langle A_{\mathrm{lab}}^{l,m*}(0)\,A_{\mathrm{lab}}^{l,m}(\tau)\right\rangle}{(A_{\mathrm{PAS}}^{2,0\;2})} \tag{41.13}$$

Substitution of Equation 41.13 into 41.11 yields the following:

$$\frac{d\rho^{\S}}{dt}=-C_{\gamma}\,\textstyle\sum_{l=0}^{2}\sum_{m=-l}^{l}(-1)^{l+m}[\hat{\mathrm{T}}^{l,m},[\hat{\mathrm{T}}^{l,-m},\rho^{\S}(0)]]\times\displaystyle\int_{0}^{\infty}G_{l,m}(t)\,e^{im\omega_0\tau}\,d\tau \tag{41.14}$$

where $C_{\gamma}=A_{\mathrm{PAS}}^{2,0\;2}$ and is dependent on the Hamiltonian $\hat{\mathrm{H}}_{\lambda}^{\S}$.

The spectral density is defined as (see Eq. 39.3b)

$$J_{l,m}(m\omega_0)=\int_{0}^{\infty}G_{l,m}(t)\,e^{im\omega_0\tau}\,d\tau \tag{41.15}$$

Substituting Equation 41.15 in Equation 41.14 yields the following:

$$\frac{d\rho^{\S}}{dt}=-C_{\gamma}\,\textstyle\sum_{l=0}^{2}\sum_{m=-l}^{l}(-1)^{l+m}[\hat{\mathrm{T}}^{l,m},[\hat{\mathrm{T}}^{l,-m},\rho^{\S}(0)]]\times J_{l,m}(m\omega_0) \tag{41.16}$$

The master equation can be solved in several ways to calculate NMR relaxation times (rates). The simplest in concept is to solve the master equation (Eq. 41.16) for the relaxation of the density matrix using the matrix representations of $\hat{\mathrm{T}}^{l,m}$ and $\rho^{\S}(0)$:

$$\frac{d\left\langle\hat{\mathrm{I}}_{\mathrm{op}}\right\rangle}{dt}=\mathrm{Tr}\left[\hat{\mathrm{I}}_{\mathrm{op}}\cdot\frac{d\rho^{\S}}{dt}\right] \tag{41.17}$$

An alternative approach is to use the following relations verified in *spintensors_matrix.nb* (Spiess, 1978, pp. 109, 110):

$$\mathrm{Tr}\{[[\hat{\mathrm{T}}^{l,m},[\hat{\mathrm{T}}^{l,-m},\rho^{\S}(0)]]]\cdot\hat{\mathrm{I}}_{\mathrm{op}}\}=\mathrm{Tr}\{[[\hat{\mathrm{T}}^{l,-m},[\hat{\mathrm{T}}^{l,m},\hat{\mathrm{I}}_{\mathrm{op}}]]\cdot\rho^{\S}(0)]\} \tag{41.18}$$

The commutation relations of the $\hat{\mathrm{T}}^{l,m}$ with the spin angular momentum operators $\hat{\mathrm{I}}_{\mathrm{op}}$ (see *spintensors_matrix.nb*) are as follows (Spiess, 1978)[2]:

---

[2] But modified to match our definitions of the spherical tensor operators.

$$[\hat{\mathrm{I}}^{\pm}, \hat{\mathrm{T}}^{l,m}] = \sqrt{l(l+1) - m(m \pm 1)}\, \hat{\mathrm{T}}^{l,m\pm 1} \tag{41.19a}$$

$$[I_z, \hat{\mathrm{T}}^{l,m}] = m\hat{\mathrm{T}}^{l,m} \tag{41.19b}$$

Since $[\hat{\mathrm{T}}^{l,-m}, [\hat{\mathrm{T}}^{l,m}, \hat{\mathrm{I}}_{\mathrm{op}}]] = [[\hat{\mathrm{I}}_{\mathrm{op}}, \hat{\mathrm{T}}^{l,m}], \hat{\mathrm{T}}^{l,-m}]$, these equations allow the double commutators of the master equation (Eq. 41.18) to be written in terms of single commutators

$$\left\langle \frac{d\hat{\mathrm{I}}_z}{dt} \right\rangle = -C_\gamma \textstyle\sum_{l=0}^{2} \sum_{m=-l}^{l} (-1)^{l+m} [\hat{\mathrm{T}}^{l,m}, \hat{\mathrm{T}}^{l,-m}] \times m\, J_{l,m}(m\omega_0) \tag{41.20a}$$

and

$$\left\langle \frac{dI^{\pm}}{dt} \right\rangle = -C_\gamma \textstyle\sum_{l=0}^{2} \sum_{m=-l}^{l} (-1)^{l+m} [\hat{\mathrm{T}}^{l,m\pm 1}, \hat{\mathrm{T}}^{l,-m}] \times \sqrt{l(l+1) - m(m \pm 1)} \times J_{l,m}(m\omega_0) \tag{41.20b}$$

Further simplification can be achieved by using the Clebsch–Gordan coefficients to evaluate the spherical tensor commutators in Equations 41.20a and 41.20b (see *ClebschGordan.nb*). The results are as follows:

$$\begin{aligned}\left\langle \frac{d\hat{\mathrm{I}}_z}{dt} \right\rangle = & -\sqrt{2} \times C_\gamma \{(J[1,-1,-\omega] + J[1,1,\omega])\} \left\langle \hat{\mathrm{T}}^{1,0} \right\rangle \\ & -\sqrt{\frac{2}{5}} \times C_\gamma \{(4J[2,-2,-2\omega] + 4J[2,2,2\omega] + J[2,-1,-\omega] + J[2,1,\omega])\} \left\langle \hat{\mathrm{T}}^{1,0} \right\rangle \\ & -\sqrt{\frac{2}{5}} \times C_\gamma \{(2J[2,-2,-2\omega] + 2J[2,2,2\omega] - 2J[2,-1,-\omega] - 2J[2,1,\omega])\} \left\langle \hat{\mathrm{T}}^{3,0} \right\rangle\end{aligned} \tag{41.21a}$$

$$\begin{aligned}\left\langle \frac{d\hat{\mathrm{I}}^{\pm}}{dt} \right\rangle = & -C_\gamma \{2J[1,0,0] + 2J[1,\mp 1,\mp\omega]\} \left\langle \hat{\mathrm{T}}^{1,\pm 1} \right\rangle \\ & -\frac{2}{\sqrt{5}} \times C_\gamma \{2J[2,\mp 2,\mp 2\omega] + 3J[2,\mp 1,\mp\omega] + 3J[2,0,0] + 2J[2,\pm 1,\pm\omega]\} \left\langle \hat{\mathrm{T}}^{1,\pm 1} \right\rangle \\ & -\frac{2}{\sqrt{5}} \times C_\gamma \{\sqrt{6}J[2,\mp 2,\mp 2\omega] - \sqrt{6}J[2,\mp 1,\mp\omega] - \sqrt{6}J[2,0,0] + \sqrt{6}J[2,\pm 1,\pm\omega]\} \left\langle \hat{\mathrm{T}}^{3,\pm 1} \right\rangle\end{aligned} \tag{41.21b}$$

Equations 41.21a and 41.21b are identical to the results derived by Spiess (1978, pp. 110–111, eqs. 4.42 and 4.43). Equation 41.21a corresponds to T_1 (spin lattice) relaxation. Equation 41.21b corresponds to T_2 (spin–spin) relaxation.

$\langle \hat{\mathrm{I}}_z \rangle$ and $\langle \hat{\mathrm{T}}^{10} \rangle$, and $\langle \hat{\mathrm{I}}^{\pm} \rangle$ and $\langle \hat{\mathrm{T}}^{1\pm 1} \rangle$ are proportional and the constant of proportionality is independent of *m*. They are calculated by using commutators of the $\hat{\mathrm{T}}^{l,m}$ as described by Spiess (1978, pp. 113–114, eqs. 4.53 and 4.54). Different Hamiltonians $\hat{\mathrm{H}}_\lambda$ give rise to different commutators and constants of proportionality. The essential commutator relations of the different Hamiltonians for a single nuclear spin type are given in Table 41.1.

TABLE 41.1 Important commutators of spin space tensors

Hamiltonian	$[\hat{T}^{10},\hat{T}^{10}]$	$[\hat{T}^{11},\hat{T}^{1-1}]$	$[\hat{T}^{22},\hat{T}^{2-2}]$	$[\hat{T}^{21},\hat{T}^{2-1}]$[a]
D_{homo}[b]	0	NA[c]	$\frac{1}{2}(I(I+1)*\hat{1}-\hat{I}_{z1}\cdot\hat{I}_{z2})\cdot(\hat{I}_{z1}+\hat{I}_{z2})$	$\left(\frac{1}{2}\hat{I}_1\cdot\hat{I}_2-\hat{I}_{z1}\cdot\hat{I}_{z2}\right)\cdot(\hat{I}_{z1}+\hat{I}_{z2})$
$J_{\text{homo}}(I=S)$[b]	0	$\frac{1}{2}\hat{I}_1\cdot\hat{I}_2\cdot(\hat{I}_z+\hat{S}_z)$	$\frac{1}{2}(I(I+1)*\hat{1}-\hat{I}_{z1}\cdot\hat{I}_{z2})\cdot(\hat{I}_{z1}+\hat{I}_{z2})$	$\left(\frac{1}{2}\hat{I}_1\cdot\hat{I}_2-\hat{I}_{z1}\cdot\hat{I}_{z2}\right)\cdot(\hat{I}_{z1}+\hat{I}_{z2})$
Q	0	NA[c]	$(2I(I+1)*\hat{1}-2\hat{I}_z^2-\hat{1})\cdot\hat{I}_z$	$\left(2I(I+1)*\hat{1}-4\hat{I}_z^2-\frac{1}{2}*\hat{1}\right)\cdot\hat{I}_z$

[a] $\hat{I}_1\cdot\hat{I}_2=\hat{I}_{x1}\cdot\hat{I}_{x2}+\hat{I}_{y1}\cdot\hat{I}_{y2}+\hat{I}_{z1}\cdot\hat{I}_{z2}$, $\hat{I}_1^2=I_1(I_1+1)*\hat{1}=\hat{I}_2^2=I_2(I_2+1)*\hat{1}$ and $\hat{1}$ is the unit matrix.

[b] Spin I_1 and spin I_2 are the same type of nuclei and have the same nuclear spin quantum number I and same Larmor frequency.

[c] $A^{l,m}=0$ for the dipolar and quadrupolar Hamiltonians.

QUADRUPOLAR RELAXATION, *I*=1

For the quadrupolar Hamiltonian $\hat{H}_Q$, we calculate the following relationships between the quadrupolar spin tensor commutators and the nuclear spin tensor $\hat{I}_z$ (see *ClebschGordan.nb*):

$$l=1:\ [\hat{T}^{1,1},\hat{T}^{1,-1}]=\sqrt{2}\,\hat{T}^{1,0}=\sqrt{2}\,a_1\hat{I}_z \tag{41.22a}$$

$$l=2:\ 2\times[\hat{T}^{2,2},\hat{T}^{2,-2}]-[\hat{T}^{2,1},\hat{T}^{2,-1}]=\sqrt{10}\,\hat{T}^{1,0}=\sqrt{10}\,a_2\,\hat{I}_z \tag{41.22b}$$

$$l=3:\ [\hat{T}^{2,2},\hat{T}^{2,-2}]+2\times[\hat{T}^{2,1},\hat{T}^{2,-1}]=\sqrt{10}\,\hat{T}^{3,0} \tag{41.22c}$$

As verified using matrix representation of the $\hat{T}^{l,m}$ in *spintensors_matrix.nb*, $\hat{T}^{3,0}$ is zero for $I=1$.[3]

Solving for a_1 and a_2, we obtain the following:

$$a_1=\frac{[\hat{T}^{1,1},\hat{T}^{1,-1}]}{\sqrt{2}} \tag{41.23a}$$

$$a_2=\frac{2[\hat{T}^{2,2},\hat{T}^{2,-2}]-[\hat{T}^{2,1},\hat{T}^{2,-1}]}{\sqrt{10}} \tag{41.23b}$$

Evaluation of these commutators in Table 41.1 and Equations 41.22a and 41.22b is necessary to calculate the relaxation rates predicted in Equations 41.21a and 41.21b. The commutators in Table 41.1 were calculated by using the definitions of the internal Hamiltonian $\hat{T}_\lambda^{l,m}$ in terms of ladder operators found in Table 31.2B, calculating the desired commutators in *commutators.nb*, then simplifying the program

---

[3] It is also zero for homonuclear dipolar and J-coupling of $I=1/2$ nuclear spins.

[4] Sometimes, it is easier to do a calculation by hand than to write a generic program to do it!

results *by hand*[4] using the ladder operator commutators defined in Equations 19.3e, 19.3f, 19.4, 19.5a, and 19.5b.[5] The commutator $[\hat{T}_Q^{1,1}, \hat{T}_Q^{1,-1}]$ does not contribute to relaxation for quadrupolar nuclei because corresponding real space autocorrelation functions $\left\langle \overset{=}{A}^{0,0*}(0)\overset{=}{A}^{0,0}(\tau)\right\rangle$ and $\left\langle \overset{=}{A}^{1,m*}(0)\overset{=}{A}^{1,m}(\tau)\right\rangle$ are both zero due to the traceless character of $\overset{=Q}{A}_{\mathrm{PAS}}$. The $\hat{T}_Q^{3,0}$ and $\hat{T}_Q^{3,\pm1}$ terms in Equations 41.21a and 41.21b vanish (see the matrix evaluation in *spintensors_matrix.nb*) for $I=1$.

Therefore, the contributing commutators for quadrupolar $I=1$ nuclei are as follows (Spiess, 1978, Table 4.1.):

$$[\hat{T}^{2,2}, \hat{T}^{2,-2}] = \{2\hat{I}^2 - 1 - 2\hat{I}_z^2\}.I_z = \{2I(I+1) - 1 - 2\hat{I}_z^2\}.\hat{I}_z \tag{41.24a}$$

$$[\hat{T}^{2,1}, \hat{T}^{2,-1}] = \left\{2\hat{I}^2 - \frac{1}{2} - 4I_z^2\right\}.\hat{I}_z = \left\{2I(I+1) - \frac{1}{2} - 4\hat{I}_z^2\right\}.\hat{I}_z \tag{41.24b}$$

Substituting Equations 41.24a and 41.24b into Equation 41.22b yields the following:

$$a_2 = \frac{\left\{2I(I+1) - \frac{3}{2}\right\}}{\sqrt{10}} \tag{41.25}$$

Thus, for $\left\langle d\hat{I}_z/dt\right\rangle$ and $I=1$, $a_2 = \left(\sqrt{5}/2\sqrt{2}\right)$, and the product $\sqrt{2/5}\times a_2 = 1/2$, so

$$\left\langle \frac{d\hat{I}_z}{dt}\right\rangle = -\frac{1}{2}\times C_Q(4J[2,-2,-2\omega] + 4J[2,2,2\omega] + J[2,-1,-\omega] + J[2,1,\omega])\left\langle \hat{I}_z\right\rangle \tag{41.26a}$$

Similarly, for $\left\langle d\hat{I}^{\pm}/dt\right\rangle$ and $I=1$, so $\sqrt{5}/2\sqrt{2}\times 2/\sqrt{5} = 1/\sqrt{2}$, so

$$\left\langle \frac{d\hat{I}^{\pm}}{dt}\right\rangle = -\frac{1}{\sqrt{2}}\times C_Q\{2J[2,\mp2,\mp2\omega] + 3J[2,\mp1,\mp\omega] + 3J[2,0,0] + 2J[2,\pm1,\pm\omega]\}\left\langle \hat{I}^{\pm}\right\rangle \tag{41.26b}$$

Equations 41.26a and 41.26b can be further simplified by using the relation $J[l,-m,-m\omega] = J[l,m,m\omega]$, yielding for quadrupolar relaxation of an $I=1$ nucleus:

$$\left\langle \frac{d\hat{I}_z}{dt}\right\rangle = -\frac{1}{2}\times C_Q(8J[2,2,2\omega] + 2J[2,1,\omega])\left\langle \hat{I}_z\right\rangle \tag{41.27a}$$

$$\left\langle \frac{d\hat{I}^{\pm}}{dt}\right\rangle = -\frac{1}{\sqrt{2}}\times C_Q\{2J[2,2,2\omega] + 5J[2,1,\omega] + 3J[2,0,0]\}\left\langle \hat{I}^{\pm}\right\rangle \tag{41.27b}$$

---

[5] The *commutators.nb* program in its present form cannot automatically simplify the results. Students and researchers can improve the program if they wish.

For an $I=1$ quadrupolar nucleus like deuterium, $C_Q = {A_{\mathrm{PAS}}^{2,0}}^2 = \left(\sqrt{\frac{3}{2}}\frac{e^2qQ}{2I(2I-1)\hbar}\right)^2 = \frac{3}{8}\left(\frac{e^2qQ}{\hbar}\right)^2$. With Equations 41.27a and 41.27b, this yields the same expressions derived by Spiess (1978, Table 4.3), Abragam (1983, pp. 313, 314), and Torchia and Szabo (1982, eq. 8).

Therefore, for an $I=1$ nucleus, the quadrupolar relaxation rates (inverses of relaxation times) are as follows:

$$\frac{1}{T_1} = \frac{1}{2}\times C_Q(8J[2,2,2\omega]+2J[2,1,\omega]) \tag{41.28a}$$

$$\frac{1}{T_2} = \frac{1}{\sqrt{2}}\times C_Q\{2J[2,2,2\omega]+5J[2,1,\omega]+3J[2,0,0]\} \tag{41.28b}$$

HOMONUCLEAR RELAXATION OF DIPOLAR AND J-COUPLED SPINS (E.G., TWO *I* = 1/2 COUPLED SPINS)

Equations 41.21a and 41.21b also apply to dipolar and J-coupling of homonuclear nuclei. However, the commutators required to calculate the constants a_1 and a_2 are different (see Table 41.1) (Spiess, 1978, Table 4.2):

$$[\hat{T}^{1,1}, \hat{T}^{1,-1}] = \frac{1}{2}\hat{I}_1\cdot\hat{I}_2\cdot(\hat{I}_{z1}+\hat{I}_{z2}) \tag{41.29a}$$

$$[\hat{T}^{2,2}, \hat{T}^{2,-2}] = \frac{1}{2}(\hat{I}^2-\hat{I}_1\cdot\hat{I}_2)\cdot(\hat{I}_{z1}+\hat{I}_{z2}) \tag{41.29b}$$

$$[\hat{T}^{2,1}, \hat{T}^{2,-1}] = \left(\frac{1}{4}\hat{I}_1^+\cdot\hat{I}_2^- + \frac{1}{4}\hat{I}_1^-\cdot\hat{I}_2^+ - \frac{1}{2}\hat{I}_{z1}\cdot\hat{I}_{z2}\right)\cdot(\hat{I}_{z1}+\hat{I}_{z2}) \tag{41.29c}$$

where $\hat{I}_1\cdot\hat{I}_2 = (\hat{I}_{x1}\cdot\hat{I}_{x2}+\hat{I}_{y1}\cdot\hat{I}_{y2}+\hat{I}_{z1}\cdot\hat{I}_{z2})$, $\hat{I}^2 = I(I+1)$, and I is the nuclear spin quantum number of each of the homonuclear coupled spins. These commutators are verified using matrix expressions for coupled spins $I=1/2$ in *spintensor_couple_matrix.nb* and were derived for all I by hand using commutator expressions for $\hat{T}^{l,m}_{\mathrm{D\_homo}}$.

The allowed values of total angular momentum for two coupled spins I_1 and I_2 are given by the addition theorem of angular momentum (Levine, 1974, pp. 248–252):

$$F = I_1+I_2, I_1+I_2-1, \ldots, |I_1-I_2| \tag{41.30}$$

and for each value of F, m takes on $(2F+1)$ values

$$m = F, F-1, \ \ldots, -F \tag{41.31}$$

As pointed out by Spiess[114] and verified by hand, forming $F^2 = (I_1 + I_2)^2$ leads to the relation $\hat{\mathrm{I}}_1 \cdot \hat{\mathrm{I}}_2 = \frac{1}{2} F(F+1) - 2I(I+1)$. This in turn leads to the following expressions for a_1 and a_2 as functions of F:

$$a_1(F) = \frac{1}{4\sqrt{2}}\left(F(F+1) - 2I(I+1)\right) \tag{41.32}$$

$$a_2(F) = \frac{1}{2\sqrt{10}}\left(3I(I+1) - \frac{1}{2}F(F+1)\right) \tag{41.33}$$

Since we are interested in the expectation values $\langle I_z \rangle$ and $\langle I^+ \rangle$, we need the weighted average of the a_1 and a_2 values over all possible values of F and the corresponding substates (see Eq. 41.31). The number of substates for each F value is $(2F+1)$ and the intensity of each substate is $F(F+1)$, so each F factor is weighted by $(2\mathrm{F}+1)\, F\, (F+1)$. The weighted averages are given by

$$\bar{\mathrm{a}}_1 = \frac{1}{4\sqrt{2}}\left(\frac{\sum_{F=0}^{2\mathrm{I}}(2F+1)F^2(F+1)^2}{I(I+1)\sum_{F=0}^{2\mathrm{I}}(2F+1)F(F+1)} - 2\right) I(I+1) \tag{41.34}$$

$$\bar{\mathrm{a}}_2 = \frac{1}{2\sqrt{10}}\left(3 - \frac{\sum_{F=0}^{2\mathrm{I}}(2F+1)F^2(F+1)^2}{2I(I+1)\sum_{F=0}^{2\mathrm{I}}(2F+1)F(F+1)}\right) I(I+1) \tag{41.35}$$

Also, it is easily verified by induction (*see spintensor_couple_matrix.nb*) that

$$\frac{\sum_{F=0}^{2\mathrm{I}}(2F+1)F^2(F+1)^2}{2I(I+1)\sum_{F=0}^{2\mathrm{I}}(2F+1)F(F+1)} = \frac{4}{3} \tag{41.36}$$

This yields the following:

$$\bar{\mathrm{a}}_1 = \frac{1}{6\sqrt{2}} I(I+1) \tag{41.37}$$

$$\bar{\mathrm{a}}_2 = \frac{\sqrt{10}}{12} I(I+1) \tag{41.38}$$

Thus, for two homonuclear dipole coupled $I = 1/2$ spins (such as two ^{1}H nuclei), there are only $l = 2$ contributions, and $\bar{\mathrm{a}}_2 = \sqrt{10}/16$, so $\sqrt{2/5} \times a_2 = 1/8$, and the $\hat{\mathrm{T}}^{3,0}$ and $\hat{\mathrm{T}}^{3,\pm 1}$ terms in Equations 41.22a and 41.22b vanish (see their evaluation in *spintensor_couple_matrix.nb*). Therefore,

$$\left\langle \frac{d\hat{\mathrm{I}}_z}{dt} \right\rangle = -\frac{1}{8} \times C_{\mathrm{D\_homo}}\left(4J[2,-2,-2\omega] + 4J[2,2,2\omega] + J[2,-1,-\omega] + J[2,1,\omega]\right) \left\langle \hat{\mathrm{I}}_z \right\rangle = -\left(\frac{1}{T_1}\right)\left\langle \hat{\mathrm{I}}_z \right\rangle \tag{41.39a}$$

Similarly,

$$\left\langle \frac{d\hat{\mathrm{I}}^{\pm}}{dt} \right\rangle = -\frac{\sqrt{2}}{8} \times C_{\mathrm{D\_homo}} \{2J[2,2,2\omega] + 5J[2,1,\omega] + 3J[2,0,0]\} \left\langle \hat{\mathrm{I}}^{\pm} \right\rangle = -\left(\frac{1}{T_2}\right) \left\langle \hat{\mathrm{I}}^{\pm} \right\rangle \tag{41.39b}$$

where for the homonuclear dipolar Hamiltonian $C_{\mathrm{D\_homo}} = A_{\mathrm{PAS}}^{2,0\;2} = \left(\sqrt{\frac{3}{2}} \frac{\mu_0 \gamma^2}{r_{I_1 I_2}^3} \right)^2$ and γ is the gyromagnetic ratio of the coupled nuclear spins.

CHEMICAL SHIFT RELAXATION

A different approach is required for calculation of chemical shift NMR relaxation times. Unlike the dipolar and quadrupolar Hamiltonians where products of two spin angular momentum operators ($\hat{\mathrm{I}}_1$ and $\hat{\mathrm{I}}_2$ for homonuclear dipolar and $\hat{\mathrm{I}}$ and $\hat{\mathrm{I}}$ for quadrupolar) are required, the chemical shift Hamiltonian is built from a product of a single spin angular momentum operator $\hat{\mathrm{I}}$ and the magnetic field $\mathbf{B} = \{0,0,B_0\}$. Therefore, *the* $l = 2$ *spin tensors for the chemical shift Hamiltonian* (see Table 31.2) can be expressed in terms of *the* $l = 1$ *spherical tensors for a nuclear spin* (see Spiess, 1978, p. 115; Table 31.1):

$$\hat{\mathrm{T}}_{\mathrm{CS}}^{l,m} = B_0 b_{l,m} \hat{\mathrm{T}}_{1,m}^{I} \tag{41.40}$$

with $b_{0,0} = 1, b_{1,0} = 0, b_{2,\pm 2} = 0, b_{2,0} = \sqrt{\frac{2}{3}}, b_{1,1} = \frac{1}{\sqrt{2}}, b_{1,-1} = \frac{-1}{\sqrt{2}}, b_{2,\pm 1} = \frac{1}{\sqrt{2}}$.

This representation of the $\hat{\mathrm{T}}_{\mathrm{CS}}^{l,m}$ is substituted in Equations 41.20a and 41.20b, *with the result that only the* $\hat{\mathrm{T}}_{1,m}^{I}$ *cause relaxation*. For an $I = 1/2$ nuclear spin (Spiess, 1978, Eq. 4.38'),

$$\left\langle \frac{d\hat{\mathrm{I}}_z}{dt} \right\rangle = -C_{\mathrm{CS}} \textstyle\sum_{l=0}^{2} \sum_{m=-1}^{1} (-1)^{l+m} b_{l,m} b_{l,-m} [\hat{\mathrm{T}}_{1,m}^{I}, \hat{\mathrm{T}}_{1,-m}^{I}] \times m J_{l,m}(m\omega_0) \tag{41.41a}$$

and

$$\left\langle \frac{dI^{\pm}}{dt} \right\rangle = -C_{\mathrm{CS}} \textstyle\sum_{l=0}^{2} \sum_{m=-1}^{1} (-1)^{l+m} b_{l,m} b_{l,-m} [\hat{\mathrm{T}}_{1,m\pm 1}^{I}, \hat{\mathrm{T}}_{1,-m}^{I}] \times \sqrt{2 - m(m \pm 1)} \times J_{l,m}(m\omega_0) \tag{41.41b}$$

Using the same methods as in the previous sections (see *ClebschGordan.nb*), this yields the following:

$$\left\langle \frac{d\hat{\mathrm{I}}_z}{dt} \right\rangle = -\frac{1}{\sqrt{2}} \times C_{\mathrm{CS}} (-J[2,-1,-\omega] - J[2,1,\omega] - J[1,-1,-\omega] - J[1,1,\omega]) \left\langle \hat{\mathrm{T}}_{1,0}^{I} \right\rangle \tag{41.42a}$$

and

$$\left\langle \frac{d\hat{\mathrm{I}}^{\pm}}{dt} \right\rangle = -\frac{1}{\sqrt{2}} C_{\mathrm{CS}} \left\{ \pm 2J[0,0,0] \pm J[1,\mp 1,\mp \omega] \pm J[2,\mp 1,\mp \omega] \pm \frac{4}{3} J[2,0,0] \right\} \left\langle \hat{\mathrm{T}}^{I}_{1,\pm 1} \right\rangle \tag{41.42b}$$

Recognizing that the $l = 2$ spectral densities are actually $l = 1$ and are expressed in terms of the nuclear spin operators $\hat{\mathrm{T}}^{I}_{1,m}$, we proceed by calculating $a_1 = -1/\sqrt{2}$, and find $\hat{\mathrm{T}}^{\mathrm{I}}_{1,0} = \frac{-1}{\sqrt{2}} \hat{\mathrm{I}}_z$ and $\hat{\mathrm{T}}^{I}_{1,\pm 1} = \frac{-1}{\sqrt{2}} \hat{\mathrm{I}}^{\pm}$, yielding finally

$$\left\langle \frac{d\hat{\mathrm{I}}_z}{dt} \right\rangle = -\frac{1}{2} \times C_{\mathrm{CS}} (J[2,-1,-\omega] + J[2,1,\omega] + J[1,-1,-\omega] + J[1,1,\omega]) \left\langle \hat{\mathrm{I}}_z \right\rangle \tag{41.43a}$$

$$\left\langle \frac{d\hat{\mathrm{I}}^{\pm}}{dt} \right\rangle = -\frac{1}{2} C_{\mathrm{CS}} \left\{ \mp 2J[0,0,0] \mp J[1,\mp 1,\mp \omega] \mp J[2,\mp 1,\mp \omega] \mp \frac{4}{3} J[2,0,0] \right\} \left\langle \hat{\mathrm{I}}^{\pm} \right\rangle \tag{41.43b}$$

where $C_{\mathrm{CS}} = A_{\mathrm{PAS}}^{2,0\ 2} = \left(\sqrt{\frac{3}{2}} \delta_{zz} \right)^2 = \frac{3}{2} \delta_{zz}^2 = \frac{3}{2} ((\sigma_{zz} - \sigma_{\mathrm{iso}})\gamma)^2$. These expressions are the same as those obtained by Spiess.

EXPLANATION OF *spintensors_matrix.nb*

This notebook uses matrix representation of nuclear spin angular momentum operators and of spin space tensors to verify some important commutation rules used in the calculation of relaxation rates for homonuclear spins. The user is told to evaluate *matrep2.nb*, then close it without saving changes.

The first cells use matrix representations of $I = 1$ and $I = 3/2$ spin angular momentum operators to verify Equations 19.3e, 19.3f, 19.4, 19.5a, and 19.5b.

The next cells define the spin space tensors T[*l,m*] from Table 31.2B in terms of the $I = 1$ spin angular momentum operators iplus[1], imin[1], iz[1], and isq[1].

The next cells calculate the Trot[*l,m*] to the rotating frame by propagating the T[*l,m*]. Equation 41.8 is verified.

The next cells verify some important commutator relations (Eqs. 41.18, 41.19a, and 41.19b) for both $I = 1$ and $I = 3/2$ (Spiess, 1978, p.109).

The next cells verify that T[3,0], T[3,1], and T[3,−1] are zero for $I = 1$.

EXPLANATION OF *ClebschGordan.nb*

This notebook shows how to use the built-in Mathematica function ClebschGordan and then uses it to verify some important NMR relaxation rate expressions.

After introducing the syntax of the function, the next cells use the built-in Mathematica function Off to suppress the nonphysical and nontriangular Clebsch–Gordan results.

The next cells show how to evaluate the product of two spin space spherical tensors, in this case T[2,1] and T[2,−1]. This yields a specific combination of $l=1$, 2, 3, and 4 terms.

The next cells show how to decompose a T[*l*,*m*], in this case T[3,0], into a specific combination of products of $l=2$ and $l=1$ terms.

The next cells decompose T[1,0] into a specific sum of products of $l=1$ and $l=2$ terms.

The next cells define the function comm[T[*l*1_,*m*1_],T[*l*2_,*m*2_]], which calculates the commutators $[T_{l1,m1}, T_{l2,m2}]$.

The next cells apply the comm function to evaluate dI_z/dt for quadrupolar nuclei (Eq. 41.20a) in terms of the T[2,*m*] and the spectral densities j[2,*m*,*mω*]. Then dI_{min} is evaluated in the same way using Equation 41.20b.

The next cells evaluate the commutators shown in Table 41.1.

The next cells define the b[*l*,*m*] terms in Equation 41.40 that relate the chemical shift Hamiltonian T[*l*,*m*] spin space tensors to the T_I[*l*,*m*] single nuclear spin spherical tensors (Table 31.1).

The next cells evaluate dI_z/dt for chemical shift relaxation according to Equations 41.20a and 41.20b.

The next cells evaluate the direct product of individual nuclear spin spherical tensors (Table 31.1) for two different nuclear spins *I* and *S*. These products yield a new Tnew[*L*,*M*] in terms of the $l=1$ nuclear spin spherical tensors for *I* and *S*.

The next cells define the specific sets of rules (commie) for commutators of these products in Table 42.1.

The commie rules are used to evaluate Equations 42.7a and 42.7b. These yield the same results as obtained by Spiess (1978, Eqs. 2.11 and 2.11a), *except* for the J[0,0,0] and J[0,0, −*ω*0i + *ω*0s] terms, which differ by a factor of 3 due to the different definition of T[$L=0$, $M=0$].

EXPLANATION OF *spintensor_couple_matrix.nb*

This notebook evaluates spin tensor commutators and other relations needed for homonuclear or heteronuclear coupled nuclear spins. For convenience, we assume that the spins are both $I=1/2$.

The first cells calculate the direct product matrix representations of nuclear spin operators for the two coupled $I=1/2$ spins (e.g., iz1, iz2, ix1, and ix2).

Next the matrix representations of the spin space spherical tensors T[*l*,*m*] are calculated.

Matrix commutators are then calculated for the commutators of the T[*l*,*m*]. These are used to verify Equations 41.29a, 41.29b, and 41.29c.

The next cells verify that T[3,0] = 0 for two coupled $I = 1/2$ spins.

The next cells verify Equations 41.36, 41.37, and 41.38.

The next cells verify the commutators presented in Table 42.1.

HOMEWORK

Homework 41.1: Use Equations 41.7–41.9 to derive Equation 41.10.

Homework 41.2: Verify Equations 41.21a and 41.21b.

Homework 41.3: Verify Equations 41.24a and 41.24b using commutator relationships.

Homework 41.4: Verify Equation 41.25.

Homework 41.5: Verify the equivalence of Equations 41.27a and 41.27b to those derived by Spiess, Abragam, and Torchia and Szabo.

Homework 41.6: Derive Equations 41.29a, 41.29b, and 41.29c using commutator relations.

Homework 41.7: Starting with Equations 41.21a and 41.21b, go through the full derivation to obtain Equations 41.42a and 41.42b.

CHAPTER 42

HETERONUCLEAR DIPOLAR AND J RELAXATION

Nuclear magnetic resonance (NMR) relaxation due to heteronuclear dipolar or J-coupling of unlike spins I and S requires a slightly different approach than presented in the previous chapter. In this case, the $\hat{\mathrm{T}}^{l,m}_{D\_\mathrm{hetero}}$ and $\hat{\mathrm{T}}^{l,m}_{J\_\mathrm{hetero}}$ must be transformed to the doubly rotating frame at the respective resonant (Larmor) frequencies of the unlike I and S nuclear spins. Again, we closely follow the derivation from Spiess (1978, pp. 119–122).

The derivation starts as before by taking the density operator $\rho(t)$ and fluctuating internal Hamiltonian $\hat{\mathrm{H}}_\lambda(t)$ (where $\lambda = D$_hetero or J_hetero) to the doubly rotating frame of the observed nuclei as indicated in Equations 42.1 and 42.2:

$$\rho_{\mathrm{rot}}(t) = e^{-i(\omega_{0I}\hat{\mathrm{I}}_z + \omega_{0S}\hat{\mathrm{S}}_z)t}\ \rho(t)\ e^{i(\omega_{0I}\hat{\mathrm{I}}_z + \omega_{0S}\hat{\mathrm{S}}_z)t} \tag{42.1}$$

where ω_{0I} and ω_{0S} are the respective resonant frequencies of the I and S nuclei and we again define $\rho^{\S} = \rho_{\mathrm{rot}} - \rho_{\mathrm{eq}}$ as the deviation of the density operator from equilibrium, and

$$\hat{\mathrm{H}}^{\mathrm{rot}}_\lambda(t) = e^{-i(\omega_{0I}\hat{\mathrm{I}}_z + \omega_{0S}\hat{\mathrm{S}}_z)t}\ \hat{\mathrm{H}}_\lambda(t)\, e^{i(\omega_{0I}\hat{\mathrm{I}}_z + \omega_{0S}\hat{\mathrm{S}}_z)t} \tag{42.2}$$

Since only the spin space components $\hat{\mathrm{T}}^{L,M}_\lambda$ of $\hat{\mathrm{H}}_\lambda$ are affected by the transformation in Equation 42.2, we can write[1]

$$\hat{\mathrm{T}}^{L,M}_{\mathrm{rot}\lambda}(t) = e^{-i(\omega_{0I}\hat{\mathrm{I}}_z + \omega_{0S}\hat{\mathrm{S}}_z)t}\,\hat{\mathrm{T}}^{L,M}_\lambda\, e^{i(\omega_{0I}\hat{\mathrm{I}}_z + \omega_{0S}\hat{\mathrm{S}}_z)t} \tag{42.3}$$

However, because the $\hat{\mathrm{T}}^{L,M}_\lambda$ are composed of products of spin angular momentum operators of unlike spins with different rotating frames, it is not immediately obvious how to evaluate Equation 42.3 as we did in Equation 41.8. The solution is to "decompose" the $\hat{\mathrm{T}}^{L,M}_\lambda$ Hamiltonian spherical tensor operators into *nuclear* spin spherical tensor operators of the component I and S nuclear spins (see Table 31.1 for the definitions).

---

[1] The capitalization of L and M is necessary for consistency with the Mathematica notebook *ClebschGordan.nb* and with Spiess' derivation.

A Primer of NMR Theory with Calculations in Mathematica®, First Edition. Alan J. Benesi.

This is achieved by using the *direct product* of the *nuclear* spin tensor operators and the Clebsch–Gordan coefficients as shown in *ClebschGordan.nb* (Spiess, 1978, p. 119):

$$\hat{\mathrm{T}}_{\lambda}^{L,M} = \sum_{m1=-1}^{1} \mathrm{ClebschGordan}\big[\{1, m1\}, \{1, M-m1\}, \{L, M\}\big]\hat{\mathrm{T}}^{I}_{1,m1}\,\hat{\mathrm{T}}^{S}_{1,M-m1} \qquad (42.4)$$

The Clebsch–Gordan coefficients found by Mathematica for the $L=0$, $M=0$ terms in Equations 42.4, 42.6, and 42.7a are too small by the factor $-\sqrt{3}$ (Spiess, 1978, Equation 2.11a). After accounting for this difference the result obtained is identical to that of Spiess (1978, Equations 4.42″ and 4.43″) (see *ClebschGordan.nb*).

With this substitution and proceeding as in the previous chapter, this yields the master equation (compare with Equation 41.11):

$$\begin{aligned}\frac{d\rho^{\S}}{dt} &= -C_{\gamma}\, \textstyle\sum_{L=0}^{2} \sum_{M=-L}^{L} \sum_{m1=-1}^{1} \mathrm{ClebschGordan}[\{1, m1\}, \{1, M-m1\}, \{L, M\}] \\ &\quad \times \mathrm{ClebschGordan}[\{1, m1\}, \{1, M-m1\}, \{L, -M\}] \\ &\quad [\hat{\mathrm{T}}^{\mathrm{I}}_{1,m1}\,\hat{\mathrm{T}}^{\mathrm{S}}_{1,M-m1},[\hat{\mathrm{T}}^{\mathrm{I}}_{1,-m1}\,\hat{\mathrm{T}}^{\mathrm{S}}_{1,-M+m1},\rho^{\S}(0)]] \\ &\quad \times \int_{0}^{\infty} < \overset{=}{\mathrm{A}}^{L,-M}(t)\; \overset{=}{\mathrm{A}}^{L,M}(t-\tau) > e^{i(m1\omega_{0I}+(M-m1)\omega_{0S})\tau}\, d\tau \end{aligned} \qquad (42.5a)$$

where

$$C_{D\_\mathrm{hetero}} = A_{\mathrm{PAS}}^{2,0\;2} = \left(\sqrt{\frac{3}{2}}\,\frac{\mu_0\,\gamma_I\gamma_S}{r_{IS}^{3}}\right)^{2} \text{ and } C_{J\_\mathrm{hetero}} = A_{\mathrm{PAS}}^{2,0\;2} = \left(\sqrt{\frac{3}{2}}\,2\pi J\right)^{2} \qquad (42.5b)$$

This, in turn yields the following:

$$\begin{aligned}\frac{d\rho^{\S}}{dt} &= -C_{\gamma} \sum_{L=0}^{2}\sum_{M=-L}^{L}\sum_{m1=-1}^{1} (-1)^{L+M}\, \mathrm{ClebschGordan}[\{1, m1\}, \{1, M-m1\}, \{L, M\}] \\ &\quad \times \mathrm{ClebschGordan}[\{1, m1\}, \{1, M-m1\}, \{L, -M\}] \\ &\quad [\hat{\mathrm{T}}^{I}_{1,m1}\,\hat{\mathrm{T}}^{S}_{1,M-m1},[\hat{\mathrm{T}}^{\mathrm{I}}_{1,-m1}\,\hat{\mathrm{T}}^{S}_{1,-M+m1},\rho^{\S}(0)]] \times J_{L,M}(m1\,\omega_{0I} + (M-m1)\omega_{0S}) \end{aligned} \qquad (42.6)$$

Equation 42.6 is the master equation that can be used to directly solve for ($d\rho^{\S}/dt$). If matrix representations of the nuclear spin tensors $\hat{\mathrm{T}}^{I}_{1,m}$ and $\hat{\mathrm{T}}^{S}_{1,m}$ are used, remember that these must be expressed in the coupled direct product representation.

By restricting the calculation to the expectation values as in the previous chapter, we can again reduce the double commutators to single commutators and then solve for the relaxation of either nuclear spin (in this case the I spin):

$$\begin{aligned}\left\langle \frac{d\hat{\mathrm{T}}^{I}_{1,0}}{dt} \right\rangle &= -C_{\gamma} \sum_{L=0}^{2}\sum_{M=-L}^{L}\sum_{m1=-1}^{1} (-1)^{L+M}\, \mathrm{ClebschGordan}[\{1, m1\}, \{1, M-m1\}, \{L, M\}] \\ &\quad \times \mathrm{ClebschGordan}\,[\{1, m1\}, \{1, M-m1\}, \{L, -M\}] \\ &\quad [\hat{\mathrm{T}}^{I}_{1,m1}\,\hat{\mathrm{T}}^{S}_{1,M-m1},\hat{\mathrm{T}}^{I}_{1,-m1}\,\hat{\mathrm{T}}^{S}_{1,-M+m1}] \times m1\, J_{L,M}(\omega_0{}') \end{aligned} \qquad (42.7a)$$

TABLE 42.1 Spherical nuclear spin commutators for coupled heteronuclear spins *I* and *S*[a]

Commutators for coupling of unlike spins[b]	
Commutator and result[c]	High-temperature reduced-density operator result[d]
$[\hat{T}^I_{1,1}\hat{T}^S_{1,0}, \hat{T}^I_{1,-1}\hat{T}^S_{1,0}] = -\hat{T}^{S\ 2}_{1,0}\hat{T}^I_{1,0}$	$= -\frac{1}{3}S(S+1)\left\langle \hat{T}^I_{1,0} \right\rangle$
$[\hat{T}^I_{1,0}\hat{T}^S_{1,-1}, \hat{T}^I_{1,0}\hat{T}^S_{1,1}] = -(\hat{T}^I_{1,0})^2\hat{T}^S_{1,0}$	$= -\frac{1}{3}I(I+1)\left\langle \hat{T}^S_{1,0} \right\rangle$
$[\hat{T}^I_{1,1}\hat{T}^S_{1,\pm1}, \hat{T}^I_{1,-1}\hat{T}^S_{1,\mp1}] = \frac{1}{2}\Big\{\Big(\pm I(I+1) \mp (\hat{T}^I_{1,0})^2\Big)\hat{T}^S_{1,0}$	$= \pm\frac{1}{3}I(I+1)\left\langle \hat{T}^S_{1,0} \right\rangle$
$+\Big(S(S+1) - (\hat{T}^S_{1,0})^2\Big)\hat{T}^I_{1,0}\Big\}$	$+\frac{1}{3}S(S+1)\left\langle \hat{T}^I_{1,0} \right\rangle$
$[\hat{T}^I_{1,\pm1}\hat{T}^S_{1,0}, \hat{T}^I_{1,0}\hat{T}^S_{1,0}] = \mp\hat{T}^{S\ 2}_{1,0}\hat{T}^I_{1,\pm1}$	$= \mp\frac{1}{3}S(S+1)\left\langle \hat{T}^I_{1,\pm1} \right\rangle$
$[\hat{T}^I_{1,\pm1}\hat{T}^S_{1,\pm1}, \hat{T}^I_{1,0}\hat{T}^S_{1,\mp1}] = \left\{\frac{1}{2} \pm \Big(S(S+1) \mp (\hat{T}^S_{1,0})^2 + \hat{T}^S_{1,0}\Big) \mp \hat{T}^I_{1,0}\hat{T}^S_{1,0}\right\}\hat{T}^I_{1,\pm1}$	$= \pm\frac{1}{3}S(S+1)\left\langle \hat{T}^S_{1,\pm1} \right\rangle$
$[\hat{T}^I_{1,\pm1}\hat{T}^S_{1,\mp1}, \hat{T}^I_{1,0}\hat{T}^S_{1,\pm1}] = \left\{\frac{1}{2} \pm \Big(S(S+1) \mp (\hat{T}^S_{1,0})^2 - \hat{T}^S_{1,0}\Big) \pm \hat{T}^I_{1,0}\hat{T}^S_{1,0}\right\}\hat{T}^I_{1,\pm1}$	$= \pm\frac{1}{3}S(S+1)\left\langle \hat{T}^S_{1,\pm1} \right\rangle$

[a] Based on Spiess (1978) table 4.5, verified using matrix representation in *spintensor_couple_matrix.nb.*

[b] Use the general relation [AB,CD]= −[CD,AB] to obtain "reverse" commutators.

[c] Verified using l=1 spherical tensor definitions in Table 31.1 and commutators in Chapter 18. Also verified using matrix representations of the l=1 spherical tensors.

[d] Verified using reduced matrix representation for "high" temperature (any temperature above ca. 2° K), see Chapter 14 equations 5a, 5b, and *equildensitymatrix.nb*.

and

$$\left\langle \frac{d\hat{T}^I_{1,\pm1}}{dt} \right\rangle = -C_\gamma \sum_{L=0}^{2} \sum_{M=-L}^{L} \sum_{m1=-1}^{1} (-1)^{L+M}\,\mathrm{ClebschGordan}\,[\{1, m1\}, \{1, M-m1\}, \{L, M\}]$$

$$\times\,\mathrm{ClebschGordan}\,[\{1, m1\}, \{1, M-m1\}, \{L, -M\}]$$

$$[\hat{T}^I_{1,m1\pm1}\ \hat{T}^S_{1,M-m1}, \hat{T}^I_{1,-m1}\ \hat{T}^S_{1,-M+m1}] \times m1\, J_{L,M}(\omega_0') \tag{42.7b}$$

where $\omega_0' = (m1\,\omega_{0I} + (M-m1)\omega_{0S}$. The necessary commutation relations are listed in Table 42.1.

Only the expectation values for the *I* spins are given. The expressions for the expectation values $(d\hat{T}^S_{1,0}/dt)$ and $(d\hat{T}^S_{1,\pm1}/dt)$ are identical to those for $(d\hat{T}^I_{1,0}/dt)$ and $(d\hat{T}^I_{1,\pm1}/dt)$ after swapping *S* for *I* in Equations 42.7b and 42.8a:

$$
\begin{aligned}
\left\langle \frac{d\hat{\mathrm{T}}^{I}_{1,0}}{dt} \right\rangle = -C_\lambda \Bigg(& \frac{1}{6} S(S+1) \times \big\{ 2J[0,0,-\omega_I+\omega_S] + 2J[0,0,\omega_I-\omega_S] \\
& + J[1,-1,-\omega_I] + J[1,1,\omega_I] + J[1,0,-\omega_I+\omega_S] + J[1,0,\omega_I-\omega_S] \\
& + 2J[2,-2,-\omega_I-\omega_S] + 2J[2,2,\omega_I+\omega_S] + J[2,-1,-\omega_I] \\
& + J[2,1,\omega_I] + \frac{1}{3} J[2,0,-\omega_I+\omega_S] + \frac{1}{3} J[2,0,\omega_I-\omega_S] \big\} \Bigg) \hat{\mathrm{T}}^{I}_{1,0} \\
& + -C_\lambda \Bigg(\frac{1}{6} I(I+1) \times \big\{ -2J[0,0,-\omega_I+\omega_S] - [-2J[0,0,\omega_I-\omega_S] \\
& - J[1,0,-\omega_I+\omega_S] - J[1,0,\omega_I-\omega_S] + 2J[2,-2,-\omega_I-\omega_S] \\
& + 2J[2,2,\omega_I+\omega_S] - \frac{1}{3} J[2,0,-\omega_I+\omega_S] - \frac{1}{3} J[2,0,\omega_I-\omega_S] \big\} \Bigg) \left\langle \hat{\mathrm{T}}^{S}_{1,0} \right\rangle
\end{aligned}
\tag{42.8a}
$$

$$
\begin{aligned}
\left\langle \frac{d\hat{\mathrm{T}}^{I}_{1,\pm1}}{dt} \right\rangle = -C_\lambda \Bigg(& \frac{1}{6} S(S+1) \times \big\{ 2J[0,0,\mp\omega_I \pm\omega_S] + 2J[0,0,0] + J[1,\mp1,\mp\omega_I] \\
& + J[1,\mp1,\mp\omega_S] + J[1,\pm1,\pm\omega_S] + J[1,0,\mp\omega_I \pm\omega_S] \\
& + 2J[2,\mp2,\mp\omega_I \mp\omega_S] + J[2,\mp1,\mp\omega_I] + J[2,\mp1,\mp\omega_S] \\
& + J[2,\pm1,\pm\omega_S] + \frac{1}{3} J[2,0,\mp\omega_I \pm\omega_S] + \frac{4}{3} J[2,0,0] \big\} \Bigg) \left\langle \hat{\mathrm{T}}^{I}_{1,\pm1} \right\rangle
\end{aligned}
\tag{42.8b}
$$

Since $\hat{\mathrm{T}}^{I}_{1,0} = \hat{\mathrm{I}}_z$, $\hat{\mathrm{T}}^{S}_{1,0} = \hat{\mathrm{S}}_z$ and $J[L, M, -M\,\omega_0'] = J[L, -M, M\,\omega_0']$ equations 8a may be rewritten as

$$
\frac{\left\langle d\hat{\mathrm{I}}_z \right\rangle}{dt} = -\frac{1}{T_{1II}} \left\langle \hat{\mathrm{I}}_z \right\rangle - \frac{1}{T_{1IS}} \left\langle \hat{\mathrm{S}}_z \right\rangle \tag{42.9a}
$$

where

$$
\begin{aligned}
\frac{1}{T_{1II}} = C_\lambda \Bigg(& \frac{1}{6} S(S+1) \times 4J[0,0,\omega_I-\omega_S] + 2J[1,1,\omega_I] + 2J[1,0,\omega_I-\omega_S] \\
& + 4J[2,2,\omega_I+\omega_S] + 2J[2,1,\omega_I] + \frac{2}{3} J[2,0,\omega_I-\omega_S] \Bigg)
\end{aligned}
\tag{42.9b}
$$

and

$$
\begin{aligned}
\frac{1}{T_{1IS}} = C_\lambda \Bigg(& \frac{1}{6} I(I+1) \times \{4J[0,0,\omega_I-\omega_S] + 2J[1,0,\omega_I-\omega_S] \\
& + 4J[2,2,\omega_I+\omega_S] + \frac{2}{3} J[2,0,\omega_I-\omega_S] \Bigg)
\end{aligned}
\tag{42.9c}
$$

For the S spin, all Is and Ss are swapped, yielding the following:

$$\frac{\left\langle d\hat{\mathrm{S}}_z \right\rangle}{dt} = -\frac{1}{T_{1SS}}\left\langle \hat{\mathrm{S}}_z \right\rangle - \frac{1}{T_{1SI}}\left\langle \hat{\mathrm{I}}_z \right\rangle \tag{42.10a}$$

with

$$\begin{aligned} \frac{1}{T_{1SS}} = C_\lambda \Bigg(& \frac{1}{6} I(I+1) \times 4J[0, 0, \omega_S - \omega_I] + 2J[1, 1, \omega_S] + 2J[1, 0, \omega_S - \omega_I] \\ & + 4J[2, 2, \omega_I + \omega_S] + 2J[2, 1, \omega_S] + \frac{2}{3} J[2, 0, \omega_S - \omega_I] \Bigg) \end{aligned} \tag{42.10b}$$

and

$$\begin{aligned} \frac{1}{T_{1SI}} = C_\lambda \Bigg(& \frac{1}{6} S(S+1) \times \{ +4J[0, 0, \omega_S - \omega_I] + 2J[1, 0, \omega_S - \omega_I] \\ & + 4J[2, 2, \omega_I + \omega_S] + \frac{2}{3} J[2, 0, \omega_S - \omega_I] \Bigg) \end{aligned} \tag{42.10c}$$

Remembering that we are looking at deviations from equilibrium, $\left\langle \hat{\mathrm{I}}_z(t) \right\rangle = \mathrm{Trace}[\hat{\mathrm{I}}_z \cdot \rho_{\S}] = \mathrm{Trace}[\hat{\mathrm{I}}_z \cdot (\rho_{\mathrm{rot}} - \rho_{\mathrm{eq}})] = \left\langle \hat{\mathrm{I}}_z(t) \right\rangle - \left\langle \hat{\mathrm{I}}_{z\_\mathrm{eq}} \right\rangle$ and $\left\langle \hat{\mathrm{S}}_z \right\rangle = \left\langle \hat{\mathrm{S}}_z(t) \right\rangle - \left\langle \hat{\mathrm{S}}_{z\_\mathrm{eq}} \right\rangle$, it is apparent that Equations 42.9a and 42.10a are coupled and must be solved simultaneously. Together, these equations comprise the Solomon (1955) equations and predict cross-relaxation effects. Due to these, heteronuclear dipolar or J T_1 relaxation in general is not monoexponential.

However, it is often the case that T_1 relaxation rates of coupled spins are measured with decoupling of one of the coupled spins (e.g., an inversion recovery experiment observing ^{13}C while decoupling ^{1}H). In this case (let ^{1}H be the S spin), $\left\langle \hat{\mathrm{S}}_z(t) \right\rangle = 0$ and $\left\langle \hat{\mathrm{S}}_z \right\rangle = -\left\langle \hat{\mathrm{S}}_{z\_\mathrm{eq}} \right\rangle$, and the relaxation rate of the I spins is given by $(1/T_{1II})$. The only effect of the S nucleus decoupling is the nuclear Overhauser effect on the I magnetization.

For T_2 relaxation, $\left\langle \dfrac{d\hat{\mathrm{T}}^I_{1,\pm 1}}{dt} \right\rangle = \dfrac{\mp 1}{\sqrt{2}} \dfrac{d\hat{\mathrm{I}}^\pm}{dt}$ and $\left\langle \hat{\mathrm{T}}^I_{1,\pm 1} \right\rangle = \dfrac{\mp 1}{\sqrt{2}} \hat{\mathrm{I}}^\pm$. Incorporation of the other simplifications discussed earlier allows Equation 42.8b to be expressed as

$$\frac{\langle d\hat{\mathrm{I}}^+ \rangle}{dt} = -\frac{1}{T_{2I}} \langle \hat{\mathrm{I}}^+ \rangle \tag{42.11a}$$

where

$$\begin{aligned} \frac{1}{T_{2I}} = C_\lambda \Bigg(& \frac{1}{6} S(S+1) \times \big\{ 2J[0, 0, \omega_I - \omega_S] + 2J[0, 0, 0] + J[1, 1, \omega_I] \\ & + 2J[1, 1, \omega_S] + J[1, 0, \omega_I - \omega_S] + 2J[2, 2, \omega_I + \omega_S] \\ & + J[2, 1, \omega_I] + 2J[2, 1, \omega_S] + \frac{1}{3} J[2, 0, \omega_I - \omega_S] + \frac{4}{3} J[2, 0, 0] \big\} \Bigg) \end{aligned} \tag{42.11b}$$

For T_2 relaxation, $\left\langle I_{\mathrm{eq}}^{+} \right\rangle = 0$ and there is no dependence of $\left(\left\langle d\hat{\mathrm{I}}^{+} \right\rangle / dt\right)$ on the S spin, so the relaxation is exponential and is described successfully by the Bloch equation. The T_2 relaxation of the I spin is not affected by decoupling of the S spin. The expression for T_2 relaxation of the S spin is obtained by swapping the I and S labels in Equations 42.10c and 42.11a.

CHAPTER 43

CALCULATION OF AUTOCORRELATION FUNCTIONS, SPECTRAL DENSITIES, AND NMR RELAXATION TIMES FOR JUMP MOTIONS IN SOLIDS

The last two chapters presented the mathematical connection between NMR relaxation in *spin space* and the angular reorientation of the principal axis system (PAS) in *real space* of a nuclear spin Hamiltonian. The angular motion in *real space* is described quantitatively by the autocorrelation function $G_{l,m}(\tau) = \left\langle A_{\text{lab}}^{l,m*}(0)\, A_{\text{lab}}^{l,m}(\tau)\right\rangle \Big/ (A_{\text{PAS}}^{2,0})^2$ (Eq. 39.1), which decays with time for $l = 1$ and for $l = 2$.[1] In this chapter, autocorrelation functions are calculated for jump motions that dominate NMR relaxation rates in solid samples (Torchia and Szabo, 1982; Wittebort and Szabo, 1978). These, in turn, are used with the formalism from the previous chapters to *calculate quantitative NMR relaxation times*.

The general N-site jump model can in principle be used to describe any type of angular reorientation dynamics. This model was described in detail by Torchia and Szabo and is modified slightly here to accommodate Mathematica calculations. Suppose that the PAS of a given Hamiltonian jumps between N different sites relative to a crystal-fixed or molecule-fixed reference frame. For any of the N sites *j*, the orientation of the PAS relative to the crystal frame can be described by the Euler angles κ_j, λ_j, ξ_j. For a static powder sample of a solid, the Euler angles necessary to bring the crystal frame into coincidence with the laboratory reference frame are the powder average angles α, β, and γ (Scheme 43.1). Because there is no preferred *x* or *y* axis in the laboratory reference frame, γ can be arbitrarily set to zero.

$$\overset{=}{\mathrm{A}}_j\,[\text{pas}] \xrightarrow{\kappa_j\lambda_j\xi_j} \overset{=}{\mathrm{A}}_j\,[\text{crystal}] \xrightarrow{\alpha\beta\gamma} \overset{=}{\mathrm{A}}_j\,[\text{lab}] \qquad (43.1)$$

---

[1] $G_{0,0}(\tau) = \text{constant}$.

A Primer of NMR Theory with Calculations in Mathematica®, First Edition. Alan J. Benesi.

This transformation is achieved with Wigner rotations as shown in Equation 43.2:

$$\overline{\overline{\mathrm{A}}}_j^{\,l,m}\,(\mathrm{lab}) = \textstyle\sum_{l=1}^{2} \sum_{r=-l}^{+l} D_{rm}^{l}(\alpha\beta\gamma) \sum_{q=-l}^{+l} \overline{\overline{\mathrm{A}}}_j^{\,l,q}\,(\mathrm{pas})\, D_{qr}^{l}(\kappa_j \lambda_j \xi_j) \tag{43.2}$$

The equilibrium probability that the Hamiltonian PAS is in site j is $p_{eq}(j)$, and R_{jk} is the first-order rate constant in s^{-1} for jumping from site j to site k. In some cases, the sites are *not* equivalent, so $R_{jk} \neq R_{kj}$, but microscopic reversibility requires that $R_{jk}\, p_{eq}(j) = R_{kj}\, p_{eq}(k)$. In order to calculate relaxation rates when there are inequivalent sites, it is necessary to create a symmetric jump matrix $\overline{\overline{\mathrm{R}}}$ with elements

$$\overline{\overline{\mathrm{R}}}_{jk} = \overline{\overline{\mathrm{R}}}_{kj} = \sqrt{\mathrm{R}_{jk}\mathrm{R}_{kj}} \tag{43.3}$$

and

$$\overline{\overline{\mathrm{R}}}_{jj} = -\textstyle\sum_{k \neq j} \mathrm{R}_{jk} \tag{43.4}$$[2]

After this symmetrization, one diagonalizes $\overline{\overline{\mathrm{R}}}$ to obtain the N eigenvalues λ_n and eigenvectors $\overline{\mathrm{X}}_n$, with

$$\overline{\overline{\mathrm{R}}}\,\overline{\mathrm{X}}_n = \lambda_n \overline{\mathrm{X}}^n \tag{43.5}$$

where the N eigenvalues and eigenvectors are labeled $n = 1, 2, \ldots, N$, and $n = 1$ corresponds to the eigenvalue $\lambda_1 = 0$ with $p_{eq}(j) = (\overline{\mathrm{X}}_j^1)^2$. These relations are verified in the notebook *torchiaszabotetqcceta_book.nb.*

In *the crystal-fixed reference frame*, the *general* expression for the autocorrelation function $C_{a,aa}^{l}(t)$ is given by

$$C_{a,aa}^{l}(t) = \textstyle\sum_{n=-l}^{l} \sum_{n'=-l}^{l} \left\langle D_{n,a}^{l*}(\kappa(0), \lambda(0), \xi(0)), D_{n',aa}^{l}(\kappa(t), \lambda(t), \xi(t)) \right\rangle \tag{43.6a}$$

where $D_{n,a}^{l*}$ is the complex conjugate of $D_{n,a}^{l}$.

Especially in the case where the Hamiltonian PAS has axial symmetry ($\eta = 0$) such as for the dipolar Hamiltonian or nearly axial symmetry as for the deuterium quadrupolar Hamiltonian ($\eta \leq 0.1$), it is convenient to use *spherical polar angles to describe the position of the PAS z axis in the crystal-fixed frame*. In this case, the Euler angle κ is irrelevant and the spherical polar angles are given by $\Theta_j = \lambda_j$ and $\Phi_j = \pi - \xi_j$ (Torchia and Szabo, 1982). In terms of the spherical polar jump angles Θ_j and Φ_j, $C_{a,aa}^{l}(t)$ is given by

$$C_{a,aa}^{l}(t) = \textstyle\sum_{n=-l}^{l} \sum_{n'=-l}^{l} \left\langle D_{n,a}^{l*}(0, \Theta(0), \Phi(0)), D_{n',aa}^{l}(0, \Theta(t), \Phi(t)) \right\rangle \tag{43.6b}$$

In the case of N-site jumps, the autocorrelation functions $C_{a,aa}^{l}(t)$ in the crystal-fixed frame are given by (using Euler jump angles $\kappa_j, \lambda_j, \xi_j$)

$$\begin{aligned} C_{a,aa}^{l}(t) = {} & \textstyle\sum_{n=1}^{N} \sum_{k=1}^{N} \sum_{j=1}^{N} \sum_{q=-l}^{l} \sum_{r=-l}^{l} \frac{A_{\mathrm{PAS}}^{l,q*}(0)\, A_{\mathrm{PAS}}^{l,r}}{(A_{\mathrm{PAS}}^{2,0})^2} \\ & e^{\lambda_n t}\, \overline{\mathrm{X}}_k^1\, \overline{\mathrm{X}}_k^n\, \overline{\mathrm{X}}_j^1\, \overline{\mathrm{X}}_j^n\, D_{q,a}^{l*}(\kappa_k, \lambda_k, \xi_k)\, D_{r,aa}^{l}(\kappa_j, \lambda_j, \xi_j) \end{aligned} \tag{43.7a}$$

---

[2] We reverse the labels of Torchia and Szabo so that label j refers to the row number and letter k refers to the column number of the rate matrix.

or if there is axial symmetry and spherical polar angles are used,

$$C^{l}_{a,aa}(t) = \sum_{n=1}^{N} \sum_{k=1}^{N} \sum_{j=1}^{N} \sum_{q=-l}^{l} \sum_{r=-l}^{l} \frac{A^{l,q*}_{\mathrm{PAS}}(0)\, A^{l,r}_{\mathrm{PAS}}}{(A^{2,0}_{\mathrm{PAS}})^{2}} \\ e^{\lambda_n t}\, \overline{\mathrm{X}}^{1}_{k}\, \overline{\mathrm{X}}^{n}_{k}\, \overline{\mathrm{X}}^{1}_{j}\, \overline{\mathrm{X}}^{n}_{j}\, D^{l*}_{q,a}(0, \Theta_k, \Phi_k)\, D^{l}_{r,aa}(0, \Theta_j, \Phi_j) \qquad (43.7\mathrm{b})$$

The time-dependence is embodied exclusively in the $e^{\lambda_n t}$ term.[3]

In the laboratory reference frame pertinent to NMR relaxation, the autocorrelation functions (see Eq. 39.1) are as follows:

$$G_{l,m}(\tau) = \frac{\left\langle A^{l,m*}_{\mathrm{lab}}(0)\, A^{l,m}_{\mathrm{lab}}(\tau) \right\rangle}{(A^{2,0}_{\mathrm{PAS}})^{2}} = \sum_{l=1}^{2} \sum_{a=-l}^{l} \sum_{aa=-l}^{l} D^{l*}_{a,m}(\alpha, \beta, 0)\, D^{l}_{aa,m}(\alpha, \beta, t)\, C^{l}_{a,aa}(t) \qquad (43.8)$$

where α and β are the powder average angles necessary to align the crystal-fixed frame z axis and the laboratory (magnet) reference frame z axis.

The spectral densities are given by Equation 39.3[4]:

$$J_{l,m}(m\,\omega) = \int_{0}^{\infty} G_{l,m}(t)\,\mathrm{Cos}(m\,\omega t)\,dt \qquad (43.9)$$

If the autocorrelation functions are single exponential decays with a single characteristic correlation time τ, that is, $G_{l,m}(\tau) = \mathrm{const}\, e^{-t/\tau}$ (see Eq. 39.2), then

$$J_{l,m}(m\,\omega) = \mathrm{const}\,\frac{\tau}{1 + m^{2}\,\tau^{2}\,\omega^{2}} \qquad (43.10)$$

Since the l value of $J_{l,m}(m\ \omega)$ refers to the rank of the autocorrelation functions contributing to relaxation, and only $l = 2$ autocorrelation functions contribute to dipolar or quadrupolar relaxation, it is common in the literature to abbreviate the spectral densities $J_{2,m}(m\ \omega)$ as $J_{m}(m\ \omega)$ (Torchia and Szabo, 1982).

The calculated $J_{l,m}(m\ \omega)$ can then be inserted into the relevant expressions from Chapters 41 and 42 to calculate explicit NMR relaxation times. Two examples of such calculations for deuterium relaxation times are provided in the notebooks *torchiaszabotetqcceta_book.nb* and *c2jumpstorchiaszabo_book.nb.* The first notebook uses a 4-site tetrahedral jump model that is applicable to water in ice Ih (Wittebort et al. 1988). The second uses a 2-site C_2 symmetry jump model that applies to water in gypsum and other solid hydrates (Reeves, 1969; Weiss and Weiden, 1980). Both calculations show that the relaxation times are a function of the powder average angles α and β. For the purpose of comparison, the powder average relaxation times were calculated for both types of motion.

---

[3] As shown in torciaszabotetqcceta_book.nb, the sign of the eigenvalues in Mathematica are opposite those used in the paper by Torchia and Szabo.

[4] Torchia and Szabo have incorporated a factor of 2 in their definition of the spectral density (their Equation 10). Compare their Equation 8 with our Equation 40.29a to see how the factor arises.

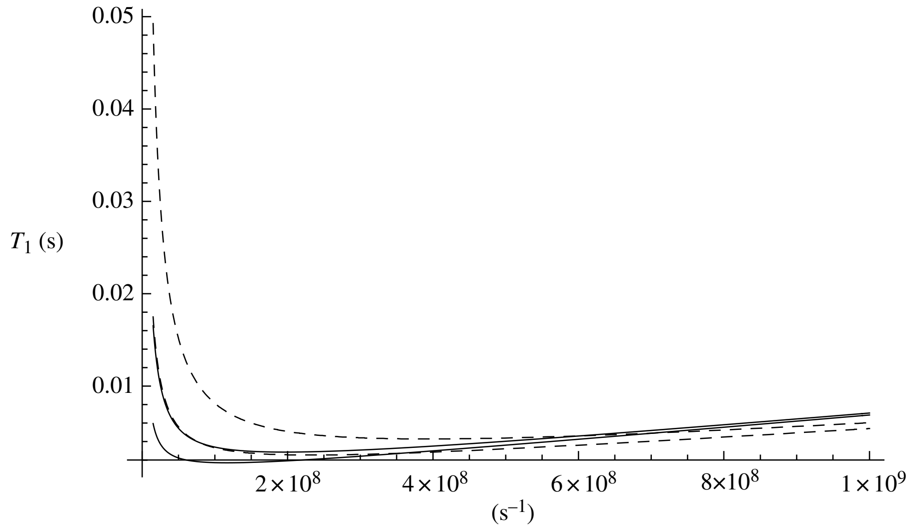

Figure 43.1 The deuterium powder average T_1 (s) vs. the jump rate constant k (s^{-1}) for tetrahedral jumps (solid lines) and C_2 symmetry jumps with θ=magic angle (dashed lines) near the minimum in T_1 values. The upper curves for both types of jump were calculated for ν_{Larmor}=76.78 MHz. The lower curves were calculated for ν_{Larmor}=45.84 MHz. In all cases, qcc=200 kHz, η=0.

The dependence of the powder average deuterium T_1 and T_2 values on the site-to-site jump frequency $\nu_{\text{jump}}=k$ is shown in Figures 43.1 and 43.2 for tetrahedral jumps and C_2 symmetry jumps with θ=magic angle[5]:

Despite the significant difference in the geometry of the jumps, there is not much difference in the relaxation times for any specific jump rate constant.

The dependence of the $\log_{10}(T_1)$ and $\log_{10}(T_2)$ values (again the powder average relaxation times were used) on the $\log_{10}$(jump rate constant) is shown in Figures 43.3 and 43.4 for tetrahedral jumps, C_2 symmetry jumps with θ=magic angle, and isotropic rotational diffusion (see Chapter 44). In the case of isotropic rotational diffusion, D_{rot} was used as the "jump" rate constant.

Figures 43.1 through 43.4 demonstrate that the nature of the reorientational motion has less effect on the relaxation rate (i.e., inverse of T_1 or T_2) than the rate of the reorientational motion. Less than an order of magnitude separates the T_1 and T_2 values for tetrahedral jumps, C_2 symmetry jumps, and isotropic rotational diffusion when the motions have the same jump rate constants or rotational diffusion coefficient.

One important difference in the relaxation behavior for the different types of motion is not apparent in Figures 43.3 and 43.4. While jump rate constants in solids are typically 10^1 to $10^6\,s^{-1}$, rotational diffusion coefficients of small molecules in

---

[5] The symmetry axis for C_2 symmetry jumps is the bisector of the angle between the two allowed jump positions. The angle θ is the angle between the bisector and the allowed jump positions.

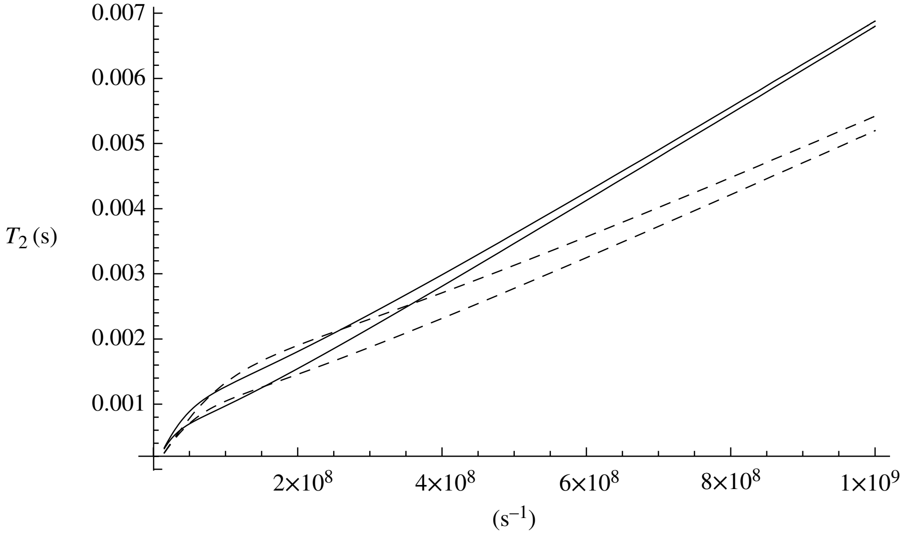

Figure 43.2 The deuterium powder average T_2 (s) vs. the jump rate constant k (s^{-1}) for tetrahedral jumps (solid lines) and C_2 symmetry jumps with θ = magic angle (dashed lines) in the same range of jump rates as Figure 43.1. The upper curves for both types of jump were calculated for $\nu_{\text{Larmor}} = 76.78$ MHz. The lower curves were calculated for $\nu_{\text{Larmor}} = 45.84$ MHz. In all cases, qcc = 200 kHz, $\eta = 0$.

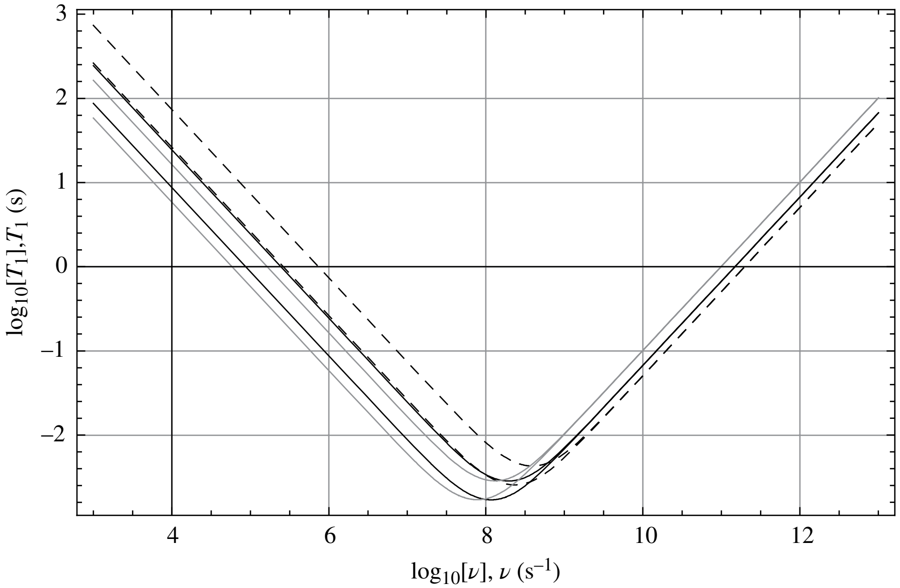

Figure 43.3 $\text{Log}_{10}T_1$ vs. $\log_{10}$(jump rate constant) for tetrahedral jumps (solid black lines), C_2 symmetry jumps with θ = magic angle (dashed black lines), and isotropic rotational diffusion (solid gray lines). See Chapter 44 for further information about NMR relaxation by isotropic rotational diffusion. For tetrahedral and C_2 symmetry jumps, the jump rate constant k in s^{-1} was used. For isotropic rotational diffusion, the rotational diffusion coefficient D_{rot} in rad s^{-1} was used as the jump rate constant. The upper curves for each type of motion were calculated for $\nu_{\text{Larmor}} = 76.78$ MHz. The lower curves were calculated for $\nu_{\text{Larmor}} = 45.84$ MHz. In all cases, qcc = 200 kHz, $\eta = 0$. For tetrahedral and C_2 symmetry jumps, the powder average T_1 values were used.

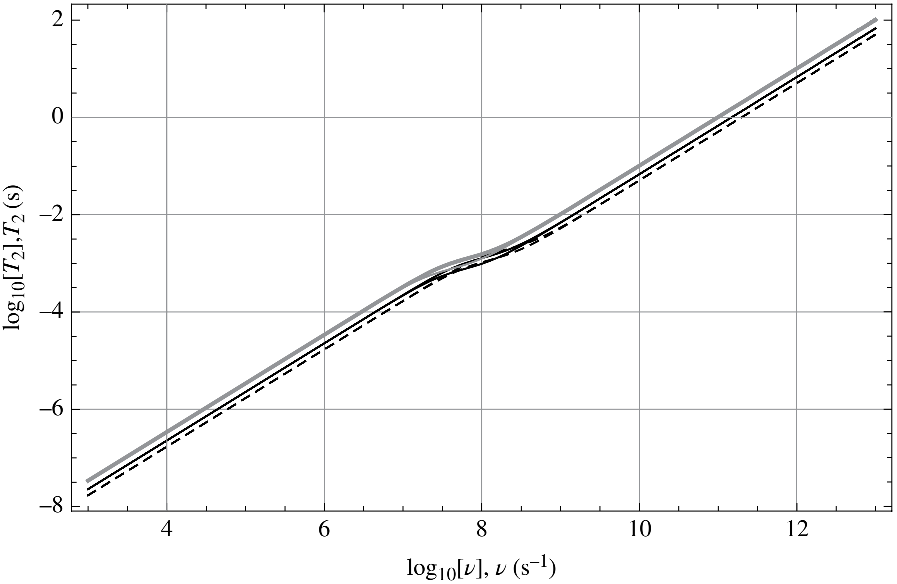

Figure 43.4 $\text{Log}_{10}T_2$ and $\log_{10}$(jump rate constant) for tetrahedral jumps (solid black lines), C_2 symmetry jumps with θ = magic angle (dashed black lines), and isotropic rotational diffusion (solid gray lines). See Chapter 44 for further information about NMR relaxation by isotropic rotational diffusion. For tetrahedral and C_2 symmetry jumps, the jump rate constant k in s^{-1} was used. For isotropic rotational diffusion, the rotational diffusion coefficient D_{rot} in rad s^{-1} was used. The upper curves for each type of motion were calculated for $\nu_{\text{Larmor}} = 76.78$ MHz. The lower curves were calculated for $\nu_{\text{Larmor}} = 45.84$ MHz. In all cases, qcc = 200 kHz, $\eta = 0$. For tetrahedral and C_2 symmetry jumps, the powder average T_1 values were used.

liquids at ambient temperatures are typically 10^{10} to 10^{12} rad s^{-1}. This means that one is more likely to be in the "extreme narrowing" region of relaxation for liquid-state samples (i.e., the right-hand sides of Fig. 43.3 and 43.4) where there is no dependence of the relaxation times on the Larmor frequency, while one is much more likely to observe very short T_1 (and T_2) values in solids since typical solid-state jump rate constants are often near the T_1 minimum.

Overall, it is clear that NMR relaxation times are useful for determining approximate jump rate constants for solids and rotational diffusion coefficients for liquids. For solids, rates of reorientational motions can also be elucidated by obtaining variable-temperature powder spectra, as discussed in Chapter 38.

EXPLANATION OF *torchiaszabotetqcceta_book.nb*

This notebook calculates deuterium NMR relaxation times T_1 and T_2 for a static powder sample of a solid in which the deuterium PAS experiences tetrahedral jumps.

The user is told to evaluate *wigrot.nb* and then close it without saving.

The 4×4 symmetric jump matrix R is constructed according to Equation 43.4. Because each allowed PAS jump angle is assumed to be equivalent and able to jump to any of the other three jump angles, the jump matrix is inherently symmetric.

Next the eigenvalues and eigenvectors for R are calculated with the built-in Mathematica functions Eigenvalues and Eigenvectors. The eigenvectors, named X, are then orthogonalized and normalized using the built-in Mathematica function Orthogonalize. The resulting eigenvectors are renamed X.

The following cells verify the eigenvalues and eigenvectors using Equation 43.5.

The next cells define the complex conjugates *D*1conj and *D*2conj of the *wigrot.nb* *D*1 and *D*2 functions. These are necessary for the calculation. Note that it is necessary to tell the Mathematica program that the Euler angles are real.

Next, the tetrahedral angle is calculated and shown to be twice the magic angle.

The following cell defines the set of four allowed latitudinal spherical polar angles θ of the deuterium PAS in the crystal-fixed frame. The next cell defines the set of four allowed longitudinal angles ϕ in the crystal-fixed frame. It is shown how to select particular angles from the sets.

The exponential in Equations 43.7a and 43.7b is evaluated and has an argument of the opposite sign from that of Torchia and Szabo (1982, Eq. 23). Mathematica yields eigenvalues of the opposite sign than those calculated by these authors.

Using Equation 43.7b, the next cells calculate $C^1_{a,aa}(t)$ for $l = 1$, called ce[1,a_,aa_]. Although thl = 1 autocorrelation function in the crystal-fixed frame is not used for deuterium relaxation, it would be for chemical shift relaxation. Note that it requires the antisymmetric PAS terms for the rank 1 real space spherical tensor and that we have assumed axial symmetry ($\eta = 0$) by using the spherical polar angles θ and ϕ.

Next, Equation 43.7b is used to calculate $C^2_{a,aa}(t)$ for $l = 2$, called ce[2,a_,aa_] in the crystal-fixed frame. Despite the fact that we assume $\eta = 0$ in order to neglect jump angles κ_1 in Equation 43.7a, η appears in the resulting expressions. We make the replacement $\eta \rightarrow 0$ to create the function ceax[2,a_,aa_].

The laboratory frame autocorrelation functions Gax[2,*m*_] is created according to Equation 43.8. Again it is assumed that $\eta = 0$.

The laboratory frame autocorrelation functions G[2,*m*_] are then created. These leave η in as a variable since η is typically less than or equal to 0.1 for deuterium. The calculations of the G[2,*m*_] require long times, about 1540 s each on my 2012 vintage laptop PC.

The order parameter S^2 for tetrahedral jumps is then calculated by letting $t \rightarrow \infty$ and $e^{-4kt} \rightarrow 0$ (Lipari and Szabo, 1982, Appendix). The result, $S^2 = 19\,\eta^2/144$, is essentially zero for deuterium since $\eta \leq 0.1$.

The only time-dependent components in the G[2,*m*] expressions are the $e\lambda^{jt}$ terms. We recognize that we can replace each complex exponential with the corresponding spectral density according to Equations 43.9 and 43.10.

We abbreviate the spectral densities $J_{2,m}(m\,\omega) = J_m(m\,\omega)$ and calculate $J_0(0)$, $J_1(\omega)$, and $J_2(2\,\omega)$ according to Equation 43.10. We name the corresponding spectral densities jd0, jd1, and jd2. Equation 43.10 is evaluated for each of the four eigenvalues.

The next cells calculate the spectral densities in the crystal-fixed reference frame by replacing the exponential time-dependence with the corresponding frequency-dependence contained in the jd0, jd1, and jd2 terms.

The $l=1$ and $l=2$ spectral densities are calculated in the crystal-fixed frame and are called the $j[1,m,a,aa]$.

Then we return to the laboratory frame $l=2$ spectral densities needed to calculate deuterium relaxation times. The spectral densities J[2,0], J[2,1], J[2,2], J[1,0] and J[1,1] are calculated according to Equation 43.8 with the complex exponentials replaced with the $j[1,m,a,aa]$ from the crystal-fixed frame. The much simpler axial versions Jax[2,0], Jax[2,1] and Jax[2,2] are then calculated by substituting $\eta \rightarrow 0$.

The expressions obtained for the laboratory frame J[1,*m*]'s are then used to create the functions J20[ω_,k_,α_, β_,η_], J21[ω_,k_,α_, β_,η_], and J22[ω_,k_,α_, β_,η_]. A few numerical examples of spectral densities are calculated.

The approximate quadrupolar coupling constant (qcc) for deuterium in D_2O ice is 216 kHz, with $\eta=0.1$. The inverse *T*1inv and *T*2inv functions are then calculated according to Equations 41.28a and 41.28b. These have an angular dependence on the powder average α and β Euler angles required to bring the crystal-fixed axis system into coincidence with the lab (magnet) frame. The orientationally dependent T_1 and T_2 functions are given by the inverses of the *T*1inv and *T*2inv functions.

Several plots and contour plots of T_1 values are made in the following cells. For the example calculation, the maximum and minimum T_1 values as a function of the α and β Euler angles were 0.104 and 0.069 s, respectively. The ratio of maximum to minimum was 1.5.

The next cells attempt to calculate the powder average *T*1intinv by the direct integration, but this takes much too long. The built-in numerical integration function NIntegrate is much faster. The functions *T*1intinvN, *T*2intinvN, *T*1intN, and *T*2intN are then created.

In the next cells, plots are made of *T*1intN vs. tetrahedral jump rate $\nu=k$. These plots show that the minimum powder average T_1 values as a function of jump rate are obtained at lower Larmor frequencies. Note that the direct plots of T_1 and T_2 are only shown in the immediate vicinity of the T_1 minimum so that both sides of the minimum show a dependence on the Larmor frequency.

Plots of *T*2intN vs. ν do not show a minimum but do show a change of slope near the same frequency as the minimum in *T*1intN.

Plots of $\log_{10}T_1$ and $\log_{10}T_2$ vs. $\log_{10}\nu$ show the relaxation time-dependence over a huge range of jump frequencies. The logarithmic plot clearly shows the onset of "extreme narrowing," where the T_1 and T_2 values no longer depend on the Larmor frequency, and $T_1=T_2$. This occurs when the jump rate $k \gg \nu_{\mathrm{Larmor}}$.

EXPLANATION OF *c2jumpstorchiaszabo_book.nb*

This notebook is very similar to *torchiaszabotetqcceta_book.nb*. It calculates the eigenvalues, eigenvectors, Caa'[*t*], Cm[*t*], Jm([ω], T_1 and T_2 for a deuterium PAS experiencing C_2 symmetry jumps about the bisector of the water H–O–H (D–O–D) bond angle. The user is told to evaluate *wigrot.nb,* then close it without saving changes.

The 2×2 jump matrix R is defined. The eigenvalues λ and eigenvectors X of R are found. The complex conjugates *D*1conj and *D*2conj of the Wigner rotation elements *D*1 and *D*2 are defined.

For convenience, we define the *z* axis of the crystal-fixed frame to be aligned with the bisector of the D–O–D bond angle. The two allowed latitudinal jump angles are designated $\theta=\{\theta,\theta\}$. The two allowed longitudinal jump angles are designated as $\phi=\{0,\pi\}$.

We recognize that the time-dependent components in the autocorrelation function are monoexponentials and replace them with the "bare" spectral densities jd0, jd1, and jd2. These are used with Equation 43.9 to calculate the spectral densities in the crystal-fixed reference frame *j*[1,0,*a*_,*aa*_], *j*[1,1,*a*_,*aa*_], *j*[2,0,*a*_,*aa*_], *j*[2,1,*a*_,*aa*_], *j*[2,2,*a*_,*aa*_]. Again, the implicit assumption is made that the deuterium PAS has axial symmetry. This allows the Euler angles α, β, and γ to be replaced with the spherical polar angles θ and ϕ.

The *j*[*l*,*m*]'s are then used to calculate the laboratory frame spectral densities J[2,0], J[2,1], and J[2,2] necessary to calculate deuterium relaxation times. These expressions are then converted into function J20, J21, and J22.

The relaxation rates *T*1inv and *T*2inv are created using Equations 41.28a and 41.28b, respectively. The *T*1 and *T*2 function are then created.

The powder average relaxation rate functions *T*1intinvN and *T*2intinvN are then defined. The inverses of these functions are used to create the *T*1intN and *T*2intn functions.

Plots of *T*1intN and *T*2intN are made, again showing that the minimum powder average T_1 and point of inflection in powder average T_2 are found at the same jump frequency and that the T_1 and T_2 increase with increasing jump frequency. Note that the direct plots of T_1 and T_2 are only shown in the immediate vicinity of the T_1 minimum so that both sides of the minimum show a dependence on the Larmor frequency. The logarithmic plot clearly shows the onset of "extreme narrowing," where the T_1 and T_2 values no longer depend on the Larmor frequency, and $T_1=T_2$. This occurs when the jump rate $k \gg \nu_{\text{Larmor}}$.

The angular dependence of the T_1 and T_2 values is more dramatic for C_2 symmetry jumps than for tetrahedral jumps. The T_1 values for qcc = 233.3 kHz and a Larmor frequency 45.65 MHz range from 0.00218 to 0.00871 depending on the α and β Euler angles relating the crystal-fixed frame to the lab frame. The T_1 is shortest for the "horn" frequencies of the rigid powder pattern and longest for the "parallel edges" as shown in some of the ListPlot3D plots.

HOMEWORK

Homework 43.1: Calculate the powder average T_1 and T_2 for C_3 symmetry jumps around a symmetry axis for a deuterated methyl group ($-CD_3$) as a function of the jump rate constant *k*. Is there an angular dependence of the relaxation times?

Homework 43.2: When the jump rate is in the intermediate exchange regime and there is intensity loss in the powder spectrum, is the "true" relaxation time the same as the experimentally observed relaxation time?

CHAPTER 44

CALCULATION OF AUTOCORRELATION FUNCTIONS AND SPECTRAL DENSITIES FOR ISOTROPIC ROTATIONAL DIFFUSION

Although anisotropic rotational diffusion can occur in liquids (Tang and Benesi, 1994; Woessner, 1996), in most cases at ambient temperatures deviations from *isotropic rotational diffusion* are very small. This is considerably different than the solid state where fixed angular jumps occur between allowed orientations on a rigid crystal fixed reference frame. Instead of a crystal fixed reference frame, the reference frame for angular autocorrelation functions in liquids is taken to be the initial orientation of the principal axis system (PAS) at $t=0$, which can be called the *molecular reference frame*. As shown here, it is convenient to use *spherical harmonics* to obtain the autocorrelation functions. The *isotropic rotational diffusion equation* is as follows (Abragam, 1983, p. 298, 299):

$$\frac{\partial p}{\partial t} = D_{\text{rot}} \nabla^2 p = D_{\text{rot}} \left\{ \frac{1}{\sin\theta} \frac{\partial}{\partial\theta} \left(\sin\theta \frac{\partial p}{\partial\theta} \right) + \frac{1}{\sin^2\theta} \frac{\partial^2 p}{\partial^2\phi} \right\} \tag{44.1}$$

where $p(\theta,\phi,t)$ is the probability of finding the z axis of the PAS at θ, ϕ at time t. The ensemble average mean square angular displacement is $\overline{\theta^2} = 4 D_{\text{rot}} t$.

The general solution to Equation 44.1 is:

$$p(\theta,\phi,t) = \textstyle\sum_{l=0}^{\infty} \sum_{m=-l}^{l} C_{l,m} Y_{l,m}(\theta,\phi) e^{-l(l+1)D_{\text{rot}}t} \tag{44.2}$$

where the $Y_{l,m}(\theta,\phi)$ terms are the orthonormalized spherical harmonics, and the $C_{l,m}$ are constants obtained from the initial conditions. In this case, the initial condition is that the z axis of the Hamiltonian PAS is at $\Omega_0 = \theta_0, \phi_0$ at $t=0$. From this assumption it follows that $C_{l,m} = Y^*_{l,m}(\theta_0,\phi_0)$, and the probability at time t of finding the z axis at $\Omega = \theta, \phi$ given that it was at θ_0, ϕ_0 at $t=0$ is given by[136]

$$p(\theta,\phi,\theta_0,\phi_0,t) = \textstyle\sum_{l=0}^{\infty} \sum_{m=-l}^{l} Y^*_{l,m}(\theta_0,\phi_0) Y_{l,m}(\theta,\phi) e^{-l(l+1)D_{\text{rot}}t} \tag{44.3}$$

A Primer of NMR Theory with Calculations in Mathematica®, First Edition. Alan J. Benesi.

In order to calculate quantitative spectral densities for nuclear magnetic resonance (NMR) relaxation, we need to know the numerical values of the NMR autocorrelation functions $G_{l,m}(\tau) = \frac{< A_{\text{lab}}^{l,m*}(0) A_{\text{lab}}^{l,m}(\tau) >}{(A_{\text{PAS}}^{2,0\ 2})}$. However, it is more convenient to use the spherical harmonics $Y_{l,m}(\theta,\phi)$ than the $A_{\text{mol}}^{l,m}$ to describe the time-dependent position of the PAS z axis. Using this approach, the spherical harmonic autocorrelation functions $G_{l,m}^{Y}(t)$ are given by

$$G_{l,m}^{Y}(t) = \int_0^{2\pi}\int_0^{\pi}\int_0^{2\pi}\int_0^{\pi} p(\theta,\phi,\theta_0,\phi_0,t)\, Y_{l,m}(\theta_0,\phi_0)\cdot Y_{l,m}^{*}(\theta,\phi)\sin\theta\,\sin\theta_0\; d\theta\; d\theta_0 d\phi\; d\phi_0 \tag{44.4a}$$

Substituting from Equation 44.3 yields the following:

$$\begin{aligned} G_{l,m}^{Y}(t) = \int_0^{2\pi}\int_0^{\pi}\int_0^{2\pi}\int_0^{\pi} &\textstyle\sum_{l=0}^{\infty} \sum_{m=-l}^{l} Y_{l,m}^{*}(\theta_0,\phi_0) Y_{l,m}(\theta,\phi)\, e^{-l(l+1)D_{\text{rot}}t}\; Y_{l,m}(\theta_0,\phi_0) \\ &\cdot Y_{l,m}^{*}(\theta,\phi)\sin\theta\;\sin\theta_0\; d\theta\; d\theta_0 d\phi\; d\phi_0 \end{aligned} \tag{44.4b}$$

Autocorrelation functions calculated with Equation 44.4 are shown in *isotropicrotdiffy.nb*. NMR relaxation depends only on the $l=1$ or $l=2$ terms of the $A_{\text{mol}}^{l,m}$ and corresponding $Y_{l,m}$, so the summation in Equation 44.4 can be truncated to yield the l-dependent autocorrelation functions:

$$\begin{aligned} G_{l,m}^{Y}(t) = \int_0^{2\pi}\int_0^{\pi}\int_0^{2\pi}\int_0^{\pi} &Y_{l,m}^{*}(\theta_0,\phi_0) Y_{l,m}(\theta,\phi) e^{-l(l+1)D_{\text{rot}}t}\; Y_{l,m}(\theta_0,\phi_0) \\ &\cdot Y_{l,m}^{*}(\theta,\phi)\, sin\theta\; sin\theta_0\; d\theta\, d\theta_0 d\phi\, d\phi_0 \end{aligned} \tag{44.5}$$

The *isotropicrotdiffy.nb* notebook shows that $G_{l,m}^{Y}(t)$ depends only on l (i.e., they are *independent* of m), with $G_{1,m}^{Y}(t) = \frac{1}{3} e^{-2D_{\text{rot}}t}$, and $G_{2,m}^{Y}(t) = \frac{1}{5} e^{-6D_{\text{rot}}t}$.

At $t=0$ $G_{1,m}^{Y}(0) = 1/3$ and $G_{2,m}^{Y}(0) = 1/5$, but because they were obtained with spherical harmonics they do not contain the real space NMR parameters δ and η needed to calculate the spectral densities. These are incorporated here in the constant const_l. If we let $\tau_l = 1/l(l+1)D_{\text{rot}}$, the "NMR-normalized" $G_{l,m}^{\text{NMR}}(\tau) = \frac{\text{const}_l}{A_{\text{PAS}}^{2,0\ 2}} * G_{l,m}^{\text{Y}}(\tau) = \frac{\text{const}_l}{A_{\text{PAS}}^{2,0\ 2}} * e^{-\frac{\tau}{\tau_l}}$. Because the z axis of the PAS at $\tau=0$ defines the reference frame, the constant const_l is given by

$$\text{const}_l = \textstyle\sum_{m'=-l}^{l} A_{\text{PAS}}^{l,m'*}\, A_{\text{PAS}}^{l,m'} = \sum_{m'=-l}^{l} -1^{l+m'}\, A_{\text{PAS}}^{l,-m'}\, A_{\text{PAS}}^{l,m'} \tag{44.6}$$

For $l=1$, this yields (see *isotropicrotdiffy.nb*) $\text{const}_1 = 2(\rho_{xy}{}^2 + \rho_{xz}{}^2 + \rho_{yz}{}^2)$. For $l=2$, $\text{const}_2 = \frac{3}{2}\left(1+\frac{\eta^2}{3}\right)\delta_{zz}^2$.

The corresponding *unnormalized NMR* spectral densities are as follows:

$$j_l(m\omega) = \int_0^{\infty} \mathrm{const}_l\, e^{-\frac{\tau}{\tau_l}} \cos(m\omega t)\,dt = const_l\, \frac{\tau_l}{1+\tau_l^{\,2}\,(m\omega)^2} \tag{44.7a}$$

where $\tau_1 = 1/2D_{\mathrm{rot}}$ and $\tau_2 = 1/6D_{\mathrm{rot}}$.

The *normalized* NMR spectral density[1] is as follows:

$$J_l(m\omega) = \frac{\mathrm{const}_l}{(A_{PAS}^{2,0\;2})} \frac{\tau_l}{1+\tau_l^{\,2}\,(m\omega)^2} \tag{44.7b}$$

The normalized spectral densities calculated in Equation 44.6b can then be used in the appropriate expressions from the previous chapters to calculate explicit relaxation rates. For example, quadrupolar T_1 and T_2 *relaxation of an I=1 quadrupolar nucleus* where only $l=2$ contributes is given by Equations 41.28a and 41.28b. Inserting the spectral densities from Equation 44.6b yields the following:

$$\frac{1}{T_1} = \frac{1}{2} \times C_Q \left(8 * \frac{\mathrm{const}_2}{(A_{\mathrm{PAS}}^{2,0\;2})} * \frac{\tau_2}{1+\tau_2^{\,2}\,(2\omega)^2} + 2 * \frac{\mathrm{const}_2}{(A_{\mathrm{PAS}}^{2,0\;2})} * \frac{\tau_2}{1+\tau_2^{\,2}\,\omega^2} \right) \tag{44.8a}$$

$$\frac{1}{T_2} = \frac{1}{\sqrt{2}} \times C_Q \left\{ 2 * \frac{\mathrm{const}_2}{(A_{\mathrm{PAS}}^{2,0\;2})} * \frac{\tau_2}{1+\tau_2^{\,2}\,(2\omega)^2} + 5 * \frac{\mathrm{const}_2}{(A_{\mathrm{PAS}}^{2,0\;2})} * \frac{\tau_2}{1+\tau_2^{\,2}\,\omega^2} + 3 * \frac{\mathrm{const}_2}{(A_{\mathrm{PAS}}^{2,0\;2})} * \tau_2 \right\} \tag{44.8b}$$

where $C_Q = A_{\mathrm{PAS}}^{2,0\;2} = \left(\sqrt{\frac{3}{2}} \frac{e^2qQ}{2I(2I-1)\hbar} \right)^2 = \frac{3}{8}\left(\frac{e^2qQ}{\hbar} \right)^2$. The relaxation times behave exactly like those calculated for tetrahedral and C_2 symmetry jumps in the last chapter, except that for small molecules in liquids the rotational diffusion coefficients D_{rot} are on the order of 10^{11} to $10^{12}\,\mathrm{s}^{-1}$ at ambient temperature. Because $\tau_2\,\omega_{\mathrm{Larmor}} \ll 1$, it follows that the corresponding relaxation times are independent of the Larmor frequency (e.g., magnetic field strength), and the so-called "extreme narrowing" condition is met.

EXPLANATION OF *isotropicrotdiffy.nb*

The user is told to evaluate *wigrot.nb,* then close it without saving changes.

The built-in Mathematica function SphericalHarmonicY differs from the desired form necessary for equivalence of the Legendre polynomials and the $m=0$ spherical harmonics Y_{lm}. The necessary correction factor is $\sqrt{4\pi/2l+1}$. This equivalence is necessary because the solutions to the rotational diffusion equations are generally expressed in terms of Legendre polynomials.

---

[1] Remember that the normalized NMR spectral density is used in equations that multiply it by $(A_{PAS}^{2,0})^2$.

The needed spherical harmonic functions Y[n_,m_,θ_,ϕ_] and Yconj[n_,m_,θ_,ϕ_] are defined in the next cells. A couple of examples are then given.

Then Equation 44.3 is introduced in a comment.

Equation 44.4b is evaluated, but the summation for Equation 44.3 is only carried out from $l=0$ to $l=6$. G1[m] and G2[m] are calculated, and both are shown to be independent of m. When multiplied by the inverse of the square of the correction factor $2l+1/4\pi$, the results match the well-known results G1[t] = 1/3 $e^{-2D\mathrm{rot}\,t}$ and G2[t] = 1/5 $e^{-2\,D\mathrm{rot}\,t}$.

To convert these spherical harmonic autocorrelation functions into NMR autocorrelation functions, Equation 44.6 is evaluated for $l=1$ and $l=2$. The results can be used to calculate relaxation times with Equations 44.7 and 41.28a and 41.28b.

HOMEWORK

Homework 44.1: What are the autocorrelation functions if the Mathematica built-in function SphericalHarmonicY is used rather than the corrected form?

Homework 44.2: Calculate the isotropic rotational diffusion relaxation times T_1 and T_2 for

1. a deuterium nucleus with $\frac{e^2qQ}{\hbar} = 2\pi * 215$ kHz, assuming that $\tau_2 = 1\times10^{-10}$ s
2. a ^{13}C nucleus dipolar coupled to a covalently bonded ^{1}H nucleus 1.09 Angstroms away, again assuming $\tau_2 = 1\times10^{-10}$ s

CHAPTER 45

CONCLUSION

Many important topics have *not* been covered in this primer, such as magnetic resonance imaging, solid-state cross-polarization, unpaired electron spin–nuclear spin interactions, and zero field nuclear magnetic resonance (NMR). It is the author's hope that with the theoretical tools that have been introduced, the NMR researcher and NMR student will be well equipped to handle such topics. For example, solid-state cross-polarization experiments are based on heteronuclear dipolar cross-relaxation in the presence of simultaneous radio frequency spin locks of the heteronuclei. Unpaired electron spin–nuclear spin interactions are based on strong dipolar and J-coupling between unpaired electrons and nuclear spins. Magnetic resonance imaging relies on the spatial encoding of NMR signals in the presence of magnetic field gradients. Zero field NMR takes advantage of slow T_1 relaxation to shuttle the NMR sample away from a polarizing magnetic field to a detector at zero field. The possibilities for enlightening NMR experiments are endless. NMR provides a miraculous window into the atomic world.

A Primer of NMR Theory with Calculations in Mathematica®, First Edition. Alan J. Benesi.

BIBLIOGRAPHY

Abragam A. *The Principles of Nuclear Magnetism*. New York: Oxford University Press; 1983.

Bak M, Nielsen NC. REPULSION, a novel approach to efficient powder averaging in solid-state NMR. J Magn Reson 1997;125:132–139.

Bax A. *Two Dimensional Nuclear Magnetic Resonance in Liquids*. Boston: Springer; 1982.

Bax A, Griffey RH, Hawkins BL. Correlation of proton and nitrogen-15 chemical shifts by multiple quantum NMR. J Magn Reson 1983;55:301.

Benesi AJ. Series expansion of propagators. J Magn Reson Ser A 1993;103:230–233.

Bloch F, Siegert A. Magnetic resonance in nonrotating fields. Phys Rev 1940;57:522–527.

Bodenhausen G, Ruben DJ. Natural abundance nitrogen-15 NMR by enhanced heteronuclear spectroscopy. Chem Phys Lett 1980;69:185–189.

Derome AE, Williamson MP. Rapid pulsing artifacts in double-quantum-filtered COSY. J Magn Reson 1990;88:177–185.

Diezemann G, Sillescu H. Revisiting angular jump models of molecular reorientations in viscous liquids. J Chem Phys 1999;111:1126–1136.

Doddrell DM, Pegg DT, Bendall MR. Distortionless enhancement of NMR signals by polarization transfer. J Magn Reson 1982;48:323–327.

Ernst RR, Bodenhausen G, Wokaun A. *Principles of Magnetic Resonance in One and Two Dimensions*. Oxford: Oxford University Press; 1987.

Feynman RP. *QED—The Strange Theory of Light and Matter*. Princeton: Princeton University Press; 1985.

Garbow JR, Weitekamp DP, Pines A. Bilinear rotation decoupling of homonuclear scalar interactions. Chem Phys Lett 1982;93:504–509.

Geil B, Fujara F, Sillescu H. ^{2}H NMR time domain analysis of ultraslow reorientations in supercooled liquids. J Magn Reson 1998;130:18–26.

Geil B, Kirschgen TM, Fujara F. Mechanism of proton transport in hexagonal ice. Phys Rev B 2005;72:014304-1–014304-7.

Gerstein BC, Dybowski CR. *Transient Techniques in the NMR of Solids—An Introduction to Theory and Practice*. Orlando: Academic Press, Inc.; 1985.

Gerstein BC. Rudimentary NMR—the classical picture. In: Grant DM, Harris RK, editors. *Encyclopedia of NMR*. Volume 7, Chichester: John Wiley & Sons Ltd.; 2002. p 4197–4204.

Guntert P, Schaefer N, Otting G, Wuthrich K. POMA—a complete mathematica implementation of the NMR product operator formalism. J Magn Reson Ser A 1993;101:103–105.

Heisenberg W. Über den Anschaulichen Inhalt der Quantentheoritischen Kinematik und Mechanik. Z Phys 1927;43:172–198.

Hoult DI. The magnetic resonance myth of radio waves. Concepts Magn Reson 1989;1:1–5.

A Primer of NMR Theory with Calculations in Mathematica®, First Edition. Alan J. Benesi.

Hoult DI, Bhakar B. NMR signal reception: virtual photons and coherent spontaneous emission. Concepts Magn Reson 1997;9:277–297.

Hull WE. Experimental aspects of two-dimensional NMR. In: Croasmun WR, Carlson RMK, editors. *Two-Dimensional NMR Spectroscopy—Applications for Chemists and Biochemists*. 2nd ed. New York: VCH Publishers, Inc.; 1994.

Jacobsen NE. *NMR Spectroscopy Explained: Simplified Theory, Applications and Examples for Organic Chemistry and Structural Biology*. Hoboken: John Wiley & Sons, Inc.; 2007.

Jeener J, Meier BH, Bachmann P, Ernst RR. Investigation of exchange processes by two-dimensional NMR spectroscopy. J Chem Phys 1979;71:4546–4553.

Keeler J, Neuhaus D. Comparison and evaluation of methods for two-dimensional NMR spectra with absorption-mode lineshapes. J Magn Reson 1985;63:454–472.

Keeler J. *Understanding NMR Spectroscopy*. 2nd ed. Chichester: John Wiley & Sons, Inc.; 2010.

Lang EW, Ludemann H-D. Nuclear magnetic relaxation rate dispersion in supercooled heavy water under high pressure. J Chem Phys 1984;81:3820–3827.

Levine IN. *Physical Chemistry*. 2nd ed. New York: McGraw-Hill, Inc.; 1983.

Levine IN. *Quantum Chemistry*. 2nd ed. Boston: Allyn and Bacon, Inc.; 1974.

Levitt MH. *Spin Dynamics—Basics of Nuclear Magnetic Resonance*. 2nd ed. Chichester: John Wiley & Sons, Ltd.; 2008.

Lipari G, Szabo A. Model-free approach to the interpretation of nuclear magnetic resonance relaxation in macromolecules. 1. Theory and range of validity. J Am Chem Soc 1982; 104:4546–4559.

Mareci TH, Freeman R. Mapping proton-proton coupling via double-quantum coherence. J Magn Reson 1983;51:531–535.

Marion D, Wuthrich K. Application of phase sensitive two-dimensional correlated spectroscopy (COSY) for measurements of 1H-1H spin-spin coupling constants in proteins. Biochem Biophys Res Commun 1983;113:967–974.

Mehring M. Internal spin interactions & rotations in solids. In: Grant DM, Harris RK, editors. *Encyclopedia of NMR*. Chichester: John Wiley & Sons Ltd.; 2002.

Mehring M. *Principles of High Resolution NMR in Solids*. 2nd ed. Berlin: Springer-Verlag; 1983.

Moniz WB, Gutowsky HS. Nuclear relaxation of ^{14}N by quadrupole interactions in molecular liquids. J Chem Phys 1963;38:1155–1162.

Palmer AG III, Cavanaugh J, Wright PE, Rance M. Sensitivity improvement in proton-detected two-dimensional heteronuclear correlation spectroscopy. J Magn Reson 1991; 93:151–170.

Reeves LW. The study of water in hydrate crystals by nuclear magnetic resonance. In: Emsley W, Feeney J, Sutcliffe LH, editors. *Progress in NMR Spectrscopy*. Volume 4, Oxford: Pergamon; 1969.

Sakurai JJ. In: Tuan SF, editor. *Modern Quantum Mechanics*. Redwood City: Addison-Wesley; 1985.

Schmidt-Rohr K, Spiess HW. *Multidimensional Solid-State NMR and Polymers*. London: Academic Press; 1994.

Shaka AJ, Keeler J, Frenkiel T, Freeman R. An improved sequence for broadband decoupling: WALTZ-16. J Magn Reson 1983;52:335–338.

Shaka AJ, Barker PB, Freeman R. Computer-optimized decoupling scheme for wideband applications and low level operation. J Magn Reson 1985;64:547–552.

Smith SA, Levante TO, Meier BH, Ernst RR. Computer simulations in magnetic resonance. An Object-Oriented Programming Approach. J Magn Reson Ser A 1994;106:75–105.

Solomon I. Relaxation processes in a system of two spins. Phys Rev 1955;99:559–565.

Sorensen OW, Eich GW, Levitt MH, Bodenhausen G, Ernst RR. Product operator formalism for the description of NMR pulse experiments. Prog NMR Spectrosc 1983;16:163–192.

Spiess HW. Rotation of molecules and nuclear spin relaxation. In: Diehl P, Fluck E, Kosfeld R, editors. *NMR, Basic Principles and Progress, Volume 15, Dynamic NMR Spectroscopy*. Berlin: Springer Verlag; 1978.

States DJ, Haberkorn RA, Ruben DJ. A two-dimensional nuclear overhauser experiment with pure absorption phase in four quadrants. J Magn Reson 1982;48:286–292.

Tang X, Benesi AJ. A ^{13}C spin-lattice relaxation study of the effect of substituents on rigid-body rotational diffusion in methylene chloride solution and in the solid state. J Phys Chem 1994;98:2844–2847.

Torchia DA, Szabo A. Spin-lattice relaxation in solids. J Magn Reson 1982;49:107–121.

Vega AJ, Luz Z. Quadrupole echo distortion as a tool for dynamic NMR: application to molecular reorientation in solid trimethylamine. J Chem Phys 1987;86:1803–1813.

von Neumann J. *Mathematische Grundlagen der Quantummechanik*. Berlin: Springer; 1932.

Weiss A, Weiden N. Deuteron magnetic resonance in crystal hydrates. In: Smith JAS, editor. *Advances in Nuclear Quadrupole Resonance*. Volume 4, London: Heyden; 1980.

Wittebort RJ, Szabo A. Theory of NMR relaxation in macromolecules: restricted diffusion and jump models for multiple internal rotations in amino acid side chains. J Chem Phys 1978;69:1722–1736.

Wittebort RJ, Usha MG, Ruben DJ, Wemmer DE, Pines A. Observation of molecular reorientation in ice by proton and deuterium magnetic resonance. J Am Chem Soc 1988;110:5668–5671.

Woessner DE. Brownian motion and its effects in chemical exchange and relaxation in liquids. Concepts Magn Reson 1996;8:397–421.

Wu D, Chen A, Johnson CS Jr. An improved diffusion-ordered spectroscopy experiment incorporating bipolar gradient pulses. J Magn Reson Ser A 1995;115:260–264.

INDEX

A Primer of NMR Theory with Calculations in Mathematica®, First Edition. Alan J. Benesi.

WILEY END USER LICENSE AGREEMENT